Énergie Matériaux Télécommunications Research Centre

ULTRAFAST CARRIER DYNAMICS IN QUANTUM MATERIALS PROBED BY TIME- AND ANGLE-RESOLVED PHOTOEMISSION SPECTROSCOPY

DYNAMIQUE ULTRARAPIDE DES PORTEURS DE CHARGE DANS LES MATÉRIAUX QUANTIQUES, SONDÉE PAR LA SPECTROSCOPIE DE PHOTOÉMISSION RÉSOLUE EN TEMPS ET EN ANGLE

Par
Akib Jabed

Thèse en présentée
Docteur en Sciences de l'énergie et des matériaux de l'Institut National de la Recherche Scientifique (INRS-EMT)
et
Docteur en Lasers, matière et nanosciences de l'Université de Bordeaux
Bidiplomation-Cotutelle

Jury d'évaluation

Directeur de recherche	Prof. Fabio Boschini Institut national de la recherche scientifique
Directeur de recherche	Dr. Yann Mairesse Université de Bordeaux
Co-Directeur de recherche	Dr. Samuel Beaulieu Université de Bordeaux
Rapporteur	Prof. Cris Adriano Université de Sherbrooke
Rapporteur	Prof. Michel Côté Université de Montréal
Examinateur externe	Prof. Mauro Fanciulli CY Cergy Paris Université
Président du jury et examinateur interne	Prof. Kenneth Beyerlein Institut national de la recherche scientifique

© Droits réservés de Akib Jabed, April 16, 2026

To my parents and my sister

ACKNOWLEDGMENTS

I am deeply grateful to Prof. Fabio Boschini and Dr. Samuel Beaulieu for offering me the exceptional opportunity to pursue a truly collaborative PhD between Montreal and Bordeaux. This joint supervision not only allowed me to work within two complementary scientific environments, but also shaped my development as an experimental physicist and as an individual.

I would like to first sincerely acknowledge Prof. Fabio Boschini for his support at the very beginning of my PhD journey, when I moved to a new country for the first time. His patience, understanding, and genuine care gave me the necessary time and confidence to adapt to a new academic and cultural environment. That initial support was crucial, as settling into a new country and research system is never easy, and I am truly thankful for his constant encouragement during that period. I am particularly grateful to Dr. Nicolas Gauthier. By shadowing him in the laboratory, I learned not only how to tackle complex experimental challenges, but also how to approach problems methodically and calmly. His way of thinking and problem-solving has influenced me far beyond the laboratory and will remain with me throughout my life. I would also like to thank Dr. Francesco Goto, with whom I greatly enjoyed our beamtime experiments. We shared a very similar experimental mindset, which made our collaboration both efficient and enjoyable. The many scientific discussions we had were insightful, stimulating, and genuinely fun. I am especially thankful to Dario Armanno, with whom I spent the most time in the laboratory at INRS. He was always willing to help, particularly during my early days when I was learning data analysis in Igor, and his support made that learning process much smoother. I would also like to thank Benson Frimpong Kwaku, who played a key role at the beginning of my PhD by helping me understand the experimental setup and its operation. Sharing the same office, we spent a lot of time together both inside and outside the lab. He also introduced me to Montreal, and those moments outside the lab are some of my fondest memories.

After moving to Bordeaux, I was warmly welcomed by the members of the CELIA laboratory, and I am truly thankful for their kindness and openness. I quickly realized that the work culture in Bordeaux is different from that in Canada, and I genuinely appreciated and enjoyed this environment. I would like to express my sincere gratitude to Dr. Samuel Beaulieu not only for his valuable academic guidance, but also for his generosity and support beyond research — including lending me his bicycle, which was an immense help in my daily life and made my transition to Bordeaux much easier. He is super nice and always helpful and because of which we had really good work culture. I am deeply thankful to Dr. Sotiris Fragkos for his remarkable kindness and constant support. From helping me find an apartment to guiding me through many practical aspects of settling in Bordeaux, his help was invaluable. Beyond that, we shared many great moments in the office and during weekends — exploring the city, visiting new places, trying different restaurants, attending games, and more — all of which made my time in Bordeaux truly memorable. I would also like to thank my colleague and friend Quentin Courtade, who was always there to help in every situation, from navigating French administrative procedures to choosing food at restaurants. We shared many enjoyable moments both inside and outside the lab, and his friendship made my experience in Bordeaux even richer. I am also grateful to our newest group member, Umberto Dellasette. In the final months of my PhD, we spent a lot of time together, and I am very happy to have gained another wonderful friend. Finally, I would like to thank my co-supervisor Dr. Yann Mairesse for his valuable advice during the development of the reflectivity setup. His enthusiasm, kindness, and

cheerful attitude created a very positive working atmosphere, and I am grateful for his guidance and encouragement.

On a more personal note, I extend my heartfelt appreciation to my family for their unconditional love, patience, and encouragement. Their support has been my constant source of strength during the challenges of daily life in different countires. Finally, to my friends both within and outside academia, thank you for providing balance, perspective, and laughter along the way.

RÉSUMÉ

Cette thèse présente des études de dynamiques électroniques ultrarapides résolues en moment dans les matériaux quantiques. Les processus de diffusion des électrons, tels que les interactions électron–électron et électron–phonon, sont à l'origine des propriétés électroniques, optiques et magnétiques macroscopiques des matériaux. De plus, les caractéristiques des structures de bandes électroniques de ces matériaux sont intimement liées à ces mécanismes de diffusion : il est donc nécessaire de disposer de sondes expérimentales offrant de très hautes résolutions en énergie et en moment pour les explorer complètement. Dans ce travail, nous utilisons la spectroscopie de photoémission résolue en angle et en temps (TR-ARPES), la technique la plus performante pour accéder aux dynamiques électroniques induites par la lumière et les suivre avec une résolution exceptionnelle en énergie, en moment et en temps.

Au laboratoire ALLS, nous avons concentré notre étude sur Bi_2Te_3, un isolant topologique tridimensionnel prototypique. En combinant une sonde à basse énergie (6 eV) et une excitation pompe dans l'infrarouge moyen (300 meV), nous avons apporté la première preuve expérimentale que les modifications de la structure de bandes du bulk induites par la température modulent les canaux de diffusion électron–phonon. De manière surprenante, nous montrons qu'un déplacement de seulement 15 meV du minimum de la bande de conduction inoccupée a un fort impact sur les processus de diffusion électronique au sein de l'état de surface topologique, qui est pertinent technologiquement. Nous observons également une accumulation de porteurs en bas de la bande de conduction à basse température, ce qui est dû à la réduction de l'espace de phase associé à la diffusion inter-vallées.

Au laboratoire CELIA, en utilisant une sonde dans l'extrême ultraviolet (XUV) à 21,6 eV à polarisation ajustable et une excitation pompe à 1,2 eV couplées à un time-of-fight momentum microscope, nous avons mené deux études distinctes. Premièrement, nous avons étudié le rôle des états in-gap (états de défauts) de SnS_2. Nos résultats révèlent que contrairement aux semiconducteurs de type n conventionnels, les états de défauts de type donneur induisent une déplacement vers le bas des bandes proches de la surface. Ces états in-gap permettent de peupler la bande de conduction après excitation dans le gap, ce qui conduit à de longues durées de vie de porteurs. Nous observons également un effet de photovoltage de surface prononcé lors de l'excitation, qui résulte de la courbure préexistante de bandes. Deuxièmement, nous avons examiné le composé à onde de densité de charge (CDW) 1T-$TiSe_2$, dont la température de transition est inférieure à 200 K. Malgré un débat de longue date concernant l'origine des fluctuations CDW (couplage électron–phonon ou corrélations excitoniques), notre étude démontre que des fluctuations cohérentes de la CDW persistent au-dessus de la température de transition et sont dominées par les interactions électron–phonon.

Dans leur ensemble, ces résultats approfondissent notre compréhension de la manière dont les porteurs, les défauts et les modes collectifs façonnent les propriétés macroscopiques des matériaux quantiques. Ce travail établit une base solide vers le contrôle et l'ingénierie des états électroniques dans les dispositifs quantiques, spintroniques, électroniques et optoélectroniques de nouvelle génération.

Mots-clés : matériaux quantiques, dynamique ultrarapide, TR-ARPES, isolants topologiques, TMDCs, SnS_2, $TiSe_2$, onde de densité de charge, photovoltage de surface, états de défauts.

ABSTRACT

This thesis presents momentum-resolved studies of ultrafast electron dynamics in quantum materials. Electron scattering processes, such as electron-electron and electron-phonon scattering, underlie the macroscopic electronic, optical, and magnetic properties of materials. Furthermore, the details of the electronic band structure are intimately related to these scattering properties. Therefore, experimental probes with high energy and momentum resolutions are necessary for a comprehensive exploration of materials. In this study, we leverage time- and angle-resolved photoemission spectroscopy (TR-ARPES), the most powerful technique for accessing and tracking light-induced electron dynamics with exquisite energy, momentum, and temporal resolutions.

At ALLS Laboratory, we focused our study on Bi_2Te_3, a prototypical 3D topological insulator. By employing a low-photon-energy probe (6 eV) and mid-infrared pump excitation (300 meV), we provided the first experimental evidence that temperature-induced modifications of the bulk band structure modulate electron-phonon scattering channels. Surprisingly, we show that even a 15 meV shift of the minimum of the unoccupied conduction band has a dramatic impact on electron scattering processes within the technologically relevant topological surface state. Furthermore, we observe an accumulation of carriers at the bottom of the conduction band at low temperature due to the reduction of the intervalley scattering phase space.

At the CELIA laboratory, using a polarization-tunable 21.6 eV extreme ultraviolet (XUV) probe and 1.2 eV pump coupled to a time-of-flight momentum microscope, we conducted two studies. First, we investigated the role of in-gap states in SnS_2. Our results reveal that, unlike conventional n-type semiconductors, donor-type defect states induce downward band bending near the surface. These in-gap states enable conduction band population through below-bandgap excitation, resulting in long carrier lifetimes. We further observe a pronounced surface photovoltage effect upon pumping due to the pre-existing band bending. Second, we examined the charge density wave (CDW) compound 1T-$TiSe_2$, which has a transition temperature below 200 K. Despite long-standing debate regarding whether CDW fluctuations are driven by electron-phonon coupling or excitonic correlations, our study demonstrates that coherent CDW fluctuations persist above the transition temperature and are dominated by electron-phonon interactions.

Collectively, these results advance our understanding of how carriers, defects, and collective modes shape the macroscopic properties of quantum materials. This work establishes a foundation for controlling and engineering electronic states in next-generation quantum, spintronic, electronic, and optoelectronic devices.

Keywords : quantum materials, Ultrafast dynamics, TR-ARPES, topological insulators, TMDCs, SnS_2, $TiSe_2$, charge density wave, surface photovoltage, defect states

SOMMAIRE RÉCAPITULATIF

Les matériaux quantiques représentent un domaine de la physique de la matière condensée où des effets quantiques se manifestent à des échelles macroscopiques, donnant naissance à des propriétés exotiques absentes des matériaux conventionnels. Ces systèmes (qui incluent les isolants topologiques, les dichalcogénures de métaux de transition (TMDCs) et les composés à onde de densité de charge (CDW)) présentent des phénomènes émergents gouvernés par de fortes corrélations électroniques, la topologie, la dimensionalité réduite et le couplage complexe entre les degrés de liberté de charge, de spin, d'orbite et de réseau. Comprendre comment ces matériaux répondent à des perturbations externes, en particulier sur des échelles de temps ultracourtes, est essentiel à la fois pour la physique fondamentale et pour leurs applications technologiques dans les dispositifs quantiques de nouvelle génération, la spintronique et l'optoélectronique.

Un thème central qui unifie des matériaux quantiques très divers est le fait que leurs propriétés macroscopiques émergent à partir d'interactions microscopiques opérant sur des échelles d'énergie allant du meV à l'eV. De faibles perturbations externes telles que des variations de température, de concentration en porteurs, une excitation optique ou l'application de champs, peuvent faire basculer de manière spectaculaire l'équilibre entre phases concurrentes, induisant des transitions métal–isolant, modifiant les propriétés de transport ou révélant des états électroniques cachés. Bien que les techniques spectroscopiques à l'équilibre, telles que la spectroscopie de photoémission résolue en angle (ARPES), aient été déterminantes pour mesurer les structures électroniques à l'état fondamental, elles apportent un éclairage limité sur la manière dont les phases ordonnées se forment, évoluent ou s'effondrent hors équilibre.

Le développement des technologies laser ultrarapides a profondément transformé l'étude des matériaux quantiques en permettant des mesures résolues en temps sur des échelles comparables aux dynamiques électroniques et vibrationnelles intrinsèques. La spectroscopie de photoémission résolue en temps et en angle (TR-ARPES) étend l'ARPES conventionnelle au domaine temporel, permettant l'observation directe de l'évolution des structures de bandes électroniques et des populations de porteurs après excitation. Dans une expérience typique de TR-ARPES, une impulsion pompe ultracourte met le système hors équilibre, tandis qu'une impulsion sonde retardée émet des photoélectrons dont l'énergie cinétique et l'angle d'émission encodent la structure électronique instantanée. En faisant varier le délai pompe–sonde, la TR-ARPES reconstruit l'évolution temporelle du système électronique, donnant un accès unique aux états inoccupés, aux voies de relaxation des porteurs, aux processus de diffusion, à la renormalisation des bandes et aux états électroniques transitoires inaccessibles à l'équilibre.

Malgré des progrès significatifs, des questions fondamentales demeurent quant à la manière dont les porteurs redistribuent énergie et impulsion dans les matériaux quantiques, à l'influence des défauts et de la courbure de bandes sur les dynamiques hors équilibre, et au rôle des modes collectifs tels que les phonons et les ondes de densité de charge dans les réponses ultrarapides. Comprendre ces processus à un niveau microscopique est crucial, car ils déterminent directement les propriétés de transport, les réponses optiques et la stabilité des phases, qui sont des facteurs clés pour la compréhension fondamentale comme pour les applications en technologiques.

Cette thèse aborde ces questions à travers des investigations systématiques en TR-ARPES de trois systèmes représentatifs de matériaux quantiques : l'isolant topologique tridimensionnel

Bi_2Te_3, le semi-conducteur à couches SnS_2 et le composé à onde de densité de charge 1T-$TiSe_2$. Chaque système présente une physique distincte issue de mécanismes microscopiques différents, tout en illustrant ensemble des principes communs gouvernant le comportement hors équilibre des matériaux quantiques. Ce travail s'appuie sur deux plateformes TR-ARPES complémentaires de pointe : l'une optimisée pour une haute résolution en énergie et en impulsion près du centre de la zone de Brillouin (ALLS Laboratory, Canada), et l'autre offrant une large couverture en impulsion avec un contrôle de la polarisation (CELIA Laboratory, France), permettant une caractérisation approfondie sur différentes régions de l'espace des impulsions et sous différentes conditions d'excitation.

Cadre théorique : ARPES et TR-ARPES

Avant de présenter les résultats expérimentaux, il est essentiel d'établir le fondement théorique de la spectroscopie de photoémission. L'ARPES repose sur l'effet photoélectrique : lorsque des photons d'énergie $h\nu$ dépassent la fonction de travail Φ du matériau, des électrons sont photoémis avec une énergie cinétique

$$E_{\mathrm{kin}} = h\nu - \Phi - |E_B|, \tag{1}$$

où E_B est l'énergie de liaison à l'intérieur du solide. En mesurant à la fois l'énergie cinétique et l'angle d'émission des photoélectrons, l'ARPES cartographie directement la structure de bandes électronique $E(\mathbf{k})$, où $\mathbf{k}$ est l'impulsion cristalline.

Le processus de photoémission est généralement interprété dans le cadre du modèle en trois étapes, qui sépare le processus en : (i) excitation optique d'un électron depuis un état initial vers un état final du cristal, (ii) transport du photoélectron jusqu'à la surface, et (iii) échappement dans le vide. Bien que ce modèle phénoménologique néglige les effets de corps multiples et suppose des étapes indépendantes, il rend compte de la plupart des observations expérimentales. Plus précisément, la photoémission est gouvernée par la règle d'or de Fermi, où la probabilité de transition dépend à la fois de l'élément de matrice dipolaire monoélectronique (encodant la polarisation du photon et les symétries orbitalaires) et de la fonction spectrale à une particule $A(\mathbf{k}, \omega)$, qui contient des informations sur les dispersions des quasi-particules et leurs durées de vie.

Dans un système de corps multiples en interaction, la fonction spectrale est reliée à la partie imaginaire de la fonction de Green électronique, qui peut s'exprimer en termes de l'auto-énergie complexe

$$\Sigma(\mathbf{k}, \omega) = \Sigma'(\mathbf{k}, \omega) + i\Sigma''(\mathbf{k}, \omega). \tag{2}$$

La partie réelle Σ' décrit la renormalisation des bandes due aux interactions, tandis que la partie imaginaire Σ'' détermine les durées de vie des quasi-particules. En analysant la dépendance en énergie et en impulsion des bandes ARPES, on peut extraire des informations sur le couplage électron–phonon, la diffusion électron–électron et d'autres effets de corps multiples.

En étendant l'ARPES au domaine temporel, la TR-ARPES donne accès aux dynamiques hors équilibre en suivant l'évolution de l'intensité de photoémission $I(\mathbf{k}, \omega, \tau)$ en fonction du retard pompe–sonde τ. Dans l'approximation de quasi-équilibre, l'intensité dépendante du temps peut s'exprimer comme

$$I(\mathbf{k}, \omega, \tau) \simeq A(\mathbf{k}, \omega, \tau)\, |M(\mathbf{k}, \omega, \tau)|^2\, f(\mathbf{k}, \omega, \tau), \tag{3}$$

où $A(\mathbf{k}, \omega, \tau)$ est la fonction spectrale dépendante du temps, $|M|^2$ représente les éléments de matrice de photoémission (qui peuvent également évoluer transitoirement), et $f(\mathbf{k}, \omega, \tau)$ est la

fonction de distribution électronique dépendante du temps. Cette factorisation montre que l'intensité TR-ARPES reflète l'évolution couplée de trois grandeurs distinctes : l'occupation (via f), les interactions de corps multiples (via A) et le caractère orbital/symétrique (via M). Distinguer ces contributions requiert une analyse soigneuse combinant des données résolues en énergie–impulsion–temps avec une modélisation théorique.

Un avantage de la TR-ARPES est sa capacité à cartographier les états électroniques inoccupés. À l'équilibre, l'ARPES est limitée aux états occupés par la distribution de Fermi–Dirac. Cependant, l'excitation optique promeut des électrons vers des états auparavant inoccupés, créant des populations transitoires au-dessus du niveau de Fermi. En suivant ces populations d'états excités, la TR-ARPES permet une cartographie directe des dispersions de bande de conduction, l'extraction des gaps et l'observation des voies de relaxation des porteurs qui gouvernent les propriétés de transport et optiques.

Plateformes expérimentales : laboratoires ALLS et CELIA

Le travail expérimental présenté dans cette thèse a été réalisé sur deux installations TR-ARPES complémentaires.

ALLS Laboratory TR-ARPES Endstation

L'installation ALLS (Advanced Laser Light Source) à l'INRS-EMT au Canada héberge un système TR-ARPES basé sur un amplificateur fibre dopée Yb haute puissance (Tangerine, Amplitude Laser) délivrant des impulsions de 150 fs à un taux de répétition de 250 kHz. Le système génère une sonde ultraviolette de 6 eV par conversion de fréquence non linéaire (génération des troisième et cinquième harmoniques dans des cristaux BBO), offrant une excellente résolution en énergie ($\sim$ 15 meV) combinée à une résolution temporelle de $\sim$ 400 fs. De manière cruciale, la ligne intègre une source pompe infrarouge moyen accordable (4 à 8 μm) générée via un amplificateur paramétrique optique (OPA) en trois étages suivi d'une génération par différence de fréquence (DFG). Cette capacité permet une excitation sélective de modes de basse énergie tels que les phonons, ouvrant la voie à des études de contrôle sélectif de modes et de pompage résonant d'excitations collectives.

Les photoélectrons sont analysés à l'aide d'un analyseur hémisphérique SPECS Astraios 190 avec un angle d'acceptation de 60°. La technologie de déflexion permet une cartographie tridimensionnelle complète (E, k_x, k_y) sans rotation mécanique de l'échantillon, en scannant électrostatiquement le faisceau d'électrons à travers l'ouverture d'entrée de l'analyseur. Le système atteint une résolution en énergie exceptionnelle (capacité jusqu'à $\sim$2 meV) et une résolution angulaire de $\sim$0.1°, ce qui le rend idéal pour l'étude de caractéristiques de basse énergie subtiles près du centre de la zone de Brillouin (point Γ).

L'axe scientifique à ALLS se concentre sur des matériaux dont la physique se situe près de Γ, tels que les gaps supraconducteurs dans les cuprates, les états de surface topologiques dans Bi_2Te_3 et les phénomènes de pseudogap. La combinaison d'une haute résolution, d'une excitation infrarouge moyen accordable et de la capacité de cartographie en impulsion fournit une plateforme puissante pour étudier la diffusion intervalle, les dynamiques médiées par les phonons et la renormalisation de bandes dépendante de la température.

Ligne TR-ARPES du laboratoire CELIA

Le laboratoire CELIA (Centre Lasers Intenses et Applications) à l'Université de Bordeaux dispose d'une ligne TR-ARPES, optimisée pour une large couverture en impulsion et un contrôle de la polarisation. Le système est piloté par un laser fibre Yb à double amplificateur (BlastBeat, Amplitude) opérant à 166 kHz, délivrant des faisceaux synchronisés de 50 W à 1030 nm.

L'innovation clé est une sonde ultraviolet extrême (XUV) à polarisation accordable, générée par génération d'harmoniques d'ordre élevé (HHG) dans l'argon, qui produit des photons de 21.6 eV avec une polarisation linéaire ajustable de manière continue. La sonde est générée en focalisant des impulsions doublées en fréquence à 515 nm dans un jet mince d'argon, puis le faisceau XUV est réfléchi et focalisé par des miroirs multicouches SiC/Mg optimisés pour 21.6 eV. Un montage quart d'onde entièrement réflectif permet un basculement rapide entre différents états de polarisation elliptique, incluant une polarisation quasi-circulaire avec $\sim$90% d'ellipticité, essentielle pour des mesures de dichroïsme circulaire pouvant sonder la courbure de Berry et le moment angulaire orbital.

Le bras pompe infrarouge (1.2 eV, fondamentale à 1030 nm) dispose d'un contrôle de polarisation indépendant via des lames d'onde motorisées, permettant des mesures systématiques dépendantes de la polarisation. L'énergie de photon plus élevée (21.6 eV vs. 6 eV à ALLS) donne accès à une région beaucoup plus large de l'espace des phases, avec des fenêtres d'énergie cinétique suffisantes pour cartographier des zones de Brillouin de surface entières, y compris des répliques d'ordre supérieur.

La détection des photoélectrons est assurée par un microscope d'impulsion temps-de-vol (GST mbH) sur mesure, qui capture simultanément la distribution complète en impulsion dans le plan (k_x, k_y) sur une large gamme d'énergies de liaison, avec une résolution en énergie globale de $\sim$44 meV et une résolution temporelle de $\sim$144 fs. Le microscope fonctionne en modes résolus en impulsion et en imagerie espace réel, permettant des mesures spatialement sélectives sur des échantillons hétérogènes ou micro-exfoliés.

Cette plateforme est optimisée pour des matériaux dont la physique pertinente s'étend à travers la zone de Brillouin, par exemple les phénomènes de vallée (valléetronique) dans les TMDCs, la cartographie de surface de Fermi dans les matériaux à CDW et la détermination de textures orbitalaires via l'ARPES dichroïque. La combinaison d'une polarisation accordable, d'une large couverture en impulsion et d'une acquisition complète 4D (E, k_x, k_y, t) fournit des capacités uniques pour étudier la diffusion dépendante de l'impulsion, les excitations sélectives par symétrie et les textures orbitale/spin dans les états excités.

Ensemble, ces deux installations offrent des atouts complémentaires : ALLS fournit une résolution ultime près de Γ avec un contrôle accordable en infrarouge moyen, tandis que CELIA permet une cartographie complète de la zone de Brillouin avec une sélectivité en polarisation. Cette thèse exploite ces deux plateformes afin d'obtenir une vision complète, résolue en impulsion et en temps, des dynamiques ultrarapides des porteurs dans une diversité de matériaux quantiques.

Diffusion intervallée contrôlée par la température dans Bi_2Te_3

La première étude majeure porte sur l'isolant topologique tridimensionnel Bi_2Te_3 et se concentre sur la manière dont la renormalisation des bandes induite par la température contrôle les proces-

sus de diffusion ultrarapide des porteurs. Les isolants topologiques se caractérisent par un volume isolant et des états de surface métalliques polarisés en spin, protégés par la symétrie par renversement du temps. Comprendre les dynamiques des porteurs dans les états du volume et de surface est essentiel pour des applications potentielles en spintronique et en calcul quantique, mais le rôle de la température dans la modulation des voies de diffusion reste largement inexploré.

Approche expérimentale et observations

En utilisant la plateforme TR-ARPES d'ALLS avec une sonde de 6 eV et une pompe infrarouge moyen de 300 meV, nous avons cartographié la structure électronique inoccupée de Bi_2Te_3 dopé p en fonction de la température (30 k à 180 k) et du délai pompe–sonde. L'énergie de pompe de 300 meV permet des transitions optiques directes de la bande de valence occupée vers la bande de conduction, excitant spécifiquement des électrons dans l'état de résonance de surface légèrement décalé du point Γ.

Aux courts délais pompe–sonde ($\sim$0.5 ps), les mesures révèlent une population d'un continuum d'états de bande de conduction reliant la vallée Γ (minimum local de bande de conduction au centre de zone) et les vallées Q (minima absolus de bande de conduction situés à $k \approx \pm 0.15$ Å^{-1}). Au cours des picosecondes suivantes, une accumulation d'intensité particulièrement longue apparaît aux vallées Q et persiste pendant des dizaines de picosecondes. Cette signature a été rapportée auparavant et attribuée à la formation d'un exciton topologique spatialement indirect, liant des électrons de surface (dans l'état de surface topologique) à des trous du volume.

Cependant, nos mesures systématiques dépendantes de la température révèlent un comportement incompatible avec cette interprétation excitonique. Nous observons que la position en énergie de l'accumulation d'intensité reste essentiellement constante pour toutes les températures, sans décalage ni renormalisation mesurable qui serait attendu pour un état excitonique lié.

Renormalisation des bandes dépendante de la température

Le résultat clé émerge d'une analyse approfondie de l'évolution en température de la structure de bandes du volume : en intégrant l'intensité de photoémission sur les premières 5 ps à chaque température et en extrayant des courbes de distribution en énergie (EDCs) au point Γ, nous quantifions la dépendance en température du gap du volume. Lorsque la température augmente de 30 k à 180 k, le minimum de bande de conduction à Γ se décale vers le bas d'environ 15 meV, tandis que le maximum de bande de valence se décale vers le haut, réduisant le gap direct du volume d'un total de $\sim$62 meV. Cette renormalisation est en excellent accord quantitatif avec des calculs *ab initio* incluant à la fois la dilatation thermique et les contributions du couplage électron–phonon.

De manière cruciale, la position des vallées Q reste quasi inchangée sur le même intervalle de température (< 3 meV de décalage). Cette renormalisation asymétrique a des conséquences profondes sur la diffusion des porteurs : à basse température, le minimum Γ se situe significativement au-dessus des minima Q, conduisant à un faible recouvrement spectral et à une diffusion intervalle $\Gamma \leftrightarrow Q$ inefficace. À haute température, en revanche, le décalage vers le bas de la bande à Γ augmente le recouvrement spectral, ouvrant un nouveau canal de diffusion efficace de Q vers Γ.

Dynamiques ultrarapides et espace de phase de diffusion

Les mesures résolues en temps révèlent directement les conséquences de cet espace de phase modifié. À 30 k, après la photoexcitation initiale, les porteurs s'accumulent rapidement dans les vallées Q tandis que la vallée Γ reste appauvrie, ne présentant qu'une population transitoire qui décroît en quelques picosecondes. À 180 k, au contraire, une population longue durée persiste à la vallée Γ, accompagnée d'un poids spectral réduit aux vallées Q.

Pour quantifier cet effet, nous définissons un paramètre de recouvrement spectral en multipliant des EDCs normalisées de la vallée Γ (temps précoces, 0 à 5 ps) et de la vallée Q (temps tardifs, 18 à 22 ps). Cette métrique de recouvrement reflète directement l'espace de phase disponible pour la diffusion électron–phonon intervalle. Nous trouvons que le recouvrement spectral augmente de manière monotone avec la température, et suit étroitement le rapport d'intensité I_Γ/I_Q extrait des données résolues en temps. Cela montre que le transfert de poids spectral de Q vers Γ est gouverné par des changements dépendants de la température de l'espace de phase de diffusion électron–phonon.

Simulations Monte Carlo cinétiques

Afin de valider cette interprétation et d'isoler le rôle des modifications de structure de bandes, nous avons mis en œuvre des simulations Monte Carlo cinétiques (KMC) de la dynamique de diffusion électron–phonon. Le modèle représente la bande de conduction comme une grille discrète d'états électroniques et calcule les probabilités de diffusion via la règle d'or de Fermi avec un élément de matrice électron–phonon simplifié. La seule différence entre les simulations à différentes températures est un décalage de 16 meV du minimum de la vallée Γ (ce qui correspond à l'observation expérimentale) tandis que tous les autres paramètres (population phononique, force de couplage électron–phonon) sont maintenus constants.

Malgré leur simplicité, les simulations KMC reproduisent avec succès les deux observations expérimentales majeures : (i) la formation d'une accumulation d'intensité longue durée aux vallées Q à basse température, et (ii) le transfert de poids spectral de Q vers Γ à haute température. En faisant varier séparément la population phononique (distribution de Bose–Einstein) et la structure de bandes dans les simulations, nous montrons que la renormalisation des bandes (et non la seule augmentation de la population phononique) est le facteur dominant contrôlant l'efficacité de la diffusion $Q \to \Gamma$.

Ces résultats établissent que même un décalage modeste ($\sim$15 meV) du bord de la bande induit par la température peut profondément remodeler les dynamiques ultrarapides des porteurs en modulant l'espace de phase de diffusion disponible. L'accumulation d'intensité longue durée aux vallées Q résulte d'un effet de goulot d'étranglement : à basse température, le faible recouvrement spectral entre Γ et Q supprime la diffusion intervalle, provoquant une accumulation des porteurs aux minima Q, où l'état de surface topologique offre une densité d'états limitée pour une relaxation ultérieure. À haute température, un couplage $\Gamma \leftrightarrow Q$ renforcé permet une rétrodiffusion efficace de Q vers Γ, réduisant la durée de vie de la population aux vallées Q.

Implications

Nos résultats posent des défis importants à l'interprétation excitonique proposée précédemment pour l'accumulation d'intensité. Par ailleurs, l'analyse du dichroïsme linéaire montre que cette accumulation présente une symétrie trigonale caractéristique des états du volume plutôt que la symétrie hexagonale de l'état de surface topologique, ce qui soutient son interprétation comme une accumulation de charge dans la bande de conduction du volume aux vallées Q.

Au-delà de la résolution de ce débat spécifique, ce travail établit la température comme un paramètre de contrôle efficace pour l'ingénierie des voies de diffusion dans les isolants topologiques. Ces résultats peuvent également être pertinents pour comprendre les performances thermoélectriques exceptionnelles de Bi_2Te_3, puisque la diffusion intervallée impacte directement la conductivité thermique et le facteur de mérite thermoélectrique. Plus largement, cette étude montre que des modifications subtiles de structure de bandes (facilement négligées à l'équilibre) peuvent avoir des conséquences majeures sur les dynamiques de porteurs hors équilibre, soulignant l'importance d'investigations TR-ARPES dépendantes de la température.

Dynamiques médiées par les défauts et photovoltage de surface dans SnS_2

La deuxième étude majeure examine le semi-conducteur de van der Waals feuilleté disulfure d'étain (SnS_2), en se concentrant sur la manière dont des défauts intrinsèques créent des états électroniques dans le gap influençant profondément la courbure de bandes à l'équilibre ainsi que les dynamiques ultrarapides induites par la lumière. Les TMDCs suscitent un intérêt intense pour l'optoélectronique, la photocatalyse et les applications énergétiques, mais le rôle des défauts (omniprésents dans les matériaux réels) dans la gouvernance de la réponse optique et des dynamiques des porteurs demeure partiellement compris.

Structure électronique à l'équilibre et texture orbitale

SnS_2 cristallise dans la structure 1T de type CdI_2 avec une coordination octaédrique de l'étain, présentant un gap indirect dans le visible ($\sim$2.2 eV) qui reste presque indépendant de l'épaisseur. En utilisant une ARPES XUV résolue en polarisation au CELIA, nous avons cartographié la structure de bande de valence le long des directions de haute symétrie M–Γ–M et K–Γ–K tout en faisant tourner de manière continue l'axe de polarisation linéaire de la sonde XUV à 21.6 eV.

Les mesures révèlent des bandes de valence dispersives dominées par le caractère S $3p$, avec une dispersion relativement plus forte le long de M–Γ–M que le long de K–Γ–K. En calculant le dichroïsme linéaire dans les distributions angulaires de photoélectrons (LDAD), défini comme la différence $I_p - I_s$ entre les intensités de photoémission en polarisation p et s, nous extrayons des informations sur le caractère orbital dans le plan et hors du plan des états électroniques.

Les cartes LDAD présentent des signatures dichroïques nettes en accord avec les prédictions DFT : la bande de valence la plus haute près de Γ montre un dichroïsme négatif (émission plus forte en polarisation s), indiquant un caractère orbital dominant dans le plan (p_x, p_y), tandis que des états plus profonds montrent un dichroïsme positif (émission plus forte en polarisation p), caractéristique des orbitales hors du plan (p_z). Le long de K–Γ–K, le caractère orbital évolue de

dans le plan près de Γ vers hors du plan près de K, là encore en accord avec la théorie. Ces mesures confirment expérimentalement la texture orbitale et démontrent la puissance de l'ARPES résolue en polarisation pour caractériser des matériaux feuilletés.

États dans le gap et courbure de bandes

Au-delà des bandes de valence et de conduction attendues, les mesures révèlent deux familles distinctes d'états dans le gap : (i) une large signature s'étendant du maximum de bande de valence (VBM) jusqu'à $\sim$1.5 eV au-dessus du VBM, et (ii) une signature plus étroite située à $\sim$2.4 eV au-dessus du VBM, juste en dessous du minimum de bande de conduction (CBM). Ces états dans le gap sont détectables immédiatement après le clivage et persistent durant les mesures.

Afin d'en étudier l'origine et l'évolution, nous avons suivi sur le long terme le spectre de photoémission pendant 42 hour après la préparation de surface. Les données révèlent une augmentation progressive du poids spectral des deux familles d'états dans le gap, accompagnée d'un décalage vers le bas en énergie (vers des énergies de liaison plus élevées) de l'ensemble de la structure de bande de valence. Cette évolution indique le développement d'une courbure de bandes vers le bas, un gradient de potentiel de surface issu d'une redistribution de charge près de la surface.

Les états dans le gap sont attribués à des défauts donneurs, principalement des lacunes de soufre avec une contribution plus faible d'interstitiels d'étain, en accord avec des études théoriques et expérimentales antérieures sur SnS_2. Dans les semi-conducteurs de type n, des défauts donneurs créent des états ionisés positivement près de la surface. Pour atteindre l'équilibre, des électrons se transfèrent du volume vers des états de défauts de surface, formant une couche d'accumulation électronique à la surface et une région de déplétion positivement chargée dans le volume proche surface. Cette séparation de charge génère un champ électrique interne pointant du volume vers la surface, provoquant une courbure vers le bas des bandes de conduction et de valence près de la surface.

La corrélation observée (augmentation du poids spectral dans le gap accompagnant une courbure de bandes vers le bas renforcé) confirme directement que les défauts donneurs de surface pilotent la courbure de bandes dans SnS_2. Ce scénario est analogue à des observations dans d'autres systèmes, tels que Bi_2Se_3 (où des lacunes de Se induisent une courbure vers le bas) et le phosphore noir dopé par des alcalins (où des électrons donnés créent des effets similaires).

Photovoltage de surface induit par la lumière

Sous excitation optique par des impulsions pompe infrarouges de 1.2 eV, nous observons un effet marqué de photovoltage de surface transitoire (SPV), se manifestant par un décalage rigide vers le haut en énergie de l'ensemble du spectre de photoémission. En intégrant l'intensité de photoémission sur l'espace des impulsions et en ajustant la position de la bande de valence à différents délais pompe–sonde, nous quantifions le décalage induit par le SPV en fonction du temps et de la fluence.

Les dynamiques temporelles présentent un comportement caractéristique du SPV : un décalage linéaire vers le haut débutant à des délais pompe–sonde négatifs (avant l'arrivée de la pompe), suivi d'un changement abrupt de pente à temps zéro. Le décalage à délais négatifs pro-

vient d'interactions électromagnétiques entre le champ électrique de surface induit par le SPV et les photoélectrons se propageant dans le vide, un effet purement cinématique dont l'échelle de temps dépend de l'énergie cinétique des photoélectrons et de la géométrie pompe–sonde.

L'amplitude du SPV croît approximativement de manière linéaire avec la fluence, atteignant $\sim$70 meV à 3.9 mJ/cm^2. Ce décalage vers le haut correspond à un aplatissement partiel de la courbure de bandes vers le bas à l'équilibre : la photoexcitation redistribue la charge dans la région de cintrage, générant un champ compensateur qui réduit le potentiel net de surface. L'observation du SPV confirme l'existence d'une courbure de bandes préalable et démontre que l'excitation optique peut moduler transitoirement les champs de surface dans SnS_2.

Pour isoler les dynamiques ultrarapides intrinsèques des porteurs des décalages rigides induits par le SPV, nous avons développé une procédure de correction : à chaque délai pompe–sonde, la position de la bande de valence est extraite par ajustement gaussien, puis l'ensemble du spectre est translaté rigidement en énergie afin de supprimer le déplacement dépendant du temps. Cette correction SPV est essentielle pour une interprétation quantitative des dynamiques photoinduites, car le décalage rigide peut sinon masquer ou imiter une évolution spectrale réelle.

Excitation sous-gap et dynamiques ultrarapides des porteurs

Après correction des décalages induits par le SPV, les cartes TR-ARPES différentielles (signal pré-pompe soustrait) révèlent des dynamiques ultrarapides riches. L'énergie de photon de la pompe 1.2 eV est bien inférieure au gap fondamental $\sim$2.2 eV, pourtant nous observons clairement une population de la bande de conduction après excitation. Ceci se produit via des transitions optiques depuis des états dans le gap vers la bande de conduction, un processus en deux étapes où les états dans le gap agissent comme niveaux intermédiaires permettant une absorption sous-gap.

Les dynamiques résolues en temps révèlent quatre caractéristiques principales :

1. **Photoémission assistée par laser (LAPE) :** signaux positifs extrêmement brefs au temps zéro, provenant de processus cohérents à deux photons (XUV+IR), fournissant une détermination *in situ* du recouvrement temporel et une largeur de corrélation croisée $\sim$140 fs.
2. **Déplétion des états dans le gap :** signal différentiel négatif marqué (création de phototrous) dans les états bas du gap ($\sim$1.5 eV au-dessus du VBM), suivi d'une récupération sur des échelles de temps de $\sim$1 ps (composante rapide) et $\sim$5 ps (composante lente).
3. **Dynamiques des états hauts du gap :** les états dans le gap juste sous le CBM montrent un signal LAPE initial, suivi d'une déplétion croissante à plus long temps ($\sim$50 ps), suggérant une migration de lacunes des états bas vers les états hauts du gap.
4. **Population longue durée de la bande de conduction :** signal positif fort au-dessus de 2.5 eV correspondant à des électrons excités au minimum de bande de conduction (situé aux points M), avec des durées de vie dépassant la fenêtre de mesure ($>$10 ps). Les cartes de contours à énergie constante visualisent directement l'accumulation de porteurs dans les poches au point M.

Les dynamiques observées sont cohérentes avec le mécanisme suivant : (i) les photons sous-gap promeuvent des électrons depuis les états bas du gap vers la bande de conduction, créant des lacunes dans le gap ; (ii) ces lacunes se redistribuent par diffusion entre différentes familles d'états dans le gap ; (iii) les électrons photoexcités s'accumulent au minimum indirect de la bande

de conduction avec des durées de vie longues, en raison du désaccord en impulsion entre les extrémas direct (Γ) et indirect (M), supprimant la recombinaison radiative.

La possibilité de peupler la bande de conduction via une excitation sous-gap médiée par des états de défauts a des implications importantes pour la compréhension de l'activité photocatalytique et des propriétés d'absorption dans le visible de SnS_2, où l'on sait que les défauts peuvent améliorer les performances malgré un gap fondamental important.

Implications

Cette étude établit SnS_2 comme un système modèle où la physique des défauts, la courbure de bandes et les dynamiques ultrarapides sont intrinsèquement couplés. Les résultats clés sont :

- des états de défauts donneurs (principalement des lacunes de soufre) créent du poids spectral dans le gap et induisent une courbure de bandes vers le bas à la surface ;
- l'excitation optique génère un photovoltage de surface transitoire qui aplatit partiellement le cintrage de bandes à l'équilibre, nécessitant une correction soigneuse pour l'analyse quantitative ;
- les états dans le gap permettent l'injection optique de porteurs dans la bande de conduction via une excitation sous-gap, conduisant à des populations excitées de longue durée ;
- les dynamiques ultrarapides reflètent à la fois la redistribution des lacunes au sein des familles d'états dans le gap et la population du minimum indirect de la bande de conduction.

Ces résultats montrent que les matériaux réels (avec des défauts inévitables) présentent des comportements bien plus riches que ceux prédits par des structures de bandes idéales. L'interaction entre défauts, courbure de bandes et dynamiques induites par la lumière doit être prise en compte pour interpréter correctement les mesures à l'équilibre et résolues en temps dans les semi-conducteurs feuilletés. En outre, la méthodologie développée ici combinant cartographie de bandes résolue en polarisation, suivi à long terme, quantification du SPV et dynamiques résolues en temps avec correction soignée fournit un cadre de travail pour étudier d'autres phénomènes médiés par les défauts dans les TMDCs et matériaux feuilletés apparentés.

Fluctuations CDW dominées par le couplage électron–phonon dans 1T-$TiSe_2$

La troisième étude majeure aborde un débat de longue date concernant l'origine des fluctuations d'onde de densité de charge (CDW) dans le matériau CDW prototypique 1T-$TiSe_2$. En dessous de $\sim$200 k, $TiSe_2$ subit une transition de phase vers un état CDW $2 \times 2 \times 2$ caractérisé par une modulation périodique de la densité de charge et une distorsion de réseau commensurable. Le mécanisme microscopique à l'origine de cette transition fait l'objet de débats depuis des décennies : une perspective l'attribue à une condensation excitonique (appariement électron–trou), tandis qu'une autre met l'accent sur une instabilité de type Jahn–Teller pilotée par le réseau (couplage électron–phonon). Au-dessus de la température de transition T_{CDW}, des signatures de fluctuations CDW à courte portée persistent jusqu'à température ambiante, mais leur origine et l'interaction dominante qui les gouverne restent mal établies.

Approche expérimentale et observations à l'équilibre

En utilisant la microscopie d'impulsion XUV résolue en temps au CELIA, nous avons cartographié l'intensité de photoémission 4D $I(E, k_x, k_y, t)$ de 1T-$TiSe_2$ à température ambiante (295 k) (bien au-dessus de $T_{\mathrm{CDW}} = 200k$) sous excitation par des impulsions pompe infrarouges de 1.2 eV. Afin de minimiser les effets de suppression des éléments de matrice de photoémission, nous avons fait tourner de manière continue l'axe de polarisation linéaire de la sonde XUV à 21.6 eV et intégré sur tous les états de polarisation, assurant une sensibilité uniforme à travers la zone de Brillouin.

La structure de bandes à l'équilibre (pré-pompe) révèle des signatures nettes de fluctuations CDW :

— **Bande Se $4p$ repliée :** bien au-dessus de T_{CDW}, une bande faiblement dispersive vers le bas est visible au point M dans les coupes énergie–impulsion. Cette bande de valence repliée est la signature ARPES canonique de la reconstruction CDW $2 \times 2 \times 2$, qui replie la zone de Brillouin de sorte que les points Γ et M deviennent équivalents, permettant l'hybridation entre les états Se $4p$ (Γ) et Ti $3d$ (M) states.

— **Déplétion de poids spectral à M :** des contours à énergie constante près de E_F montrent une perte de poids spectral marquée au sein des poches au point M ("hot spots"), rappelant la formation de pseudogap dans d'autres TMDCs tels que 2H-TaSe2 et analogue à la physique du pseudogap dans les cuprates.

Les deux signatures persistent à température ambiante pour des fluences de pompe substantielles (0.95 mJ/cm^2), indiquant des fluctuations CDW robustes. L'analyse par courbes de distribution en impulsion (MDC) confirme la dispersion de type trou de la signature Se $4p$ repliée.

De manière remarquable, la position de la bande repliée et ses caractéristiques spectrales restent essentiellement inchangées entre les conditions d'équilibre et les conditions photoexcitées (au recouvrement pompe–sonde), montrant que les fluctuations CDW ne sont pas totalement fondues même sous un pompage optique fort. Des calculs de premiers principes ont montré que les modes excitoniques sont supprimés au-dessus de T_{CDW}, et des études dépendantes de la fluence indiquaient que les excitons devraient être détruits au-delà de $\sim$0.04 mJ/cm^2. La persistance de la réplique repliée à 0.95 mJ/cm^2 plaide donc contre une origine purement excitonique.

Fusion ultrarapide et dynamiques de récupération

Les mesures résolues en temps révèlent que les fluctuations CDW subissent une fusion partielle et une récupération rapide après photoexcitation. Les contours différentiels à énergie constante (signal pré-pompe soustrait) au niveau de Fermi et à temps zéro montrent :

— Signal positif (rouge) : population des poches de bande de conduction Ti $3d$ au point M, formant des structures elliptiques creuses.

— Signal négatif (bleu) : suppression du poids spectral Se $4p$ replié au centre des poches au point M.

En suivant l'intensité de photoémission dans des régions énergie–impulsion correspondant à différents traits (bande de conduction, bande repliée, états dans le gap), nous extrayons des dynamiques de population dépendantes du temps :

— **Dynamiques des électrons chauds (bande de conduction Ti $3d$) :** population induite par la lumière suivie d'une décroissance exponentielle, avec une durée de vie dépendant

fortement de l'énergie excédentaire : décroissance plus rapide pour les électrons de plus haute énergie, cohérente avec la diffusion électron–phonon et électron–électron vers le bas de bande.

— **Dynamiques de la bande CDW repliée (ROI sans fond) :** suppression ultrarapide limitée par la réponse instrumentale $\sim$170 fs, suivie d'une récupération avec une constante de temps $\sim$700 fs. Après soustraction de la récupération exponentielle, des oscillations résiduelles sont observées avec une fréquence $\sim$3.5 Thz.

L'analyse de Fourier identifie cette oscillation comme le mode d'amplitude CDW A_{1g} : un phonon cohérent correspondant à une modulation périodique de l'amplitude de la distorsion de réseau CDW. Ce mode a été observé précédemment dans 1T-$TiSe_2$ en dessous de T_{CDW} mais constitue ici une observation en photoémission résolue en temps d'un mode d'amplitude cohérent survivant dans le régime fluctuant à température ambiante, avec une durée de vie inhabituellement longue.

Analyse temporelle et mécanisme

Une comparaison révélatrice apparaît lorsque l'on trace la dynamique d'intensité de la bande repliée en parallèle de la température électronique dépendante du temps (extraite d'ajustements de Fermi–Dirac) et de la population totale d'états excités Ti $3d$. L'observation clé est que le minimum d'intensité de la bande repliée (fusion maximale) est décalé par rapport au maximum de température électronique d'environ 140 fs, soit approximativement une demi-période du mode d'amplitude à 3.5 Thz.

Ce décalage temporel est incompatible avec une fusion thermique directe d'un ordre excitonique, qui devrait se produire lorsque la température électronique est maximale. Il suggère plutôt une suppression cohérente via l'excitation du mode d'amplitude : la photoexcitation lance des oscillations cohérentes de l'amplitude CDW, et l'intensité de la bande repliée est minimisée lorsque l'amplitude atteint son minimum au cours du premier demi-cycle d'oscillation.

De plus, l'échelle de temps de la fusion correspond au temps de montée de la population excitée totale Ti $3d$ et corrèle avec des mesures de diffraction électronique ultrarapide montrant une extinction $\sim$130 fs de l'intensité de diffusion diffuse au point M, attribuée à un durcissement du phonon acoustique mou au point M sous l'effet des porteurs photoexcités.

Ensemble, ces observations pointent vers un mécanisme médié par les phonons : la photoexcitation durcit le phonon lié au CDW, réduisant la diffusion électron–phonon entre les états Se $4p$ et Ti $3d$ states et supprimant ainsi la réplique repliée fluctuante. Les oscillations cohérentes du mode d'amplitude modulent ensuite la dynamique de récupération.

Analyse théorique : auto-énergie électron–phonon

Afin de tester si les interactions électron–phonon seules peuvent rendre compte des signatures de fluctuations CDW observées, nous avons réalisé des calculs théoriques de la réponse linéaire en DFT (DFPT) incorporant des corrections dynamiques d'auto-énergie électron–phonon via le formalisme de Fan–Migdal. Aucun terme de couplage excitonique n'a été inclus—les calculs traitent uniquement la maille normale (non distordue) 1×1 avec une diffusion électron–phonon dépendante de la température.

La fonction spectrale électronique calculée à des températures juste au-dessus de T_{CDW} théorique (qui est $\sim$1105 k en DFPT harmonique, correspondant au point où le phonon acoustique au point M devient mou) reproduit les principales caractéristiques expérimentales : une réplique Se $4p$ repliée à M, des répliques Ti $3d$ à Γ, et une déplétion de poids spectral (“hot spots”) dans les poches au point M. Lorsque la température augmente vers $T^* \approx 1600k$ (environ 500 k au-dessus de T_{CDW}), le phonon acoustique mou au point M durcit, la force de couplage électron–phonon λ diminue, et les caractéristiques de répliques fluctuantes s'atténuent continûment jusqu'à ce que la structure électronique approche le résultat DFT nu.

La fonction spectrale phononique calculée au point M montre qu'une partie du poids spectral s'étend vers des fréquences négatives dans le régime fluctuant ($T_{\mathrm{CDW}} < T < T^*$), indiquant que les mouvements atomiques fluctuent entre des configurations normales et des configurations de type CDW, en accord avec les distorsions périodiques fluctuantes observées en diffraction à l'équilibre et en diffusion diffuse X.

Ces résultats théoriques démontrent que des fluctuations électron–phonon seules, pilotées par un mode phononique acoustique mou (mais stable), suffisent à générer les bandes repliées, la redistribution de poids spectral et les excitations du mode d'amplitude observées expérimentalement. Bien que des corrélations excitoniques puissent contribuer de manière secondaire, les calculs (qui omettent entièrement les excitons) reproduisent avec succès les observations expérimentales, établissant le couplage électron–phonon comme mécanisme dominant.

Conclusions générales

En conclusion, cette thèse établit la spectroscopie de photoémission résolue en temps et en angle comme une approche particulièrement importante pour étudier les dynamiques ultrarapides des porteurs dans les matériaux quantiques. À travers des investigations détaillées de Bi_2Te_3, SnS_2 et 1T–$TiSe_2$, elle montre comment une renormalisation subtile des bandes, l'espace de phase de diffusion intervallée, les états dans le gap induits par les défauts et la courbure de bandes, ainsi que l'ordre collectif piloté par le réseau, façonnent conjointement le comportement électronique hors équilibre. Ces résultats fournissent une image microscopique, résolue en impulsion, des voies de relaxation largement inaccessibles aux sondes à l'équilibre, et ils clarifient comment des variations apparemment faibles de dispersion ou d'électrostatique peuvent produire des conséquences dynamiques disproportionnées.

Plus largement, la thèse positionne la spectroscopie ultrarapide résolue en impulsion comme un cadre essentiel pour relier interactions microscopiques et macroscopiques : elle révèle comment les matériaux quantiques redistribuent énergie et impulsion après excitation, comment des phases concurrentes sont sélectivement stabilisées ou supprimées, et comment surfaces et défauts peuvent devenir des paramètres de contrôle actifs hors équilibre. À l'avenir, des avancées continues en résolution temporelle, en accordabilité de l'énergie de photon et en intégration multimodale étendront encore la portée de la TR-ARPES vers un contrôle quantitatif des états émergents, ouvrant de nouvelles stratégies pour l'ingénierie de fonctionnalités quantiques ultrarapides dans les technologies électroniques et optoélectroniques de prochaine génération.

TABLE DES MATIÈRES

ACKNOWLEDGMENTS ..... **v**

RÉSUMÉ ..... **vii**

ABSTRACT ..... **ix**

SOMMAIRE RÉCAPITULATIF ..... **xi**

TABLE DES MATIÈRES ..... **xxv**

1 INTRODUCTION **1**

LISTE DES ABRÉVIATIONS **1**

2 THEORETICAL FRAMEWORK OF TIME- AND ANGLE-RESOLVED PHOTOEMISSION SPECTROSCOPY **11**

2.1 INTRODUCTION 12

2.2 THEORETICAL BACKGROUND OF ARPES 13

2.2.1 Matrix Element effect in ARPES 24

2.3 TR-ARPES 27

2.3.1 Overview 27

2.3.2 Theoretical Background of TR-ARPES Intensity 28

2.3.3 Experimental aspects of TR-ARPES 31

2.4 CONCLUSION 39

3 EXPERIMENTAL SETUPS FOR TIME- AND ANGLE-RESOLVED PHOTOEMISSION SPECTROSCOPY **51**

3.1 INTRODUCTION 52

3.2 TR-ARPES ENDSTATION AT ALLS LABORATORY 53

3.2.1 Laser System 53

3.2.2 Probe Generation : 6 eV (206 nm) 54

3.2.3 Pump Generation : Tunable NIR–MIR via OPA + DFG 55

3.2.4 Beam Characterization 55

3.2.5 TR-ARPES endstation 56

3.2.6 Temporal and energy resolution of the System 57

3.2.7 Electron Analyzer and Detection 58

3.3 TIME- AND POLARIZATION-RESOLVED XUV MOMENTUM MICROSCOPY AT CELIA LABORATORY 62

3.3.1 Laser Source 62

3.3.2 Pump and Probe generation ... 62
3.3.3 Polarization charaterization ... 65
3.3.4 Long term stability ... 66
3.3.5 Pump and probe spot sizes characterization ... 67
3.3.6 Time and energy resolution ... 68
3.3.7 Momentum Microscope ... 70
3.4 CONCLUSION ... 71
4 CONTROL OF INTERVALLEY SCATTERING IN Bi_2Te_3 VIA TEMPERATURE-DEPENDENT BAND RENORMALIZATION ... 77
4.1 INTRODUCTION ... 78
4.2 RESULTS ... 90
4.2.1 Time-resolved ARPES mapping of the unoccupied states of p-doped Bi_2Te_3 ... 90
4.2.2 Temperature dependence of bulk band dispersion and ultrafast electron dynamics ... 93
4.2.3 Temperature-induced changes of the scattering phase space ... 95
4.2.4 KMC calculations ... 98
4.2.5 Electron-phonon toy-model ... 98
4.2.6 Ultrafast charge dynamics in the scattering phase space ... 99
4.2.7 Fluence dependence of the energy gap at Γ ... 101
4.2.8 Symmetry of the intensity buildup ... 101
4.2.9 Shift of bulk valence band and evidence of surface state exposed underneath the VBM ... 103
4.3 CONCLUSION ... 105
5 ULTRAFAST LIGHT-INDUCED DYNAMICS MEDIATED BY IN-GAP STATES IN LAYERED SnS_2 ... 115
5.1 INTRODUCTION ... 116
5.2 BACKGROUND CONCEPTS ... 117
5.2.1 Transition metal dichalcogenides ... 117
5.2.2 Tin disulfide (SnS_2) atomic and electronic structure ... 118
5.2.3 Gap states ... 120
5.2.4 Band bending ... 121
5.2.5 Surface Photovoltage ... 122
5.3 RESULTS AND DISCUSSION ... 124
5.3.1 Experimental Methodology ... 124

5.3.2 Band Structure Mapping and XUV Photoemission Linear Dichroism 124

5.3.3 In-Gap States and Band Bending 127

5.3.4 Pump-Induced Dynamical Surface Photovoltage 129

5.3.5 Surface Photovoltage Correction Method 131

5.3.6 Conduction Band Mapping and Ultrafast Carrier Dynamics 133

5.3.7 Conclusions 135

6 ELECTRON-PHONON-DOMINATED CHARGE-DENSITY-WAVE FLUCTUATIONS IN $TiSe_2$ ACCESSED BY ULTRAFAST NONEQUILIBRIUM DYNAMICS 147

6.1 INTRODUCTION 148

6.2 BACKGROUND CONCEPT 149

6.2.1 $TiSe_2$ 149

6.2.2 Charge Density Wave 150

6.3 RESULTS 151

6.3.1 Equilibrium and Nonequilibrium Electronic Band Structure Mapping 151

6.3.2 Ultrafast Melting and Recovery of RT-CDW Fluctuations 154

6.4 DISCUSSION 157

6.5 CONCLUSIONS 162

7 CONCLUSION AND FUTURE PERSPECTIVES 173

8 APPENDIX 177

8.1 APPENDIX I : LIGHT-INDUCED ASYMMETRIC PSEUDOGAP BELOW T_c IN CUPRATES [1] 177

8.2 APPENDIX II : ENHANCING MOMENTUM COVERAGE IN ANGLE-RESOLVED PHOTOEMISSION SPECTROSCOPY WITH HEMISPHERICAL ANALYZER 178

8.3 APPENDIX III : TESTING A PARABOLIC MIRROR MOUNT FOR HHG PROBE BEAM AT THE ALLS LABORATORY 179

8.4 APPENDIX IV : DEVELOPING A REFLECTIVITY MEASUREMENT SETUP FOR SNSE AT THE CELIA LABORATORY 180

8.5 APPENDIX V : SCIENTIFIC CONTRIBUTIONS 181

8.6 APPENDIX VI : LIST OF PUBLICATIONS 182

1 INTRODUCTION

The modern understanding of condensed matter is rooted in quantum mechanics, which governs how atoms bond and how electrons move and interact in solids. Much of today's technology—transistors, integrated circuits, lasers, and power electronics—relies on conventional metals, semiconductors, and insulators whose macroscopic properties can be accurately described using classical or semiclassical models, despite their microscopic quantum origin. In these materials, quantum effects are largely averaged out. Over the past few decades, however, a broad class of materials has emerged in which quantum-mechanical effects manifest explicitly even at macroscopic length, energy, and time scales. These systems—now collectively referred to as quantum materials [1–3]—exhibit macroscopic properties governed directly by quantum-mechanical many-body interactions, dimensionality and quantum geometrical properties.

Prominent examples of quantum materials include unconventional superconductors [4], Mott insulator [5, 6], excitonic insulators [7–9], charge-density-wave compounds [10, 11], topological insulators [12, 13], topological semimetals [14, 15], topological superconductors [16], and a rapidly expanding family of two-dimensional semiconductors [17] etc.

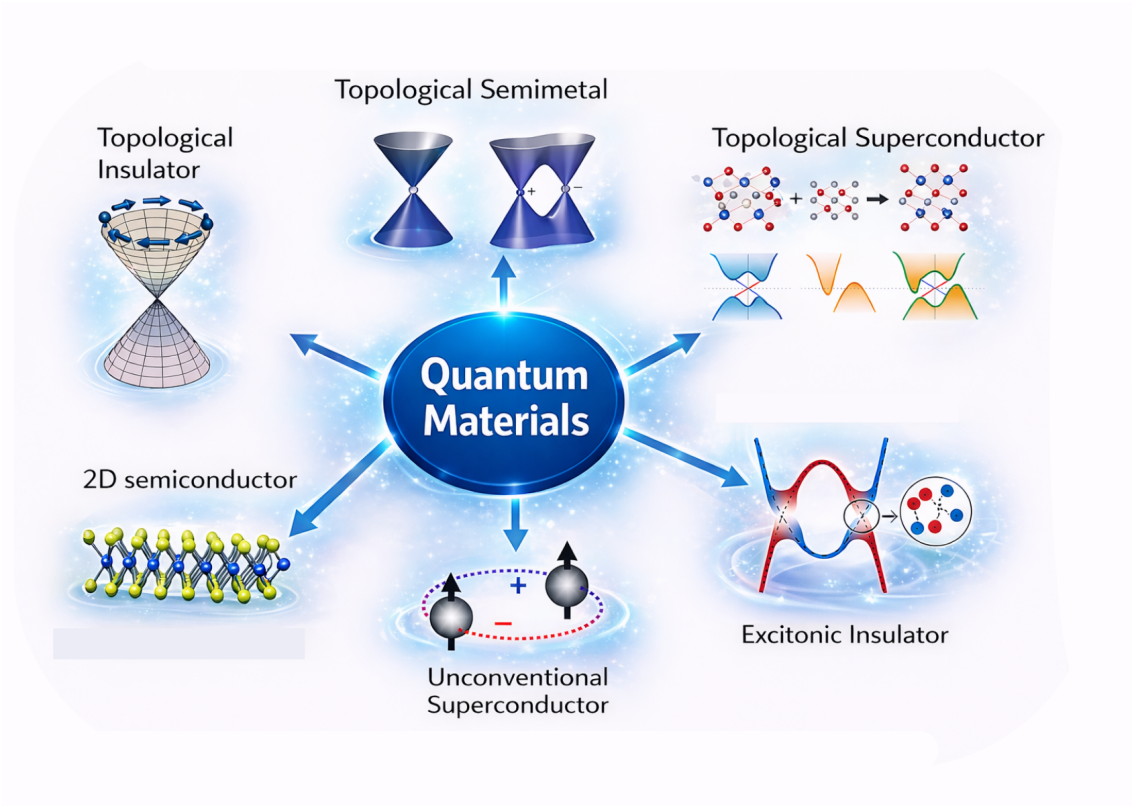


FIGURE 1.1 : Different classes of quantum materials.

Among the plethora of quantum materials, in this thesis work I will focus mainly on three classes :

Topological Insulator - The term topological insulator combines two key concepts : topology and insulator. Topology is a branch of mathematics and physics that deals with properties of objects that remain unchanged under smooth, continuous deformations. In condensed matter physics, topology provides a framework for classifying electronic phases using global, quantized quantities—known as topological invariants—which distinguish one phase from another in a way that cannot be altered without closing an energy gap. An insulator, in the conventional solid-state sense, is a phase of matter characterized by a bandgap separating the valence and conduction bands, preventing charge transport in the bulk. A topological insulator is an electronic phase of matter in which a bulk bandgap coexists with gapless conducting states at the surface (or edges in lower dimensions). Remarkably, these surface states exist despite the insulating bulk and are robust against ordinary disorder and imperfections. This robustness originates from the non-trivial topology of the bulk electronic wavefunctions, which enforces the presence of metallic boundary states at the interface between the material and the topologically trivial vacuum. Time-reversal symmetry protects these states and leads to spin–momentum locking, whereby the electron spin is rigidly tied to its momentum, strongly suppressing elastic backscattering. As a result, the surface electronic structure forms a Dirac-like energy–momentum dispersion with spin-polarized states. Owing to their symmetry-protected nature, relativistic Dirac-like surface fermions, and strong sensitivity to external perturbations such as light, magnetic fields, and reduced dimensionality, topological insulators provide a powerful platform for exploring fundamental quantum phenomena, nonequilibrium dynamics, and topology-driven phase transitions. These properties also make them promising candidates for future applications in spintronics and quantum information science.

Closely related topological phases include topological semimetals, in which nontrivial band topology enforces symmetry-protected crossings between valence and conduction bands in the bulk, resulting in an intrinsically gapless electronic structure, in contrast to topological insulators whose bulk band is gapped. Topological superconductors extend the concept of band topology to superconducting systems, where electron–hole mixing due to pairing gives rise to Bogoliubov–de Gennes quasiparticle bands whose topology cannot be continuously deformed into that of a conventional superconductor without closing the superconducting gap or breaking a protecting symmetry.

2D semiconductor- Two-dimensional semiconductors are atomically thin materials (Prototypical examples are transition-metal dichalcogenide such as MoS_2,WS_2,$MoSe_2$, WSe_2 etc) in which electronic motion is confined to a single layer, leading to electronic and optical properties that differ qualitatively from their bulk counterparts. Reduced dimensionality and weak dielectric screening strongly enhance Coulomb interactions, resulting in large exciton binding energies, pronounced many-body effects, and strong light–matter coupling. Broken inversion symmetry and strong spin–orbit coupling in many 2D semiconductors lift spin degeneracies and lock spin and valley de-

grees of freedom to crystal momentum, enabling spin–valley coupled phenomena and the emerging field of valleytronics. These internal quantum numbers allow optical initialization, manipulation, and readout of valley and spin states using circularly polarized light, opening possibilities for information encoding beyond charge in nanoscale devices. Owing to their exceptional tunability through gating, strain, stacking, and twist angle, two-dimensional semiconductors provide a versatile platform to explore emergent quantum phases and nonequilibrium dynamics. At the same time, their compatibility with ultra-scaled transistors, spintronic and valleytronic concepts, and quantum optoelectronic devices places them at the center of efforts to translate quantum material phenomena into practical technologies.

Charge density wave - Charge density waves are correlated electronic phases in which the electronic charge density and the crystal lattice develop a periodic modulation, spontaneously breaking translational symmetry. This instability is most prominent in low-dimensional or layered materials, where electron–phonon coupling, Fermi-surface geometry, and electronic correlations cooperatively drive the formation of an ordered state. The resulting reconstruction of the electronic structure opens partial or full gaps at the Fermi level, often reducing metallicity and giving rise to collective excitations associated with amplitude and phase fluctuations of the order parameter. Charge density waves provide a canonical example of emergent order arising from coupled electronic and lattice degrees of freedom and frequently compete or coexist with superconductivity and other correlated phases.

Across all these material classes, a unifying feature is that electrons do not act as independent particles. Instead, their charge, spin, orbital motion, lattice coupling, and topological properties become strongly entangled, and the resulting physical behavior is governed by a delicate balance among competing interactions. Because these interactions often operate on comparable energy scales (eV to sub-eV), relatively small external perturbations—such as changes in temperature, carrier concentration, pressure, strain, dimensionality, or applied electric and magnetic fields—can tip this balance and drive phase transitions between states that differ not only in symmetry, but in their fundamental nature. A striking example is the correlation-driven metal–insulator transition, where the electrical resistivity can change by many orders of magnitude [18]. Understanding how such emergent phases arise from microscopic interactions, and how they transform into one another under external stimuli, remains a central challenge of modern condensed matter physics. At the same time, this extreme sensitivity underpins the technological promise of quantum materials. In this context, topological insulators and semimetals provide robust spin and charge transport protected against disorder, topological superconductors offer potential platforms for fault-tolerant quantum information processing, and excitonic and low-dimensional systems enable coherent electron–hole condensates, strong light–matter coupling, and ultrafast optoelectronic control. Unconventional superconductors might play a crucial forward-looking role by revealing correlation-driven pairing mechanisms that may guide the design of future high Tc, low-loss superconductors for energy-efficient power transmission, superconducting electronics, and quantum coherent devices. The exceptional tunability of two-dimensional, where multiple quantum phases

can be accessed within a single platform—makes them ideal testbeds for both discovering new quantum states of matter and engineering quantum functionalities.

Probing quantum materials in equilibrium

To uncover the microscopic origin of these emergent phases and their intricate interplay of degrees of freedom, it is essential to directly probe the electronic, lattice, and spin structure of quantum materials. Angle-resolved photoemission spectroscopy (ARPES) [19, 20] is the primary momentum-resolved probe of the single-particle spectral function, directly mapping electronic band dispersions, Fermi surfaces, and energy gaps. ARPES has been instrumental in revealing Dirac surface states and band inversion in topological insulators, Weyl and Dirac nodes and Fermi-arc surface states in topological semimetals, superconducting and pseudogaps in unconventional superconductors, and band back-folding or hybridization gaps associated with charge density wave or excitonic order. Spin-resolved ARPES [21, 22] further extends this capability by providing direct access to the spin texture of electronic states. Complementary real-space information is obtained from scanning tunneling microscopy and spectroscopy (STM/STS)[23, 24], which probe the local density of states with atomic resolution. STM/STS enables direct visualization of gap magnitude and symmetry, impurity-induced bound states, quasiparticle interference patterns of topological surface states, localized zero-bias modes at vortices or edges in candidate topological superconductors, and spatial modulations associated with charge density wave or excitonic order. Linear optical, infrared, and terahertz spectroscopies [25] probe the frequency-dependent complex conductivity and dielectric response, providing access to superconducting condensate spectral weight, low-energy gap formation, carrier scattering rates, and collective excitations in charge-ordered systems, as well as characteristic interband responses of Dirac and Weyl fermions. Core-level and resonant X-ray spectroscopies, including XPS [26], XAS [27], and RIXS [28, 29]„ add element- and orbital-selective sensitivity, enabling quantitative analysis of valence states, correlation strength, spin–orbit coupling, excitonic excitations, and subtle changes in local bonding across electronic phase transitions. Together, these establish comprehensive equilibrium descriptions linking symmetry, topology, and interactions to observable properties.

Ultrafast spectroscopy as a dynamical probe

While equilibrium spectroscopic probes such as ARPES provide detailed access to the ground-state electronic structure and encode intrinsic single-particle lifetimes through spectral linewidths, they remain fundamentally limited to equilibrium or linear-response information. As a result, they do not directly capture the real-time evolution of excited carrier populations, the sequence of scattering processes, or how ordered phases are dynamically formed, modified, or suppressed following external perturbations—processes that play a decisive role in determining macroscopic properties of quantum materials where competing interactions are closely balanced. The development of ultrafast femtosecond laser technology has fundamentally transformed the study of quantum materials. The ability to generate optical pulses with durations comparable to intrinsic electronic and lattice timescales enables controlled access to nonequilibrium states that are inaccessible under

steady-state conditions. In a pump–probe scheme, an ultrashort pump pulse drives the system out of equilibrium, while a time-delayed probe pulse interrogates its transient response. This approach makes it possible to directly follow the temporal evolution of electronic, spin, and lattice degrees of freedom, establishing time as a fundamental experimental axis alongside energy and momentum.

Ultrafast optical and terahertz pump–probe spectroscopy [30, 31] probes the nonequilibrium response of quantum materials through time-dependent changes in reflectivity, transmission, or low-frequency conductivity, providing direct access to carrier relaxation, collective modes, gap dynamics, and light–matter coupling in a non-destructive manner and under device-relevant conditions. Its principal limitation is that the response is inherently momentum integrated and often depth averaged, so the measured dynamics cannot be directly assigned to specific bands, valleys, or surface versus bulk states, requiring comparison with momentum-resolved probes for microscopic interpretation. Time-resolved X-ray and electron-based techniques, including time-resolved X-ray diffraction, ultrafast electron diffraction, and time-resolved resonant inelastic X-ray scattering, directly access lattice motion, symmetry breaking, and collective excitations, offering a unique window into phonon-driven phase transitions, charge-density-wave melting, and light-induced structural transformations [32, 33]. While these methods excel at disentangling structural and collective degrees of freedom, they generally do not directly resolve the low-energy electronic band dispersions and quasiparticle occupations near the Fermi level that govern transport and ultrafast carrier dynamics. Time-resolved scanning tunneling microscopy and spectroscopy [34, 35] provide atomic-scale, real-space sensitivity to transient changes in the local density of states, enabling the study of spatial inhomogeneity, defects, vortex cores, and localized bound states such as Majorana modes. However, because they lack momentum resolution and probe only local electronic structure, they cannot capture the full momentum-dependent evolution of electronic bands or scattering processes following excitation.

Among these techniques, time- and angle-resolved photoemission spectroscopy (TR-ARPES) [36] which is an extention of ARPES in time domain offers unique access to electronic band structure with energy, momentum and temporal resolution. In a typical experiment, an ultrafast pump pulse excites the system out of equilibrium, and a delayed probe pulse photoemits electrons whose kinetic energy and emission angle encode the instantaneous electronic band structure and occupation. By varying the pump–probe delay, TR-ARPES reconstructs the evolution of electronic structure in real time, enabling direct observation of carrier relaxation pathways, band renormalization, gap dynamics, momentum-selective scattering, and transient or light-induced electronic states. This thesis utilizes the TR-ARPES as the primary experimental method to probe quantum materials.

Out of equilibrium carrier dynamics as a central open problem

Despite remarkable progress in ultrafast spectroscopy, many fundamental questions in quantum materials remain unresolved, largely because their defining properties emerge from a subtle interplay of strong electronic interactions, topology, symmetry, and reduced dimensionality that ex-

tends beyond single-particle band theory. In such materials, electronic correlations, defects, band bending, and lattice coupling drive significant deviations from simplified band-structure descriptions and strongly influence nonequilibrium carrier dynamics. These factors govern relaxation pathways, population lifetimes, and the stability of ordered phases away from equilibrium. Understanding such nonequilibrium processes at a microscopic level therefore remains a central challenge, as they directly determine how quantum phases emerge, compete, and respond to external perturbations.

A common aspect is therefore the need to understand how charge carriers respond to external perturbations and evolve in time. In strongly interacting and low-dimensional systems, key processes such as scattering, energy redistribution, coupling to lattice and collective modes, and charge separation often occur on ultrafast timescales and play a decisive role in determining transport properties, optical response, and phase stability. For instance, in topological insulators such as Bi_2Se_3, ultrafast spectroscopy reveals that photoexcited carriers in the conduction band rapidly thermalize into the topological surface state within a few hundred femtoseconds, followed by a slower, picosecond-scale relaxation of spin-polarized surface carriers. These distinct relaxation processes govern surface transport and demonstrate that bulk and surface states follow fundamentally different nonequilibrium pathways [37]. In 2D semiconductors such as monolayer MoS_2, ultrafast pump–probe spectroscopies reveal that photoexcitation generates tightly bound excitons whose populations relax through exciton–exciton annihilation on hundreds-of-femtoseconds timescales, trapping of excitons by surface or defect states on a few-picosecond timescale, and interband carrier–phonon scattering on tens-of-picoseconds timescales, thereby dictating photoluminescence efficiency and carrier transport [38]. In the charge-density-wave of the Mott insulator 1T-TaS_2, ultrafast time-resolved core-level photoemission spectroscopy reveals a prompt collapse of long-range charge order within tens of femtoseconds after photoexcitation, followed by picosecond-scale electron–phonon thermalization into a transient, short-range ordered charge-density-wave state [39]. This measurement demonstrate that the stability of the charge-density-wave phase, and its competition with metallic or other ordered states, is governed by how energy is redistributed from the electronic system into lattice degrees of freedom on ultrafast timescales. Understanding how carriers move through momentum space, how relaxation pathways are selected, and how interactions shape these dynamics is therefore central to clarifying the microscopic behavior of quantum materials. Ultrafast carrier dynamics thus provides a focused and broadly relevant framework for addressing fundamental questions across a wide range of quantum phases, linking microscopic interactions to macroscopic functionality.

Scope of this thesis

This thesis investigates ultrafast carrier dynamics in representative quantum materials where electronic structure, lattice coupling, and defects play a central role in shaping nonequilibrium behavior. The work focuses on three classes of systems : a three-dimensional topological insulator, a layered semiconductor, and a charge-density-wave material. By tracking how excited carriers redistribute energy and momentum following optical excitation, the thesis aims to identify the microsco-

pic mechanisms that govern relaxation pathways, population lifetimes, and transient modifications of electronic structure. Particular emphasis is placed on understanding how band renormalization, intervalley scattering, defect-induced in-gap states, band bending, and collective lattice modes influence ultrafast dynamics. To address these questions, time- and angle-resolved photoemission spectroscopy is employed as the primary experimental technique, providing direct access to the momentum-resolved electronic structure and carrier populations in real time. Through a combination of high-resolution measurements and comparison with theoretical modeling, this thesis seeks to establish a microscopic link between electronic structure, interactions, and nonequilibrium carrier dynamics in quantum materials.

The thesis is organized as follows. Chapter 2 introduces the basics of ARPES and TR-ARPES followed by detailed description of the two TR-ARPES end-stations at ALLS and CELIA Laboratory where I worked during my thesis period in Chapter 3. Chapter 4 presenting a comprehensive TR-ARPES study of temperature-induced band renormalization and intervalley scattering in a three-dimensional topological insulator. Chapter 5 presents ultrafast sub-bandgap light induced dynamics mediated by defect States. Chapter 6 explores the long standing debate of the origin of Charge density wave $TiSe_2$ wheather purely electronic excitonic insulator or from the electron lattice contribution followed by conclusion in chapter 7.

Bibliographie

[1] J Orenstein. Ultrafast spectroscopy of quantum materials. *Phys. Today*, 65(9) :44–50, September 2012. doi : 10.1063/PT.3.1717.

[2] B Keimer and J E Moore. The physics of quantum materials. *Nat. Phys.*, 13(11) :1045–1055, November 2017. doi : 10.1038/nphys4302.

[3] Y Tokura, M Kawasaki, and N Nagaosa. Emergent functions of quantum materials. *Nat. Phys.*, 13(11) :1056–1068, November 2017. doi : 10.1038/nphys4274.

[4] G R Stewart. Unconventional superconductivity. *Adv. Phys.*, 66(2) :75–196, April 2017. doi : 10.1080/00018732.2017.1331615.

[5] M Imada, A Fujimori, and Y Tokura. Metal-insulator transitions. *Rev. Mod. Phys.*, 70(4) : 1039–1263, October 1998.

[6] M S Laad and L Craco. Mott transitions : A brief review. *Adv. Quantum Technol.*, 7(12), December 2024.

[7] D Jérome, T M Rice, and W Kohn. Excitonic insulator. *Phys. Rev.*, 158(2) :462–475, June 1967. doi : 10.1103/PhysRev.158.462.

[8] S Mor, M Herzog, C Monney, and J Stähler. Ultrafast charge carrier and exciton dynamics in an excitonic insulator probed by time-resolved photoemission spectroscopy. *Prog. Surf. Sci.*, 97(4) :100679, December 2022. doi : 10.1016/j.progsurf.2022.100679.

[9] T Kaneko and Y Ohta. A new era of excitonic insulators. November 2024. doi : 10.7566/JPSJ.94.012001.

[10] G Grüner. The dynamics of charge-density waves. *Rev. Mod. Phys.*, 60(4) :1129–1181, October 1988. doi : 10.1103/RevModPhys.60.1129.

[11] K Rossnagel. On the origin of charge-density waves in select layered transition-metal dichalcogenides. *J. Phys. Condens. Matter*, 23(21) :213001, June 2011. doi : 10.1088/0953-8984/23/21/213001.

[12] M Z Hasan and C L Kane. Colloquium : Topological insulators. *Rev. Mod. Phys.*, 82(4) : 3045–3067, November 2010. doi : 10.1103/RevModPhys.82.3045.

[13] X L Qi and S C Zhang. Topological insulators and superconductors. *Rev. Mod. Phys.*, 83(4) : 1057–1110, October 2011. doi : 10.1103/RevModPhys.83.1057.

[14] N P Armitage, E J Mele, and A Vishwanath. Weyl and dirac semimetals in three-dimensional solids. *Rev. Mod. Phys.*, 90(1), January 2018. doi : 10.1103/RevModPhys.90.015001.

[15] B Q Lv, T Qian, and H Ding. Experimental perspective on three-dimensional topological semimetals. *Rev. Mod. Phys.*, 93(2), April 2021. doi : 10.1103/RevModPhys.93.025002.

[16] M Sato and Y Ando. Topological superconductors : a review. *Rep. Prog. Phys.*, 80(7) :076501, July 2017. doi : 10.1088/1361-6633/aa6ac7.

[17] Enter 2D quantum materials. *Nat. Mater.*, 19(12) :1255, December 2020. doi : 10.1038/s41563-020-00867-3.

[18] M Imada, A Fujimori, and Y Tokura. Metal-insulator transitions. *Rev. Mod. Phys.*, 70(4) : 1039–1263, October 1998. doi : 10.1103/RevModPhys.70.1039.

[19] A Damascelli. Probing the electronic structure of complex systems by ARPES. *Phys. Scr.*, T109 :61, 2004.

[20] J A Sobota, Y He, and Z X Shen. Angle-resolved photoemission studies of quantum materials. *Rev. Mod. Phys.*, 93(2), May 2021. doi : 10.1103/RevModPhys.93.025006.

[21] J H Dil. Spin- and angle-resolved photoemission on topological materials. *Electron. Struct.*, 1 (2) :023001, April 2019.

[22] C-Y Lin, L Moreschini, and A Lanzara. Present and future trends in spin ARPES. *Europhys. Lett.*, 134(5) :57001, June 2021.

[23] Ø Fischer, M Kugler, I Maggio-Aprile, C Berthod, and C Renner. Scanning tunneling spectroscopy of high-temperature superconductors. *Rev. Mod. Phys.*, 79(1) :353–419, March 2007. doi : 10.1103/RevModPhys.79.353.

[24] J X Yin, S H Pan, and M Z Hasan. Probing topological quantum matter with scanning tunnelling microscopy. *Nat. Rev. Phys.*, 3(4) :249–263, March 2021. doi : 10.1038/s42254-021-00293-7.

[25] C Giannetti, M Capone, D Fausti, M Fabrizio, F Parmigiani, and D Mihailovic. Ultrafast optical spectroscopy of strongly correlated materials and high-temperature superconductors : a non-equilibrium approach. *Adv. Phys.*, 65(2) :58–238, March 2016. doi : 10.1080/00018732.2016.1194044.

[26] R Escamilla, E Carvajal, M Cruz-Irisson, F Morales, L Huerta, and E Verdin. XPS study of the electronic density of states in the superconducting Mo_2B and Mo_2BC compounds. *J. Mater. Sci.*, 51(13) :6411–6418, July 2016. doi : 10.1007/s10853-016-9938-z.

[27] H Elnaggar, M W Haverkort, M H Hamed, S S Dhesi, and F M F de Groot. Tensor description of x-ray magnetic dichroism at the fe l2,3-edges of Fe_3O_4. *J. Synchrotron Radiat.*, 28(Pt 1) : 247–258, January 2021.

[28] M Mitrano and Y Wang. Probing light-driven quantum materials with ultrafast resonant inelastic x-ray scattering. *Commun. Phys.*, 3(1), October 2020. doi : 10.1038/s42005-020-00447-6.

[29] M Mitrano, S Johnston, Y J Kim, and M P M Dean. Exploring quantum materials with resonant inelastic x-ray scattering. *Phys. Rev. X.*, 14(4), December 2024. doi : 10.1103/PhysRevX.14.040501.

[30] A de la Torre, D M Kennes, M Claassen, S Gerber, J W McIver, and M A Sentef. Colloquium : Nonthermal pathways to ultrafast control in quantum materials. *Rev. Mod. Phys.*, 93 (4), October 2021. doi : 10.1103/RevModPhys.93.041002.

[31] A Bera, S Bera, S Kalimuddin, S Gayen, M Kundu, B Das, and M Mondal. Review of recent progress on THz spectroscopy of quantum materials : superconductors, magnetic and topological materials. *Eur. Phys. J. Spec. Top.*, 230(23) :4113–4139, December 2021. doi : 10.1140/epjs/s11734-021-00216-8.

[32] D Filippetto, P Musumeci, R K Li, B J Siwick, M R Otto, M Centurion, and J P F Nunes. Ultrafast electron diffraction : Visualizing dynamic states of matter. *Rev. Mod. Phys.*, 94(4), December 2022.

[33] X Jiang, Q Qiu, and Y Peng. Time-resolved x-ray scattering study on quantum materials. *Chin. Physics B*, 34(10) :107801, October 2025.

[34] K Liang, L Bi, Q Zhu, H Zhou, and S Li. Ultrafast dynamics revealed with time-resolved scanning tunneling microscopy : A review. *ACS Appl. Opt. Mater.*, 1(5) :924–938, May 2023. doi : 10.1021/acsaom.2c00169.

[35] A van Houselt and H J W Zandvliet. Colloquium : Time-resolved scanning tunneling microscopy. *Rev. Mod. Phys.*, 82(2) :1593–1605, May 2010. doi : 10.1103/RevModPhys.82.1593.

[36] F Boschini, M Zonno, and A Damascelli. Time-resolved ARPES studies of quantum materials. *Rev. Mod. Phys.*, 96(1), February 2024. doi : 10.1103/RevModPhys.96.015003.

[37] J A Sobota, S-L Yang, D Leuenberger, A F Kemper, J G Analytis, I R Fisher, P S Kirchmann, T P Devereaux, and Z-X Shen. Ultrafast electron dynamics in the topological insulator Bi_2Se_3 studied by time-resolved photoemission spectroscopy. *J. Electron Spectros. Relat. Phenomena*, 195 :249–257, August 2014.

[38] H-S Tsai, Y-H Huang, P-C Tsai, Y Chen, H Ahn, S-Y Lin, and Y-J Lu. Ultrafast exciton dynamics in scalable monolayer MoS_2 synthesized by metal sulfurization. *ACS Omega*, 5(19) : 10725–10730, May 2020.

[39] S Hellmann, M Beye, C Sohrt, T Rohwer, F Sorgenfrei, H Redlin, M Kalläne, M Marczynski-Bühlow, F Hennies, M Bauer, A Föhlisch, L Kipp, W Wurth, and K Rossnagel. Ultrafast melting of a charge-density wave in the mott insulator 1T-TaS_2. *Phys. Rev. Lett.*, 105(18) :187401, October 2010.

2 THEORETICAL FRAMEWORK OF TIME- AND ANGLE-RESOLVED PHOTOEMISSION SPECTROSCOPY

Summary : This chapter introduces the fundamental theoretical principles of angle-resolved photoemission spectroscopy (ARPES) and its extension into the time domain, time- and angle-resolved photoemission spectroscopy (TR-ARPES), the central technique used throughout this thesis to investigate the physics of quantum materials, specifically, in my case topological insulator and transition metal dichalcogenides. The chapter begins with a discussion of the fundamental photoemission process, including the conservation laws governing energy and momentum, the three-step model of photoemission, and the formulation of the ARPES intensity in terms of the single-particle spectral function, photoemission matrix elements, and the Fermi–Dirac distribution. Building on this foundation, by combining the conventional pump-probe method with ARPES, we discussed the theoretical foundation of TR-ARPES. The effects of the temporal evolution on each term of the ARPES intensity are discussed, highlighting the roles of electron–electron scattering and electron–boson scattering. The chapter further outlines essential experimental considerations relevant to TR-ARPES, including the generation of ultrafast pump and probe pulses, photoelectron detection schemes, and standard sample preparation protocols adopted by the community. Particular attention is given to the fundamental trade-offs inherent to TR-ARPES experiments, such as those between energy, momentum, and temporal resolution, photoelectron count rate, and space-charge effects, which ultimately define the achievable experimental parameter space. The theoretical concepts developed here provide the essential framework for the upcoming chapters that follow, where TR-ARPES is applied to topological insulators and layered transition metal dichalcogenides to uncover the microscopic mechanisms governing ultrafast carrier dynamics. The majority of the description I have covered in this chapter follows from excellent review articles by Damascelli et. al [1, 2], Sobota et al. [3], Zhang et al. [4], Na et al. [5], Boschini et al. [6], as well as Wang et al. [7].

2.1 Introduction

Angle Resolved Photoemission Spectroscopy (ARPES) is a very powerful technique that provides direct access to the electronic band structure and many-body interactions, which determine the physical properties of solids. The basic principle underlying ARPES is the photoelectric effect, discovered by Hertz in 1887 [8] and explained by Einstein through the quantum nature of light [9].

ARPES is a photon-in, electron-out experiment. When light impinges on a sample, it can be absorbed and ionize the material if the energy of the photons is higher than the work function of the material. Electrons can then escape from the material with maximum kinetic energy of $h\nu$-Φ, where ν is the photon frequency and Φ is the work function of the material, which typically lies in the range 4-5 eV for most materials. By resolving both the kinetic energy and emission angle of photoelectrons, ARPES permits direct measurement of the electronic band structure, enabling the mapping of constant energy contours/Fermi surfaces and the investigation of many-body interactions. As a result, ARPES has become an essential tool for studying the electronic properties of quantum materials, including high-temperature superconductors, topological insulators, and other strongly correlated materials [3, 6].

The first measurement of electronic band structure using ARPES was performed in 1973 [10, 11]. Over the past few decades, this field has witnessed major advances both in instrumentation and scientific discoveries. These advances were enabled by the progress of advanced light sources, including third-generation synchrotrons [12–17], deep-UV lasers [18–22], high-harmonic generation (HHG) [23–29]. In parallel, improve instrumentation has been developed, for instance 2D and 3D electron detectors [30–36], and efficient spin detectors [37–40]. These technological advancements have allowed ARPES to reveal the electronic structure of μm or even sub-μm size samples via Micro-ARPES/Nano-ARPES [41–47], to access spin-resolved electronic structure via spin-ARPES [48–55], to map the full 3D band structure by tuning the photon energy [56–58], Polarization tunable Circular Dichroism ARPES (CD-ARPES) provides information about Berry Curvature and Orbital Angular momentum [59–64].

The advent of femtosecond laser sources has enabled the extension of ARPES into the time domain by combining it with pump–probe techniques, made possible by their ultrashort and coherent light pulses. In time-resolved ARPES (TR-ARPES) [5, 6, 65–76], an ultrashort pump pulse drives the system out of equilibrium, while a time-delayed probe pulse photoemits electrons, providing snapshots of the transient and unoccupied electronic structure. This approach enables direct access to nonequilibrium carrier dynamics, energy relaxation pathways, and the ultrafast evolution of collective excitations.

In this chapter, we present the theoretical framework underlying ARPES and TR-ARPES. We begin by introducing the basic principles of photoemission, followed by a discussion of energy and momentum conservation, the sudden and three-step approximations, and the role of matrix

elements. We then extend the formalism to the time-resolved regime, establishing the foundation required to interpret the experimental results presented in the subsequent chapters.

2.2 Theoretical Background of ARPES

A typical ARPES experiment involves irradiating a single-crystal sample with monochromatic light of photon energy $h\nu$. A fraction of these electrons is collected by a spectrometer that records their kinetic energy E_{kin} and emission angles (ϑ, ϕ). Here, ϑ denotes the polar angle relative to the surface normal, while ϕ represents the azimuthal angle defined with respect to the experimental geometry shown in Fig. 2.1a. The energetics of the photoemission process are also shown in Fig. 2.1b. Applying the principle of energy conservation yields the binding energy E_{B} of the photoemitted electron inside the solid directly, which is given by -

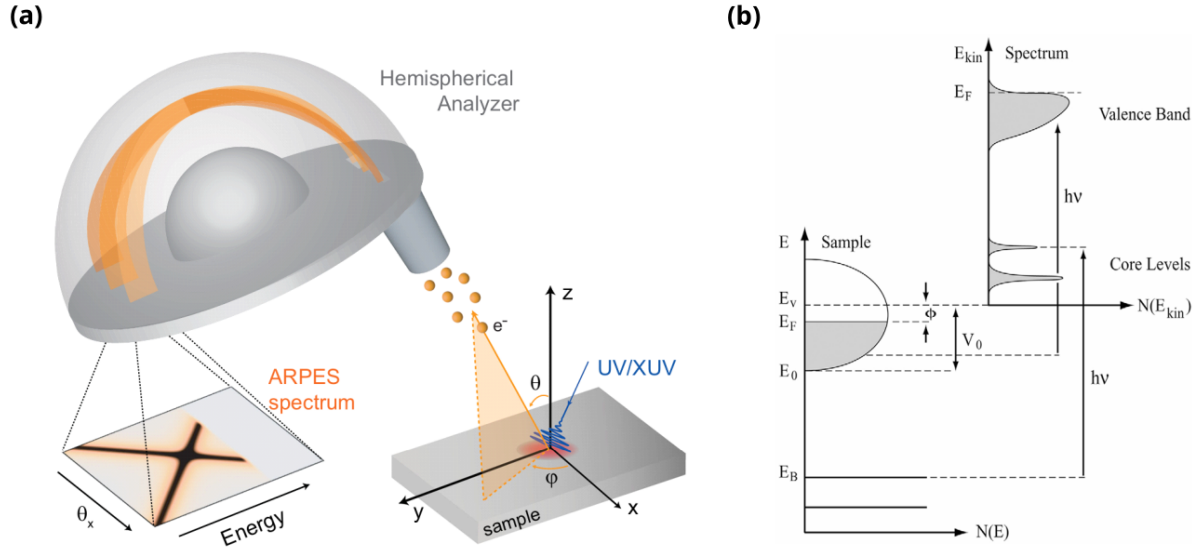


FIGURE 2.1 : Angle-resolved photoemission spectroscopy (ARPES).(a). Schematic of a standard ARPES experiment. A monochromatic UV/XUV beam (photon energy $h\nu$) illuminates the sample and ejects photoelectrons with kinetic energy E_{kin} along directions specified by the polar angle ϑ and azimuthal angle φ. An electron analyzer (illustrated here as a hemispherical analyzer) collects the emitted electrons and resolves both E_{kin} and the emission angles, yielding a two-dimensional ARPES intensity map. Adapted from [6], with permission from the publisher. (b). Energetic of the photoemission process. The electron energy distribution generated by incident photons and measured as a function the photoelectrons' kinetic energy E_{kin} (right) is more conveniently expressed in terms of the binding energy E_B (left) as a function of the density of states inside the solid ($E_B = 0$ at E_F). Adapted from [1], with permission from the publisher.

$$E_{\mathrm{kin}} = h\nu - \Phi - |E_B|. \tag{2.1}$$

We also get the photoemitted electrons wavevector or momentum in vacuum (outside the material) **K** where its modulus is given by $|\mathbf{K}| = \frac{1}{\hbar}\sqrt{2mE_{\mathrm{kin}}}$. We can decompose **K** into its parallel

$\mathbf{K}_{||} = \mathbf{K}_x + \mathbf{K}_y$ and perpendicular component $\mathbf{K}_\perp = \mathbf{K}_z$ in terms of the polar angle ϑ and azimuthal angle ϕ as -

$$K_x = \frac{1}{\hbar}\sqrt{2mE_{\text{kin}}}\,\sin\vartheta\cos\varphi, \tag{2.2}$$

$$K_y = \frac{1}{\hbar}\sqrt{2mE_{\text{kin}}}\,\sin\vartheta\sin\varphi, \tag{2.3}$$

$$K_z = \frac{1}{\hbar}\sqrt{2mE_{\text{kin}}}\,\cos\vartheta. \tag{2.4}$$

Our goal is to determine the relation between the Binding energy E_B and the crystal momentum **k** of electrons propagating inside the solid. Note that in most of the low-energy ARPES experiments ($h\nu < 100$ eV) the photon momentum $\mathbf{k}_{\text{photon}}$ contribution can be neglected. For example, at a photon energy of 100 eV, the photon momentum is $\kappa = \frac{2\pi}{\lambda}$ = 0.05 Å^{-1} which is just 3 % of the typical Brillouin zone size of cuprate superconductor $\frac{2\pi}{a} \simeq 1.6$ Å^{-1}. If we consider a typical 21.2 eV photon source, which is widely used in ARPES measurement, the $\mathbf{k}_{\text{photon}}$ contribution is only 0.5 %. Consequently, the photon momentum can be safely neglected in the momentum balance of the photoemission process.

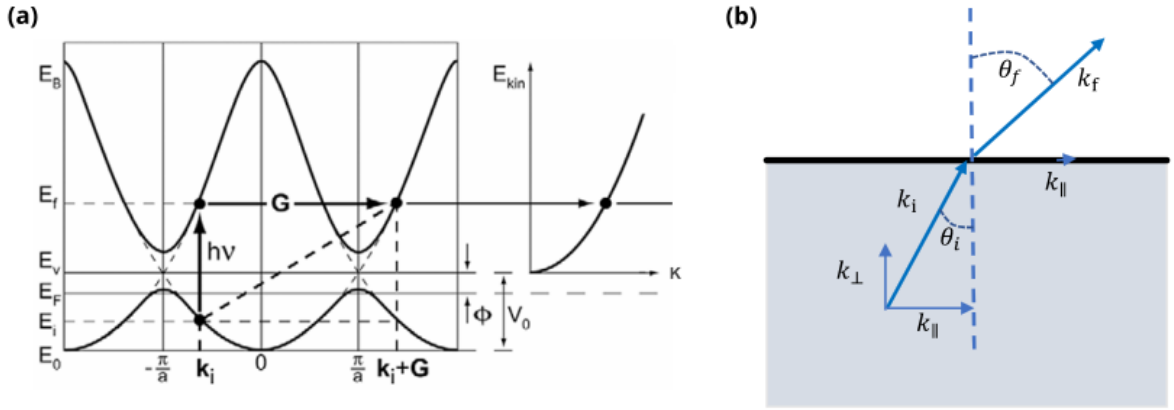


FIGURE 2.2 : (a) Kinematics of the photoemission process within the three-step model. An electron is optically excited from an occupied valence-band state to an unoccupied state inside the crystal via direct optical transition. At the surface, the lattice supplies the required momentum to match the electron wave function to a free-electron–like final state in vacuum. The surface is modeled as a potential step V_0, representing the work function barrier that the photoelectron must overcome to escape into vacuum. Adapted from [2], with permission from the publisher. (b) Refraction of the photoelectron on the surface. By translational invariance along the interface, the parallel component of the photoelectron momentum, $k_{||}$, remains conserved during transmission from the crystal to vacuum.

Under this approximation, the photoemission process can be viewed as a transition between an initial electronic state inside the crystal and a final free-electron state in vacuum. Momentum conservation within the periodic lattice allows for the exchange of crystal momentum with the lattice in integer multiples of the reciprocal lattice vectors **G**. As a result, optical transitions inside the bulk are commonly described as vertical transitions in the reduced-zone scheme, where the initial and final crystal momenta are equal ($\mathbf{k}_i = \mathbf{k}_f$). However, ARPES directly measures the absolute

momentum of photoelectrons in vacuum and therefore naturally favors the extended-zone picture, in which momentum conservation can be expressed as $\mathbf{k}_i = \mathbf{k}_f + \mathbf{G}$ as shown in Fig. 2.2a. The presence of the surface plays a crucial role in determining which components of momentum are conserved. While translational symmetry is preserved parallel to the surface, it is broken along the surface normal. As a consequence, only the component of the crystal momentum parallel to the surface $\mathbf{k}_{||}$ within a reciprocal lattice vector $\mathbf{G}_{||}$ is conserved, whereas the perpendicular component $\mathbf{k}_{\perp}$ is not strictly conserved, as schematically shown in Fig. 2.2. Therefore, we can express

$$\mathbf{k}_{||} = \mathbf{K}_{||} = \frac{1}{\hbar}\sqrt{2mE_{\mathrm{kin}}}\,\sin\vartheta. \tag{2.5}$$

Although $\mathbf{k}_{\perp}$ is not conserved across the surface, it is commonly estimated within a free-electron final-state approximation as

$$\mathbf{k}_{\perp} = \frac{1}{\hbar}\sqrt{2m\,(E_{\mathrm{kin}}\cos^2\vartheta + V_0)}, \tag{2.6}$$

where V_0 is an empirical parameter called inner potential that refers to the energy of the bottom of the valence band with reference to the vacuum level E_v shown in Fig. 2.1b, accounting for the average crystal potential experienced by the final state [3].

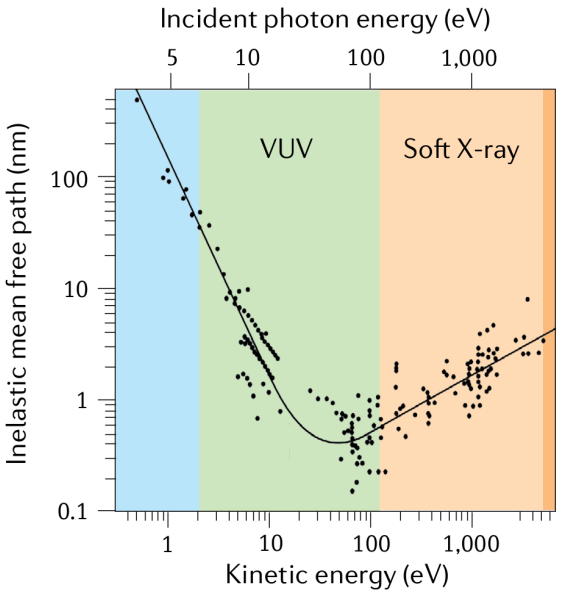


FIGURE 2.3 : Universal curve of the inelastic mean free path. The photoelectron inelastic mean free path is shown as a function of kinetic energy E_{kin} (bottom axis) and incident photon energy (top axis). VUV : vacuum ultraviolet. Adapted from [4, 77], with permission from the publisher.

At low photon energies, the photon momentum $\mathbf{k}_{\mathrm{photon}}$ becomes negligible, allowing the simplified momentum–energy relations derived above to remain valid for ARPES. More generally, a fundamental limitation of all photoemission-based techniques is that the probing depth of ARPES measurements is limited by the electron's inelastic mean free path inside the material, which follows a universal curve [77] as shown in Fig. 2.3. The typical value for the mean free path at photon

energy around 100 eV is only a few Angstroms, and it reaches several nanometers for energy greater than 1 keV. This implies that only electrons near the surface, typically a few atomic layers, contribute to the measurements. However, surfaces are typically contaminated with multiple layers of adsorbates such as water, hydrocarbons, and other contaminants from the environment. So in order to perform ARPES measurement, we need to prepare atomically clean and long-range ordered surfaces. This is achieved by preparing the samples in-situ using exfoliation, cleaving, ion bombardment and annealing, epitaxial thin film growth by Molecular Beam Epitaxy (MBE), Pulsed Laser Deposition (PLD) etc. Once the clean surface is obtained, it will remain clean for a limited lifetime because of the adsorption of the residual gas atoms and molecules. In order to maintain a clean surface at least for 10-20 hours, we need an ultra high vacuum (UHV) chamber in $\sim 10^{-10}$ mbar pressure [4]; however, this strongly depends on the sample.

Up to this point, the discussion has focused on the kinematic relations that allow ARPES to reconstruct the binding energy and momentum of electrons inside a solid. However photoemission process in solids is inherently complex. From the quantum mechanical point of view, photoemission is fundamentally a one-step process (Fig. 2.4a) in which photon absorption, electron removal, and electron detection are treated as a single coherent process [78–80]. In this framework, an optical transition from an initial state to final states consisting of many-body wave functions must satisfy the appropriate boundary conditions at the surface. The initial state corresponds to an N-electron many-body eigenstate of the semi-infinite crystal. After photoemission, one electron is removed from the system; therefore, the final state consists of an (N-1)-electron eigenstate of the ionized crystal together with the emitted photoelectron. This photoelectron wave function must propagate as a plane wave in vacuum—representing the escaped electron—while retaining finite amplitude inside the crystal to ensure overlap with the initial state. The final-state photoelectron wave function can be described as a time-reversed LEED state. In conventional low-energy electron diffraction (LEED), an incident low-energy electron beam impinges on a crystal surface and undergoes reflection and multiple scattering from the surface atomic potential. In the time-reversed picture relevant for photoemission, the photoelectron emerges from the solid and retraces, in reverse, the same scattering paths that an incoming LEED electron would follow. Consequently, the final-state wave function is asymptotically a free-electron–like plane wave in vacuum, while inside the crystal it decays rapidly into the bulk and simultaneously satisfies the crystalline boundary conditions through a superposition of damped Bloch waves [81, 82]. Within the one-step model, energy and momentum conservation apply to the N-electron system and the impinging photon-

$$E_f^N - E_i^N = h\nu, \tag{2.7}$$

$$\mathbf{k}_f^N - \mathbf{k}_i^N = \mathbf{k}_{h\nu}, \tag{2.8}$$

where i and f refer to the initial and final state, respectively, and $k_{h\nu}$ is the momentum of the incoming photon. However, due to the analytical complexity of the one-step model, the quantitative analysis of the experimental data of the photoemission process is often performed under the as-

sumption of an independent particle picture and sudden approximation, disregarding many-body interactions and the relaxation of the system under photoemission itself. In addition, the process is simplified even further using the phenomenological three-step model (Fig. 2.4b), where the process is considered as three independent processes [83]. Although in some cases, the one-step formalism is required to fully explain spectral intensities of the photoemission process however this model quite successfully captures the photoemission process remarkably well and will be adopted for the remainder of this discussion.

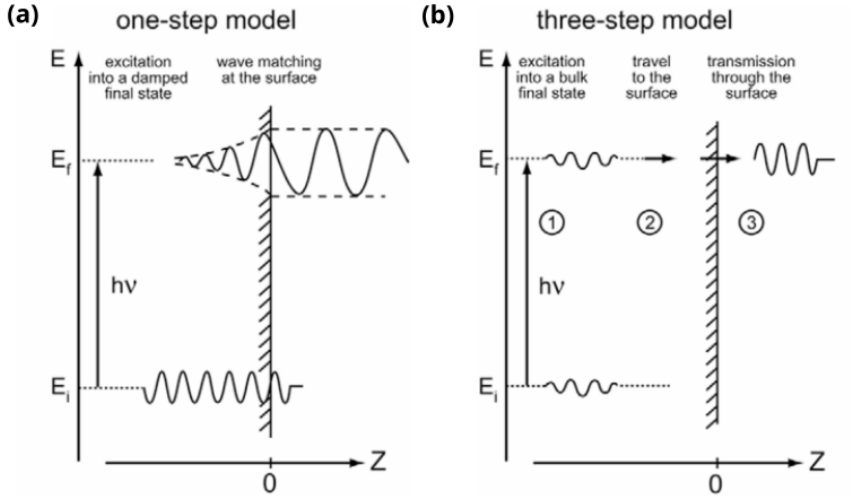


FIGURE 2.4 : One-step and three-step descriptions of the photoemission process. Schematic representations of the one-step (a) and three-step (b) model of the photoemission process. Adapted from [2], with permission from the publisher.

Three-step model and sudden approximation : In this model, the photoemission process is subdivided into three independent steps : I. Photoexcitation of an electron into a final bulk state - This step contains all the information about the intrinsic electronic structure of the material. II. Travel of the excited photoelectron to the surface - This process can be described in terms of the mean free path that is imposed by the elastic and inelastic scattering processes, and is proportional to the probability for the excited electrons to reach the surface. The inelastic scattering gives rise to a continuous background in the spectra. III. Escape of the photoelectron into vacuum - This step can be described by the probability of transmission through the surface and to ultimately reach to the detector. It depends on the energy of the excited electron and the material's work function.

Within this framework, let us consider an N electron system with ground state Ψ_i^N with energy E_i^N, which absorbs a photon of energy $h\nu$ and is excited into a possible final state Ψ_f^N with energy E_f^N. The interaction between the electrons and the electromagnetic field is described in terms of the electronic momentum operator **p** and electromagnetic vector potential **A**. Throughout this

discussion here, the scalar potential is set to $\Phi = 0$, corresponding to the velocity gauge, in which the interaction is expressed in the $\mathbf{A} \cdot \mathbf{p}$ form. This description is valid in the linear response regime and within the electric-dipole approximation. Under these assumptions, the Hamiltonian describing the interaction can be written as -

$$\hat{H} = \frac{1}{2m} (\mathbf{p} - e\mathbf{A})^2 + V(\mathbf{r}), \tag{2.9}$$

$$= \frac{\mathbf{p}^2}{2m} + V(\mathbf{r}) - \frac{e}{2m} \mathbf{A} \cdot \mathbf{p} - \frac{e}{2m} \mathbf{p} \cdot \mathbf{A} + \frac{e^2}{2m} \mathbf{A}^2, \tag{2.10}$$

$$= \frac{\mathbf{p}^2}{2m} + V(\mathbf{r}) - \frac{e}{2m} \mathbf{A} \cdot \mathbf{p} - \frac{e}{2m} (-i\hbar \nabla \cdot \mathbf{A}) + \frac{e^2}{2m} \mathbf{A}^2, \tag{2.11}$$

$$= \frac{\mathbf{p}^2}{2m} + V(\mathbf{r}) - \frac{e}{2m} \mathbf{A} \cdot \mathbf{p} \tag{2.12}$$

$$= \hat{H}_0 + \hat{H}_{\text{int}}, \tag{2.13}$$

where $\hat{H}_0 = \frac{p^2}{2m} + V(r)$ is the unperturbed Hamiltonian operator, and $\hat{H}_{int} = -\frac{e}{2m} \mathbf{A} \cdot \mathbf{p}$ is the perturbed hamiltonian operator that describes the light matter interaction.

We can write the transition probability w_{fi} from Ψ_i^N to Ψ_f^N by the Fermi's golden rule :

$$w_{fi} = \frac{2\pi}{\hbar} \left| \langle \Psi_f^N \mid H_{\text{int}} \mid \Psi_i^N \rangle \right|^2 \delta \left(E_f^N - E_i^N - h\nu \right), \tag{2.14}$$

here $E_i^N = E_i^{N-1} - E_B^{\mathbf{k}}$ and $E_f^N = E_f^{N-1} + E_{kin}$ are the initial and final states energies of the N-particle system and $E_B^{\mathbf{k}}$ is the binding energy of the photoelectron that has a kinetic energy E_{kin} with momentum **k**. In order to express the photoemission intensity in terms of the transition probability w_{fi}, it is convenient to reformulate the problem in terms of the emitted photoelectron and the remaining (N-1) electron system. This separation, however, is nontrivial because the photoemission process inevitably perturbs the many-body system, which then relaxes in response to the removal of an electron. A widely used approximation to address this complexity is the sudden approximation, in which the photoemission process is assumed instantaneous. In this picture, the photoelectron is removed so rapidly that it does not interact further with the (N-1) electron system after emission. As a result, the remaining electrons experience a sudden change in the effective potential due to the instantaneous creation of a photohole, rather than a gradual, adiabatic evolution. Equivalently, the electron is considered to be removed instantaneously, causing the effective potential of the system to change discontinuously at the moment of emission. Importantly, within the sudden approximation, the final N-electron wave function can be factorized into a product of the photoelectron wave function and an excited state of the (N-1) electron system. Within this framework, Fermi's golden rule can be applied to obtain the instantaneous transition probability w_{fi}. The sudden approximation is extensively employed in many-body calculations of photoemission spectra and is formally justified in the limit of high photoelectron kinetic energies, where post-collisional interactions between the escaping photoelectron and the remaining system are negligible. Never-

theless, it has been found that the spectral features predicted within the sudden approximation are often preserved even at relatively low photon energies.

Under the sudden approximation, we can write both N-particle initial state Ψ_i^N and final state Ψ_f^N in terms of a single Slater determinant product of one electron orbital ϕ^k and (N-1) particle term :

$$\Psi_i^N = \mathcal{A}\,\phi_i^{\mathbf{k}}\,\Psi_i^{N-1}, \tag{2.15}$$

$$\Psi_f^N = \mathcal{A}\,\phi_f^{\mathbf{k}}\,\Psi_f^{N-1}, \tag{2.16}$$

where $\mathcal{A}$ is the antisymmetrization operator to satisfy Pauli's principle, $\phi_i^{\mathbf{k}}$ and $\phi_f^{\mathbf{k}}$ are the wavefunctions of the electron before and after absorbing the photon, with the same **k** vector due to momentum conservation. The wavefunction Ψ_i^{N-1} is given by :

$$\Psi_i^{N-1} = c_k \Psi_i^N, \tag{2.17}$$

where c_k is the annihilation operator for an electron with momentum **k**. The state Ψ_i^{N-1} is generally not an eigenstate of the (N-1) particle Hamiltonian, since the sudden removal of an electron from the interacting N-electron ground state leaves the remaining system in a nonstationary, excited configuration. However the final excited sate of the (N-1) remaining electrons Ψ_f^{N-1}, can therefore be expanded as a superposition of eigenstates Ψ_m^{N-1} of the (N-1) particle Hamiltonian with energy E_m^{N-1}. The total transition probability is then obtained by summing over all possible excited states m. However, it is important to emphasize that the final N-particle wave function Ψ_f^N cannot be factorized into two independent parts when the sudden approximation breaks down. In such cases, detailed screening of the photoelectron and its interactions with photoholes must be explicitly accounted for [84]. Now if we plug in eq. 2.15 and eq. 2.16 into eq. 2.14 we get

$$w_{f,i} = \sum_m w_{m,i} = \frac{2\pi}{\hbar} \sum_m \left| \langle \phi_f^{\mathbf{k}} \mid H_{\text{int}} \mid \phi_i^{\mathbf{k}} \rangle \langle \Psi_m^{N-1} \mid \Psi_i^{N-1} \rangle \right|^2 \delta\Big(E_{\mathbf{kin}} + E_m^{N-1} - E_i^N - h\nu\Big), \tag{2.18}$$

$$= \frac{2\pi}{\hbar} \left| \langle \phi_f^{\mathbf{k}} \mid H_{\text{int}} \mid \phi_i^{\mathbf{k}} \rangle \right|^2 \sum_m \left| \langle \Psi_m^{N-1} \mid \Psi_i^{N-1} \rangle \right|^2 \delta\Big(E_{\mathbf{kin}} + E_m^{N-1} - E_i^N - h\nu\Big). \tag{2.19}$$

The total photoemission intensity $I(\mathbf{k}, E_{kin})$ measured at momentum **k** as a function of E_{kin} is proportional to $\sum_{f,i} w_{f,i}$ i.e.

$$I(\mathbf{k}, E_{kin}) \propto \sum_{f,i} w_{f,i}, \tag{2.20}$$

$$= \frac{2\pi}{\hbar} \sum_{f,i} \left| \langle \phi_f^{\mathbf{k}} \mid H_{\text{int}} \mid \phi_i^{\mathbf{k}} \rangle \right|^2 \sum_m \left| \langle \Psi_m^{N-1} \mid \Psi_i^{N-1} \rangle \right|^2 \delta\Big(E_{\mathbf{kin}} + E_m^{N-1} - E_i^N - h\nu \Big), \tag{2.21}$$

$$= \frac{2\pi}{\hbar} \sum_{f,i} \left| \langle \phi_f^{\mathbf{k}} \mid H_{\text{int}} \mid \phi_i^{\mathbf{k}} \rangle \right|^2 \sum_m \left| \langle \Psi_m^{N-1} \mid c_k \mid \Psi_i^{N} \rangle \right|^2 \delta\Big(E_{\mathbf{kin}} + E_m^{N-1} - E_i^N - h\nu \Big), \tag{2.22}$$

$$= \sum_{f,i} |M_{f,i}|^2 \sum_m \left| c_{m,i}^k \right|^2 \delta\Big(E_{\mathbf{kin}} + E_m^{N-1} - E_i^N - h\nu \Big). \tag{2.23}$$

where $M_{f,i} = \left| \langle \phi_f^{\mathbf{k}} \mid H_{\text{int}} \mid \phi_i^{\mathbf{k}} \rangle \right|$ is the one-electron dipole matrix element often termed as "matrix element", $\left| c_{m,i}^k \right|^2 = \left| \langle \Psi_m^{N-1} \mid \Psi_i^{N-1} \rangle \right|^2$ describes the probability of (N-1) system to be in the excited state m after an electron removed from an initial state i. In the case of a non-interacting particle system, there exists a single state $m = m'$ for which $\Psi_i^{N-1} = \Psi_{m'}^{N-1}$. In this situation, only the corresponding $\left| c_{m,i}^k \right|^2 = 1$, while all others vanish. As a result, provided the photoemission matrix element is nonzero, the photoemission process involves a single well-defined excitation energy. In an idealized theoretical description, this corresponds to a delta-function-like contribution in energy, as illustrated in Fig. 2.5a. By contrast, in an interacting or strongly correlated system, the sudden removal of the photoelectron leads to an overlap of Ψ_i^{N-1} with many eigenstates of Ψ_m^{N-1}. As a result, the photoemission spectrum no longer corresponds to a single sharp excitation. Instead, the spectral weight is redistributed over multiple final states, giving rise to a principal peak accompanied by additional satellite features corresponding to all the overlapped excited m states that are created in the process, as shown in Fig. 2.5b. In practice, ARPES measurements do not resolve ideal delta-function features. Both non-interacting and interacting systems exhibit finite linewidths due to intrinsic lifetime effects, thermal broadening, and the finite energy and momentum resolution of the experiment.

In treating photoemission from solids, especially for correlated electron systems, where most of the $|c_{m,i}^{\mathbf{k}}|^2$ are nonzero, the Green's-function approach is the standard and most effective framework. The propagation of a single electron in a many-body system is described by the time-ordered one-electron Green's function $G(\mathbf{k}, t - t')$, which represents the probability amplitude that an electron added at time t' to a Bloch state of momentum **k** is found in the same state at a later time t. By Fourier transforming $(\mathbf{k}, t - t')$ with respect to time, one obtains its energy–momentum representation, $G(\mathbf{k}, \omega) = G^+(\mathbf{k}, \omega) + G^-(\mathbf{k}, \omega)$, where $G^+(\mathbf{k}, \omega)$ and $G^-(\mathbf{k}, \omega)$ denote the electron-addition and electron-removal Green's functions, respectively. Now at zero temperature ($T = 0$)

$$G^{\pm}(\mathbf{k}, \omega) = \sum_m \frac{\left| \langle \Psi_m^{N\pm1} \mid c_{\mathbf{k}}^{\pm} \mid \Psi_i^N \rangle \right|^2}{\omega - E_m^{N\pm1} + E_i^N \pm i\eta}, \tag{2.24}$$

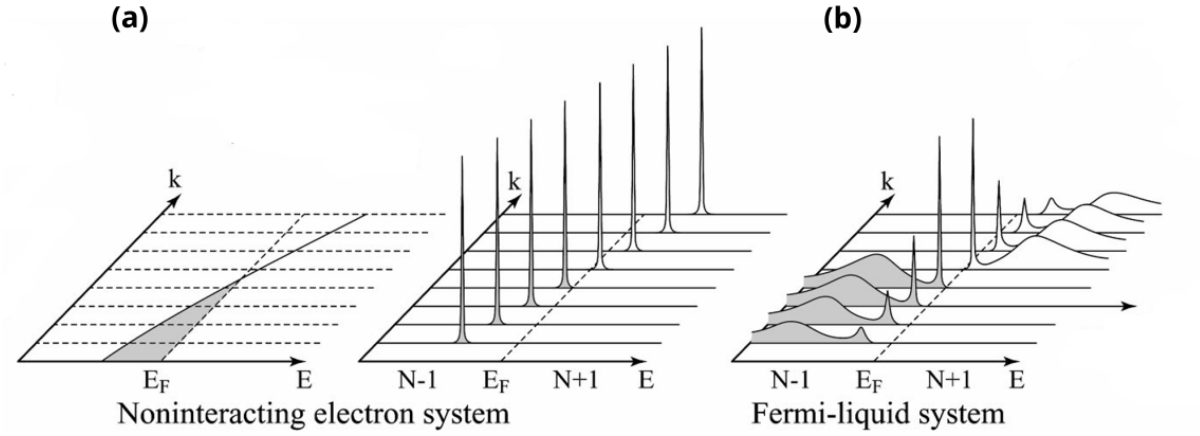


FIGURE 2.5 : Momentum-resolved one-electron removal or addition spectra. (a) Noninteracting system with a single energy band dispersion near E_F and (b) Interacting Fermi liquid system. Adapted from [1], with permission from the publisher.

where $c^{+}_{\mathbf{k}} = c^{\dagger}_{\mathbf{k}\sigma}$ ($c^{-}_{\mathbf{k}} = c_{\mathbf{k}\sigma}$) is creation (annihilation) operator that creates (annihilate) an electron with of energy ω, momentum $\mathbf{k}$ and spin σ for the N particle initial state Ψ^{N}_{i}. The sums run over all eigenstates $\Psi^{N\pm1}_{m}$ of the $(N\pm1)$-particle system with eigenvalues $E^{N\pm1}_{m}$. The parameter $\eta > 0$ is an infinitesimal, and for simplicity, $\hbar$ is chosen to be unity. In the limit $\eta \to 0^{+}$, using the identity $(x \pm i\eta)^{-1} = \mathcal{P}\left(\frac{1}{x}\right) \mp i\pi\,\delta(x)$, with $\mathcal{P}$ the principal value, we can express the Green's function as

$$G^{\pm}(\mathbf{k},\omega) = \sum_{m} \left| \left\langle \Psi^{N\pm1}_{m} \,\middle|\, c^{\pm}_{\mathbf{k}} \,\middle|\, \Psi^{N}_{i} \right\rangle \right|^{2} \left[\mathcal{P}\left(\frac{1}{\omega - E^{N\pm1}_{m} - E^{N}_{i}} \right) - i\pi\,\delta\left(\omega - E^{N\pm1}_{m} - E^{N}_{i}\right) \right]. \quad (2.25)$$

We define the single-particle spectral function as

$$A^{\pm}(\mathbf{k},\omega) = \sum_{m} \left| \langle \Psi^{N\pm1}_{m} \,|\, c^{\pm}_{\mathbf{k}} \,|\, \Psi^{N}_{i} \rangle \right|^{2} \delta\left(\omega - E^{N\pm1}_{m} + E^{N}_{i}\right). \quad (2.26)$$

From eq. 2.25 and eq. 2.26 we can write

$$A(\mathbf{k},\omega) = A^{+}(\mathbf{k},\omega) + A^{-}(\mathbf{k},\omega) = -\frac{1}{\pi}\,\mathrm{Im}\,G(\mathbf{k},\omega), \quad (2.27)$$

with $A^{-}(\mathbf{k},\omega)$ and $A^{+}(\mathbf{k},\omega)$ represents the one electron removal spectra and one electron addition spectra and $G(\mathbf{k},\omega) = G^{+}(\mathbf{k},\omega) + \left[G^{-}(\mathbf{k},\omega)\right]^{*}$ defines the retarded Green's function. The one-electron removal and addition spectra can be directly probed with photoemission and inverse photoemission, respectively. By comparing eq. 2.26 with eq. 2.23, the ARPES intensity can be written as-

$$I(\mathbf{k},\omega) \propto |M_{f,i}|^{2} * A^{-}(\mathbf{k},\omega). \quad (2.28)$$

We now introduce finite-temperature effects ($T \neq 0$) into the Green's function formalism [85]. To incorporate the fact that the photoemission probes only the occupied states, we need to introduce

the Fermi-Dirac function $f(\omega) = \left(e^{\omega/(k_{\rm B}T)} + 1\right)^{-1}$. Then we express -

$$I(\mathbf{k}, \omega) = I_0(\mathbf{k}, \nu, \mathbf{A}) f(\omega) A^{-}(\mathbf{k}, \omega), \tag{2.29}$$

where $\mathbf{k} = \mathbf{k}_{||}$ is the in-plane electron momentum, ω the electron energy with respect to Fermi level, $I_0(\mathbf{k}, \nu, \mathbf{A})$ is proportional to the one-electron matrix element $|M_{f,i}|^2 = \left|\langle \phi_f^{\mathbf{k}} \,|\, H_{\rm int} \,|\, \phi_i^{\mathbf{k}} \rangle\right|^2$ which depends on the interaction hamiltonian, i.e. on the electron momentum as well as incoming photon energy and polarization. It is also worth mentioning that, to limit the broadening by Fermi Dirac distribution ($k_{\rm B}T$ term), ARPES measurements need to be carried out at low temperature. Furthermore, in deriving eq. 2.29 neither extrinsic background contributions nor the broadening associated with the finite energy and momentum resolution have been included. These factors, however, must be accounted for when performing quantitative analysis of experimental spectra.

Now if we want to extend the photoemission description to the many-body interaction case, it can be done by the correction to the Green's function, expressing it in terms of the electron self energy $\Sigma(\mathbf{k}, \omega) = \Sigma'(\mathbf{k}, \omega) + i\,\Sigma''(\mathbf{k}, \omega)$. The real and imaginary part contains the information of band renormalization and lifetime of an electron, respectively, with respect to the bare band energy $\varepsilon_{\mathbf{k}}$ and momentum $\mathbf{k}$ due to many-body interaction effects. By using the self-energy we can express the one electron's Green's function as -

$$G(\mathbf{k}, \omega) = \frac{1}{\omega - \varepsilon_{\mathbf{k}} - \Sigma(\mathbf{k}, \omega)}, \tag{2.30}$$

and then the spectral function ($A(\mathbf{k}, \omega) = -(1/\pi)\,\mathrm{Im}\, G(\mathbf{k}, \omega)$) will be -

$$A(\mathbf{k}, \omega) = -\frac{1}{\pi} \frac{\Sigma''(\mathbf{k}, \omega)}{\left[\omega - \varepsilon_{\mathbf{k}} - \Sigma'(\mathbf{k}, \omega)\right]^2 + \left[\Sigma''(\mathbf{k}, \omega)\right]^2}. \tag{2.31}$$

Because $G(t - t')$ is a linear-response quantity to an external perturbation, causality enforces Kramers–Kronig relations between real and imaginary parts of its Fourier Transform $G(\mathbf{k}, \omega)$. So if we get the full $A(\mathbf{k}, \omega) = -(1/\pi)\,\mathrm{Im}\, G(\mathbf{k}, \omega)$ by combining photoemission with inverse photoemission, then we can calculate the $\mathrm{Re}\, G(\mathbf{k}, \omega)$ and thereby determine both $\Sigma'(\mathbf{k}, \omega)$ and $\Sigma''(\mathbf{k}, \omega)$ directly from the equations above. However in practice, high-quality inverse photoemission data is extremely difficult to obtain, which means that self-energies $\Sigma(\mathbf{k}, \omega)$ are typically inferred from ARPES alone using certain approximations [86], otherwise in general the exact calculation of $\Sigma(\mathbf{k}, \omega)$ and corresponding $A(\mathbf{k}, \omega)$ is an extremely difficult task. Note that for a non interacting system $\Sigma(\mathbf{k}, \omega) = 0$ and $A(\mathbf{k}, \omega) = \delta(\omega - \varepsilon_{\mathbf{k}})$, which is consistent with eq. 2.19. For an interacting system intuitively, $\Sigma'(\mathbf{k}, \omega)$ shifts the bare band $\varepsilon_{\mathbf{k}}$ to a renormalized position $\tilde{\varepsilon}_{\mathbf{k}} = \varepsilon_{\mathbf{k}} + \Sigma'(\mathbf{k}, \omega)$, while $\Sigma''(\mathbf{k}, \omega)$ part broadens the δ-function of the noninteracting case. If $\tau_s(\mathbf{k})$ is a single-particle lifetime which characterizes all relaxation processes of an excited single particle with energy $\varepsilon_{\mathbf{k}}$, then it is inversely proportional to the imaginary part, $\tau_s(\mathbf{k}) = \hbar/2\Sigma''(\mathbf{k}, \omega)$ and can be obtained from quantitative analysis of the ARPES line shape. Now if we plug into the self-energy terms

(contained in the spectral function from eq. 2.31) in ARPES intensity (eq. 2.29) we get -

$$I(\mathbf{k},\omega) = I_0(\mathbf{k},\nu,\mathbf{A}) f(\omega)\, A^{-}(\mathbf{k},\omega) \tag{2.32}$$

$$I(\mathbf{k},\omega) = -\frac{1}{\pi}\, I_0(\mathbf{k},\omega)\, f(\omega)\, \frac{\Sigma''(\mathbf{k},\omega)}{\left[\omega - \varepsilon_{\mathbf{k}} - \Sigma'(\mathbf{k},\omega)\right]^2 + \left[\Sigma''(\mathbf{k},\omega)\right]^2}. \tag{2.33}$$

The above equation shows the capability of ARPES to directly probe the electron–removal spectral function, providing access to many-body correlations information via the self-energy term. In order to analyze the spectral lineshape ($A(\mathbf{k},\omega)$), experimentally, two main strategies are often followed from the measured photoemission signal ($I(\mathbf{k},\omega)$). The first approach is to analyze the energy dependence of photoemission intensity at fixed momentum $\mathbf{k}^*$, widely known as the energy distribution curve (EDC) in the ARPES community. In the second approach, we analyze the momentum dependence at a fixed binding energy ω^*, referred to as the momentum distribution curve (MDC). In Fig. 2.6, I present one example of ARPES data analysis using EDC/MDC where a si-

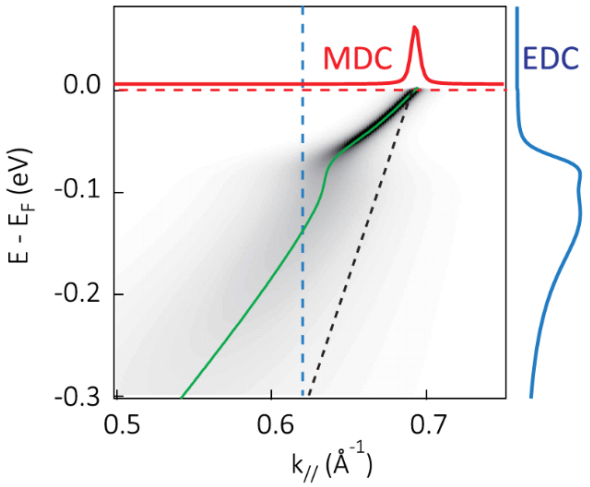


FIGURE 2.6 : Photoemission intensity $I(\mathbf{k},\omega)$ as a function of energy and momentum. Representative momentum-distribution (MDC, red) and energy-distribution (EDC, blue) curves taken at the dashed guides are displayed above and to the right, respectively. The green curve traces the quasiparticle dispersion obtained from MDC peak positions; the black dashed line is the assumed bare-band dispersion used in the simulation. Adapted from [3], with permission from the publisher.

mulated energy-momentum cut is shown. We can extract the band dispersion by fitting the peak of the EDCs or MDCs although in general both procedures will not produce identical results because of the energy and momentum dependence of both the electron self-energy and the dipole matrix element [87]. In Fig. 2.6, the EDC and MDC are presented by blue line and red line, respectively. A complex EDC line shape (blue) is present due to an energy-dependent electron–phonon self-energy. In this case a standard approach to extract the interaction effect consists in first, extracting the band dispersion by using MDC peak fitting which is represented by the green line in Fig. 2.6, then second, to map the fitted results onto eq. 2.31 considering $\Sigma(\omega)$ is $k_{\|}$-independent only for

the momentum along the cut and also guessing a reasonable background lineshape [88]. In MDC analysis, the momentum width $\Delta k_{\parallel}$ is related to the imaginary part of the self energy $\Sigma''(\omega)$ by

$$\Sigma''(\omega) \ = \frac{\partial \varepsilon_k}{\partial k} \frac{\Delta k_{\parallel}}{2}, \tag{2.34}$$

where $\frac{\partial \varepsilon_k}{\partial k}$ is the bare band velocity. So if the bare dispersion is specified, we can extract the $\Sigma''(\omega)$. In practice, the bare band ε_k (the black dashed line in Fig. 2.6a) is unknown and is estimated empirically from the data [89]. The $\Sigma'(\omega)$ can be easily extracted by looking at the energy renormalization shift compared to the bare dispersion, which is related by

$$\Sigma'(\omega) \ = \omega - k \frac{\partial \varepsilon_k}{\partial k}, \tag{2.35}$$

After extracting $\Sigma'(\omega)$ and $\Sigma''(\omega)$ to understand the interaction mechanism involved in our ARPES data, we need a model to decompose them into different interactions mechanisms such electron–electron and electron–phonon or any other possible interactions. In order to constrain the model [90] Kramers–Kronig relations between $\Sigma'(\omega)$ and $\Sigma''(\omega)$ can be used, although the result depends strongly on assumptions made for the unoccupied part of the dispersion.

2.2.1 Matrix Element effect in ARPES

Our focus so far has been on understanding $A(\mathbf{k}, \omega)$ from the ARPES signal $I(\mathbf{k}, \omega)$. Here we focus on the influence of the matrix element term $I_0(\mathbf{k}, \nu, \mathbf{A}) \propto |M_{f,i}|^2 = \left| \langle \phi_f^{\mathbf{k}} \,|\, H_{\text{int}} \,|\, \phi_i^{\mathbf{k}} \rangle \right|^2$ which was previously introduced within the three step model and under the dipole approximation. Our understanding so far is that it acts as a factor that modulates photoemission intensity, and may even result in complete suppression of intensity. To dive deep, let us write down the interaction Hamiltonian from eq. 2.13 as $\hat{H}_{int} = -\frac{e}{2m} \mathbf{A} \cdot \mathbf{p} = -\frac{e}{2m} A\epsilon \cdot \mathbf{p}$ where ϵ is a unit vector along the light polarization direction of the vector potential $\mathbf{A}$. Using the commutation relation $\mathbf{p}/m = -i[\mathbf{x}, H]$ We can show the dipole matrix element is -

$$|M_{f,i}|^2 \propto \left| \langle \phi_f^{\mathbf{k}} \,|\, \epsilon \cdot \mathbf{x} \,|\, \phi_i^{\mathbf{k}} \rangle \right|^2. \tag{2.36}$$

From this equation, it is very clear that three factors influence the matrix element : the wavefunction properties, the photon energy, and its polarization/direction of incidence i.e., experimental geometry. First, the symmetry and orbital texture of the wave function lead to intensity variations within the Brillouin zone, whereas the crystal's space-group symmetry can suppress or enhance signals at symmetry-equivalent points across different Brillouin zones [91]. The ARPES signal can be viewed as a coherent superposition of photoelectron waves carrying the spatial and phase information of the hybridized initial orbital, leading to characteristic intensity modulations in 3D $\mathbf{k}$ space [92, 93]. Also, since the matrix element term is related to the initial state $|\, \phi_i^{\mathbf{k}} \rangle$, the dipole transition matrix element plays a central role in ARPES extracting the microscopic information about

$|\,\phi_i^{\mathbf{k}}\rangle$ [92, 94]. Second, varying the photon energy allows ARPES to probe different k_z planes of the three-dimensional Brillouin zone. Because the band dispersion along k_z depends on the orbital character and the symmetry of the crystal, scanning photon energy reveals how these factors shape the electronic structure. Finally, the light's polarization, which is also linked to the measurement geometry. So the full evaluation of the dipole matrix element can be very challenging —because of the detailed measurement geometry and orbital hybridization [93] — however, the symmetry and conservation laws provide a good prediction. For example, when we perform photoemission along the crystal mirror symmetry plane of the sample, we can extract the parity of the initial state $|\phi_{\mathbf{k}}^i\rangle$ by measuring the photoemission intensity for different linear polarization geometries. This idea is generalized to determining the orbital character of bands throughout the Brillouin zone [93, 95–97]. For orbital-selective measurements, the chosen light polarization (s or p) and the target orbital must share the same parity with respect to a virtual mirror plane set for the ARPES system [4, 98, 99]. Fig. 2.7, for example, illustrates how linear polarization shapes the angular distributions of photoelectrons emitted from s-, p-, and d-orbitals. By using linearly polarized s and p light, we get linear dichroism that allows us to distinguish orbital character. Similarly, we can use left- and right-circularly polarized light from which we get circular dichroism in the photoelectron angular distribution [100]. The circular dichroism in ARPES is sensitive to the local handedness of the wavefunction, time-reversal symmetry of the electronic states, and linked with the local Berry curvature [59, 101–103], spin- and orbital-angular momentum [102, 104]. Note that interpretation of circular dichroism ARPES data is not straightforward as final-state effects and contributions from $\nabla \cdot \mathbf{A} \neq 0$ can introduce strong geometry and photon-energy dependent circular dichroism signal [105–110].

Having established the ARPES foundations and the information it provides, I now focus on its time-domain extension : time-resolved ARPES (TR-ARPES)—which forms the core methodology for my thesis work presented here. The following section is mainly adapted from [5, 6]

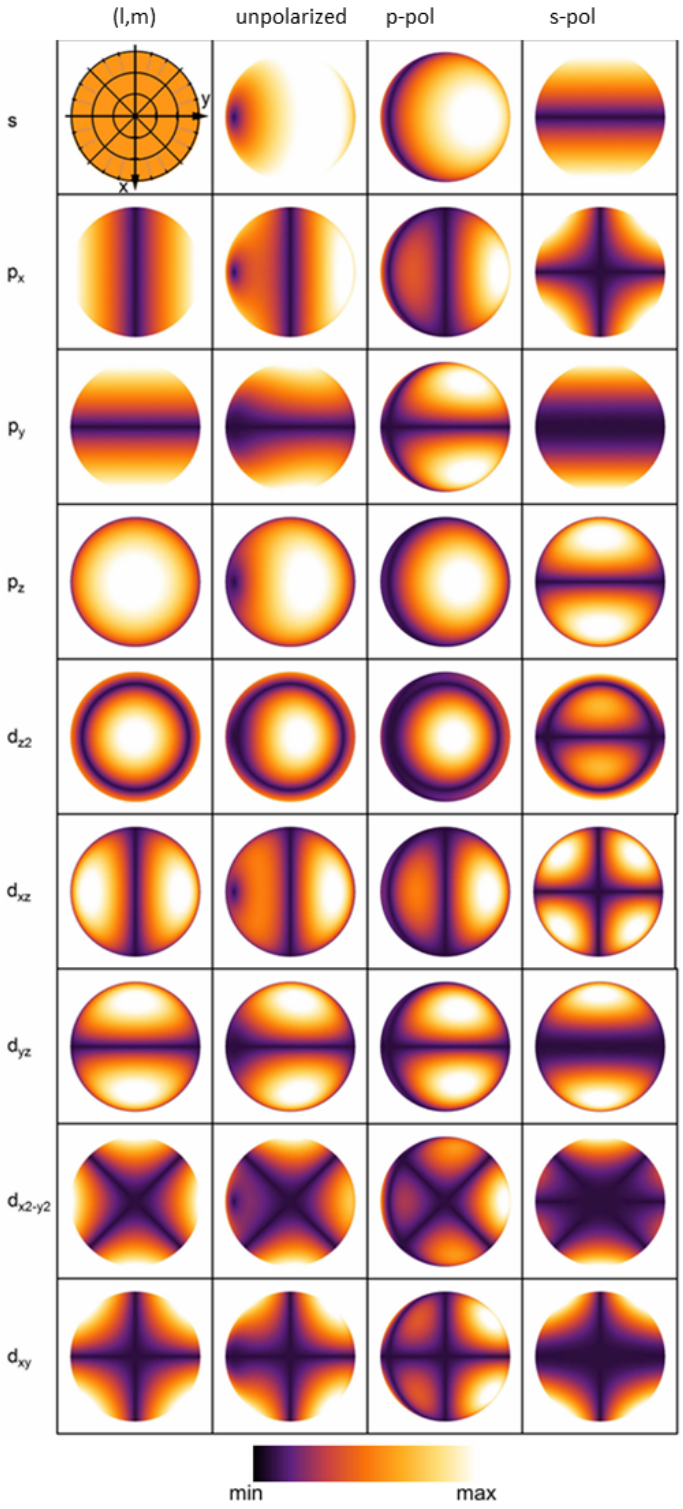


FIGURE 2.7 : Dipole matrix-element effects on angular photoemission patterns. Effect of dipole matrix–element–driven angular emission on the photoelectron patterns from s-, p-, and d-orbitals for different linear polarizations where light comes from the left at an incidence angle of 60°. With unpolarized or p-polarized light, the photoelectron distributions reflect the atomic orbital (l, m). In contrast, s polarization strongly suppresses spectral weight along the yz scattering plane. Adapted from [92], , with permission from the publisher.

2.3 TR-ARPES

While Static ARPES reveals equilibrium electronic properties of matter, TR-ARPES adds access to ultrafast dynamics : it tracks how the electronic distribution evolves following a pump pulse excitation. Such optical excitation typically drives the electron population beyond Fermi–Dirac distribution, launches specific collective excitation (e.g., phonons), and leads to new emerging nonequilibrium and/or metastable phases of matter with no equilibrium counterpart. Accordingly, TR-ARPES does not merely probe intrinsic single-particle motion; it maps how photoexcited electrons interact with each other and with collective excitations, and how electronic properties are modified by selective excitations of specific collective modes. This dynamical view is also central for applications because the design and engineering of new materials strongly rely on their dynamical response, such that the performance of devices—whether under an applied bias (microelectronics) or illumination (photovoltaics)—is governed by nonequilibrium electronic distributions and their dynamical behavior, which set macroscopic figures of merit such as resistivity and energy-conversion efficiency. TR-ARPES therefore serves both fundamental and technological aims, providing a direct, momentum-resolved characterization of out-of-equilibrium behavior in quantum materials.

2.3.1 Overview

The development of femtosecond laser technology has paved the way for extending ARPES into the time domain. The TR-ARPES technique relies on the use of two ultrashort laser pulses : a pump pulse to excite the system into an out-of-equilibrium state and a probe pulse to photoemit electrons from the sample. The relative delay between the two pulses is controlled via a motorized translation stage, thus allowing the light-induced electron dynamics of the system to be tracked with femtosecond temporal resolution. Since my thesis is solely based on using the TR-ARPES technique, I will briefly discuss this technique, starting with a simple example just to be familiar with the data. In the example sketched in Fig.2.8a, a pump pulse (typically visible–infrared) drives the system out of equilibrium, while a UV (~ 6 eV) or XUV (> 10 eV) probe pulse photoemits from the sample under investigation. The detector records the emitted photoelectrons with angular resolution, revealing time-dependent changes in electronic band structure and occupancy. An illustration of the TR-ARPES map is shown in Fig.2.8b, considering a p-doped topological insulator Bi_2Te_3 dispersion. The top row depicts energy–momentum snapshots at selected pump–probe delays τ. For negative delays ($\tau < 0$, far left), the probe arrives before the pump, so no pump-induced changes appear in the photoemission signal (apart from slow effects persisting between two consecutive pump pulses, e.g., local heating of the sample or surface photovoltage, which is related to the generation of an electric field at the sample surface). At temporal overlap ($\tau \approx 0$, center-left), the map shows an out-of-equilibrium electronic distribution due to the vertical optical transitions driven by the pump. Then the next map (center-right) shows at timescales ($\tau \sim 1\ ps$), where the pump-induced excited hot carriers thermalize into a quasiequilibrium Fermi–Dirac distri-

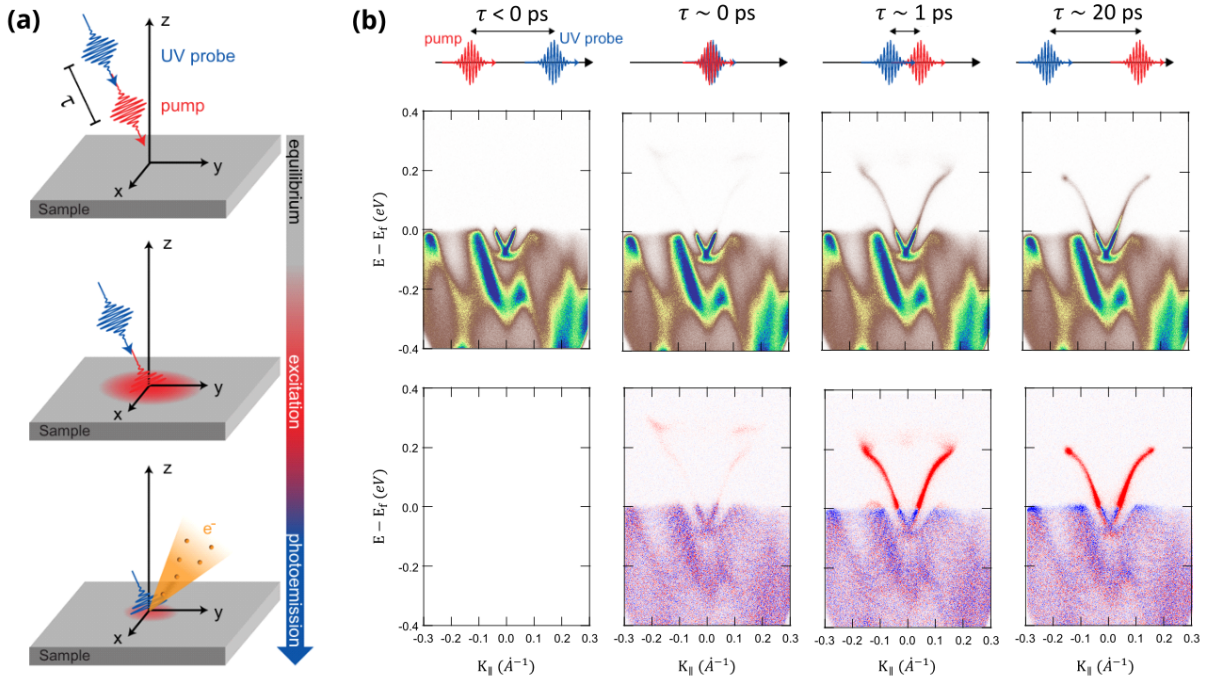


FIGURE 2.8 : Working principles of TR-ARPES. (a) Pump–probe schematic : two ultrashort pulses are separated by a delay $\tau > 0$. The pump drives the system out of equilibrium; the probe initiates photoemission (Adapted from [6], with permission from the publisher). (b) Example for a Topological insulator dispersion. *Top :* TR-ARPES maps at selected delays τ. The red dashed arrow marks the pump photon energy and the corresponding vertical promotion from occupied to unoccupied states. *Bottom :* Differential maps visualize pump-induced spectral-weight redistribution.

bution characterized by an effective electronic temperature. Finally, the right panel shows the map for longer positive delays ($\tau \gg 0 \sim 20\ ps$), in which the system relaxes back to its equilibrium conditions by transferring the energy to the lattice and other collective modes. The bottom row of Fig. 2.8b shows differential TR-ARPES maps, defined as $I(\mathbf{k},\omega)_\tau - I(\mathbf{k},\omega)_{\tau<0}$, for the same positive delays as above, where $I(\mathbf{k},\omega)_\tau$ is the photoemission intensity at momentum $\mathbf{k}$, energy ω, and delay τ. Red (blue) denotes an increase (decrease) in photoemission intensity relative to equilibrium and is commonly interpreted as population (depletion). This differential representation provides an alternative way to view the TR-ARPES data, directly highlighting the pump-induced changes in the band structure. However, direct interpretation can be complicated by multiple transient contributions to the measured intensity. Thus, the interpretation of TR-ARPES data is often not so straightforward and can easily lead to misinterpretation of the corresponding physics.

2.3.2 Theoretical Background of TR-ARPES Intensity

In the previous section, we developed an understanding of equilibrium ARPES signals. In TR-ARPES, this understanding can be extended to the quasiequilibrium regime and to the strictly

out-of-equilibrium regime. However, we restrict the discussion to the quasiequilibrium regime for this work.

Quasi-equilibrium description : Understanding a system's transient response upon pump pulse perturbation is far from straightforward. We need to consider the effects of the pump pulse's electric field, potential appearance of new transient states of matter, and other highly nonthermal processes [111–114]. In most cases, however, after the initial pump-induced excitation, the electrons thermalize into a quasiequilibrium state within 10 to 100 fs, and it has been shown that the adiabatic band picture (i.e., the equilibrium band structure) survives even at zero pump probe delay and high pump intensity [115]. In this regime, for a single-band system, the TR-ARPES signal can be approximated by extending the equilibrium ARPES formalism of eq. 2.29 into the time domain as

$$I(\mathbf{k},\omega,\tau) \;\simeq\; A(\mathbf{k},\omega,\tau)\left|M(\mathbf{k},\omega,\tau)\right|^2 f(\mathbf{k},\omega,\tau), \tag{2.37}$$

which is also known as generalized Kadanoff-Baym approximation [116]. A direct consequence

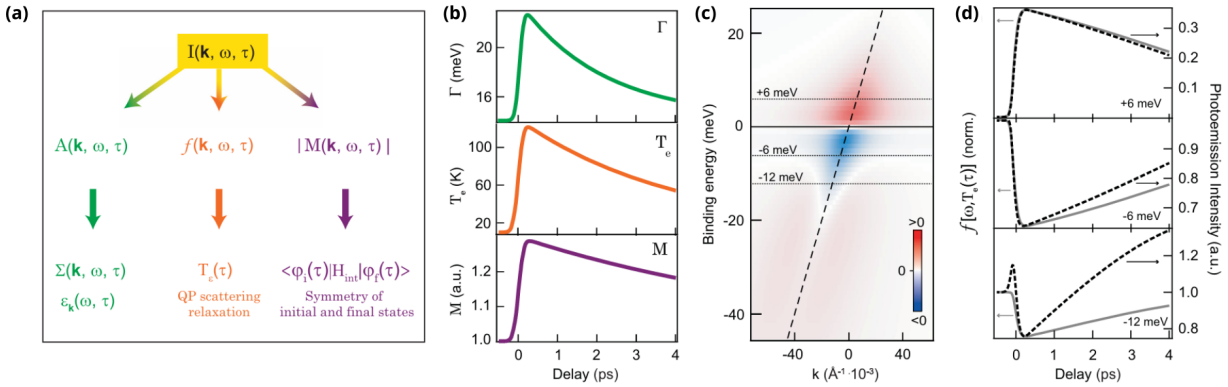


FIGURE 2.9 : Schematic of the various components shaping transient photoemission intensity and their intertwined contributions in TR-ARPES. (a) Breakdown of the different contributions of spectral function, occupation, and matrix elements and the information each encodes that characterizes the transient photoemission intensity $I(\mathbf{k},\omega;\tau)$. (b) Hypothetical time traces of spectral broadening Γ, electronic temperature T_e, and matrix element $|M|$, with $\Gamma(\tau) = \Gamma_{\mathrm{imp}} + \beta\left[\omega^2 + \pi^2 k_B^2 T_e^2(\tau)\right]$ (shown at $\omega = 0$, using $\Gamma_{\mathrm{imp}} = 14$ meV and $\beta = 8$). (c) Simulated differential TR-ARPES map at $\tau = 3$ ps for a linear dispersion (black dashed line), considering the transient parameters in (b) and incorporating the ω-dependent Γ. (d) Transient intensity at three binding energies from (c) (black dashed) compared with the evolution expected from $T_e(\tau)$ alone in (b) (grey solid), underscoring their distinct dynamics. Adapted from [6], with permission from the publisher.

of eq. 2.37 is that the transient photoemission intensity $I(\mathbf{k},\omega,\tau)$ reflects the simultaneous evolution of three distinct quantities : the occupation $f(\mathbf{k},\omega,\tau)$, the dipole matrix element $|M(\mathbf{k},\omega,\tau)|^2$, and the spectral function $A(\mathbf{k},\omega,\tau)$ (Fig. 2.9). As illustrated in Fig. 2.9b each of these terms can change independently—for example, A through variations in the spectral broadening Σ'', f through the time-dependent electronic temperature T_{e}, and in $|M|$ through pump-induced modifications of orbital character or symmetry. Because all three contributions enter multiplicatively into the measured intensity, variation in $I(\mathbf{k},\omega,\tau)$ cannot be uniquely attributed to any single one of them. Fig. 2.9d compares the transient photoemission intensity at three binding energies (black dashed traces) of

a simulated linearly dispersive medium (Fig. 2.9c) with the evolution of electronic distribution based on only changes in the T_e alone (solid gray). Notably, the TR-ARPES signal is not necessarily able to replicate the transient electronic distribution (bottom panel of Fig. 2.9d) or the single-particle lifetime τ_s (described by Γ in Fig. 2.9b). Instead, it reflects the coupled influence of all three different contributions as shown in Fig. 2.9a. To understand this better, let us discuss the transient evolution of each term and how to interpret its contributions.

Occupation $f(\mathbf{k},\omega;\tau)$ *:* In equilibrium ARPES, $f(\omega) = [1+\exp(\omega/k_\mathrm{B}T)]^{-1}$ is momentum-independent and restricts ARPES to occupied states. In TR-ARPES, the pump promotes carriers into unoccupied states in some specific regions of the 3D Brillouin zone, potentially leading to a highly anisotropic momentum space, at least for short delays ($\tau \sim 0$). At later times after going through thermalization processes such as electron–electron, electron-boson and electron-impurity scatterings, hot electrons redistribute over the entire 3D momentum space, and only then can $f(\mathbf{k},\omega,\tau \gg 0)$ be approximated as a k-independent Fermi–Dirac distribution with a time dependent effective electronic temperature $T_\mathrm{e}(\tau)$. The pump can create a nonthermal electronic distribution at very early delays. Combined with TR-ARPES's momentum resolution, this enables direct mapping of band dispersions in the unoccupied states, extraction of band gaps, and tests of *ab initio* band-structure calculations. Moreover, by tracking how photoinjected carriers in the unoccupied states thermalize and relax back to equilibrium, TR-ARPES yields qualitative and quantitative insight into multiparticle scatterings (e.g., electron dynamics in graphene), ultrafast changes in screening and dispersion (e.g., via detecting coherent phonons), and fundamental electron–boson couplings (e.g., through signatures of quantized decay processes).

Matrix elements $\left|M(\mathbf{k},\omega;\tau)\right|^2$ *:* In TR-ARPES, the transient evolution of matrix element $M(\mathbf{k},\omega,\tau)$ is often neglected. However, such evolution has recently been observed both theoretically [117] and experimentally [118]. This is especially relevant in multiorbital systems, where the initial-state wave function may result from a complex interplay of different or layer-dependent orbital characters. Consequently, unless a single, well-defined orbital is studied, $M(\mathbf{k},\omega,\tau)$ should be explicitly considered for describing the transient evolution of photoemission intensity $I(\mathbf{k},\omega;\tau)$. Manipulating the polarization of the probe enables obtaining direct evidence of transient matrix-element changes [118]. Recent studies [119, 120] show that performing polarization and dichroism studies with TR-ARPES enables precise tracking of light-induced modifications of the symmetry of the initial photoemission state wavefunction, which opens up a new direction.

Spectral function $A(\mathbf{k},\omega;\tau)$ *:* The spectral function $A(\mathbf{k},\omega;\tau)$ captures many-body interactions as well as transient changes of the band-structure and density of states. Photoexcitation can adiabatically modify bare band dispersions through coherent or incoherent phonons, and can transiently modify the many-body interaction, i.e., self-energy $\Sigma(\tau)$ due to various effects ranging from transient modification of the screening and scattering phase space to light-induced phase transitions.

TR-ARPES intrinsically links transient carrier redistribution to many-body interactions, electronic/bosonic DOS, and the symmetries of initial/final states. By disentangling various transient contributions to eq. 2.37 Carefully, TR-ARPES allow us to directly identify light-driven phenomena in condensed matter.

2.3.3 Experimental aspects of TR-ARPES

The advancement of TR-ARPES is the result of technological progress in ultrafast laser systems, nonlinear optics —specifically harmonic generation in nonlinear crystals and high-harmonic generation —and the development of electron spectrometers. In Fig. 2.10 [5], I present a historical

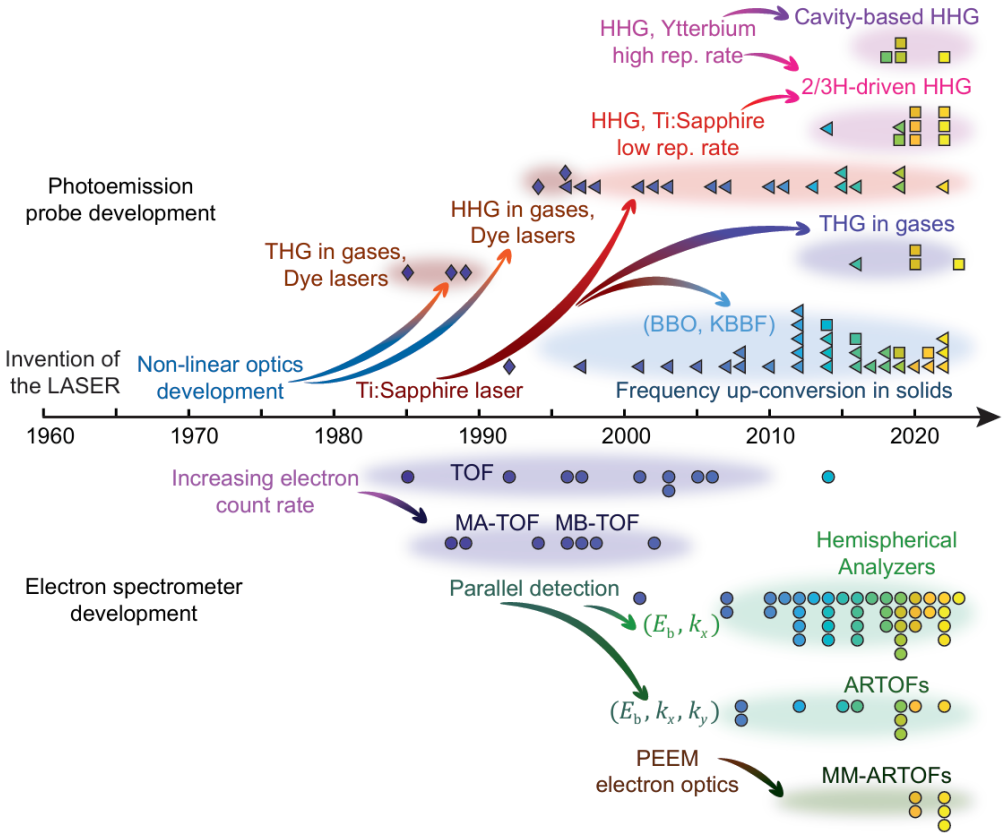


FIGURE 2.10 : Historical timeline of TR-ARPES. Probe sources (diamonds : dye; triangles : Ti :sapphire; squares : Yb-doped) and their paired electron spectrometers (circles) are placed by publication year; each pair denotes a distinct setup. Although early TR-ARPES in the 1980s used higher photon energies, the field expanded rapidly around 2005 with Ti :sapphire–based 6 eV probes and parallel detection on hemispherical analyzers. Subsequent advances pushed photon energy, repetition rate, and energy resolution via harmonic-driven and cavity-enhanced HHG. On the detection side, TOF analyzers were adopted for higher throughput at low repetition rates, followed by increased parallelization with ARTOF and MM–ARTOF instruments that add spatial resolution. Abbreviations : T/FHG (third/fourth harmonic generation), HHG (high-harmonic generation), TOF (time-of-flight), MA (multi-anode), MB (magnetic-bottle), PEEM (photoemission electron microscopy), MM (momentum microscope). Adapted from [5], with permission from the publisher.

overview of ultrafast laser systems and the evolution of photoelectron spectrometers that has led to the current state of TR-ARPES. In the following, I discuss the key aspects of TR-ARPES measurements, which fall into three main categories : the light sources that generate the pump and probe, the photoelectron spectrometer for detection, and the sample under study.

1. Light Source : In TR-ARPES, one must generate a probe pulse to photoemit and a pump pulse to excite the system in an out-of-equilibrium state.

i. Probe Source : In TR-ARPES, unlike conventional ARPES, a pulsed laser source is required because most electronic dynamics occur on femtosecond timescales, necessitating femtosecond temporal resolution; and UV/XUV pulses are commonly used as probes in this regime. They are produced by frequency upconversion of visible-IR laser pulses in nonlinear crystals, and high-order harmonic generation (HHG). I present in Fig. 2.11 a survey of probe photon sources used in TR-ARPES over recent years, where the marker color encodes the publication year, while the marker shape identifies the source's gain medium. Up to ∼6–7 eV, probes are commonly generated from the Fundamental Frequency (FF) of Yb-based or Ti :Sapphire lasers by third harmonic generation (THG), fourth harmonic generation (FHG) or sum frequency generation (SFG) between the various components in nonlinear crystals. To reach higher photon energy, it is necessary to perform

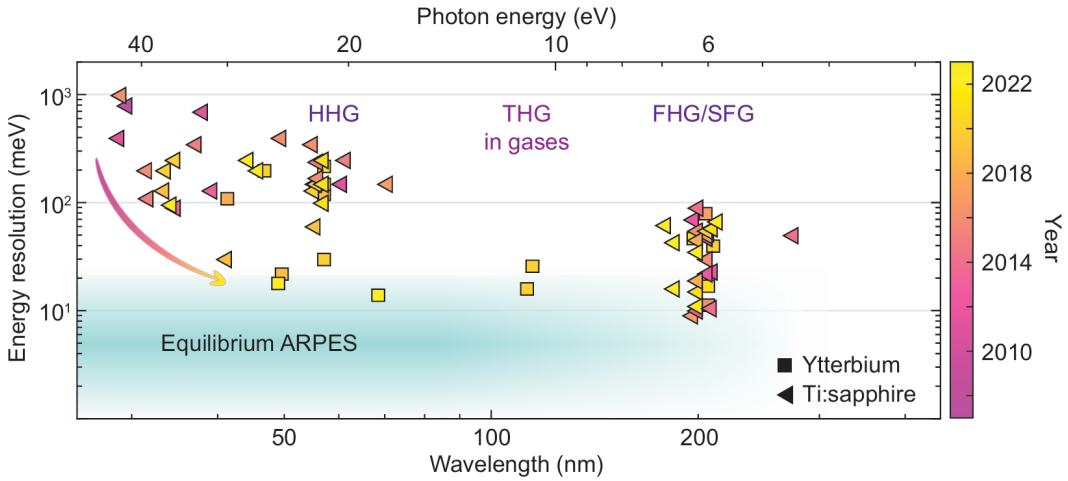


FIGURE 2.11 : Survey of TR-ARPES probe sources. Energy resolution ΔE (from a Fermi-edge fit on polycrystalline metal, typically Au) plotted versus photon energy. The color of each marker represents the publication year, while the square and triangular shape identifies Yb and Ti :sapphire light source. Solid-state frequency up-conversion provides 4.5–7 eV photons and has steadily matured, underscoring its reliability and relevance. Gas-phase UV-driven THG extends to ∼11 eV with good ΔE, though fewer implementations exist. HHG sources—especially Yb-based—have achieved major improvements in energy resolution in recent years (indicated by the gradient arrow). Adapted from [5], with permission from the publisher.

non-linear optics in gases. THG in Xe can reach ∼11 eV, while higher energies are obtained via high-order harmonic generation in gases (HHG). However, sources based on THG and HHG grew more slowly than 6-eV sources, due to the limitation of the commercial Ti :sapphire laser technology. Indeed, HHG requires high energy per pulse and high intensity, which was only possible at

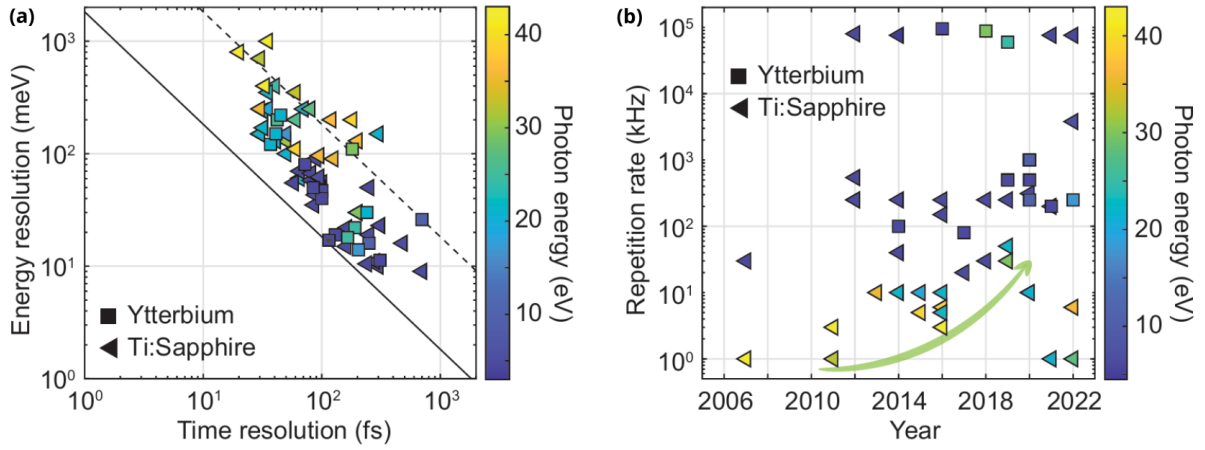


FIGURE 2.12 : Survey of TR-ARPES probe sources : time–bandwidth product and repetition rate. (a) Energy resolution ΔE (from a cold Fermi edge) versus time resolution Δt (pump–probe cross-correlation). The solid line marks the Gaussian transform limit (1825 meV·fs); the dashed line indicates $10\times$ this limit. Recent XUV implementations now approach the time–bandwidth performance of 6 eV probes. (b) Probe repetition rate versus publication year. Ti :sapphire systems spanning $\sim$10 kHz–10 MHz have long supported 6 eV generation. Ti :sapphire–based HHG progressed from $\sim$1 kHz to $\sim$100 kHz, while Yb-doped platforms pushed HHG beyond 100 kHz. Adapted from [5], with permission from the publisher

kHz repetition rates. This limitation has been released by the advent of Yb-based laser sources, operating at 100 kHz and above.

Because of the required high intensity, HHG sources often use very short Ti :sapphire laser pulses, typically in the 20 fs range. However, this produces pulses with broad bandwidths and poor energy resolution (hundreds of meV). There is thus a trade-off between temporal and energy resolution, which is summarized in Fig.2.12a. State-of-the-art Ti :sapphire and Yb-doped 6-eV sources approach the line, depicting the Fourier limit, and offer the widest tunability of ΔE and Δt. HHG near $\sim$25 eV can match this performance in some implementations, whereas above $\sim$30 eV typical resolutions remain > 100 meV. The evolution of the repetition rate of probe sources as a function of publication year is shown in Fig.2.12b. This shows Ti :sapphire-based 6 eV source spanning 10 kHz to $>$10 MHz for decades. In contrast HHG has progressed steadily from 100 kHz to 1 MHz to increase event-count rates while maintaining sufficient pulse energy for efficient harmonic generation. While Ti :sapphire-based systems were the only sources up until 2018, with the highest repetition rates in the 100 kHz regime. Since then, the development of Yb-based fiber laser technology has enabled HHG operation in the 100 kHz-1 MHz range, and repetition rates can be pushed even further using cavity-enhanced schemes, which approach $\sim$100 MHz and have been successfully implemented in TR-ARPES.

ii. Pump sources. In TR-ARPES, the pump pulse perturbs the system from equilibrium, and then the system returns to its equilibrium or a metastable state through various relaxation processes. The pump photon energy should be below the work function of the material. To minimize pump-probe time jitter, the pump is typically derived from the same laser oscillator as the probe, although two independent lasers can also be used; but to achieve a stable delay, they need to be

synchronized. The laser fundamental frequency (FF) and its second harmonic are most commonly used. However, nonlinear frequency conversion (OPO/OPA, SHG/THG, DFG) provides broad tunability from the THz to the visible and has been recently emerging to study new exciting physics such as Floquet Bloch engineering, driving phonon oscillations, etc. A universal consequence of pumping is an increase in average sample temperature (because of which maintaining sub-10 K sample temperatures at negative delays is typically challenging in TR-ARPES). This thermal load can be reduced by lowering the repetition rate at fixed absorbed fluence or by choosing spectral regions where the material is (quasi)transparent.

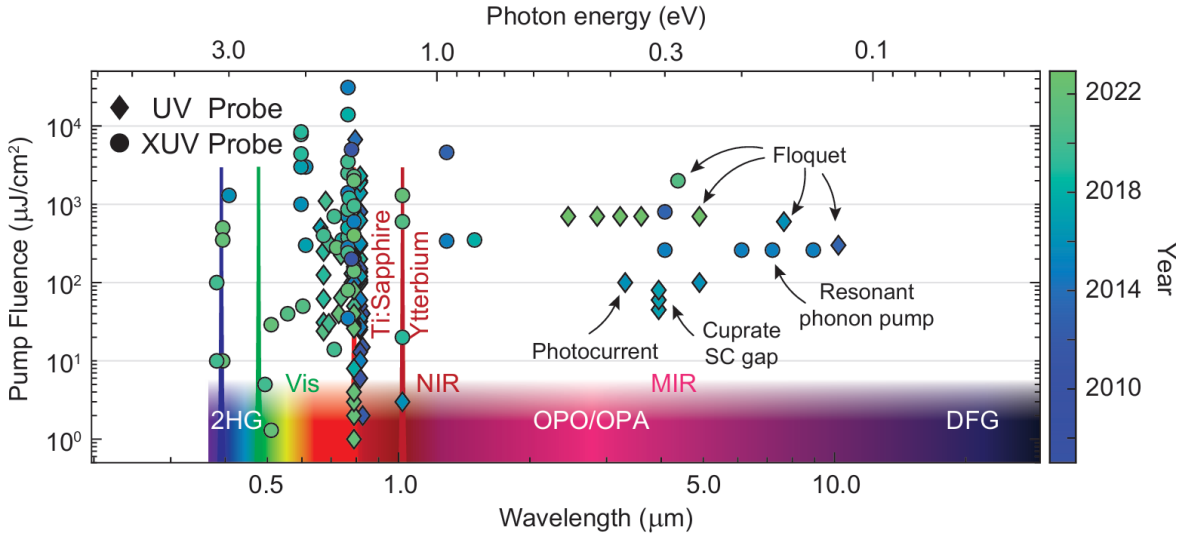


FIGURE 2.13 : Survey of pump sources in TR-ARPES. Pump fluence versus photon energy, highlighting the prevalence of Ti :sapphire fundamentals (780–840 nm) across all fluences. OPO/OPA stages extend tunability into the mid-IR, enabling Floquet engineering and resonant driving of bosonic modes. The second harmonic of the fundamental and OPA outputs, as well as 2H-driven OPA, cover most of the visible range, granting access to excitonic and carrier dynamics in semiconductors and molecular systems. Adapted from [5], with permission from the publisher.

A survey of published TR-ARPES studies highlights the two most varied parameters - pump fluence and photon energy in Fig.2.13 in which the marker color encodes publication year, and the marker shape indicates the probe photon energy. The prevalence of Ti :sapphire pumps near 1.55 eV, spanning an entire fluence range, is mainly due to the versatility of this source in terms of fluence, polarization, pulse duration, and spot size, and due to the fact that the photon energy is above the bandgap of many semiconductors. By contrast, Yb-based fundamentals at 1.2 eV lie below many semiconductor gaps, limiting the use of FF for pumping. However Yb Yb-based laser systems commonly incorporate OPO/OPA stages for near-/mid-IR, or using Difference frequency generation (DFG) seeded by signal and idler output of OPA to generate multi-THz (> 10 THz) excitation. This long-wavelength regime is attractive for resonantly driving low-frequency collective modes (phonons, magnons), studying correlated electronic phases (e.g., unconventional superconductors; charge/spin density waves), controlling material properties in an ultrafast manner, or

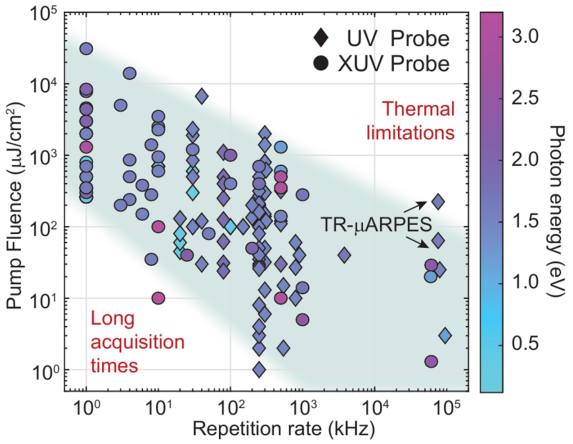


FIGURE 2.14 : Survey of pump parameters : fluence versus repetition rate in TR-ARPES. Available fluence scales loosely with repetition rate, offering roughly 1–2 orders of tunability. Low-fluence operation at low rep. rate is constrained by prohibitively long acquisition times, whereas high-fluence operation at high rep. rate is limited by sample heating and thermal damage. Adapted from [5], with permission from the publisher.

inducing hybrid light–matter states. Most mid-IR TR-ARPES studies have operated so far at relatively high fluence because available sources typically run at low repetition rates. By frequency up-conversion using OPA into the visible/UV, the pump photon energy exceeds typical semiconductor gaps; although multiphoton photoemission limits the usable fluence, these higher-energy pumps have successfully enabled studies of semiconductors, dynamic band-gap renormalization, and resonant excitation of excitons.

Figure 2.14 summarizes the pump fluence versus repetition rate used in TR-ARPES studies. The low-fluence, low-repetition-rate regime is limited by prohibitively long acquisition times, whereas the high-fluence, high-repetition-rate regime is constrained by thermal damage to the sample.

Trade-offs in Pump and Probe Parameters : Space charge (SC) is the primary constraint in TR-ARPES, as it limits the number of photoelectrons per pulse. SC can be mitigated by lowering the probe fluence or enlarging the probe spot, but small spots ($<$100 μm) are often required to access uniform single-crystal domains (and for better momentum resolution); consequently, the probe flux is typically reduced, lowering the energy count rate (ECR) and increasing acquisition time. Increasing the repetition rate offers a cleaner route to higher ECR while remaining below the SC limit, but this comes at the cost of reduced pulse energy for nonlinear frequency conversion and increased average pump power, which raises the lattice temperature and limits the usable pump fluence. At high repetition rates, the system may not fully cool down between pulses, imposing additional thermal constraints and potential sample damage. Pump fluence can be increased without raising power by shrinking the pump spot, but the pump is generally kept larger than the probe to maintain uniform excitation. Momentum resolution in TR-ARPES improves at low photon energy but at the expense of accessible k-range, reduced photoemission cross-section. Overall, TR-ARPES source

design is governed by two fundamental trade-offs : (i) the Fourier limit linking pulse duration and bandwidth, which sets the balance between time and energy resolution; and (ii) the tension between maximizing ECR and minimizing SC and thermal loading. In is worth mentioning that as a result of various trade-offs such as energy resolution, temporal resolution, and momentum resolution, all of these discussed laser platforms remain relevant. Looking ahead, high-repetition-rate free-electron lasers promise fully tunable TR-ARPES across the XUV to soft–x-ray range, enabling studies of ultrafast dynamics in a highly dispersive 3D materials and element-specific measurements via resonant TR-ARPES.

2. Photoelectron Spectrometers : Three primary electron detectors are in common use : time-of-flight (TOF) spectrometers, momentum microscopes (MMs), and hemispherical analyzers (HAs). TOF systems capture isoenergy contours across two-dimensional momentum space in a single shot. MMs operate in both real- and momentum-space modes, enabling μm-scale, region-selective measurements (e.g., on exfoliated flakes). HAs—while requiring sample motion or electrostatic deflection to cover the full 2D $\mathbf{k}$-space—typically offer superior energy/momentum resolution and a wider dynamic range in photoemission intensity.

i. Hemispherical Analyzer : The hemispherical analyzer has been the ARPES workhorse for decades, thanks to its versatility (compatible with pulsed and continuous sources from eV to keV) and its high angular and energy resolution at moderate throughput. A typical instrument comprises an input lens column, a hemispherical electrostatic deflector, and a two-dimensional detector (shown in Fig. 2.15a). The lens column images the angular distribution onto a slit at the hemispherical deflector entrance. Two concentric hemispheres biased at different potentials create a radial field that guides electrons on elliptical trajectories, dispersing kinetic energies along the detector's radial axis, while the orthogonal position encodes the emission angle within the slit acceptance. The detector thus records $I(E_{\mathrm{kin}}, \vartheta_y)$. Energy resolutions near 1 meV can be obtained, even 100 μeV being achievable under suitable conditions. Typical acceptance angles are $\pm 15^{\circ}$ with angular resolution down to $\sim 0.1^{\circ}$. Traditionally, mapping the angle perpendicular to the slit required sample rotation; modern spectrometers incorporate electrostatic deflection in the lens column to raster the beam within the accepted cone, enabling two-dimensional momentum mapping without mechanical motion.

ii. Time-of-flight : : Time-of-flight (TOF) spectrometers (presented in Fig. 2.15b) determine an electron's kinetic energy from the interval between its photoemission and its arrival at the detector. This requires a pulsed light source and a detector with sufficient temporal resolution. The repetition rate is also critical : if pulses arrive too closely in time, slow electrons from one cycle can be overtaken by fast electrons from the next, leading to ambiguity in the interpretation of the signal. In practice, pulse durations $<$ 100 ps and repetition rates $<$ **1** MHz are appropriate, making TOF well matched to many laser-based sources, including pump–probe measurements. TOF spectrometers exhibit low background because detection is intrinsically gated to the pulse train. An advantage with this kind of detector is that both axes of the area detector can image emission angles, yielding

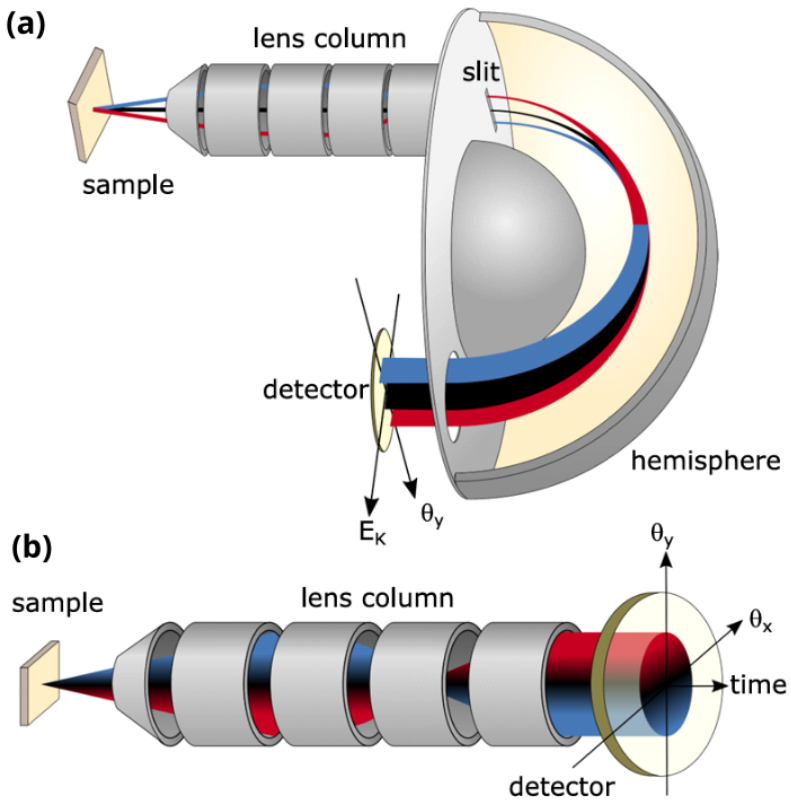


FIGURE 2.15 : Photoelectron spectrometers for ARPES. a. Hemispherical analyzer where the lens column maps the angular distribution of the photoelectrons onto the entrance slit of the hemispherical deflector, and a 2D detector detects emission angle ϑ_y and Kinetic energy $E_{\rm kin}$ of the photoelectrons. b. Time of flight detector where the lens column projects the electrons' angular distribution onto a time-resolved 2D detector, which records the emission angles $(\vartheta_x, \vartheta_y)$ along with the photoelectron flight time. Adapted from [3], with permission from the publisher.

a three-dimensional dataset $I(E_{\rm kin}, \vartheta_x, \vartheta_y)$—typically over $\sim 15^\circ$ in each angular direction—with higher overall throughput than hemispherical analyzers.

iii. Momentum microscope : In recent years, ARPES instruments using photoemission electron microscopy (PEEM) optics—often termed momentum microscopes started growing. In this method, by biasing the front lens element with an extraction voltage, the system allows to collect the full $\pm 90^\circ$ photoemission cone. Energy analysis can be implemented via a retarding field (as in PEEM), time-of-flight detection, or dispersive energy filtering with a double-hemispherical analyzer to enhance resolution and mitigate spherical aberration. The use of PEEM optics enables operation in real-space or momentum-imaging modes. A key advantage of the momentum microscope, especially with a TOF detector, is the high collection efficiency due to no entrance slits or apertures, so virtually all photoelectrons are recorded. This is particularly valuable for spin-resolved measurements. It has been demonstrated to reach sub–10 meV energy resolution.

3. Sample : Good measurements require careful sample preparation and strict control of measurement conditions. The sample must be sufficiently conductive and well grounded to avoid

charge accumulation from photoemission (space charge), which otherwise shifts photoelectron energies and broadens spectral features. For wide-band-gap semiconductors, measurements are often challenging due to charge formation; however charging can be mitigated using an electron-flood gun, surface doping, laser photoexcitation, high temperature, or developing thin films grown on conductive substrates.A practical check is to perform a flux dependence measurement, whose results should be independent of the photon flux in the absence of a space-charge problem. In addition, ARPES typically requires long-range order within the probed area. Multiple structural domains yield an incoherent superposition of signals from different regions, which increases and complicates the analysis; hence, single crystals are often preferred for ARPES. Samples should also be sufficiently flat to avoid distortions of the band dispersion.

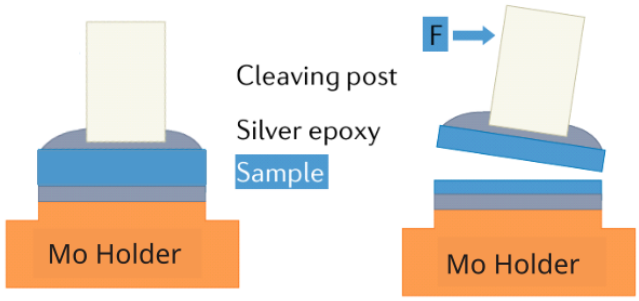


FIGURE 2.16 : In-vacuum cleaving procedure for single-crystal ARPES measurements. Schematic illustration of the in-vacuum cleaving process used for single crystals in ARPES experiments. The sample is mounted on a molybdenum (Mo) holder using silver epoxy, and a top post is subsequently glued onto the crystal surface. After curing at a controlled temperature, a mechanical force is applied to the top post under ultra-high vacuum conditions, resulting in a clean cleavage surface suitable for ARPES measurements.

Because the inelastic mean free path of 5–100 eV electrons is short, low-energy-probe ARPES is extremely surface-sensitive, with only a few atomic layers contributing. Surfaces must therefore be exceptionally clean and stable against residual gas; even a monolayer of adsorbates can scatter photoelectrons and lead to blurred spectra. The most common route to get a clean sample surface is cleaving inside the UHV chamber, as illustrated in Fig. 2.16. Prior to loading, a cleaving post (e.g., a ceramic stub) is affixed to the sample surface using a conductive silver epoxy or a high-strength Torr Seal. There exist different types of epoxy/adhesives with different cleaving strength and curing temperature which should be chosen accordingly. Samples are also mounted to the holder with conductive epoxy. Molybdenum, Copper, and stainless steel are frequently used as a sample holder owing to their excellent thermal conductivity, particularly at cryogenic temperatures. When subsequent annealing is required, adhesives are generally avoided, and spot welding or mechanical screws are used. Annealable holders are typically fabricated from refractory metals such as tantalum or molybdenum to prevent decomposition or outgassing at high temperatures. If an insulating adhesive is unavoidable, a conductive paint or graphite coating is applied afterward to ensure good electrical conductivity. For materials that cannot be cleaved, the surface can be mechanically polished and then cleaned *in situ* by sputter/anneal cycles. In some cases,

simple *in situ* degassing and annealing is sufficient to remove contaminants, such as for inert thin films and thin flakes exfoliated onto substrates. The maximum anneal temperature is limited by film stability (e.g., epitaxial graphene typically yields atomically clean surfaces at 250–400 °C). For some materials, *in situ* synthesis is the only viable route, since ARPES is naturally compatible with molecular-beam epitaxy (MBE), enabling very high-quality sample surfaces, with precise layer and stoichiometry control and even growth of chemically unstable or metastable phases. Alternatively, atmospheric exposure can be avoided by integrating material synthesis and ARPES chambers, by using removable protective capping layers, and by transporting samples in UHV-quality vacuum suitcases. During measurement, *in situ* sample control and manipulation enable tuning of the electronic structure and the material properties. Three such approaches are used in ARPES : surface electron doping, electrostatic gating, and strain, which can be integrated during measurement to explore band-structure responses under such operando conditions.

2.4 Conclusion

In this chapter, we introduced the theoretical foundations of TR-ARPES, a powerful technique for probing out-of-equilibrium electronic properties with simultaneous energy, momentum, and temporal resolution. TR-ARPES provides direct access to unoccupied and transient states, enabling the mapping of electronic states above the Fermi level, including conduction-band and unoccupied surface states. This capability allows for the determination of conduction band minima and band gaps and has facilitated its widespread application in a variety of systems, from topological insulators to semiconductors.

By examining the dynamics of excited states, TR-ARPES also enables the extraction of their lifetimes, which are critical for understanding transport and optoelectronic functionality. Moreover, the study of electron dynamics and band renormalization provides insight into electron–electron and electron–phonon interactions. Observations of band renormalization and energy-gap evolution further shed light on equilibrium properties as well as dynamically induced phase transitions under light excitation.

This theoretical framework underpins the experimental investigations presented in the following chapters, where TR-ARPES is applied to topological insulators and layered transition metal dichalcogenides to elucidate ultrafast carrier dynamics.

Bibliographie

[1] A Damascelli, Z Hussain, and Z-X Shen. Angle-resolved photoemission studies of the cuprate superconductors. *Rev. Mod. Phys.*, 75(2) :473–541, April 2003.

[2] A Damascelli. Probing the electronic structure of complex systems by ARPES. *Phys. Scr.*, T109 :61, 2004.

[3] J A Sobota, Y He, and Z-X Shen. Angle-resolved photoemission studies of quantum materials. *Rev. Mod. Phys.*, 93(2), May 2021.

[4] H Zhang, T Pincelli, C Jozwiak, T Kondo, R Ernstorfer, T Sato, and S Zhou. Angle-resolved photoemission spectroscopy. *Nat. Rev. Methods Primers*, 2(1), July 2022.

[5] M Na, A K Mills, and D J Jones. Advancing time- and angle-resolved photoemission spectroscopy : The role of ultrafast laser development. *Phys. Rep.*, 1036 :1–47, October 2023.

[6] F Boschini, M Zonno, and A Damascelli. Time-resolved ARPES studies of quantum materials. *Rev. Mod. Phys.*, 96(1), February 2024.

[7] Y Wang and M Dendzik. Recent progress in angle-resolved photoemission spectroscopy. *Meas. Sci. Technol.*, 35(4) :042002, April 2024.

[8] H Hertz. Ueber einen einfluss des ultravioletten lichtes auf die electrische entladung. *Ann. Phys.*, 267(8) :983–1000, January 1887.

[9] A Einstein. Über einen die erzeugung und verwandlung des lichtes betreffenden heuristischen gesichtspunkt. *Ann. Phys.*, 322(6) :132–148, January 1905.

[10] N V Smith and M M Traum. Angular dependence of photoemission from the (110) face of GaAs. *Phys. Rev. Lett.*, 31(20) :1247–1250, November 1973.

[11] N V Smith, M M Traum, and F J Di Salvo. Mapping energy bands in layer compounds from the angular dependence of ultraviolet photoemission. *Solid State Commun.*, 15(2) :211–214, July 1974.

[12] Y Saitoh, H Kimura, Y Suzuki, T Nakatani, T Matsushita, T Muro, T Miyahara, M Fujisawa, K Soda, S Ueda, H Harada, M Kotsugi, A Sekiyama, and S Suga. Performance of a very high resolution soft x-ray beamline BL25SU with a twin-helical undulator at SPring-8. *Rev. Sci. Instrum.*, 71(9) :3254–3259, September 2000.

[13] S V Borisenko. “one-cubed” ARPES user facility at BESSY II. *Synchrotron Radiat. News*, 25 (5) :6–11, September 2012.

[14] R Reininger, S L Hulbert, P D Johnson, J T Sadowski, D E Starr, O Chubar, T Valla, and E Vescovo. The electron spectro-microscopy beamline at national synchrotron light source II : a wide photon energy range, micro-focusing beamline for photoelectron spectro-microscopies. *Rev. Sci. Instrum.*, 83(2) :023102, February 2012.

[15] L Tamura, Z Hussain, H A Padmore, D S Robin, S Bailey, B Feinberg, and R W Falcone. Advanced light source update. *Synchrotron Radiat. News*, 25(3) :25–30, June 2012.

[16] V N Strocov, X Wang, M Shi, M Kobayashi, J Krempasky, C Hess, T Schmitt, and L Patthey. Soft-X-ray ARPES facility at the ADRESS beamline of the SLS : concepts, technical realisation and scientific applications. *J. Synchrotron Radiat.*, 21(Pt 1) :32–44, January 2014.

[17] M Hoesch, T K Kim, P Dudin, H Wang, S Scott, P Harris, S Patel, M Matthews, D Hawkins, S G Alcock, T Richter, J J Mudd, M Basham, L Pratt, P Leicester, E C Longhi, A Tamai, and F Baumberger. A facility for the analysis of the electronic structures of solids and their surfaces by synchrotron radiation photoelectron spectroscopy. *Rev. Sci. Instrum.*, 88(1) : 013106, January 2017.

[18] J D Koralek, J F Douglas, N C Plumb, J D Griffith, S T Cundiff, H C Kapteyn, M M Murnane, and D S Dessau. Experimental setup for low-energy laser-based angle resolved photoemission spectroscopy. *Rev. Sci. Instrum.*, 78(5) :053905, May 2007.

[19] G Liu, G Wang, Y Zhu, H Zhang, G Zhang, X Wang, Y Zhou, W Zhang, H Liu, L Zhao, J Meng, X Dong, C Chen, Z Xu, and X J Zhou. Development of a vacuum ultraviolet laser-based angle-resolved photoemission system with a superhigh energy resolution better than 1 mev. *Rev. Sci. Instrum.*, 79(2 Pt 1) :023105, February 2008.

[20] T Kiss, T Shimojima, K Ishizaka, A Chainani, T Togashi, T Kanai, X-Y Wang, C-T Chen, S Watanabe, and S Shin. A versatile system for ultrahigh resolution, low temperature, and polarization dependent laser-angle-resolved photoemission spectroscopy. *Rev. Sci. Instrum.*, 79(2 Pt 1) :023106, February 2008.

[21] R Jiang, D Mou, Y Wu, L Huang, C D McMillen, J Kolis, H G Giesber, J J Egan, and A Kaminski. Tunable vacuum ultraviolet laser based spectrometer for angle resolved photoemission spectroscopy. *Rev. Sci. Instrum.*, 85(3) :033902, March 2014.

[22] X Zhou, S He, G Liu, L Zhao, L Yu, and W Zhang. New developments in laser-based photoemission spectroscopy and its scientific applications : a key issues review. *Rep. Prog. Phys.*, 81(6) :062101, June 2018.

[23] S Mathias, L Miaja-Avila, M M Murnane, H Kapteyn, M Aeschlimann, and M Bauer. Angle-resolved photoemission spectroscopy with a femtosecond high harmonic light source using a two-dimensional imaging electron analyzer. *Rev. Sci. Instrum.*, 78(8) :083105, August 2007.

[24] S Eich, A Stange, A V Carr, J Urbancic, T Popmintchev, M Wiesenmayer, K Jansen, A Ruffing, S Jakobs, T Rohwer, S Hellmann, C Chen, P Matyba, L Kipp, K Rossnagel, M Bauer, M M Murnane, H C Kapteyn, S Mathias, and M Aeschlimann. Time- and angle-resolved photoemission spectroscopy with optimized high-harmonic pulses using frequency-doubled Ti :Sapphire lasers. *J. Electron Spectros. Relat. Phenomena*, 195 :231–236, August 2014.

[25] H Wang, Y Xu, S Ulonska, J S Robinson, P Ranitovic, and R A Kaindl. Bright high-repetition-rate source of narrowband extreme-ultraviolet harmonics beyond 22 ev. *Nat. Commun.*, 6 (1) :7459, June 2015.

[26] E J Sie, T Rohwer, C Lee, and N Gedik. Time-resolved XUV ARPES with tunable 24-33 ev laser pulses at 30 mev resolution. *Nat. Commun.*, 10(1) :3535, August 2019.

[27] A K Mills, S Zhdanovich, M X Na, F Boschini, E Razzoli, M Michiardi, A Sheyerman, M Schneider, T J Hammond, V Süss, C Felser, A Damascelli, and D J Jones. Cavity-enhanced high harmonic generation for extreme ultraviolet time- and angle-resolved photoemission spectroscopy. *Rev. Sci. Instrum.*, 90(8) :083001, August 2019.

[28] Q Guo, M Dendzik, An Grubišić-Čabo, Ma H Berntsen, C Li, W Chen, B Matta, Ul Starke, B Hessmo, J Weissenrieder, and O Tjernberg. A narrow bandwidth extreme ultra-violet light source for time- and angle-resolved photoemission spectroscopy. *Struct. Dyn.*, 9(2) :024304, March 2022.

[29] A Comby, D Rajak, D Descamps, S Petit, V Blanchet, Y Mairesse, J Gaudin, and S Beaulieu. Ultrafast polarization-tunable monochromatic extreme ultraviolet source at high-repetition-rate. *J. Opt.*, 24(8) :084003, August 2022.

[30] H Fellner-Feldegg, U Gelius, B Wannberg, A G Nilsson, E Basilier, and K Siegbahn. New developments in ESCA-instrumentation. *J. Electron Spectros. Relat. Phenomena*, 5(1) : 643–689, January 1974.

[31] B Wannberg. Electron optics development for photo-electron spectrometers. *Nucl. Instrum. Methods Phys. Res. A*, 601(1-2) :182–194, March 2009.

[32] G Schönhense, K Medjanik, and H-J Elmers. Space-, time- and spin-resolved photoemission. *J. Electron Spectros. Relat. Phenomena*, 200 :94–118, April 2015.

[33] C Tusche, P Goslawski, D Kutnyakhov, M Ellguth, K Medjanik, H J Elmers, S Chernov, R Wallauer, D Engel, A Jankowiak, and G Schönhense. Multi-MHz time-of-flight electronic band-structure imaging of graphene on ir(111). *Appl. Phys. Lett.*, 108(26) :261602, June 2016.

[34] K Medjanik, O Fedchenko, S Chernov, D Kutnyakhov, M Ellguth, A Oelsner, B Schönhense, T R F Peixoto, P Lutz, C-H Min, F Reinert, S Däster, Y Acremann, J Viefhaus, W Wurth, H J Elmers, and G Schönhense. Direct 3D mapping of the fermi surface and fermi velocity. *Nat. Mater.*, 16(6) :615–621, June 2017.

[35] J Maklar, S Dong, S Beaulieu, T Pincelli, M Dendzik, Y W Windsor, R P Xian, M Wolf, R Ernstorfer, and L Rettig. A quantitative comparison of time-of-flight momentum microscopes and hemispherical analyzers for time- and angle-resolved photoemission spectroscopy experiments. *Rev. Sci. Instrum.*, 91(12) :123112, December 2020.

[36] O Tkach and G Schönhense. Multimode objective lens for momentum microscopy and XPEEM : Theory. *Ultramicroscopy*, 276(114167) :114167, October 2025.

[37] E Kisker, R Clauberg, and W Gudat. Electron spectrometer for spin-polarized angle- and energy-resolved photoemission from ferromagnets. *Rev. Sci. Instrum.*, 53(8) :1137–1144, August 1982.

[38] T J Gay and F B Dunning. Mott electron polarimetry. *Rev. Sci. Instrum.*, 63(2) :1635–1651, February 1992.

[39] S Qiao, A Kimura, A Harasawa, M Sawada, J-G Chung, and A Kakizaki. A new compact electron spin polarimeter with a high efficiency. *Rev. Sci. Instrum.*, 68(12) :4390–4395, December 1997.

[40] V N Petrov, V V Grebenshikov, B D Grachev, and A S Kamochkin. New compact classical 40 kv mott polarimeter. *Rev. Sci. Instrum.*, 74(3) :1278–1281, March 2003.

[41] P Dudin, P Lacovig, C Fava, E Nicolini, A Bianco, G Cautero, and A Barinov. Angle-resolved photoemission spectroscopy and imaging with a submicrometre probe at the SPECTROMICROSCOPY-3.2L beamline of elettra. *J. Synchrotron Radiat.*, 17(4) :445–450, July 2010.

[42] A Bostwick, E Rotenberg, J Avila, and M C Asensio. Zooming in on electronic structure : NanoARPES at SOLEIL and ALS. *Synchrotron Radiat. News*, 25(5) :19–25, September 2012.

[43] J Avila and María C Asensio. First NanoARPES user facility available at SOLEIL : An innovative and powerful tool for studying advanced materials. *Synchrotron Radiat. News*, 27(2) : 24–30, March 2014.

[44] H Iwasawa, E F Schwier, M Arita, A Ino, H Namatame, M Taniguchi, Y Aiura, and K Shimada. Development of laser-based scanning μ-ARPES system with ultimate energy and momentum resolutions. *Ultramicroscopy*, 182 :85–91, November 2017.

[45] I Cucchi, I Gutiérrez-Lezama, E Cappelli, S McKeown Walker, F Y Bruno, G Tenasini, L Wang, N Ubrig, C Barreteau, E Giannini, M Gibertini, A Tamai, A F Morpurgo, and F Baumberger. Microfocus laser-angle-resolved photoemission on encapsulated mono-, bi-, and few-layer 1T'-WTe2. *Nano Lett.*, 19(1) :554–560, January 2019.

[46] I Cucchi, S Lisi, F Margot, H Henck, A Tamai, and F Baumberger. Electronic structure of 2D van der waals crystals and heterostructures investigated by spatially- and angle-resolved photoemission. *C. R. Phys.*, 22(S4) :107–131, March 2022.

[47] Y Mao, D Zhao, S Yan, H Zhang, J Li, K Han, X Xu, C Guo, L Yang, C Zhang, K Huang, and Y Chen. A vacuum ultraviolet laser with a submicrometer spot for spatially resolved photoemission spectroscopy. *Light Sci. Appl.*, 10(1) :22, January 2021.

[48] C Jozwiak, J Graf, G Lebedev, N Andresen, A K Schmid, A V Fedorov, F El Gabaly, W Wan, A Lanzara, and Z Hussain. A high-efficiency spin-resolved photoemission spectrometer combining time-of-flight spectroscopy with exchange-scattering polarimetry. *Rev. Sci. Instrum.*, 81(5) :053904, May 2010.

[49] M Hoesch, T Greber, V N Petrov, M Muntwiler, M Hengsberger, W Auwärter, and J Osterwalder. Spin-polarized fermi surface mapping. *J. Electron Spectros. Relat. Phenomena*, 124 (2-3) :263–279, July 2002.

[50] S Souma, A Takayama, K Sugawara, T Sato, and T Takahashi. Ultrahigh-resolution spin-resolved photoemission spectrometer with a mini mott detector. *Rev. Sci. Instrum.*, 81(9) : 095101, September 2010.

[51] M H Berntsen, P Palmgren, M Leandersson, A Hahlin, J Ahlund, B Wannberg, M Månsson, and O Tjernberg. A spin- and angle-resolving photoelectron spectrometer. *Rev. Sci. Instrum.*, 81(3) :035104, March 2010.

[52] T Okuda, K Miyamaoto, H Miyahara, K Kuroda, A Kimura, H Namatame, and M Taniguchi. Efficient spin resolved spectroscopy observation machine at hiroshima synchrotron radiation center. *Rev. Sci. Instrum.*, 82(10) :103302, October 2011.

[53] M Kolbe, P Lushchyk, B Petereit, H J Elmers, G Schönhense, A Oelsner, C Tusche, and J Kirschner. Highly efficient multichannel spin-polarization detection. *Phys. Rev. Lett.*, 107 (20) :207601, November 2011.

[54] T Okuda. Recent trends in spin-resolved photoelectron spectroscopy. *J. Phys. Condens. Matter*, 29(48) :483001, December 2017.

[55] Y Lin, L Moreschini, and A Lanzara. Present and future trends in spin ARPES. *EPL*, 134 (5) :57001, June 2021.

[56] R Reininger, S L Hulbert, P D Johnson, J T Sadowski, D E Starr, O Chubar, T Valla, and E Vescovo. The electron spectro-microscopy beamline at national synchrotron light source II : a wide photon energy range, micro-focusing beamline for photoelectron spectro-microscopies. *Rev. Sci. Instrum.*, 83(2) :023102, February 2012.

[57] L Tamura, Z Hussain, H A Padmore, D S Robin, S Bailey, B Feinberg, and R W Falcone. Advanced light source update. *Synchrotron Radiat. News*, 25(3) :25–30, June 2012.

[58] V N Strocov, X Wang, M Shi, M Kobayashi, J Krempasky, C Hess, T Schmitt, and L Patthey. Soft-X-ray ARPES facility at the ADRESS beamline of the SLS : concepts, technical realisation and scientific applications. *J. Synchrotron Radiat.*, 21(Pt 1) :32–44, January 2014.

[59] M Schüler, Umberto De G, H Hübener, A Rubio, M A Sentef, and P Werner. Local berry curvature signatures in dichroic angle-resolved photoelectron spectroscopy from two-dimensional materials. *Sci. Adv.*, 6(9) :eaay2730, February 2020.

[60] S Beaulieu, J Schusser, S Dong, M Schüler, T Pincelli, M Dendzik, J Maklar, A Neef, H Ebert, K Hricovini, M Wolf, J Braun, L Rettig, J Minár, and R Ernstorfer. Revealing hidden orbital pseudospin texture with time-reversal dichroism in photoelectron angular distributions. *Phys. Rev. Lett.*, 125(21) :216404, November 2020.

[61] J Schusser, H Orio, M Ünzelmann, J Heßdörfer, M P T Masilamani, F Diekmann, K Rossnagel, and F Reinert. Towards robust dichroism in angle-resolved photoemission. *Commun. Phys.*, 7(1), August 2024.

[62] S S Brinkman, X L Tan, B Brekke, A C Mathisen, Ø Finnseth, R J Schenk, K Hagiwara, M-J Huang, J Buck, M Kalläne, M Hoesch, K Rossnagel, K-H Ou Yang, M-T Lin, G-J Shu, Y-J Chen, C Tusche, and H Bentmann. Chirality-driven orbital angular momentum and circular dichroism in CoSi. *Phys. Rev. Lett.*, 132(19) :196402, May 2024.

[63] Y Yen, J A Krieger, M Yao, Iñigo Robredo, K Manna, Q Yang, E C McFarlane, C Shekhar, H Borrmann, S Stolz, R Widmer, O Gröning, V N Strocov, S S P Parkin, C Felser, M G Vergniory, M Schüler, and N B M Schröter. Controllable orbital angular momentum monopoles in chiral topological semimetals. *Nat. Phys.*, 20(12) :1912–1918, September 2024.

[64] I Sidilkover, Y Yen, S W D'Souza, J Schusser, A Pulkkinen, C R Rotundu, M Hashimoto, D Liu, Z-X Shen, J Min'ar, M Sch
"uler, H Soifer, and J A Sobota. Reexamining circular dichroism in photoemission from a topological insulator. *Phys. Rev. Res.*, 7(3), July 2025.

[65] S Mathias, L Miaja-Avila, M M Murnane, H Kapteyn, M Aeschlimann, and M Bauer. Angle-resolved photoemission spectroscopy with a femtosecond high harmonic light source using a two-dimensional imaging electron analyzer. *Rev. Sci. Instrum.*, 78(8) :083105, August 2007.

[66] E Carpene, E Mancini, C Dallera, G Ghiringhelli, C Manzoni, G Cerullo, and S De Silvestri. A versatile apparatus for time-resolved photoemission spectroscopy via femtosecond pump-probe experiments. *Rev. Sci. Instrum.*, 80(5) :055101, May 2009.

[67] G L Dakovski, Y Li, T Durakiewicz, and G Rodriguez. Tunable ultrafast extreme ultraviolet source for time- and angle-resolved photoemission spectroscopy. *Rev. Sci. Instrum.*, 81(7) : 073108, July 2010.

[68] M H Berntsen, O Götberg, and O Tjernberg. An experimental setup for high resolution 10.5 ev laser-based angle-resolved photoelectron spectroscopy using a time-of-flight electron analyzer. *Rev. Sci. Instrum.*, 82(9) :095113, September 2011.

[69] C L Smallwood, C Jozwiak, W Zhang, and A Lanzara. An ultrafast angle-resolved photoemission apparatus for measuring complex materials. *Rev. Sci. Instrum.*, 83(12) :123904, December 2012.

[70] B Frietsch, R Carley, K Döbrich, C Gahl, M Teichmann, O Schwarzkopf, Ph Wernet, and M Weinelt. A high-order harmonic generation apparatus for time- and angle-resolved photoelectron spectroscopy. *Rev. Sci. Instrum.*, 84(7) :075106, July 2013.

[71] Y Ishida, T Togashi, K Yamamoto, M Tanaka, T Kiss, T Otsu, Y Kobayashi, and S Shin. Time-resolved photoemission apparatus achieving sub-20-mev energy resolution and high stability. *Rev. Sci. Instrum.*, 85(12) :123904, December 2014.

[72] Y Ishida, T Otsu, A Ozawa, K Yaji, S Tani, S Shin, and Y Kobayashi. High repetition pump-and-probe photoemission spectroscopy based on a compact fiber laser system. *Rev. Sci. Instrum.*, 87(12) :123902, December 2016.

[73] G Rohde, A Hendel, A Stange, K Hanff, L-P Oloff, L X Yang, K Rossnagel, and M Bauer. Time-resolved ARPES with sub-15 fs temporal and near fourier-limited spectral resolution. *Rev. Sci. Instrum.*, 87(10) :103102, October 2016.

[74] M Keunecke, C Möller, D Schmitt, H Nolte, G S M Jansen, M Reutzel, M Gutberlet, G Halasi, D Steil, S Steil, and S Mathias. Time-resolved momentum microscopy with a 1 MHz high-harmonic extreme ultraviolet beamline. *Rev. Sci. Instrum.*, 91(6) :063905, June 2020.

[75] L Hellbrück, M Puppin, F Guo, D D Hickstein, S Benhabib, M Grioni, J H Dil, T LaGrange, H M Rønnow, and F Carbone. High-resolution MHz time- and angle-resolved photoemission spectroscopy based on a tunable vacuum ultraviolet source. *Rev. Sci. Instrum.*, 95(3), March 2024.

[76] C Huang, S Duan, and W Zhang. High-resolution time- and angle-resolved photoemission studies on quantum materials. *Quantum Front.*, 1(1), November 2022.

[77] M P Seah and W A Dench. Quantitative electron spectroscopy of surfaces : A standard data base for electron inelastic mean free paths in solids. *Surf. Interface Anal.*, 1(1) :2–11, February 1979.

[78] G D Mahan. Theory of photoemission in simple metals. *Phys. Rev.*, 2(11) :4334–4350, December 1970.

[79] P J Feibelman and D E Eastman. Photoemission spectroscopy—correspondence between quantum theory and experimental phenomenology. *Phys. Rev.*, 10(12) :4932–4947, December 1974.

[80] J Minár, J Braun, S Mankovsky, and H Ebert. Calculation of angle-resolved photo emission spectra within the one-step model of photo emission—recent developments. *J. Electron Spectros. Relat. Phenomena*, 184(3-6) :91–99, April 2011.

[81] J F L Hopkinson, J B Pendry, and D J Titterington. Calculation of photoemission spectra for surfaces of solids. *Comput. Phys. Commun.*, 19(1) :69–92, January 1980.

[82] S Karkare, W Wan, J Feng, T C Chiang, and H A Padmore. One-step model of photoemission from single-crystal surfaces. *Phys. Rev. B.*, 95(7), February 2017.

[83] C N Berglund and W E Spicer. Photoemission studies of copper and silver : Theory. *Phys. Rev.*, 136(4A) :A1030–A1044, November 1964.

[84] J W Gadzuk and M Šunjić. Excitation energy dependence of core-level x-ray-photoemission-spectra line shapes in metals. *Phys. Rev.*, 12(2) :524–530, July 1975.

[85] G D Mahan. *Many-particle physics*. Physics of Solids and Liquids. Springer, New York, NY, December 2010.

[86] M R Norman, H Ding, H Fretwell, M Randeria, and J C Campuzano. Extraction of the electron self-energy from angle-resolved photoemission data : Application toBi2Sr2CaCu2O8+x. *Phys. Rev. B Condens. Matter*, 60(10) :7585–7590, September 1999.

[87] M R Norman, M Eschrig, A Kaminski, and J C Campuzano. Momentum distribution curves in the superconducting state. *Phys. Rev. B Condens. Matter*, 64(18), October 2001.

[88] T Valla, A V Fedorov, P D Johnson, and S L Hulbert. Many-body effects in angle-resolved photoemission : Quasiparticle energy and lifetime of a mo(110) surface state. *Phys. Rev. Lett.*, 83(10) :2085–2088, September 1999.

[89] A A Kordyuk, S V Borisenko, A Koitzsch, J Fink, M Knupfer, and H Berger. Bare electron dispersion from experiment : Self-consistent self-energy analysis of photoemission data. *Phys. Rev. B Condens. Matter Mater. Phys.*, 71(21), June 2005.

[90] M R Norman, H Ding, H Fretwell, M Randeria, and J C Campuzano. Extraction of the electron self-energy from angle-resolved photoemission data : Application toBi2Sr2CaCu2O8+x. *Phys. Rev. B Condens. Matter*, 60(10) :7585–7590, September 1999.

[91] D Pescia, A R Law, M T Johnson, and H P Hughes. Determination of observable conduction band symmetry in angle-resolved electron spectroscopies : Non-symmorphic space groups. *Solid State Commun.*, 56(9) :809–812, December 1985.

[92] S Moser. An experimentalist's guide to the matrix element in angle resolved photoemission. *J. Electron Spectros. Relat. Phenomena*, 214 :29–52, January 2017.

[93] R P Day, B Zwartsenberg, I S Elfimov, and A Damascelli. Computational framework chinook for angle-resolved photoemission spectroscopy. *Npj Quantum Mater.*, 4(1), November 2019.

[94] S Karkare, W Wan, J Feng, Tai C Chiang, and H A Padmore. One-step model of photoemission from single-crystal surfaces. *Phys. Rev. B.*, 95(7), February 2017.

[95] Y Zhang, C He, Z R Ye, J Jiang, F Chen, M Xu, Q Q Ge, B P Xie, J Wei, M Aeschlimann, X Y Cui, M Shi, J P Hu, and D L Feng. Symmetry breaking via orbital-dependent reconstruction of electronic structure in detwinned NaFeAs. *Phys. Rev. B Condens. Matter Mater. Phys.*, 85 (8), February 2012.

[96] P D C King, S McKeown Walker, A Tamai, A de la Torre, T Eknapakul, P Buaphet, S-K Mo, W Meevasana, M S Bahramy, and F Baumberger. Quasiparticle dynamics and spin-orbital texture of the SrTiO3 two-dimensional electron gas. *Nat. Commun.*, 5(1) :3414, February 2014.

[97] C E Matt, D Sutter, A M Cook, Y Sassa, M Månsson, O Tjernberg, L Das, M Horio, D Destraz, C G Fatuzzo, K Hauser, M Shi, M Kobayashi, V N Strocov, T Schmitt, P Dudin, M Hoesch, S Pyon, T Takayama, H Takagi, O J Lipscombe, S M Hayden, T Kurosawa, N Momono, M Oda, T Neupert, and J Chang. Direct observation of orbital hybridisation in a cuprate superconductor. *Nat. Commun.*, 9(1), March 2018.

[98] T Shimojima, K Ishizaka, Y Ishida, N Katayama, K Ohgushi, T Kiss, M Okawa, T Togashi, X-Y Wang, C-T Chen, S Watanabe, R Kadota, T Oguchi, A Chainani, and S Shin. Orbital-dependent modifications of electronic structure across the magnetostructural transition in BaFe2As2. *Phys. Rev. Lett.*, 104(5) :057002, February 2010.

[99] H Iwasawa, Y Yoshida, I Hase, K Shimada, H Namatame, M Taniguchi, and Y Aiura. High-energy anomaly in the band dispersion of the ruthenate superconductor. *Phys. Rev. Lett.*, 109(6) :066404, August 2012.

[100] C M Schneider and J Kirschner. Spin- and angle-resolved photoelectron spectroscopy from solid surfaces with circularly polarized light. *Crit. Rev. Solid State Mater. Sci.*, 20(3) :179–283, January 1995.

[101] Y Liu, G Bian, T Miller, and T-C Chiang. Visualizing electronic chirality and berry phases in graphene systems using photoemission with circularly polarized light. *Phys. Rev. Lett.*, 107 (16) :166803, October 2011.

[102] J-H Park, C H Kim, J-W Rhim, and J H Han. Orbital rashba effect and its detection by circular dichroism angle-resolved photoemission spectroscopy. *Phys. Rev. B Condens. Matter Mater. Phys.*, 85(19), May 2012.

[103] S Cho, J-H Park, J Hong, J Jung, B S Kim, G Han, W Kyung, Y Kim, S-K Mo, J D Denlinger, J H Shim, J H Han, C Kim, and S R Park. Experimental observation of hidden berry curvature in inversion-symmetric bulk 2h$-$wse$_2$. *Phys. Rev. Lett.*, 121(18), October 2018.

[104] Y H Wang, D Hsieh, D Pilon, L Fu, D R Gardner, Y S Lee, and N Gedik. Observation of a warped helical spin texture in Bi2Se3 from circular dichroism angle-resolved photoemission spectroscopy. *Phys. Rev. Lett.*, 107(20) :207602, November 2011.

[105] W Jung, Y Kim, B Kim, Y Koh, C Kim, M Matsunami, S-I Kimura, M Arita, K Shimada, J H Han, J Kim, B Cho, and C Kim. Warping effects in the band and angular-momentum structures of the topological insulator Bi2Te3. *Phys. Rev. B Condens. Matter Mater. Phys.*, 84(24), December 2011.

[106] I Gierz, M Lindroos, H Höchst, C R Ast, and K Kern. Graphene sublattice symmetry and isospin determined by circular dichroism in angle-resolved photoemission spectroscopy. *Nano Lett.*, 12(8) :3900–3904, August 2012.

[107] H Mirhosseini and J Henk. Spin texture and circular dichroism in photoelectron spectroscopy from the topological insulator Bi2Te3 : first-principles photoemission calculations. *Phys. Rev. Lett.*, 109(3) :036803, July 2012.

[108] M R Scholz, J Sánchez-Barriga, J Braun, D Marchenko, A Varykhalov, M Lindroos, Yung Jui Wang, Hsin Lin, A Bansil, J Minár, H Ebert, A Volykhov, L V Yashina, and O Rader. Reversal of the circular dichroism in angle-resolved photoemission from Bi2Te3. *Phys. Rev. Lett.*, 110 (21) :216801, May 2013.

[109] J Sánchez-Barriga, A Varykhalov, J Braun, S-Y Xu, N Alidoust, O Kornilov, J Minár, K Hummer, G Springholz, G Bauer, R Schumann, L V Yashina, H Ebert, M Z Hasan, and O Rader. Photoemission ofBi2Se3with circularly polarized light : Probe of spin polarization or means for spin manipulation? *Phys. Rev. X.*, 4(1), March 2014.

[110] C-Z Xu, Y Liu, R Yukawa, L-X Zhang, I Matsuda, T Miller, and T-C Chiang. Photoemission circular dichroism and spin polarization of the topological surface states in ultrathin Bi2Te3 films. *Phys. Rev. Lett.*, 115(1) :016801, July 2015.

[111] M Sentef, A F Kemper, B Moritz, J K Freericks, Z-X Shen, and T P Devereaux. Examining electron-boson coupling using time-resolved spectroscopy. *Phys. Rev. X.*, 3(4), December 2013.

[112] A F Kemper, M A Sentef, B Moritz, T P Devereaux, and J K Freericks. Review of the theoretical description of time-resolved angle-resolved photoemission spectroscopy in electron-phonon mediated superconductors. *Ann. Phys.*, 529(9) :1600235, September 2017.

[113] F Randi, D Fausti, and M Eckstein. Bypassing the energy-time uncertainty in time-resolved photoemission. *Phys. Rev. B.*, 95(11), March 2017.

[114] A F Kemper, O Abdurazakov, and J K Freericks. General principles for the nonequilibrium relaxation of populations in quantum materials. *Phys. Rev. X.*, 8(4), October 2018.

[115] O Neufeld, W Mao, H Hübener, N Tancogne-Dejean, S A Sato, U De Giovannini, and A Rubio. Time- and angle-resolved photoelectron spectroscopy of strong-field light-dressed solids : Prevalence of the adiabatic band picture. *Phys. Rev. Res.*, 4(3), August 2022.

[116] J K Freericks and Alexander F Kemper. What do the two times in two-time correlation functions mean for interpreting tr-ARPES? *J. Electron Spectros. Relat. Phenomena*, 251 (147104) :147104, August 2021.

[117] J Freericks and H Krishnamurthy. Constant matrix element approximation to time-resolved angle-resolved photoemission spectroscopy. *Photonics*, 3(4) :58, November 2016.

[118] F Boschini, D Bugini, M Zonno, M Michiardi, R P Day, E Razzoli, B Zwartsenberg, M Schneider, E H da Silva Neto, S dal Conte, S K Kushwaha, R J Cava, S Zhdanovich, A K Mills, G Levy, E Carpene, C Dallera, C Giannetti, D J Jones, G Cerullo, and A Damascelli. Role of matrix elements in the time-resolved photoemission signal. *New J. Phys.*, 22(2) :023031, February 2020.

[119] M Schüler and S Beaulieu. Probing topological floquet states in WSe2 using circular dichroism in time- and angle-resolved photoemission spectroscopy. *Commun. Phys.*, 5(1), June 2022.

[120] M Schüler, T Pincelli, S Dong, T P Devereaux, M Wolf, L Rettig, R Ernstorfer, and S Beaulieu. Polarization-modulated angle-resolved photoemission spectroscopy : Toward circular dichroism without circular photons and bloch wave-function reconstruction. *Phys. Rev. X.*, 12(1), January 2022.

3 EXPERIMENTAL SETUPS FOR TIME- AND ANGLE-RESOLVED PHOTOEMISSION SPECTROSCOPY

Summary :

This chapter describes the experimental time- and angle-resolved photoemission spectroscopy (TR-ARPES) platforms employed throughout this thesis, focusing on two complementary setups developed and operated at the Advanced Laser Light Source (ALLS) laboratory at the Institut national de la recherche scientifique, Canada, and at the Centre Lasers Intenses et Applications (CELIA) laboratory at the University of Bordeaux, France. At ALLS, the TR-ARPES system is based on a low-photon-energy ultraviolet (6 eV) probe combined with a tunable mid-infrared pump and a hemispherical electron analyzer, providing high energy and momentum resolution. In contrast, the TR-ARPES setup at CELIA employs a polarization-tunable extreme-ultraviolet (XUV at 21.2 eV) probe and a polarization-controlled infrared pump, coupled to a time-of-flight momentum microscope, enabling simultaneous detection of both in plane momentum axis over an extended region of momentum space. This chapter provides a detailed description of both experimental platforms, covering all key components from the detector systems to the generation of the pump and probe pulses, as well as a comprehensive discussion of their experimental capabilities, including energy, momentum, and temporal resolutions. Together, these two instruments constitute a versatile and powerful experimental framework for investigating a wide range of quantum materials across a different photon energies, momentum space, and excitation conditions. The description of the ALLS laboratory setup is primarily adapted from Longa et al. [1], while the description of the CELIA laboratory setup is adapted from Comby et al. [2] and Fragkos et al. [3].

Statement of Contribution : At the ALLS laboratory, my responsibilities included maintaining, aligning, and upgrading the beamline, troubleshooting the ARPES system, and assisting user's experiment, while simultaneously conducting my own research experiments. Although the beamline infrastructure already existed, the generation and delivery of the 6 eV probe and tunable mid-infrared pump required extensive alignment, optimization, and continual adjustment. In contrast, the beamline at CELIA was already fully developed and operational when I joined. My role there focused primarily on performing the group's TR-ARPES measurements and supporting user experiments. Together, these two experimental environments provided the complementary capabilities and practical experience necessary for the results presented in the subsequent chapters.

3.1 Introduction

Following the theoretical description of time- and angle-resolved photoemission spectroscopy (TR-ARPES) presented in the previous chapter, we now have a clear understanding of the essential components required to realize a TR-ARPES experiment. At its core, a TR-ARPES setup consists of an ultrafast light source to generate the pump and probe pulses and a photoelectron detector capable of resolving the energy and momentum of the emitted electrons. In practice, however, the implementation of a TR-ARPES system inevitably involves trade-offs between key experimental parameters, including energy resolution, momentum resolution, temporal resolution, and acquisition efficiency. The optimal design of a setup, therefore, depends critically on the specific class of materials and physical phenomena under investigation. At the ALLS laboratory, the TR-ARPES platform is primarily optimized for the investigation of topological insulators and superconductors, where the most relevant electronic states are located near the Γ point of the Brillouin zone. A central objective of this platform is to investigate and actively control the electronic properties of quantum materials using tunable mid-infrared excitation. In particular, the mid-infrared pump enables mode-selective driving of low-energy electronic, lattice, and other collective modes, allowing resonant and selective driving of specific degrees of freedom of the system. Such an approach has only recently begun to be explored systematically, mainly because earlier experimental implementations were limited by the technical challenges associated with generating and integrating suitable tunable mid-infrared sources into TR-ARPES setups. These scientific goals place stringent demands on high energy and momentum resolution, favoring the use of a conventional low-photon-energy ultraviolet probe. Accordingly, the ALLS TR-ARPES platform is based on a single high-power femtosecond laser source from which both the pump and probe pulses are derived. The 6 eV probe is generated via nonlinear frequency conversion, while the tunable mid-infrared pump pulse is produced using an optical parametric amplifier followed by difference-frequency generation. This pump–probe scheme is combined with a hemispherical electron analyzer, providing the high resolution required to resolve subtle low-energy electronic features and ultrafast population dynamics.

In contrast, the TR-ARPES setup at the CELIA laboratory is designed to address materials such as transition metal dichalcogenides and graphene, where the electronic states of interest are distributed over a larger region of momentum space. Phenomena such as valley-selective physics and the extraction of information related to Berry curvature require access to extended portions of the Brillouin zone, efficient Fermi-surface mapping, and precise control over light polarization. To meet these requirements, the CELIA platform employs a polarization-tunable extreme-ultraviolet (XUV, 21.2 eV) probe generated via high-harmonic generation driven by a femtosecond laser source. The fundamental output of this same laser is used to produce a polarization-controlled infrared pump pulse, and the resulting pump–probe scheme is coupled to a time-of-flight momentum microscope for momentum-resolved photoelectron detection. This configuration enables efficient four-dimensional data acquisition, providing simultaneous access to energy, both in-plane momentum axis with wider momentum-space coverage, and time.

Together, these two TR-ARPES platforms exemplify how different experimental design choices are tailored to distinct scientific objectives. Their complementary capabilities form the experimental basis of this thesis and enable the investigation of ultrafast electron dynamics across diverse classes of quantum materials.

3.2 TR-ARPES endstation at ALLS Laboratory

In this section, I briefly discuss the first TR-ARPES setup I worked with at the Advanced Laser Light Source (ALLS) Laboratory, located at the Institut national de la recherche scientifique – Énergie, Matériaux et Télécommunications Research Centre (INRS–EMT) in Varennes, Québec, Canada. The endstation is designed to explore transient electronic and structural properties of quantum matter on femtosecond timescales. The setup consists of a high-repetition-rate Yb-based commercial laser system that delivers both a 6 eV ultraviolet probe and a tunable near infrared to mid-infrared pump which enables selective excitation schemes, allowing unique access to electronic states without an equilibrium counterpart and optical control of quantum properties on demand [4–7]. The pump is generated via a three-stage optical parametric amplification (OPA) followed by difference-frequency generation (DFG). The photoelectron spectrometer is a state-of-the-art hemispherical electron analyzer from SPECS, featuring a super-wide acceptance angle of 60°. Also by applying bias between sample holder to the analyzer entrance we are able to capture the full photoemission horizon therefore not limited by the analyzer acceptance angle anymore. Owing to the integrated deflector mode, the system supports full three-dimensional (E, k_x, k_y) band-structure mapping without mechanical sample rotation. The following discussion is mainly adapted from Ref. [1] and SPECS ASTRAIOS 190 manual [8].

3.2.1 Laser System

During my period at ALLS, the TR-ARPES endstation is driven by a Yb-doped commercial fiber amplifier, *Tangerine* (Amplitude Laser), which serves as the primary light source for both the pump and probe beams. The system delivers pulses with an energy of approximately 200 µJ and a full width at half maximum (FWHM) duration of about 150 fs. The average output power is 50 W at a repetition rate of 250 kHz. The pulse duration can be tuned by adjusting the internal grating compressor, and the repetition rate is continuously variable from a few hertz up to 2 MHz. For our TR-ARPES experiments, we typically operate the laser at 150 fs pulse duration and 250 kHz repetition rate, which provides an optimal balance between temporal resolution and photoelectron count rate. Both the pump and probe beams used in the experiment are derived from this fundamental source. As shown schematically in Fig. 3.1, the laser output is divided into two paths using a 75 :25 beam splitter (BS). The weaker branch is used to generate the 6 eV ultraviolet probe, while the more intense branch seeds a tunable optical parametric amplifier (OPA) followed by a

difference-frequency generation (DFG) stage, producing mid-infrared (MIR) pump pulses tunable from 4 to 8 µm for TR-ARPES measurements.

3.2.2 Probe Generation : 6 eV (206 nm)

The 6 eV probe beam is generated through a two-step nonlinear optical process involving second-harmonic generation (SHG) followed by sum-frequency generation (SFG). In the first stage, SHG of the 1030 nm fundamental is produced using a type-I, 1-mm-thick beta barium borate (BBO) crystal. Propagation through the BBO crystal introduces a temporal delay between the fundamental and its second harmonic due to group-velocity mismatch; this delay is compensated by inserting a calcite plate after the SHG crystal. In the second stage, a type-II, 1-mm-thick BBO crystal is used to generate the third harmonic (343 nm) via SFG between the 1030 nm fundamental and the 515 nm second harmonic. After generation, the 515 nm and 343 nm beams are spatially separated, and an adjustable delay stage is introduced into the 343 nm path to ensure precise temporal overlap. The beams are then recombined spatially and temporally in a type-I, 1-mm-thick BBO crystal, where an additional SFG process produces the fifth harmonic at 206 nm (6 eV). The resulting 6 eV probe is subsequently directed into the TR-ARPES chamber.

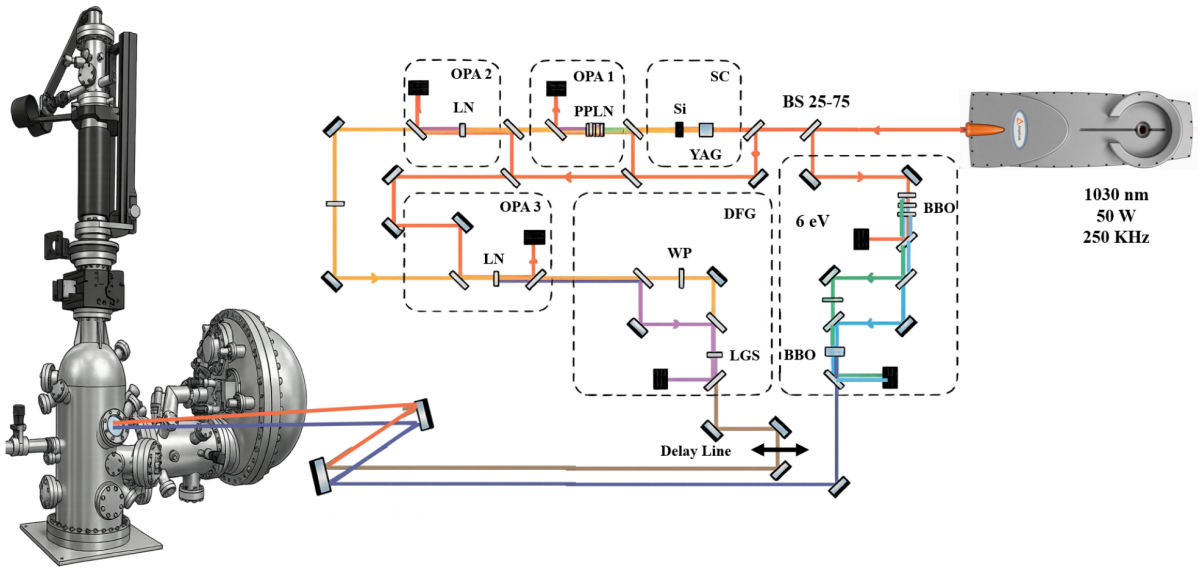


FIGURE 3.1 : Schematic of the TR-ARPES beamline at the ALLS laboratory. A Yb-based laser drives a home-built three-stage optical parametric amplifier (OPA) to produce a tunable mid-infrared pump, while another branch generates a 6 eV probe via nonlinear up-conversion. A motorized delay line in the pump arm controls the pump–probe delay. The two beams are recombined and focused onto the sample and emitted photoelectrons are analyzed with a hemispherical spectrometer. A detailed description of the beamline is provided elsewhere [1]. BS : beam splitter; SC : supercontinuum generated in a YAG ($Y_3Al_5O_{12}$) crystal; OPA1 : 1 mm PPLN ($MgO:LiNbO_3$); OPA2/OPA3 : 1.5 mm $MgO:LiNbO_3$; DFG : difference-frequency generation; LGS : $La_3Ga_5SiO_{14}$; WP : waveplate; BBO : β BaB_2O_4.

3.2.3 Pump Generation : Tunable NIR–MIR via OPA + DFG

The pump beam is generated using a three-stage optical parametric amplifier (OPA) followed by a difference-frequency generation (DFG) stage. The OPA is seeded by the high-intensity branch of a 250 kHz, 150 fs pump laser. First, supercontinuum (SC) generation is achieved by focusing the fundamental beam into a YAG crystal, producing a broadband spectrum spanning 500–2000 nm. For the present work, the SC is optimized in the 1600–1850 nm spectral region, which is relevant for the amplification stages. Temporal stretching of the SC is introduced using a silicon plate to balance parametric gain and bandwidth, and the stretched pulse serves as the seed for the first amplification stage (OPA 1). OPA 1 employs an MgO-doped periodically poled lithium niobate (PPLN) crystal in a collinear geometry with type-0 phase matching. After this stage, the generated signal and idler exhibit relatively very low average powers. The signal is then further amplified through two additional OPA stages (OPA 2 and OPA 3), both operating in collinear geometry and using bulk lithium niobate crystals with type-I phase matching, with each stage pumped by the fundamental beam. After OPA 3, the signal and idler reach average powers of approximately 5 W and 6 W, respectively. Following OPA 3, the signal and idler beams are separated, and a half-wave plate is introduced to ensure proper polarization matching for the DFG process. The beams are then recombined in a type-I lithium gallium sulfide (LGS) crystal, generating a mid-infrared output tunable from 4 μm to 8 μm with an average power exceeding 70 mW.

3.2.4 Beam Characterization

Fig. 3.2a represents the pairs of signal and idler : 1640/2770 nm (blue), 1770/2460 nm (orange) and 1830/2350 nm (green) that generates MIR wavelength centered at 4 μm (blue), 6.4 μm (orange) and 8.2 μm (green) respectively as shown in Fig. 3.2b through the DFG process. The system allows us to use pump wavelength from 1.5 μm to 8 μm by simply switching between, signal, idler or the DFG. The average output power varies between 2.5 to 4 W for signal, 1.8 to 2.3 W for the idler and 70 to 300 mW for the DFG.

The spatial beam profiles of the signal and idler outputs from the third-stage optical parametric amplifier (OPA 3) were characterized using a silicon-based camera. The near-field beam profile was measured immediately after the dichroic mirror separating the two beams, at the position where they were collimated. The signal exhibited an approximately Gaussian profile with a diameter of $\sim$2.5 mm, while the idler at the $1/e^2$.

Subsequently, both beams were focused using an anti-reflection (AR) coated plano-convex CaF_2 lens with a focal length of +200 mm to drive the difference frequency generation (DFG) process. The far-field beam profiles were measured at the focal plane corresponding to the position of the $LiGaS_2$ (LGS) crystal. Across the full tuning range of the OPA, the focal spot sizes were approximately 120 μm for the signal and 90 μm for the idler [Fig. 3.3a].

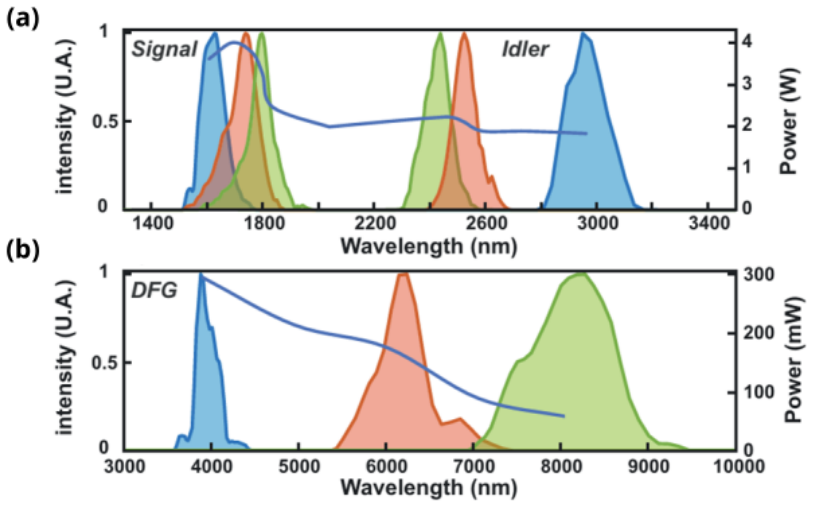


FIGURE 3.2 : Tunability of the OPA and DFG systems. (a) Tunability of the OPA system for three different signal and idler couples (blue, orange and green). (b) DFG tunability between 4 μm and 8 μm for the same pairs. The blue curve represents the average power. Adapted from Ref. [1], with permission from the author.

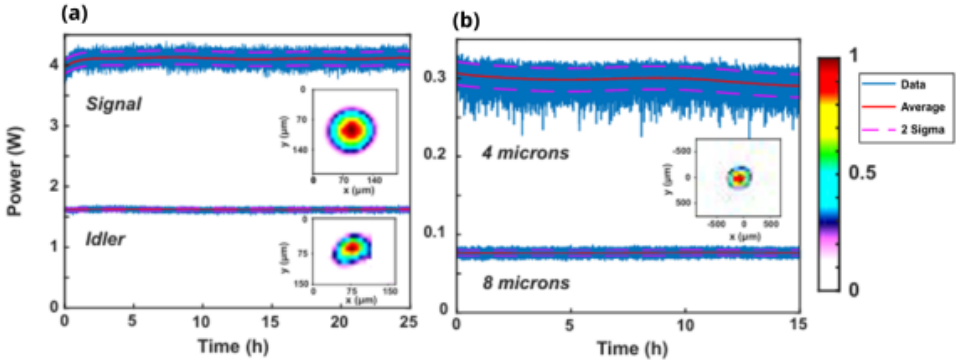


FIGURE 3.3 : Long-term stability and beam quality of the DFG output. (a) Long-term power stability for the signal (1640 nm)–idler (2770 nm) pair producing 4 μm DFG output. Insets : measured far-field beam profiles at the LGS crystal (normalized, linear scale). (b) Extended stability test of the DFG output at 4 and 8 μm; inset shows the 8 μm far-field profile (normalized, linear scale). Adapted from Ref. [1], with permission from the author.

The spatial profile of the DFG output was further characterized using a $BaSrTiO_3$ pyroelectric infrared camera (Electrophysics, model PV320-L2Z). This detector integrates an internal 10 Hz mechanical chopper and employs a 320×240 pixel array with an effective pixel size of $\sim$48.5 μm. The measured far-field DFG beam profile exhibited diameters in the range of 200–300 μm, as illustrated in 3.3b.

3.2.5 TR-ARPES endstation

After generation, the pump and probe beams are directed into the ARPES system, specifically into the UHV analysis chamber through the entrance window, where the sample is positioned for measurement. The sample is mounted on a five-axis motorized manipulator, enabling precise

spatial and angular alignment. The chamber is equipped with an electron-beam heater capable of reaching temperatures up to 700 K, as well as a closed-cycle cryostat that allows cooling to below 10 K. The base pressure of the system is approximately $8 * 10^{-11}$ mbar. A transfer arm connects the analysis chamber to a dedicated sample-preparation chamber, which includes sputtering and annealing capabilities for in situ surface cleaning. Samples are introduced through a load-lock chamber which can be transferred to the preparation chamber through transfer arm. For the detection of photoemitted electrons, the system is equipped with a SPECS Astraios 190 hemispherical analyzer. A schematic overview of the ARPES system is shown in Fig. 3.4.

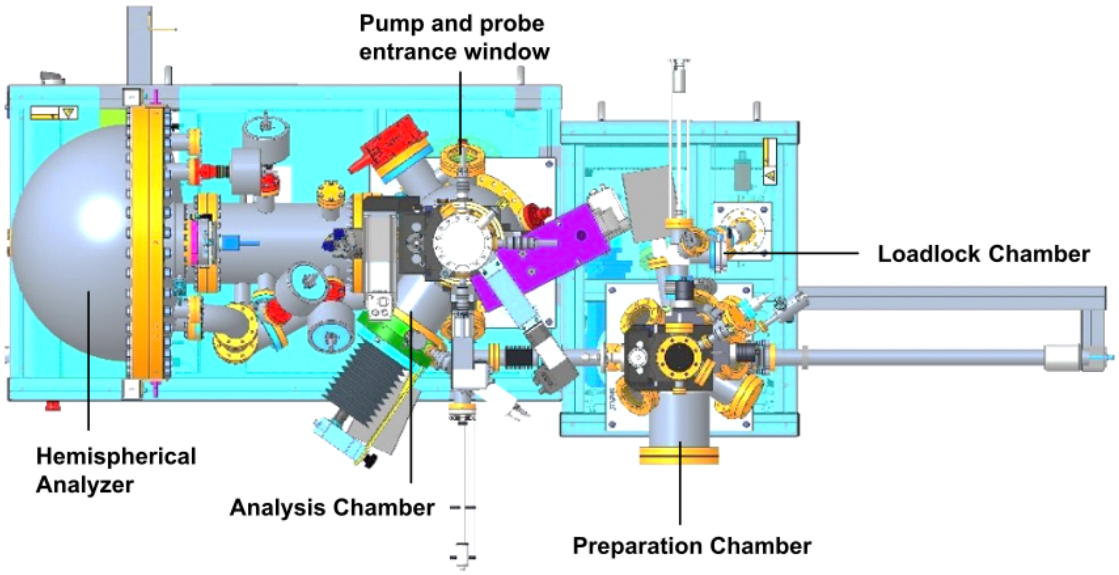


FIGURE 3.4 : Schematic of the ARPES system at ALLS laboratory.

3.2.6 Temporal and energy resolution of the System

The temporal resolution was determined using TR-ARPES measurements on the topological insulator Bi_2Te_3. The measurements were performed along the Γ–M direction using a 300 meV pump and a 6 eV probe generated via a thick BBO crystal, chosen to achieve the higher energy resolution required for the present study of topological insulators. As shown in the left three panels of Fig. 3.5, a direct-transition region was selected that persists only during the initial few femtoseconds of the pump–probe cross-correlation. The transient signal from this region was fitted with a step function followed by a single-exponential decay, convolved with a Gaussian instrument response function (Fig. 3.5), yielding a temporal resolution of 0.4 ps (FWHM). Using a thinner BBO crystal for probe generation would improve the temporal resolution to approximately 0.2 ps with this setup, at the expense of energy resolution, reflecting the Fourier-limited trade-off between time

and energy resolution. The energy resolution of the experiment was determined from the same

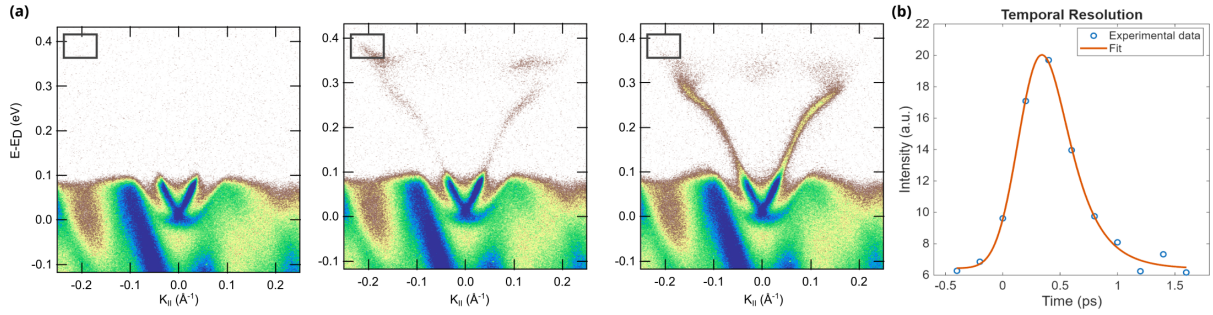


FIGURE 3.5 : Temporal resolution characterization of ALLS TR-ARPES endstation. (a) Energy–momentum snapshots of a topological insulator different pump–probe delays (-0.4, $\sim$ 0, $+0.6$ ps. A direct-transition region (boxed) is selected to capture the fastest dynamics. (b) Transient signal extracted from the boxed region (blue dots) together with the fit (solid line). The fitted data yields a temporal resolution of 0.4 ps (FWHM)

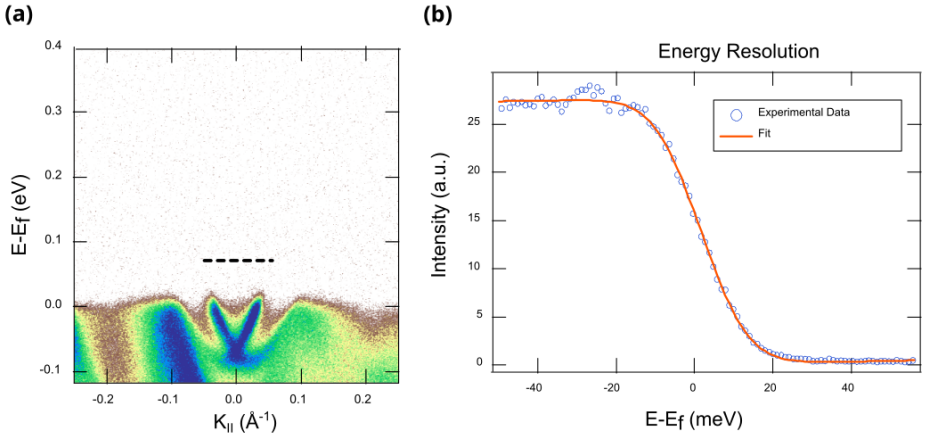


FIGURE 3.6 : Energy-resolution characterization of ALLS TR-ARPES endstation. (a) Band structure of a topological insulator near-E_F . (b) Energy–distribution curve (EDC) integrated over the shaded (pink) momentum window. Fitting the Fermi edge with a 0 K Fermi–Dirac function (convolved with a Gaussian response) yields an instrumental energy resolution of 15 meV

experimental dataset. A momentum-integration window centered on the topological surface state was selected at a negative time delay, and the corresponding energy distribution curve (EDC) was extracted, revealing a Fermi–Dirac distribution. The Fermi edge was fitted using a Fermi–Dirac function at the sample temperature of 30 K, convolved with a Gaussian instrumental response (Fig. 3.5, right panel), yielding an energy resolution of approximately 15 meV.

3.2.7 Electron Analyzer and Detection

In the following section, I describe the hemispherical analyzer integrated into our TR-ARPES endstation. The discussion is adapted from the SPECS ASTRAIOS manual [8]. The ASTRAIOS

190 comprises a multi-element transfer lens and hemispherical energy analyzer with a mean radius of 190 mm (i.e., the average of the inner and outer hemisphere radii). The two concentric hemispheres act as a band-pass energy filter for photoelectrons emitted from the sample and are coupled to a two-dimensional imaging detector. ASTRAIOS 190 supports full 2D mapping across the entire acceptance cone at a 27.5 mm working distance, enabling simultaneous high-resolution measurements in energy and momentum. A sectional schematic of the analyzer, highlighting its principal components, is shown in Fig. 3.7. The following subsections describe these components individually, outlining their roles from shaping the electron trajectories to determining the measured energy and momentum.

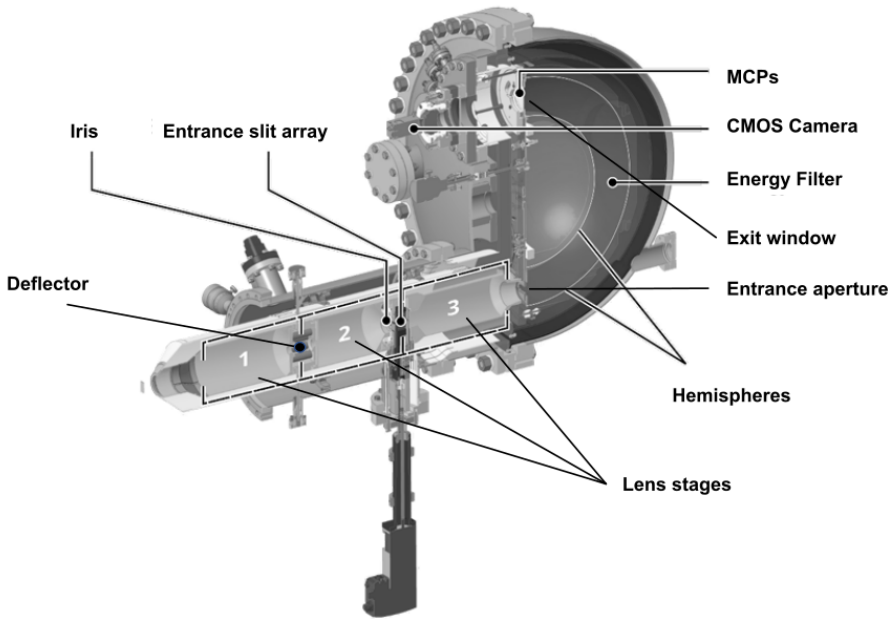


FIGURE 3.7 : ASTRAIOS sectional view showing key elements including 3 lens stages, deflector, inner and outer hemisphere. Adapted from SPECS technical manual [8], with permission.

Lens stages : Each stage of the electron-optical column shapes the photoelectron beam differently during transfer. A deflector, located between stages 1 and 2, transversely shifts the electron trajectories. Figure 3.8 illustrates the lens stages and their operating principles.

Stage 1 (objective lens)- The objective lens collects and accelerates emitted electrons, forming a real-space image. A redesigned objective achieves acceptance angles up to $\pm 30^{\circ}$ at a 27.5 mm working distance by substantially reducing spherical aberration compared to conventional ARPES optics.

Stage 2 (parallel shifting / momentum imaging)- This stage forms a k-space (momentum-distribution) image at a single spot and, with the deflector, can shift trajectories perpendicular

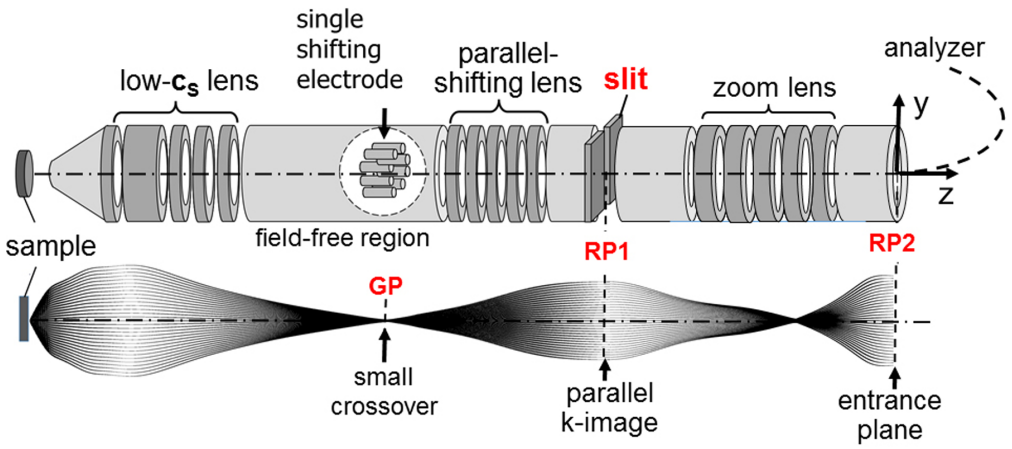


FIGURE 3.8 : Three lens stages of the hemispherical analyzer by Specs and its working principle. Adapted from SPECS technical manual [8], with permission.

to the optical axis. Crucially, divergent electrons from the sample are transformed into a parallel bundle at the analyzer entrance plane (RP2) by first focusing to a sharp real-space image at GP. A single shifting-electrode assembly in this plane raster-shifts the momentum image, enabling full mapping over the analyzer's acceptance cone. ASTRAIOS 190 introduces a *virtual entrance slit* : instead of a physical slit at the analyzer entrance, electron-optically equivalent slits are realized in an upstream relay plane (RP1) within the lens. This type of configuration allows electrons to pass through at much higher kinetic energies, which enhances resolution and detector homogeneity.

Stage 3 (zoom)- A zoom lens magnifies the k-space image by roughly a factor of two, independent of the selected lens mode, and adjusts the electron kinetic energy by accelerating or decelerating the photoelectrons before it reaches analyzer entrance plane in order to match the hemispherical analyzer pass energy. Practically, the lens column sets the pass energy E_p via a controlled retarding field characterized by the retarding ratio $R_r \equiv E_{\mathrm{kin}}/E_p$. Larger R_r (i.e., lower E_p) generally yields finer energy dispersion in the hemisphere but at the cost of reduced transmission, so R_r is chosen to optimize the resolution–count-rate trade-off for the experiment. Typically analyzer entrance slit width d together with the pass energy E_p and analyzer radius R, it governs the energy resolution and related by

$$\Delta E \;=\; E_p\left(\frac{d}{2R} \;+\; \frac{\alpha^2}{2}\right) \tag{3.1}$$

where α is the angular acceptance and R is the mean radius of the hemispherical analyzer. As it can be seen from the eq.3.1 that narrowing the slit reduces the angular spread of transmitted trajectories, so a larger fraction of electrons follow near-ideal paths to the detector, improving the ability to distinguish closely spaced energies.

Detection : The lens system of the ASTRAIOS focuses the electrons onto the entrance aperture of the hemisphere. At that point, the photoelectrons are transferred into the energy analyzer.

It is formed by an assembly consisting of an inner and outer hemispherical surface and the ground plate. As they pass through the energy filter, the electrons are dispersed by an electrostatic field between the hemispheres. It operates by dispersing photoemitted electrons along a curved path between two concentric hemispherical electrodes with radii R1 (inner radius) and R2 (outer radius). The potential difference applied across these electrodes creates an electric field that forces the electrons to follow curved trajectories, thereby separating them based on their kinetic energy. Electrons with lower kinetic energy follow tighter trajectories within the hemisphere, while those with higher kinetic energy follow wider orbits. Electrons with kinetic energy matching the analyzer's pass energy will follow the ideal path and reach the detector, while others will deviate from this path. At the exit window, the dispersive margin is narrow enough for the desired electrons to leave the analyzer while the fraction of unwanted electrons is kept from reaching the detector. Specifically, stray electrons and electrons at the very edge of the usable energy range are excluded from detection. There is a choice between five differently shaped hemisphere entrance apertures and three exit apertures. These are set in accordance with the type of measurement or work to be performed. The entrance apertures is normally set to the default entrance aperture, which is straight, with dimension 3 mm x 32 mm. The possible five apertures are provided on a disc-shaped, rotating carrier, mounted to the base. For the exit aperture each exit window has a trapezoidal outline. The shape accounts for an intrinsic trapezoid effect, which any electron optical image of a hemispherical energy analyzer is subjected to. In the angle dispersive direction, the exit windows are 32 mm long in order that all electrons in the accessible angular range can leave the energy filter. In the energy dispersive direction, the exit windows are wide enough to simultaneously record electron signals on an energy scale ranging across 10 percentage of the pass energy.

Image acquisition is performed with a 2D-CMOS detector operating in true pulse-counting mode, providing high pixel density and linear response up to $\sim 4 \times 10^6$ counts/s. This 2D CMOS detector collects the electrons, amplifies the signal and generates the data output to be processed. The detection stack consists of a micro-channel plate (MCP) chevron assembly followed by a phosphor screen viewed by a high-speed CMOS camera; fast detection algorithms yield event-by-event pulse counting. After energy dispersion in the hemisphere, electrons hits the phosphor screen, and the detector detects the position of impact in 2D from which a 2D view of energy-dispersive and angle-dispersive data is reconstructed. This instrument has an energy resolution $\Delta E \leq 2$ meV and angular resolution $\Delta\theta \leq 0.1^\circ$.

3.3 Time- and Polarization-Resolved XUV Momentum Microscopy at CELIA Laboratory

This section describes the time- and polarization-resolved XUV momentum microscopy platform used during the latter half of my doctoral work at the Centre Lasers Intenses et Applications (CELIA), Bordeaux. The beamline comprises five core modules (shown in the Fig. 3.9) (i) an amplified Yb-fiber laser whose output is split into pump and probe arms; (ii) a frequency-doubling and high-harmonic–generation (HHG) chamber for XUV probe generation; (iii) an all-reflective XUV quarter-wave plate; (iv) an XUV refocusing; and (v) polarization control, delay tuning, focusing, and recombination of pump pulse with probe. A central motivation for using an XUV probe is the need to access the larger in-plane momentum range of the Brillouin zone. As follows from Eqs. 2.5 and 2.1, the maximum detectable crystal momentum scales as $k_{\parallel}^{\max} \propto \sqrt{E_{\mathrm{kin}}}$, and therefore increases with photon energy. The 21.6 eV XUV probe generated at CELIA provides a kinetic-energy window sufficiently large to map the entire surface Brillouin zone as well as its periodic replicas in higher zones. The beamline couples the ultrafast, high-repetition-rate, polarization-tunable monochromatic XUV probe to a next-generation momentum-microscope endstation, enabling simultaneous detection of the k_x–k_y plane over an extended binding energy range. The instrument achieves an overall energy resolution of $\Delta E \approx 44$ meV and a temporal resolution of $\Delta t \approx 144$ fs. This state-of-the-art configuration enables time-, energy-, and momentum-resolved studies of orbital textures and quantum-geometric properties in quantum materials driven out of equilibrium. The following discussion is adapted from Refs. [2, 3], which provide a detailed description of our beamline.

3.3.1 Laser Source

Experiments are performed with the *BlastBeat* femtosecond laser system, comprising two Yb-doped fiber amplifiers seeded by a common oscillator. The system delivers two synchronized $50\ \mathrm{W}$ beams of $135\ \mathrm{fs}$ pulses centered at $1030\ \mathrm{nm}$ (FWHM $18.5\ \mathrm{nm}$), with a continuously tunable repetition rate from $166\ \mathrm{kHz}$ to $2\ \mathrm{MHz}$ (Tangerine Short Pulse, Amplitude). The beamline is designed to operate between $166\ \mathrm{kHz}$ and $250\ \mathrm{kHz}$. Typically, we operate at $166\ \mathrm{kHz}$ to balance good statistics in photoemission experiments and maintain the energy per pulse required for highly nonlinear processes such as HHG.

3.3.2 Pump and Probe generation

A beam-pointing stabilizer (MRC Systems GmbH) is installed at the entrance of the setup to ensure long-term stability of the laser beam. The fundamental output is first divided into two paths—a pump arm and a probe arm—using a polarizing beamsplitter. The reflected arm ($\sim$ 28 W) serves as the pump arm, although only tens to hundreds of milliwatts (mWs) are typically delivered to

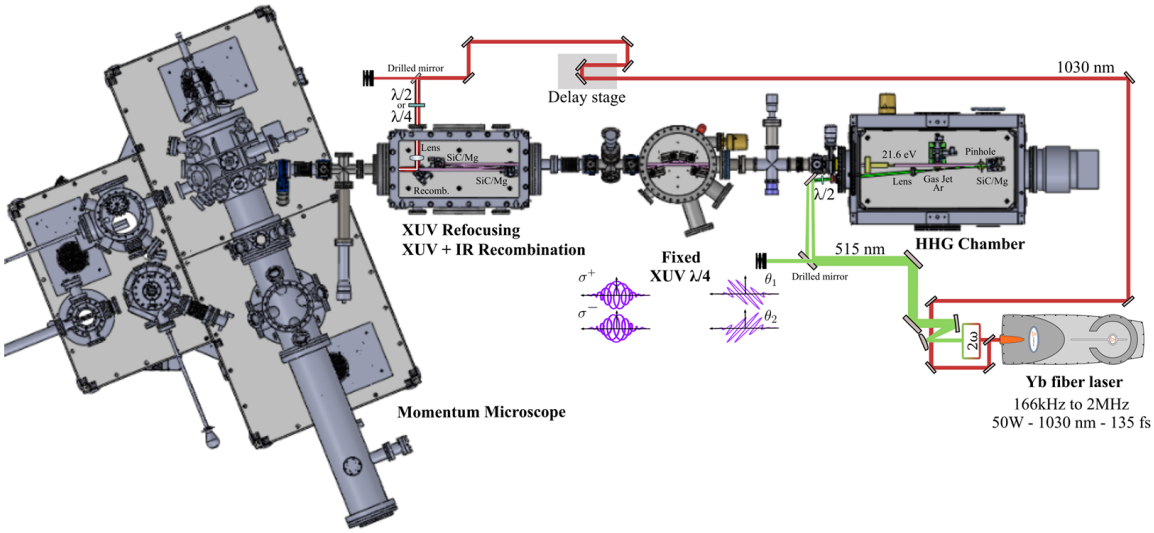


FIGURE 3.9 : Schematic of the time- and polarization-resolved extreme-ultraviolet (XUV) momentum microscopy beamline. The layout comprises a Yb-based fiber laser, a frequency-doubling module, the high-order harmonic generation chamber, the fixed all-reflective XUV quarter-wave plate, an XUV/IR recombination and refocusing chamber, and the momentum-microscope endstation. In the pump line, we have a delay stage to control the pump-probe delay. Reproduced from [3], under CC-By 4.0 license.

the sample. The transmitted arm ($\sim$ 22 W)is used to generate the probe. The beam is frequency-doubled in a 1-mm β-barium borate (BBO) crystal ($\theta = 23.4°$, $\phi = 90°$) that produces a 515 nm beam with average power of $\sim$ 7 W at 515 nm to drive the HHG. The BBO crystal is maintained at $\sim 120°$C by placing it inside an oven (Fastlite) to prevent long-term hygroscopic degradation. The 515 nm beam is expanded by a -75 mm/ $+ 300$ mm telescope ($\times 4$) and directed onto a drilled mirror (4 mm aperture). A subsequent $+125$ mm/ $- 75$ mm telescope ($\times 0.6$) reduces the beam diameter. Positioning the telescopes before and after the mirror allows precise control of the inner and outer diameters of the annular beam. The annular beam retains $\sim$ 80 % of the initial power while separating the intense visible 515 nm driving beam from the emergent XUV beam.

Before entering the HHG chamber, the beam position and pointing are actively stabilized (Polaris and K-Cube, Thorlabs) to suppress long-term laser drift. The annular beam then propagates through a zero-order half-wave plate (B. Halle) mounted on a motorized rotation stage (Newport), which allows control of the linear polarization axis of the 515-nm driving pulse. The pulses are subsequently focused by an aspheric lens with $f = 79$ mm to a spot size of down to $\sim 5 \times 5$ μm FWHM inside a thin, dense argon jet delivered into the HHG chamber through a gas nozzle made up of borosilicate gas cylinder. The gas nozzle consists of an initial 30 mm long section with 4 mm inner diameter, followed by a 3 mm long section with a 50 μm inner diameter and conical tip (Hilgenberg). A movable (x,y,z) gas catcher mounted few mm above the exit of the gas jet in order to removes excess argon, thereby minimizing XUV reabsorption. A pinhole is placed ~ 190 mm after the gas jet to block the 515 nm annular beam and transmit only the XUV beamlet propagating through the hole of the annular beam. The emerging XUV is then collimated by an $f = +200$ mm SiC/Mg multilayer mirror (NTT-AT) placed roughly ~ 200 mm away from the HHG source. The reflectivity of such

SiC/Mg multilayer mirror is $\sim 40\%$ at 21.6 eV, which simultaneously suppresses other adjacent harmonics and the mirror mount (Newfocus) is motorized for precise steering. Additional spectral filtering is achieved using a 200-nm-thick Sn foil (Luxel), which has a theoretical transmission of $\sim 22\%$ at 21.6 eV.

The XUV beam then enters the all-reflective XUV quarter-wave plate (QWP) section, which consists of four two-inch SiC mirrors (NTT-AT) at 78° incidence. This is designed to introduce a phase retardance of $\lambda/4$ between $s-$ and $p-$ polarized components at 21.6 eV. The transmission of the s component is $\sim 41\%$ while that of the p component is $\sim 21\%$. The QWP enables the generation of quasi-circularly polarized XUV light with ellipticities up to $\sim 90\%$, which is essential for our circular-dichroism measurements. The XUV-QWP assembly is mounted on a motorized translation stage (Newport) for rapid in/out from the XUV beam path, allowing the full photon flux when a linearly polarized probe is required. A key benefit of this design is that switching between different light helicities does not require any rotation of reflective optics, thus avoiding the misalignment which often occurs in rotating XUV quarter waveplate rotations even with well-designed mechanics [9].

After generation, the polarization-tunable XUV beam enters the refocusing and recombination chamber. The XUV beam is directed through a reflective telescope consisting of a concave–convex mirror pair. The XUV beam first impinges onto the concave mirror with $f = -250$ mm near normal incidence, then onto the convex mirror with $f = +350$ mm, near normal incidence. This setup refocuses the beam with an effective focal length of ~ 1000 mm directly onto the sample position in the analysis chamber of the momentum microscope with a sub-50 μm FWHM XUV spot size, which is smaller than most of the existing time-resolved XUV ARPES setups reported in the literature. Both mirrors are coated with SiC/Mg multilayers (NTT-AT), providing a peak reflectivity of $\sim 40\%$ at 21.6 eV, which further enhances spectral contrast with neighboring harmonics. The mirror mounts are motorized (Newfocus) for fine alignment. This chamber also serves as the location where the XUV probe is collinearly recombined with the IR pump.

For the IR pump line, a fraction of the 1030 nm fundamental laser is picked up from the polarizing beamsplitter and directed onto the motorized delay stage (Newport), which allows us to control the time delay between the pump and probe during our TR-ARPES measurements. The beam is then reflected into the recombination chamber by a drilled IR mirror (aperture $\phi = 5$ mm) to make it annular. The position and pointing of the beam are actively stabilized by a beam pointing stabilizer (Polaris and K-Cube, Thorlabs). A combination of $\lambda/2$ / $\lambda/4$ wave plates is placed in the path to control the polarization state of the IR beam before entering the recombination chamber. Once inside the chamber, the beam passes through a drilled lens with $f = +750$ mm and is subsequently reflected by a drilled IR mirror ($\phi = 3$ mm) at 45° that serves as the IR/XUV collinear recombination optics. To ensure the influence of 45° recombination mirror on the polarization state of the IR beam, polarimetry measurements were performed, which confirmed that the phase shift between s and p components is negligible.

3.3.3 Polarization charaterization

To determine the XUV beam ellipticity for each incident polarization-axis angle, a Rabinovitch-type XUV analyzer [10] was built from four unprotected gold mirrors at an 80° angle of incidence. At 21.6 eV, the device provides an s/p extinction ratio above 20 and can be rotated under vacuum to record Malus's-law curves. From these measurements, the polarization direction and ellipticity of the XUV beam can be inferred under the assumption of fully polarized light [11]. However, this assumption is not always valid, and the method yields only an upper bound on the ellipticity. Obtaining an exact value requires either measuring a dichroic signal [12, 13] or using an XUV quarter-wave plate [14, 15]. In HHG driven by an elliptical laser field, depolarization can naturally arise from spatial or temporal inhomogeneities. While generating linearly polarized XUV with a linearly polarized driver and then converting it to elliptical polarization with a reflective phase shifter is expected to produce a high degree of polarization.

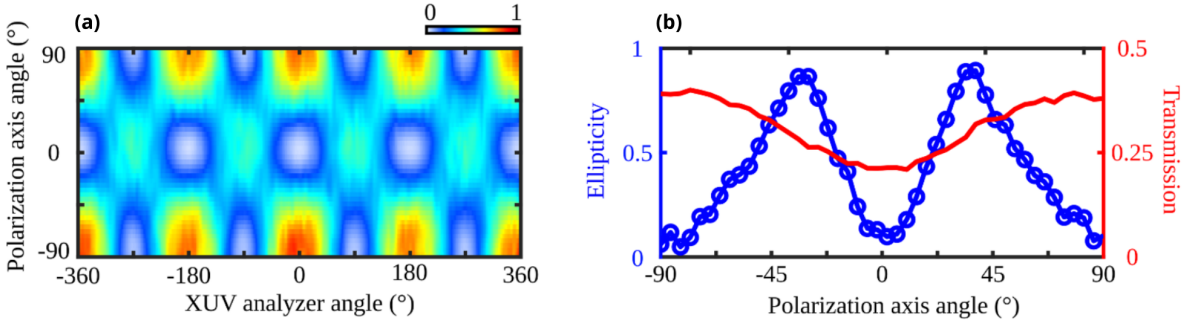


FIGURE 3.10 : Polarization characterization of the XUV source. (a) Malus's-law scans : XUV intensity vs analyzer angle for various input polarization-axis angles incident on the XUV quarter-wave plate (QWP). Here, 0° denotes p polarization and $\pm 90^\circ$ denotes s polarization.(b) Ellipticity extracted by Fourier analysis for each incident polarization angle on the QWP, shown together with the corresponding total transmission. Reproduced from Ref. [2], with permission from the publisher.

For each chosen XUV input polarization axis, Malus-law traces are recorded by continuously rotating the analyzer through 720° as shown in the Fig. 3.10a. The XUV signal shows a 180° periodic modulation in XUV analyzer angle as well as the polarization axis angle. A π phase shift is also observed when the input axis is changed from $\pm 90^\circ$ to 0°. This corresponds to XUV polarization switching from s- to p-linear polarized state. The peak intensity is lower at 0° (corresponding to p-polarization) than at $\pm 90^\circ$ (corresponding to s-polarization), consistent with the SiC s/p reflectivity ratio which is ~ 1.17 at 21.6 eV and 78° incidence. For tilted incident polarization angle axis, e.g., around -35° and $+35^\circ$, the Malus' law contrast decreases, indicating an elliptical XUV polarization state. The quarter-wave plate transmission is approximately 41% for s polarization ($\approx 80\%$ per mirror), 21% for p polarization ($\approx 68\%$ per mirror), and about 29% for tilt angles producing ellipticities around 90%.

The ellipticity of the XUV beam for each input polarization-axis angle is obtained by applying Fourier analysis to the measured Malus-law traces shown in Fig. 3.10b

$$\epsilon_{\max} = \sqrt{\frac{I_0 - 2I_1}{I_0 + 2I_1}},$$

where I_0 is the zero-frequency Fourier component and I_1 is the intensity of the oscillating component from the Fourier analysis.

When s- and p-polarized XUV light incident on the XUV quarter-wave plate around $\pm 90^\circ$ and 0° the emitted XUV is linearly polarized. By tilting the input polarization axis away from pure s- or p- polarization, the ellipticity of the XUV beam can be continuously tuned. The ellipticity reaches a maximum of approximately 90% near input angles $\pm 35^\circ$. However, the ellipticity would peak at $\pm 45^\circ$ if the SiC mirror had identical s and p reflectivities and also would show a symmetric behaviour around $\pm 90^\circ$ and 0°. But since the SiC reflectivity is higher for s polarization (red curve, Fig. 3.10b), the ellipticity maximum shifts toward smaller incident angles, i.e., more p component in order to have equal contribution after the phase shifter. This approach provides a simple and efficient method for generating ultrafast quasi-circular monochromatic XUV pulses at high-repetition-rate with rapid helicity switching, making it highly suitable for circular-dichroism ARPES.

3.3.4 Long term stability

Time- and polarization-resolved ARPES typically require acquisition times of many hours to achieve high signal-to-noise ratios [16]. This demands a very stable XUV photon flux, at the same time, stable beam pointing. Moreover, dichroism measurements require even more statistics means more acquisition time, since the relevant physics often appears as small differential signals in a specific region of a highly multidimensional dataset. To assess the long-term stability of the quasi-

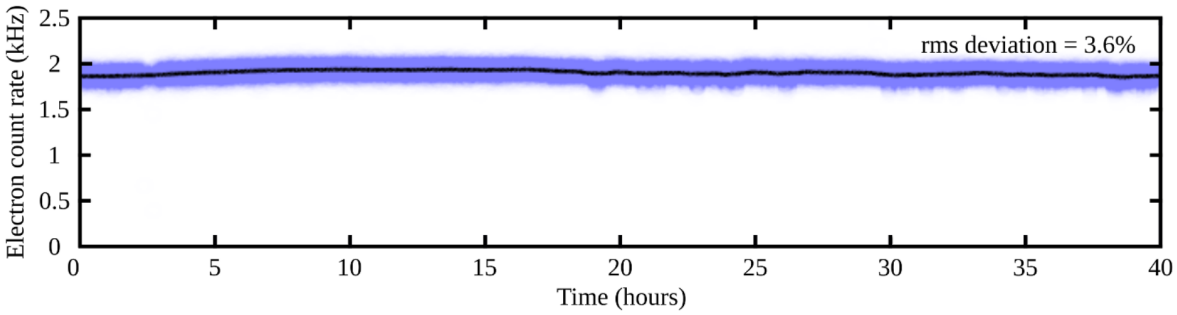


FIGURE 3.11 : Long-term stability of the quasi-circular XUV source. The Blue points show the electron count rate versus time, sampled at 1 Hz over a 40 h run. The thick black curve is a 1 h sliding average of the yield. The root-mean-square fluctuation over 40 h is 3.6%. Reproduced from Ref. [2], with permission from the publisher.

circularly polarized XUV source, the single-photon ionization rate of gas-phase molecules was

monitored at a 1 Hz sampling rate over a continuous 40 h period, as shown in Fig. 3.11. In this measurement, the quasi-circular XUV beam was directed onto a molecular beam of (+)-α-pinene ($I_p = 8.38$ eV) with a FWHM ~ 2.3 mm and positioned ~ 4 m from the HHG source where the molecular beam is seeded by 1.5 bar and the electron count rate was recorded with a COLd Target Recoil-Ion Momentum Spectrometer (COLTRIMS) [17] while switching XUV helicity every 10 min. Over the full 40 h scan, the count rate exhibited only a 3.6% root-mean-square fluctuation, indicating excellent long-term stability in both in photon flux and pointing. For reference, a pointing drift of merely 0.6 mrad would translate into a 2.3 mm shift of the XUV beam into the molecular beam, which leads to a $\sim 50\%$ decrease in ionizing signal. Such robustness is crucial for HHG-based XUV sources, especially in our time- and polarization-resolved ARPES.

3.3.5 Pump and probe spot sizes characterization

The PEEM mode of our time-of-flight momentum microscope is capable of recording real-space images of the ejected photoelectrons from the sample surface. This capability was used to characterize the pump and probe beam footprints on a 2H$-$$WSe_2$ surface. Fig 3.12a shows the XUV (21.6 eV) probe real space image. As the XUV photoemission is a single-photon process, the PEEM image directly reproduces the XUV intensity profile. Fig 3.12b shows the real space image with the IR (1.2 eV) pump; here photoemission is a multiphoton process, so the PEEM signal does not directly represent the beam footprint and we need to consider nonlinearity involved in the process.

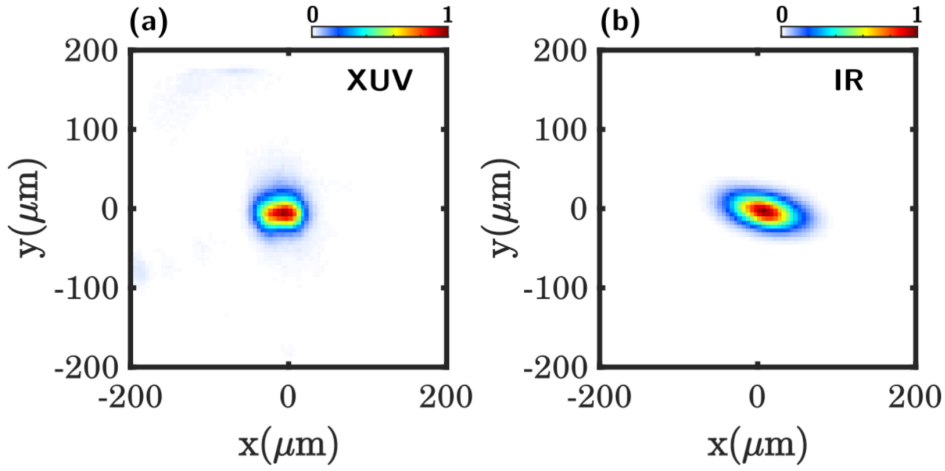


FIGURE 3.12 : XUV and IR beam spot size characterization at the sample. (a) PEEM image of the XUV (21.6 eV) probe shows the probe footprint on the sample. The FWHM of the probe spot size we get from this PEEM image is $\mathrm{FWHM} = 45\ \mu\mathrm{m}$ **(x) by** $33\ \mu\mathrm{m}$ **(y). (b) PEEM image of the IR (1.2 eV) pump. In this case we have** $60\ \mu\mathrm{m}$ **(x) by** $30\ \mu\mathrm{m}$ **(y). Reproduced from [3], under CC-By 4.0 license.**

Gaussian fits applied to the PEEM images along the x and y axes yield the pump and probe spot sizes. For the XUV probe, the extracted FWHM values are $\mathrm{FWHM} = 45\ \mu\mathrm{m}$ along x and $33\ \mu\mathrm{m}$ along y. The larger spot size along x size is partially due to the 65° angle of incidence on the surface. For the IR pump the FWHM is $60\ \mu\mathrm{m}$ along x and $30\ \mu\mathrm{m}$ along y. To quantify the effective nonlinearity of IR-driven photoemission, the total PEEM intensity, the total photoemission intensity S_{tot} was recorded as a function of incident pump power P_0. The resulting dependence exhibits a linear trend, and the log–log representation reveals a power-law scaling $S_{\mathrm{tot}} \propto P_0^{\alpha}$ with a fitted exponent $\alpha = 5.4$. The underlying pump-beam footprint can therefore be retrieved by multiplying the measured FWHM by $\sqrt{\alpha}$, yielding an effective footprint of $\sim 139\ \mu\mathrm{m}$ along x and $\sim 70\ \mu\mathrm{m}$ along y.

3.3.6 Time and energy resolution

Energy resolution and spectral bandwidth.

The energy resolution of the system was quantified from the width of the measured Fermi-edge cutoff. The total resolution ΔE_{tot} is the convolution of the XUV bandwidth $\Delta E_{h\nu}$, the time-of-flight (ToF) analyzer resolution ΔE_{ToF}, and the thermal broadening $\Delta E_{\mathrm{therm}} \simeq 4k_{\mathrm{B}}T$ ($\simeq$100 meV at room temperature) of the Fermi–Dirac distribution at temperature T :

$$\Delta E_{\mathrm{tot}}^2 = \Delta E_{h\nu}^2 + \Delta E_{\mathrm{ToF}}^2 + \Delta E_{\mathrm{therm}}^2 \tag{3.2}$$

The TOF-MM is equipped with a UHV cryostat (Lakeshore ST-400), enabling cooling to ~ 16 K using liquid Helium. Metallic Re(0001) was employed as a reference system; the crystal was flashed before measurement to ensure a clean surface. Fermi-edge cutoffs of 113 meV at room temperature and 44 meV at 16 K were obtained, as shown in Fig. 3.13b,d. Although the Re(0001) surface was flashed immediately prior to measurement, diffuse Tamm-state features are visible in the momentum maps (Fig. 3.13a,c). However, the Fermi edge itself is unaffected. The intrinsic ToF energy resolution is conveniently extracted at the bottom of the photoemission paraboloid (Fig. 3.13d) where the low-energy cutoff ($E_{\mathrm{kin}} = 0$) is not subject to thermal broadening. The measured width is $\Delta E_{\mathrm{ToF}} = 29$ meV (FWHM) as shown in Fig. 3.13e,f. The theoretical TOF resolution ΔE_{ToF} at drift energy $E_d = 20$ eV is given by,

$$\Delta E_{\mathrm{ToF}} = \frac{2E_d}{m_e}\frac{L^2}{\Delta\tau^2} \tag{3.3}$$

where $L = 650$ mm is the drift section length, $\Delta\tau = 200$ ps is the delay-line detector time resolution, m_e is the electron mass. This expression yields $\Delta E_{\mathrm{ToF}} \sim 30$ meV,in excellent agreement with experiment. Using $\Delta E_{\mathrm{ToF}} = 29$ meV and $\Delta E_{\mathrm{therm}} = 5.3$ meV at 16K in eq. 3.2 the XUV spectral bandwidth is determined to be $\Delta E_{h\nu} \approx 33$ meV. The corresponding Fourier-limited XUV pulse duration Δt_{FL} is obtained from the time–bandwidth product $\Delta E\,\Delta t_{\mathrm{FL}} = 1825\ \mathrm{meV}\cdot\mathrm{fs}$, which results

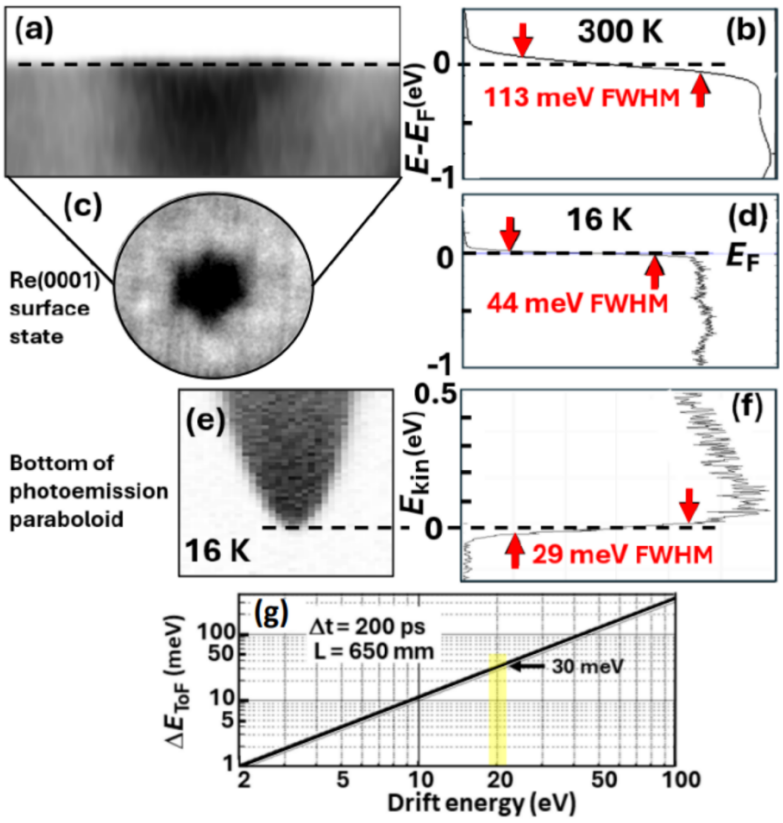


FIGURE 3.13 : Energy resolution and spectral bandwidth of time- and polarization-resolved ARPES endstation. The energy resolution was evaluated at the Fermi edge and at the $E_{\rm kin} = 0$ cutoff on Re(0001) sample, with a 20 eV drift energy in the ToF section. (a) and (c) represents, $(E - E_F)$ vs k_x and k_x vs k_y near E_F, showing the Tamm surface state. (b) and (d) report corresponding energy-distribution (Intensity vs $(E-E_F)$) profiles at 300 K and 16 K. (e) displays the bottom of the photoemission paraboloid, and (f) its intensity profile, highlighting the $E_{\rm kin} = 0$ cutoff. (g) The theoretical ToF analyzer energy resolution as a function of drift energy, which predicts ~ 30 meV at 20 eV, in agreement with panel (f). Reproduced from [3], under CC-By 4.0 license.

$\Delta t_{\rm FL} \approx 55$ fs. In practice, the XUV pulse is expected to be a few 10% longer due to the atomic dipole phase in the HHG process and associated frequency chirp [18–20].

Temporal resolution. The temporal resolution was determined from the pump–probe cross-correlation via laser-assisted photoemission (LAPE) in 2H$-$WSe$_2$, a nonresonant coherent two-photon (XUV+IR) process. The measurement was performed using a p-polarized 1.2 eV IR pump, which maximizes LAPE together with a p-polarized XUV probe. The time-dependent LAPE signal is shown in Fig. 3.14a and the corresponding fit with a Gaussian, which yields an experimental temporal resolution of 144 fs (FWHM) is shown in Fig 3.14b. Since the XUV pulse is shorter than the IR driver owing to the strong nonlinearity of HHG, the overall time resolution is limited by the IR pulse duration.

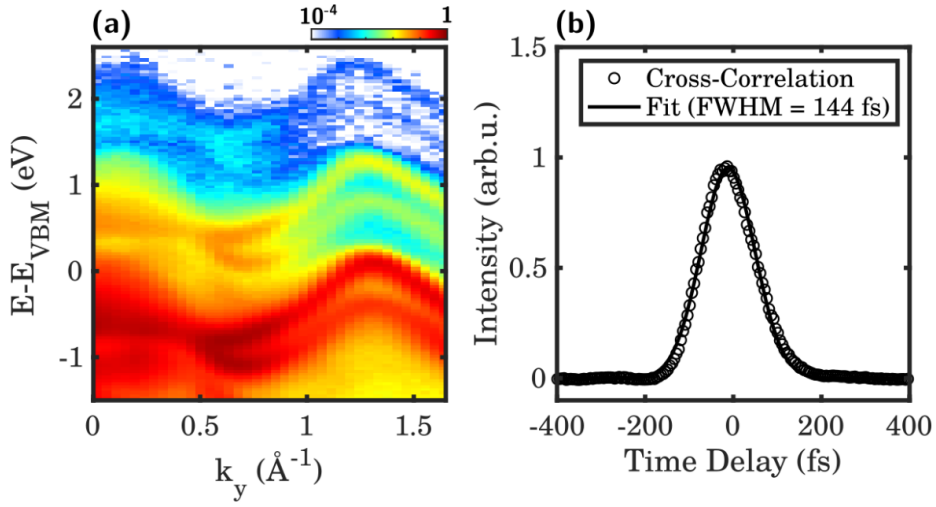


FIGURE 3.14 : Temporal-resolution characterization. Using a p-polarized IR pump (1.2 eV) and a p-polarized XUV probe, we monitored the temporal evolution of laser-assisted photoemission (LAPE) in 2H$-$WSe$_2$. LAPE—a non-resonant, coherent two-photon (XUV+IR) process—yields the pump–probe cross-correlation. (a) Energy–momentum cut along the Γ–K′ high-symmetry direction, integrated over delays from -400 to $+400$ fs. (b) Time-dependent LAPE signal with a Gaussian fit, from which the experimental temporal resolution is extracted to be 144 fs (FWHM). Reproduced from [3], under CC-By 4.0 license.

3.3.7 Momentum Microscope

The basic working principle of a momentum microscope is to apply a high positive bias to an electrostatic objective lens near the sample surface, which is able to collect photoelectrons over the full 2π solid angle in an energy across several eV. The help of advanced electron optics in the momentum microscope allows us to create images of the photoemitted electron distribution in both real and momentum space. Analogous to optical microscopy, the surface-projected band structure appears in the back focal plane (reciprocal image plane) of the objective lens. An adjustable contrast aperture in this plane can be inserted in order to select a desired momentum region to realize dark-field PEEM, i.e., momentum-resolved real-space electron distribution. Similarly, an adjustable field aperture can be placed in an intermediate real-space image plane to better define a source area down to sub-μm diameters. After that, the electrons travel in a field-free, dispersive TOF drift tube, and then finally their two-dimensional momentum and kinetic energy are recorded with an MCP coupled to a position-sensitive delay-line detector (DLD). This type of TOF-MM allow simultaneous acquisition of the full three-dimensional photoelectron distribution over the entire in-plane momentum and over a broad energy window, with rapid switching between PEEM mode (including dark-field imaging capability) and ARPES mode (with spatially resolved band mapping).

Although this detection concept is very appealing, it also has some drawbacks. First, high extractor fields in standard TOF-MMs can trigger field emission from edges or protrusions on cleaved or heterogeneous samples, imposing stricter demands on the morphology and surface quality of the sample than with hemispherical analyzers. In addition, space–charge effects, distorting angular

and energy distributions, appear at lower electron densities than in standard hemispherical analyzers. The reason is that, prior to the dispersive drift tube, fast primary and slow secondary electrons do not spread significantly along the flight axis, increasing their interaction length and time. Further, refocusing of the photoelectron disk at several focal planes amplifies these space–charge distortions.

Our TOF-MM is a prototype with better performance for $\mathbf{k}$-space imaging. Key features include enlarged arrays of contrast and field apertures and better lens optics. The enlarged array of 9 contrast apertures with increased transverse motion using piezomotors enhances Gaussian imaging in both bright- and dark-field modes, while the array of 16 field apertures enables $\mathbf{k}$-imaging with sub-micron regions of interest (ROIs). Selecting the ROI via a field aperture mitigates artifacts arising from shifts of photon-footprint shifts such as beam-pointing drifts or changing the photon energy.

For the electron-optics side, the main improvement is a new type of front-lens that supports multiple operating modes. Conventional PEEMs and MMs cathode lenses use an extractor configuration with a strong, homogeneous accelerating field (typically 4–8 kV/mm) between the sample and the extractor. Many contemporary materials require in-situ cleaving, which can leave sharp edges or protruding lamellae (e.g., in layered systems); in such cases, high extractor fields can trigger field emission at these features. By contrast, the gap-lens mode provides better $\mathbf{k}$-images at energies down to 16 eV. Using this optics, a $\mathbf{k}$-resolution of 0.01 Å^{-1} was verified by zooming into the Au(111) Shockley surface state, and the accessible $\mathbf{k}$-field of view exceeds 6 Å^{-1} at photon energies above 40 eV. In addition, the repeller mode [21] can access pump-fluence regimes not reachable in the standard configuration, as demonstrated at the FLASH free-electron laser [22].

3.4 Conclusion

In this chapter, I presented the two TR-ARPES platforms central to this thesis : (i) the ALLS endstation, employing a 6 eV probe, a tunable mid-infrared pump, and a hemispherical analyzer; and (ii) the CELIA endstation, featuring a 21.6 eV, polarization-tunable XUV probe, an IR pump, and a time-of-flight momentum microscope. These instruments are complementary by design, each optimized for probing different aspects of electronic structure in quantum materials.

At ALLS, the combination of a low photon-energy probe and a hemispherical analyzer provides exceptional energy and momentum resolution, enabling the detection of subtle spectral features in the vicinity of the Γ point, such as superconducting gaps and pseudogap states. In addition, the tunable mid-infrared pump offers control over the excitation pathway, allowing specific low-energy resonant excitation. However, this configuration is limited in temporal resolution ($\sim$200–300 fs), which constrains the ability to fully resolve out-of-equilibrium dynamics.Furthermore, the lack of polarization tunability restricts the ability to disentangle matrix-element effects and to probe orbital textures. In addition, the low photon energy limits the accessible momentum range.

In contrast, the CELIA endstation, based on a 21.6 eV XUV probe, provides access to a significantly extended region of momentum space, enabling the investigation of electronic states far from the Γ point, such as valley-selective physics in TMDCs. This setup offers improved temporal resolution, allowing better exploration of out-of-equilibrium phenomena, including light-driven states such as Floquet–Bloch bands. In addition, polarization control in the XUV, integrated with TR-ARPES, is one of a kind among current facilities, enabling detailed investigations of matrix-element effects and the study of Berry curvature, orbital texture, and spin texture. However, this setup has reduced energy and momentum resolution compared to the low-photon-energy ARPES setup at ALLS, which limits its capability to resolve subtle features or modifications in the electronic structure, and the fixed pump photon energy (1.2 eV) limits the flexibility of resonant excitation schemes for most materials.

Together, these platforms provide a comprehensive and complementary toolkit : one optimized for ultrahigh resolution near Γ, and the other for wide momentum coverage, superior temporal resolution, and polarization-selective measurements. Their combined use enables a unified, momentum-resolved understanding of ultrafast electron dynamics across a broad range of quantum materials.

Bibliographie

[1] A Longa, J-M Parent, B K Frimpong, D Armanno, N Gauthier, F Légaré, F Boschini, and G Jargot. Time-resolved ARPES with probe energy of 6.0 ev and tunable MIR pump at 250 khz. *Opt. Express*, 32(17) :29549–29557, August 2024.

[2] A Comby, D Rajak, D Descamps, S Petit, V Blanchet, Y Mairesse, J Gaudin, and S Beaulieu. Ultrafast polarization-tunable monochromatic extreme ultraviolet source at high-repetition-rate. *J. Opt.*, 24(8) :084003, August 2022.

[3] S Fragkos, Q Courtade, O Tkach, J Gaudin, D Descamps, G Barrette, S Petit, G Schönhense, Y Mairesse, and S Beaulieu. Time- and polarization-resolved extreme ultraviolet momentum microscopy. 2025.

[4] M Först, C Manzoni, S Kaiser, Y Tomioka, Y Tokura, R Merlin, and A Cavalleri. Nonlinear phononics as an ultrafast route to lattice control. *Nat. Phys.*, 7(11) :854–856, November 2011.

[5] Y H Wang, H Steinberg, P Jarillo-Herrero, and N Gedik. Observation of Floquet-Bloch states on the surface of a topological insulator. *Science*, 342(6157) :453–457, October 2013.

[6] M Mitrano, A Cantaluppi, D Nicoletti, S Kaiser, A Perucchi, S Lupi, P Di Pietro, D Pontiroli, M Riccò, S R Clark, D Jaksch, and A Cavalleri. Possible light-induced superconductivity in K3C60 at high temperature. *Nature*, 530(7591) :461–464, February 2016.

[7] A de la Torre, D M Kennes, M Claassen, S Gerber, J W McIver, and M A Sentef. Colloquium : Nonthermal pathways to ultrafast control in quantum materials. *Rev. Mod. Phys.*, 93 (4), October 2021.

[8] SPECS. Leading scientific equipment for surface analysis. `https://www.specs-group.com/`. Accessed : 2025-10-5.

[9] K Yao, F Willems, C von Korff Schmising, C Strüber, P Hessing, B Pfau, D Schick, D Engel, K Gerlinger, M Schneider, and S Eisebitt. A tabletop setup for ultrafast helicity-dependent and element-specific absorption spectroscopy and scattering in the extreme ultraviolet spectral range. *Rev. Sci. Instrum.*, 91(9) :093001, September 2020.

[10] K Rabinovitch, L R Canfield, and R P Madden. A method for measuring polarization in the vacuum ultraviolet. *Appl. Opt.*, 4(8) :1005, August 1965.

[11] P Antoine, B Carré, A L'Huillier, and Maciej Lewenstein. Polarization of high-order harmonics. *Phys. Rev. A*, 55(2) :1314–1324, February 1997.

[12] K Veyrinas, V Gruson, S J Weber, L Barreau, T Ruchon, J-F Hergott, J-C Houver, R R Lucchese, P Salières, and D Dowek. Molecular frame photoemission by a comb of elliptical

high-order harmonics : a sensitive probe of both photodynamics and harmonic complete polarization state. *Faraday Discuss.*, 194 :161–183, 2016.

[13] L Barreau, K Veyrinas, V Gruson, S J Weber, T Auguste, J-François Hergott, F Lepetit, B Carré, J-Christophe Houver, D Dowek, and P Sali'eres. Evidence of depolarization and ellipticity of high harmonics driven by ultrashort bichromatic circularly polarized fields. *Nat. Commun.*, 9(1) :4727, November 2018.

[14] T Koide, T Shidara, M Yuri, N Kandaka, K Yamaguchi, and H Fukutani. Elliptical-polarization analyses of synchrotron radiation in the 5–80-ev region with a reflection polarimeter. *Nucl. Instrum. Methods Phys. Res. A*, 308(3) :635–644, October 1991.

[15] L Nahon and C Alcaraz. SU5 : a calibrated variable-polarization synchrotron radiation beam line in the vacuum-ultraviolet range. *Appl. Opt.*, 43(5) :1024–1037, February 2004.

[16] J Maklar, S Dong, S Beaulieu, T Pincelli, M Dendzik, Y W Windsor, R P Xian, M Wolf, R Ernstorfer, and L Rettig. A quantitative comparison of time-of-flight momentum microscopes and hemispherical analyzers for time- and angle-resolved photoemission spectroscopy experiments. *Rev. Sci. Instrum.*, 91(12) :123112, December 2020.

[17] J Ullrich, R Moshammer, A Dorn, R D rner, L Ph H Schmidt, and H Schmidt-B cking. Recoil-ion and electron momentum spectroscopy : reaction-microscopes. *Rep. Prog. Phys.*, 66(9) : 1463–1545, September 2003.

[18] J Mauritsson, P Johnsson, R López-Martens, K Varjú, W Kornelis, J Biegert, U Keller, M B Gaarde, K J Schafer, and A L'Huillier. Measurement and control of the frequency chirp rate of high-order harmonic pulses. *Phys. Rev. A*, 70(2), August 2004.

[19] Y Mairesse, O Gobert, P Breger, H Merdji, P Meynadier, P Monchicourt, M Perdrix, P Salières, and B Carré. High harmonic XUV spectral phase interferometry for direct electric-field reconstruction. *Phys. Rev. Lett.*, 94(17) :173903, May 2005.

[20] K Varjú, Y Mairesse, B Carré, M B Gaarde, P Johnsson, S Kazamias, R López-Martens, J Mauritsson, K J Schafer, P H Balcou, A L'huillier, and P Salières. Frequency chirp of harmonic and attosecond pulses. *J. Mod. Opt.*, 52(2-3) :379–394, January 2005.

[21] G Schönhense, D Kutnyakhov, F Pressacco, M Heber, N Wind, S Y Agustsson, S Babenkov, D Vasilyev, O Fedchenko, S Chernov, L Rettig, B Schönhense, L Wenthaus, G Brenner, S Dziarzhytski, S Palutke, S K Mahatha, N Schirmel, H Redlin, B Manschwetus, I Hartl, Yu Matveyev, A Gloskovskii, C Schlueter, V Shokeen, H Duerr, T K Allison, M Beye, K Rossnagel, H J Elmers, and K Medjanik. Suppression of the vacuum space-charge effect in fs-photoemission by a retarding electrostatic front lens. *Rev. Sci. Instrum.*, 92(5) :053703, May 2021.

[22] H J Elmers, J Regel, T Mashoff, J Braun, S Babenkov, S Chernov, O Fedchenko, K Medjanik, D Vasilyev, J Minar, H Ebert, and G Schönhense. Rashba splitting of the tamm surface state on re(0001) observed by spin-resolved photoemission and scanning tunneling spectroscopy. *Phys. Rev. Res.*, 2(1), March 2020.

4 CONTROL OF INTERVALLEY SCATTERING IN Bi_2Te_3 VIA TEMPERATURE-DEPENDENT BAND RENORMALIZATION

Summary : The control of out-of-equilibrium electron dynamics in topological insulators is essential to unlock their potential in next-generation quantum technologies. However, the role of temperature on the renormalization of the electronic band structure and, consequently, on out-of-equilibrium electron scattering processes is still elusive. Here, using high-resolution time- and angle-resolved photoemission spectroscopy (TR-ARPES), we show that even a modest ($\sim$15 meV) renormalization of the conduction band of Bi_2Te_3 can critically affect bulk and surface electron scattering processes. Supported by kinetic Monte Carlo simulations, we show that temperature-induced changes in the bulk band structure modulate the intervalley electron-phonon scattering rate, reshaping the out-of-equilibrium response and the long-lasting charge accumulation at the bottom of the conduction band. This work establishes temperature as an effective control knob for engineering scattering pathways in topological insulators.

Statement of Contribution : The work presented in this chapter is based on a collaborative experimental effort. I conceived the experiments together with Francesco Goto and Fabio Boschini and led the TR-ARPES experimental campaign at the ALLS laboratory, including the preparation, execution, and optimization of the measurement protocols. The TR-ARPES measurements at ALLS were performed by me and Francesco Goto, with assistance from Nicolas Gauthier, Benson Frimpong Kwaku, and Dario Armanno, while additional measurements were carried out at QMI–UBC by Matteo Michiardi. I performed the analysis of the TR-ARPES data with the assistance of Francesco Goto, Nicolas Gauthier, Samuel Beaulieu, and Fabio Boschini. The kinetic Monte Carlo simulations were performed by Francesco Goto with input from Fabio Boschini and myself. The interpretation of the experimental and theoretical results was developed through discussions involving myself, Francesco Goto, Matteo Michiardi, Andrea Damascelli, Philip Hofmann, Nicolas Gauthier, Samuel Beaulieu, and Fabio Boschini. The majority of the results presented in this chapter are adapted from Jabed *et al.* [1].

4.1 Introduction

Three-dimensional topological insulators (3D TIs) [2–7] are characterized by topologically protected spin polarized metallic surface states within an insulating bulk energy gap. Such properties position TIs as prime candidates for advanced technologies such as photogalvanic current generation [8], spintronics [9, 10], quantum computing [11–13] which demand precise control of spin-polarized surface states and their interplay with bulk states. Angle-resolved photoemission spectroscopy (ARPES) has emerged as the primary experimental tool for the identification and characterization of these topological electronic states. In this context conventional ARPES has enabled the direct visualization of Dirac-like surface states and their connectivity to the bulk band structure.Subsequent extensions, including spin-resolved ARPES, revealed the helical spin-momentum locking that underpins topological protection, while Dichroic ARPES offered complementary insight into the orbital and symmetry-resolved character of these states. In contrast, time- and angle-resolved photoemission spectroscopy (TR-ARPES) has opened access to the ultrafast, nonequilibrium regime, enabling direct investigation of carrier relaxation pathways, surface–bulk coupling, and transient modifications of the electronic structure in topological insulators - insights that are inaccessible in equilibrium and are essential for realistic device-relevant operation. In this chapter, I focus on developing a fundamental understanding of three-dimensional topological insulators using TR-ARPES.

I begin by describing how angle-resolved photoemission spectroscopy (ARPES) played a central role in establishing topological insulators as a mature research field. Following the theoretical prediction of three-dimensional topological insulators by Fu and Kane [2, 14], the first experimental realization of a 3D topological insulator was achieved in the alloy $Bi_{1-x}Sb_x$ ($0.07 < x < 0.22$), as reported by Hsieh et al. [15]. ARPES measurements directly revealed metallic surface states crossing the Fermi level, while spin-resolved ARPES confirmed their helical spin polarization, as shown in Fig. 4.1. Together, these results provided clear experimental evidence of the topological nature of the surface states.

Subsequent theoretical and experimental studies identified Bi_2Se_3 and Bi_2Te3 [4, 17, 18] as the next 3D topological insulators. These materials offer a key advantage : a simple surface electronic structure characterized by a single Dirac cone at the Brillouin-zone center. In contrast to $Bi_{1-x}Sb_x$, they are free from alloy disorder, making them ideal systems for studying topological surface states.

With this background in place, we first outline the electronic structure of Bi_2Te_3, both theoretically and experimentally, as it constitutes the primary material studied in this chapter. This provides the necessary framework for the subsequent discussion of ARPES studies of 3D topological insulators. Bi_2Te_3 is a rhombohedral semiconductor (space group $R\bar{3}m$) with quintuple layers ordered Te(1)–Bi–Te(2)–Bi–Te(1) shown in Fig. 4.2a . Weak bonding between adjacent Te(1) planes enables easy cleavage along the (111) direction, yielding a Te(1)-terminated surface commonly used in experiments and simulations. Fig. 4.2b computed surface bands (red/dark gray) overlaid

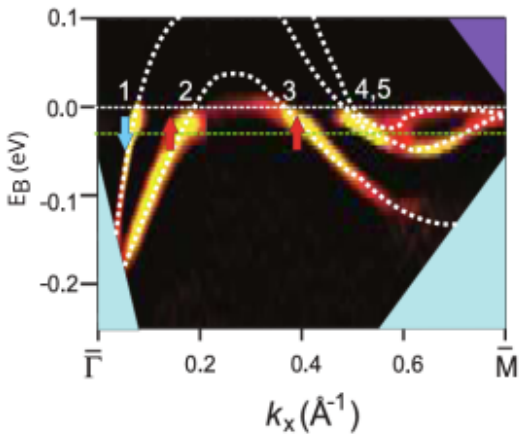


FIGURE 4.1 : ARPES measurements of $Bi_{1-x}Sb_x$, the first 3D topological insulator, revealing five surface-state crossings of the Fermi level. The arrows indicate the spin polarization of the surface bands, as directly confirmed by spin-resolved ARPES measurements. Adapted from [16], with permission from the publisher.

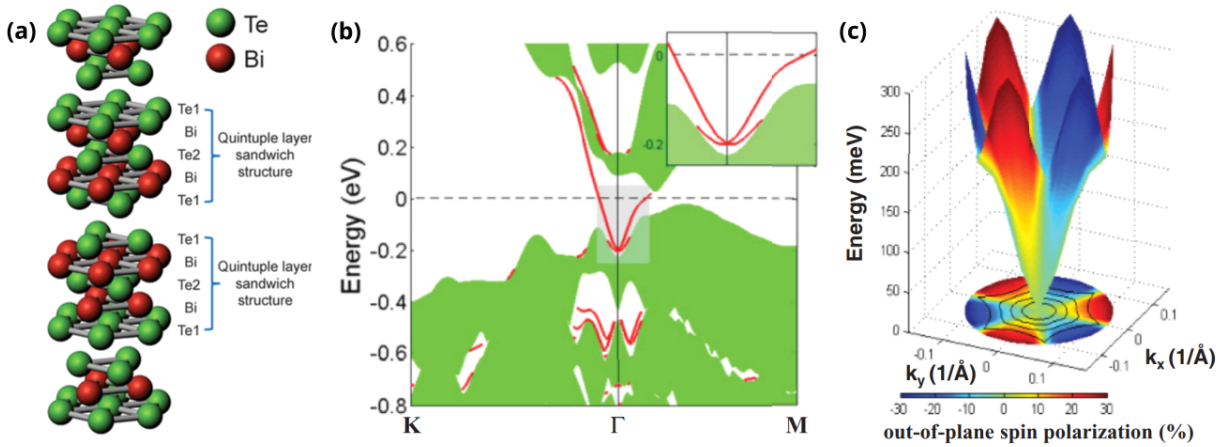


FIGURE 4.2 : (a) Rhombohedral type crystal structure of Bi_2Te_3. Adapted from [4], with permission from the publisher. (b) Electronic structure of Bi_2Te_3. Surface states are indicated by red (dark gray) lines, overlaid on the projected bulk bands (green/light gray region). The inset shows a magnified view of the area outlined by the light gray rectangle. Adapted from [19], with permission from the publisher. (c) Energy dependence of Bi_2Te_3 surface Dirac cone showing hexagonal warping. Magnitude of out-of-the-plane spin component is indicated by the color bar. Adapted from [19], with permission from the publisher.

on the projected bulk continuum (green/light gray) along high-symmetry directions of the surface Brillouin zone which show that between Γ and M an odd number (one) of surface bands crosses the Fermi level E_F. The calculation is performed by using First-principles method combined with an effective $\mathbf{k}\cdot\mathbf{p}$ Hamiltonian to reproduce the warped Dirac surface cone of Bi_2Te_3, including a finite out-of-plane spin component[19]. The Dirac surface dispersion (Fig. 4.2c) exhibits nearly circular constant-energy contours near the Dirac point, evolving to hexagonal contours at ~ 150 meV above the Dirac point and to a snowflake-like shape above ~ 200 meV. This hexagonal warping has been observed by ARPES and is well described within the $\mathbf{k}\cdot\mathbf{p}$ framework. It is to be mentioned that the band dispersion presented in Fig. 4.2b does not address matrix element effects,

which are important for describing spectral intensities in ARPES intensities that strongly depend on matrix-element effects (photon energy, polarization, and geometry).

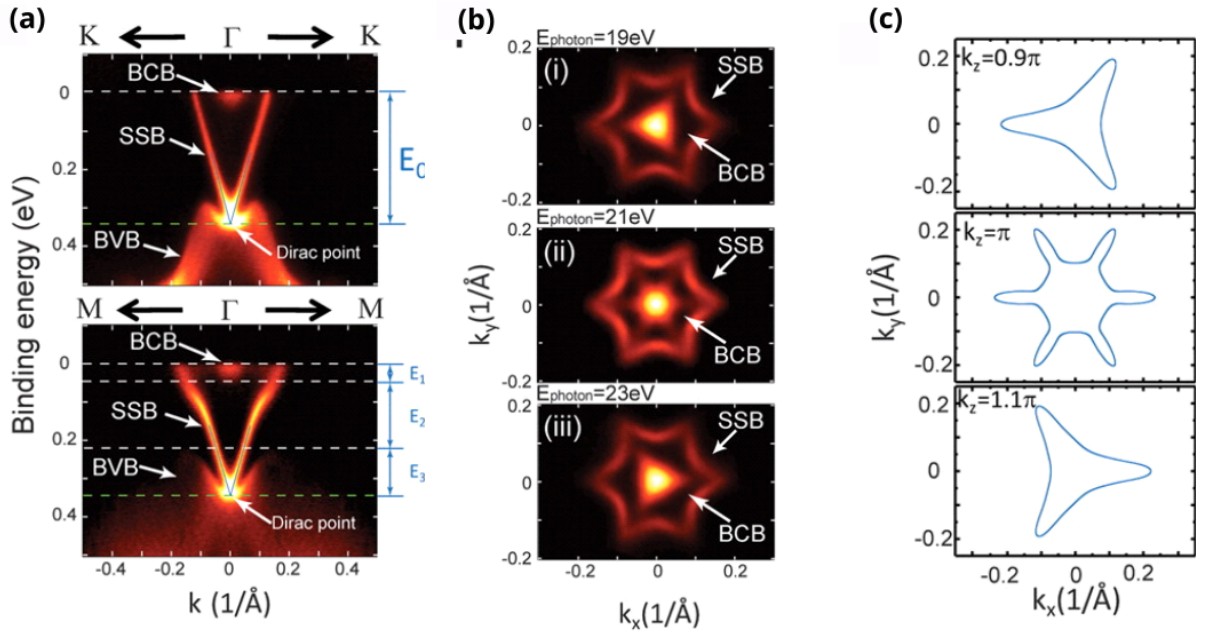


FIGURE 4.3 : a. ARPES measurements of band dispersions along $K-\Gamma-K$ (top) and $M-\Gamma-M$ (bottom) directions. The broad bulk band (BCB and BVB) dispersions are similar to those in Fig. 4.2b, whereas the sharp V-shape dispersion is from the surface state band (SSB). The apex of the V-shape dispersion is the Dirac point. Energy scales of the band structure are labeled as follows : E0 : binding energy of Dirac point (0.34 eV); E1 : BCB bottom binding energy (0.045 eV); E2 : bulk energy gap (0.165 eV); and E3 : energy separation between BVB top and Dirac point (0.13 eV). b. Photon energy–dependent Fermi Surface (FS) maps. The shape of the inner FS changes markedly with photon energies, indicating a strong k_z dependence due to its bulk nature as predicted by ab initio calculation presented in c, whereas the nonvarying hexagonal shape of the outer hexagram FS confirms its surface state origin. c. The k_z dependence of the calculated bulk FS projection on the surface BZ. Adapted from [4], with permission from the publisher.

Experimentally by performing ARPES measurements on n type Bi_2Te_3 the electronic band structure is confirmed and presented in Fig. 4.3a along both high symmetry direction ($\Gamma-M$ and $\Gamma-K$). In Fig. 4.3b it has been observed that bulk conduction band projected onto the surface BZ exhibits a triangular or snowflake-like electron pocket centered at the Γ point depending on its photon energy i.e.,k_z and surface states exhibit hexagonal symmetry and this is also supported by ab initio calculations as shown in Fig. 4.3c[4].

Having established the equilibrium electronic structure of Bi_2Te_3, we now turn to how ARPES and its advanced extensions have been used to probe the defining properties of 3D topological insulators. In this context, Bi_2Se_3 and Bi_2Te_3 have served as key model systems and have played a central role in the experimental development of the field.

Spin-resolved ARPES measurements provided the first direct experimental verification of the helical spin texture predicted for topological surface states. In both Bi_2Se_3 and Bi_2Te_3, spin-ARPES

experiments [16, 20–23] established the presence of spin–momentum locking in the surface-state electrons as presented in Fig.4.4. However, deviations from an ideal helical spin configuration have been observed experimentally, arising from strong spin–orbit coupling effects [24]. Early spin-resolved ARPES studies reported a wide range of measured spin polarizations, varying from approximately 25% [21] to 75% [22]. Subsequent theoretical work clarified that the spin polarization of the photoemitted electrons does not directly correspond to the intrinsic spin polarization of the initial electronic states [25]. Later experiments further demonstrated that the measured spin polarization can be reversed or rotated out of the surface plane by tuning the polarization of the incident photons [23, 26–28]. This behavior reflects the fundamental role of spin–orbit coupling, which entangles spin and orbital degrees of freedom such that spin is no longer a good quantum number and the eigenstates are described by mixed spin–orbital character, additionally reflects multi layer nature of TSS. Following these developments, it became clear that a complete description of topological surface states requires access not only to the spin degree of freedom but also to their orbital character. In this context, dichroic ARPES provides a powerful complementary probe, as it is sensitive to the orbital angular momentum through photoemission matrix-element effects. Using circular dichroism in ARPES, Wang et al. [29] demonstrated that the measured dichroic signal in Bi_2Se_3 encodes detailed information about the orbital texture of the surface states. By modeling the photoemission matrix elements, they showed that all three components of the spin-polarization vector can be reconstructed indirectly from dichroic ARPES data, as illustrated in Fig. 4.5. This work established a direct link between orbital angular momentum and spin texture in topological surface states, highlighting dichroic ARPES as a powerful tool for not only probing orbital information but aslo the spin texture in strongly spin–orbit–coupled systems.

While spin-resolved and dichroic ARPES have provided detailed insight into the equilibrium spin and orbital textures of topological surface states, these techniques are inherently limited to equilibrium properties. However, many fundamental questions in topological insulators—such as the coupling between bulk and surface states, carrier relaxation pathways, and the robustness of topological protection under nonequilibrium conditions—can only be addressed by accessing the ultrafast dynamics of the electronic structure. This motivated the extension of ARPES into the time domain, enabling direct momentum-resolved measurements of transient electronic states through time- and angle-resolved photoemission spectroscopy (TR-ARPES).

An extensive experimental effort to investigate topological insulators using TR-ARPES began around 2012. Early pioneering studies by Sobota et al. 2012 [30], followed closely by Crepaldi et al. 2012 [31], Hajlaoui et al. 2012 [32], Wang et al. 2012 [33] and Sobota et al. 2014 [34], provided the first momentum-resolved mapping of the unoccupied electronic structure of the topological insulators Bi_2Se_3 and Bi_2Te_3. These works revealed the dispersion of both the topological surface state (TSS) and the bulk bands above the Fermi level. Figure 4.6 shows representative TR-ARPES measurements of the unoccupied band structure of Bi_2Se_3.

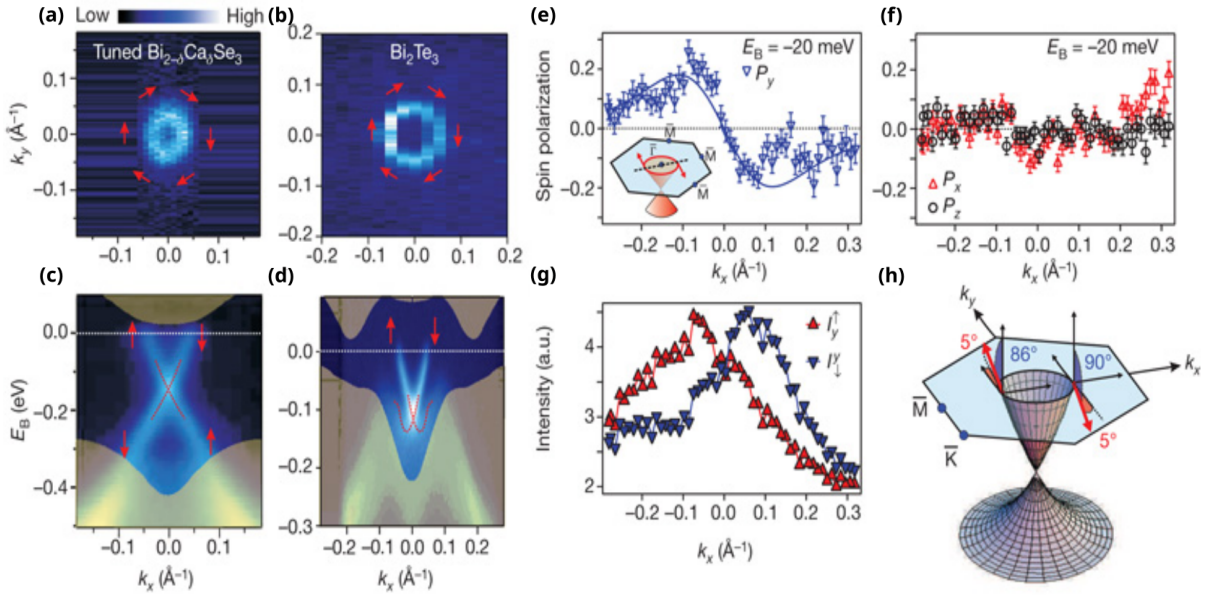


FIGURE 4.4 : Spin momentum locking of spin-helical dirac electrons using spin-resolved ARPES. (a,b) Fermi-surface maps of Bi_2Se_3 and Bi_2Te_3 measured at the Fermi level E_F. Red arrows indicate the direction of the spin projection around the Fermi surface. (c,d) Energy–momentum dispersions along the k_x momentum cut, where the dotted red lines serve as guides to the eye and the shaded regions indicate the projected bulk band structure. (e) Measured y component of the spin polarization along the Γ–M direction at a binding energy $E_b = -20$ meV, which intersects only the topological surface states. While (f) is the same but for x (red triangles) and z (black circles) components of the spin polarization. (g) Spin-resolved spectra corresponding to the y-component of the measured spin-polarization data. (h) Extracted spin-polarization vector $\mathbf{P} = (S_x, S_y, S_z)$ for electrons with $+k_x$, $-k_x$, demonstrating the helical spin texture characteristic of the topological Dirac surface state. Adapted from [20], with permission from the publisher.

From this studies it has been observed that following the pump excitation from the occupied states into the unoocupied states, charge carriers thermalizes at the bottom of conduction band and the slow bulk to surface diffusion leads to 500 fs delayed transient poupulation of Topological surface states. This studies also confirms that the conduction electrons decays faster (within first few picosecond) while topological surface states electrons stays longer tens of picoseconds. Figure 4.6b presents a schematic of the mechanism-first when the pump pulse arrives it populates the conduction band and then the electrons goes through scattering process such as interband (refers to the process in which charge carriers, such as electrons or holes, transition between different energy bands within a material — for example, from the valence band to the conduction band or between subbands in complex band structures) or intraband (refers to the process by which charge carriers are scattered within the same energy band — typically within the conduction or valence band — without changing bands) and these electrons relaxes back through the topological surface states i.e. the CB electrons acts as a source of electrons therefore TSS lasts for longer duration. As shown in Fig. 4.7, tracking the time-dependent electronic distribution allows the extraction of transient electronic temperatures and chemical potentials, which further demonstrate that the relaxation pathways for CB band and surface states follows distinct pathways. The decay

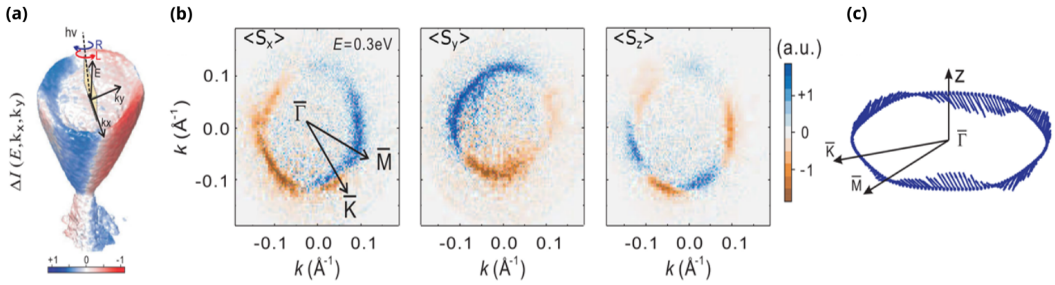


FIGURE 4.5 : Circular Dichroism ARPES of Bi_2Se_3. (a) Three-dimensional circular-dichroism ARPES map as a function of energy E and momenta k_x and k_y, obtained from the difference between photoemission intensities measured with right- and left-circularly polarized light. (b) Calculated spin-polarization components extracted from the circular-dichroism data, demonstrating that all three components of the spin-polarization vector can be reconstructed through modeling of the photoemission matrix elements. (c) Overview of the reconstructed spin-polarization texture, including an out-of-plane component associated with hexagonal warping. Adapted from [29], with permission from the publisher.

of the electronic temperature was attributed to energy transfer from electrons to phonons, often described within a two-temperature framework, whereas the relaxation of the chemical potential was linked to the redistribution and diffusion of excess charge carriers in the conduction band [31].Further studies by [35] uncovered unconventional aspects of electron–phonon scattering in topological insulators. In particular, the decay rate of conduction-band populations in Bi_2Se_3 was found to decrease with increasing temperature, a behavior opposite to that expected for conventional metals and semiconductors. Detailed analysis based on collision integrals showed that this counterintuitive trend arises directly from the temperature dependence of electron–phonon scattering phase space, underscoring the unusual nature of carrier relaxation dynamics in topological surface and bulk states.

However, although it is widely accepted that bulk bands act as charge reservoirs for the TSS [32, 36–38], it is still unclear how their specific electronic dispersion may impact ultrafast electron relaxation dynamics. In this context, Chen $et\ al.$ [39] have shown how ultrafast scattering processes in p-doped Bi_2Te_3 depend closely on the pump photon energy, *i.e.* on the specific unoccupied states that are populated by photoexcited electrons. In particular, they reported that photoexcitation with 330 meV photon energy results in slow carrier dynamics dominated by interband (intervalley) scattering since the relaxation involves intervalley scattering from Γ to the Q valley (Fig. 4.8a, followed by interband transitions from the conduction band into the surface states whereas the photo excitation with below band bandgap excitation (135 meV) results much carrier dynamics. In this case, relaxation proceeds mainly through intraband scattering within the TSS as shown in Fig. 4.8b, and because the available scattering channels are significantly reduced, the resulting relaxation time is much shorter.

By combining time-resolved ARPES with spin resolution, it becomes possible to directly map the spin texture of unoccupied electronic states in topological insulators[40–43]. Using this approach, Jozwiak et al.[42] demonstrated in 2016 that the unoccupied electronic structure of Bi_2Se_3

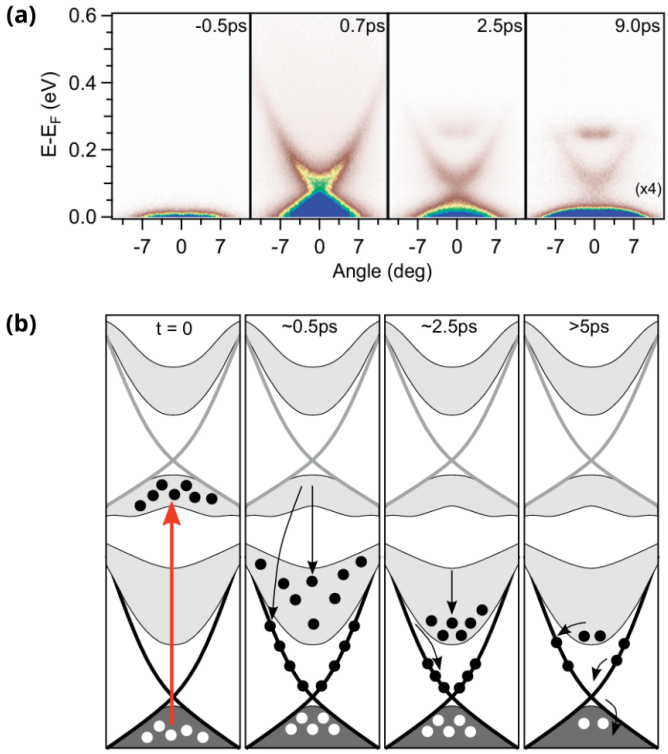


FIGURE 4.6 : Ultrafast population and relaxation dynamics of unoccupied states in the topological insulator. (a) TR-ARPES map of the unoccupied electronic structure of Bi_2Se_3 measured using a 6 eV probe and a 1.5 eV pump. Photoexcitation promotes electrons into the bulk conduction band (CB) and topological surface states (TSS). Subsequent relaxation leads to the accumulation of hot carriers near the minimum of the bulk CB. (b) Schematic of the electron dynamics in a topological insulator following optical excitation. The pump pulse excites electrons directly into the bulk conduction band (CB). Within less than 500 fs, the excited carriers relax toward the minimum of the bulk CB, from where electrons diffuse into the surface states, leading to a continuous filling of the topological surface states (TSS). Adapted from [34], with permission from the publisher.

hosts a spin-polarized surface resonance state. This unoccupied surface resonance shares a similar spin–orbital texture with the topological surface state, but exhibits opposite spin–momentum locking, as illustrated in Fig. 4.9.

Although TR-ARPES provides direct access to unoccupied and transient electronic states at positive pump–probe delays, measurements at negative delays are commonly assumed to reflect a system in thermal equilibrium and therefore to exhibit no intrinsic dynamics. This assumption can break down in materials with intrinsic surface band bending. In such systems, optical excitation redistributes charge carriers by promoting electrons into unoccupied states, thereby modifying the near-surface electrostatic potential. The resulting change in band bending gives rise to a surface photovoltage (SPV), which can persist on long timescales and consequently influence the electronic structure even at negative pump–probe delays. In TR-ARPES measurements, the SPV manifests as a rigid shift of the electronic band structure in binding energy, with the direction of the shift determined by the orientation of the light-induced surface electric field. To clarify this behavior, it is useful to first recall the surface band bending in topological insulators. Figure 4.10a shows an

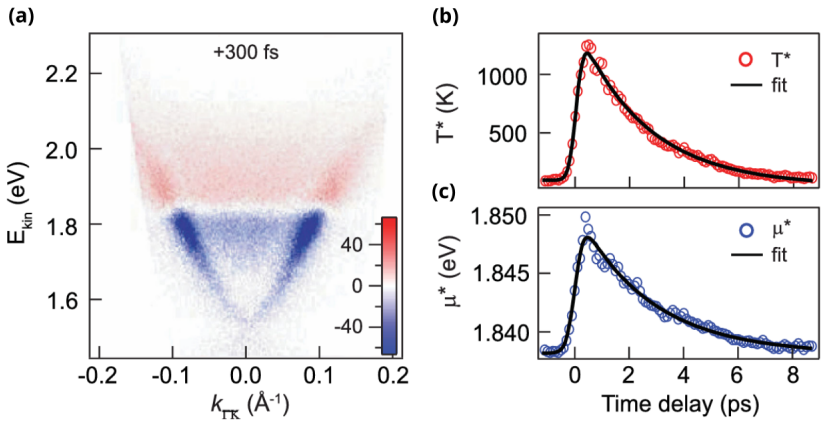


FIGURE 4.7 : Ultrafast evolution of electronic temperature and chemical potential in the TSS of Bi_2Se_3. (a) Differential pump–probe TR-ARPES spectrum obtained by subtracting the signal recorded at -500 fs from that at $+300$ fs following near-infrared optical excitation. (b,c) Time-dependent evolution of the effective electronic temperature T^* and chemical potential μ^* respectively, extracted from fits to EDCs at the Fermi momentum k_F. In both cases, the temporal behavior is well described by a single-exponential decay, yielding characteristic relaxation times of approximately 2.5 ps for T^* and 2.7 ps for μ^*. Adapted from [31], with permission from the publisher.

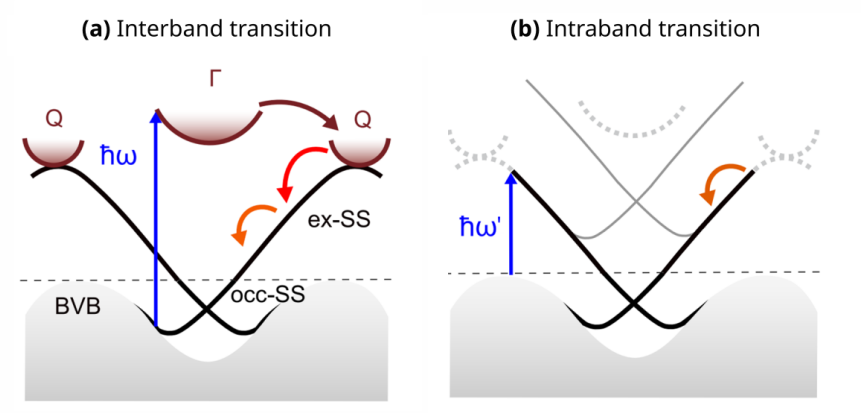


FIGURE 4.8 : Illustrations of a. interband, and b.intraband relaxation in Topological insulator under above and below bandgap excitation. Adapted from Ref.[39], with permission from the publisher.

ARPES spectrum of an n-type Bi_2Se_3, crystal, where the bulk valence band is fully occupied while the bulk conduction band is partially occupied, as schematically depicted in Fig. 4.10b. Upon p-type (Ca) doping, the corresponding ARPES spectrum and schematic band diagram are shown in Figs. 4.10c and 4.10d, respectively, where the Fermi level moves closer to the valence-band edge. Notably, measurements performed on the same p-doped sample at a later time reveal a downward shift of the entire spectrum, as shown in Fig. 4.10e. This shift is attributed to the development of surface band bending, as schematically depicted in Fig. 4.10f. Building on this picture, we consider a p-doped Bi_2Se_3 system with pre-existing band bending, as shown in Fig. 4.11. Ciocys et al. [44] demonstrated that optical excitation in such a system induces an upward shift of the electronic bands that persists for longer than 10 ns. In addition, their study revealed a chemical shift extending to negative pump–probe delays on timescales of approximately 300 ps. This long-lived shift

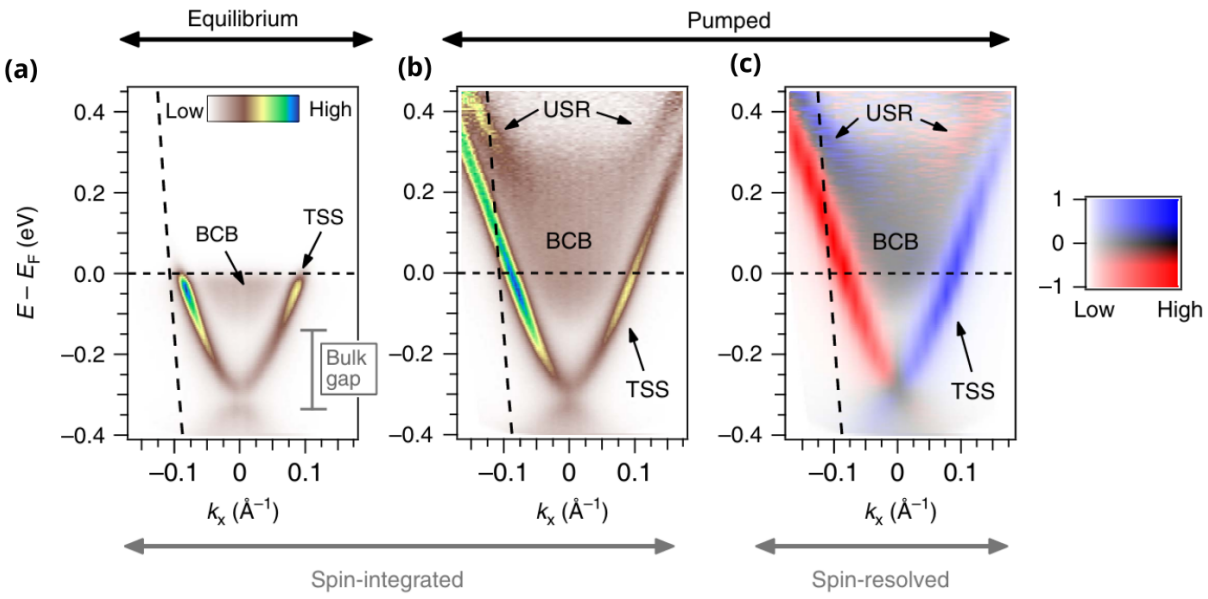


FIGURE 4.9 : Time-, spin- and angle-resolved photoemsission spectra of Bi_2Se_3. (a) Spin-integrated equilibrium spectrum measured along the Γ–K direction, revealing the bulk conduction band (BCB) and the topological surface states (TSS). (b) Spin-integrated spectrum acquired at a pump–probe delay of 0.7 ps, showing the BCB and TSS together with an unoccupied surface resonance (USR) state populated above the Fermi level. (c) Spin-resolved photoemission map corresponding to the same conditions as in (b), demonstrating that the USR state is spin-polarized but with a opposite to that of the TSS. Adapted from [42] under CC-BY 4.0 license.

was attributed to the interaction between photoelectrons and the SPV-driven electric field at the sample surface. There are many reports surface photovolatge effect can be found in literarure for examples [45], [46], [36], [47], [37], [48, 49], [10]

TR-ARPES has played a central role in experimentally revealing light-driven control and modifications of the electronic structure in topological insulators. In particular, it enabled the first experimental observation of Floquet–Bloch states (Floquet states are the time-domain analogues of Bloch states, emerging from the periodic driving of a quantum system) in the topological insulator Bi_2Se_3 [50, 51], demonstrating that an intense periodic drive can dress the Dirac surface states and generate replica sidebands of the original bands. A recent study by Mori et al. [52] reported the observation of a long-lived topological exciton in three-dimensional topological insulators. TR-ARPES measurements were performed on p-doped Bi_2Te_3 at 20 K using a $\sim$6 eV s-polarized probe and a $\sim$1.5 eV p-polarized pump. The TR-ARPES maps reveal the formation of an intensity buildup at the momentum where the topological surface state (TSS) approaches the bulk conduction band (CB), with a lifetime exceeding 40 ps, as shown in Fig. 4.12a. Disentangling whether this intensity buildup originates from the TSS or the bulk CB is intrinsically challenging due to the close proximity of the CB minimum. To address this, Mori et al. [52] overlaid density functional theory (DFT) calculations of the CB minimum onto the experimental data, represented by the black dashed line in Fig. 4.12a, showing that the calculated CB minimum lies just above the observed intensity buildup. In addition, a pronounced renormalization of the TSS dispersion is observed (Fig. 4.12b), which is attributed theoretically to the exciton binding energy . Further support for the surface-state ori-

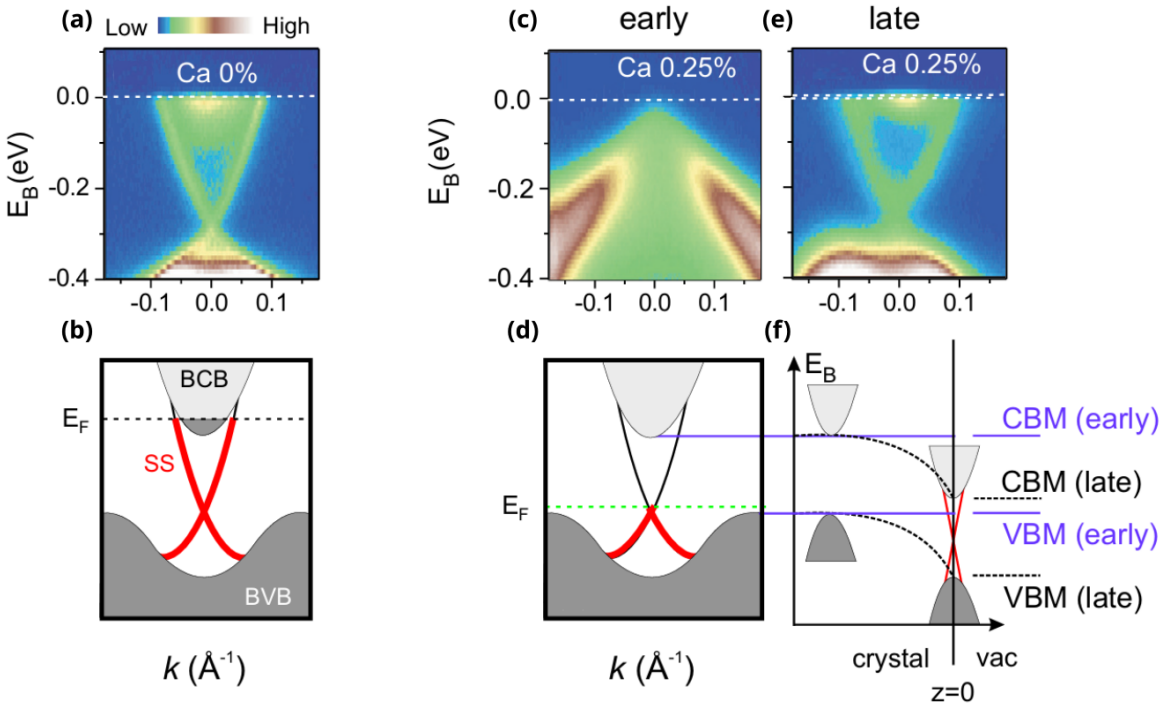


FIGURE 4.10 : Surface band bending in Bi_2Se_3. (a) ARPES spectrum of n-type Bi_2Se_3. (b) Schematic band diagram corresponding to the n-type case. (c) ARPES spectrum of p-type (Ca-doped) Bi_2Se_3 at earlier measurement time. (d) Corresponding schematic band diagram for the p-doped case. (e) ARPES spectrum acquired from the same p-doped sample at a later time, revealing a rigid downward shift of the electronic structure. (f) Schematic of the band bending effect near the surface. Adapted from [20], with permission from the publisher.

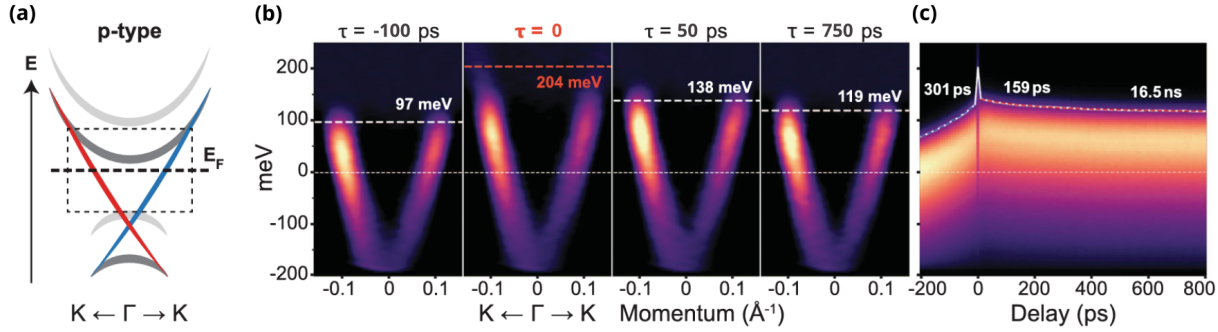


FIGURE 4.11 : Surface Photovoltage (SPV) effect on p-doped Bi_2Se_3. (a) schematic representation of p-doped Bi_2Se_3 wehre the bulk electronic bands in gray and topological surface states in red and blue, the Fermi level resides inside the bulk band gap. (b) TR-ARPES measurements acquired at various pump–probe delays (-100,0,50 and 750 ps) reveal a shift of the chemical potential induced by optical excitation. (c) Temporal evolution of the momentum-integrated intensity along the K-Γ-K direction. Adapted from [44] under CC-BY 4.0 license.

gin of the intensity buildup comes from spin-resolved TR-ARPES measurements, which reveal a spin-polarized electronic state consistent with the spin texture of the TSS as schematically shown Fig. 4.12c. Temperature-dependent measurements show that the intensity buildup forms only at low temperatures, while it is absent at higher temperatures; this behavior is consistent with ther-

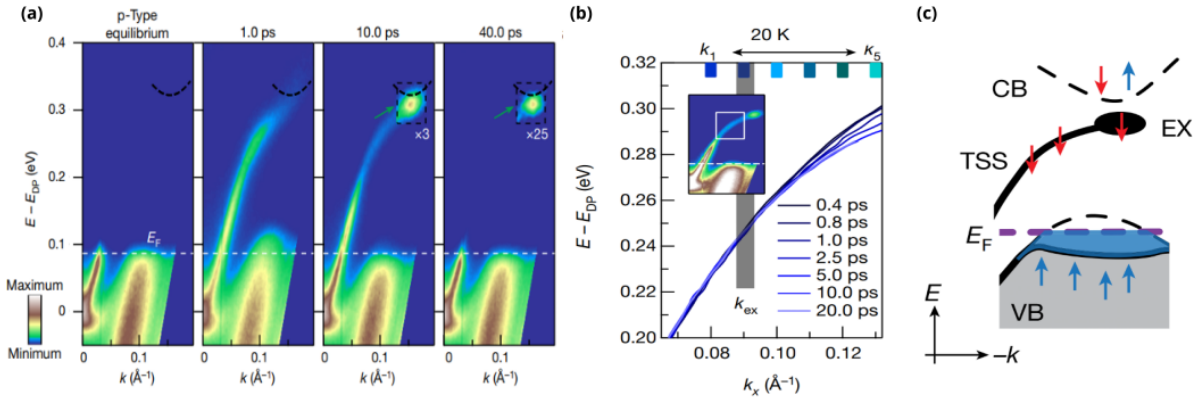


FIGURE 4.12 : Evidence of first spatially indirect topological exciton in p doped Bi_2Te_3. (a) TR-ARPES spectra of p-doped Bi_2Te_3 using 6 eV probe and 1.5 eV pump along the Γ–M direction before pumping, and at delays of 1 ps, 10 ps, and 40 ps after pumping. The curved black dashed lines indicate the conduction band (CB) from density functional theory (DFT) calculations. The green arrow marks the region of intensity buildup. (b) Time evolution of the dispersion of the TSS near the bulk-TSS connection (the white squared area in the inset) at 20K. The grey shaded line marks the estimated minimum momentum (k_ex) in which the TSS is renormalized. (c) The schematics of experimental observation using spin resolved TR-ARPES, pointing to the spin-polarization and formation of the excitonic state in the intensity buildup and the TSS. Adapted from Ref.[52], with permission from the publisher.

mal energies exceeding the exciton binding energy at higher temperatures. Moreover, analysis of energy distribution curves (EDCs) at different pump–probe delays demonstrates that, following exciton formation, the EDC peak shifts below the CB minimum by approximately 14 meV, corresponding to the exciton binding energy. At higher temperatures (180 K), no such shift is observed, and the peak position remains characteristic of the bulk CB. Taken together, these observations provide first evidence for the formation of a spatially indirect topological exciton arising from the attractive interaction between an electron localized in the TSS and a hole in the bulk valence band.

Following their above work, Mori et al. reported a subsequent study [53] interpreting these observations as evidence for a possible transient excitonic condensation. The interpretation is based on pronounced band flattening and back-bending of the transient topological surface states, as shown in Fig. 4.14. In addition, the bulk valence band is reported to acquire a Mexican-hat–like Bogoliubov dispersion with a gap-like feature in the valence band, which is widely regarded as a hallmark of excitonic condensation, together with the opening of an energy gap at the Fermi level (Fig. 4.14).

Overall, while these observations are consistent with a scenario involving the formation of a long-lived excitonic state associated with the TSS, it is still difficult to disentangle the bulk nature of the intensity buildup. To resolve this ambiguity, we perform additional measurements to unambiguously identify the nature of the intensity buildup. The results presented in this chapter directly challenge the exciton-formation interpretation.

In this chapter we present a temperature dependent TR-ARPES study of p-doped Bi_2Te_3 and, with the support of kinetic Monte Carlo (KMC) simulations, we offer first evidence of how a minor

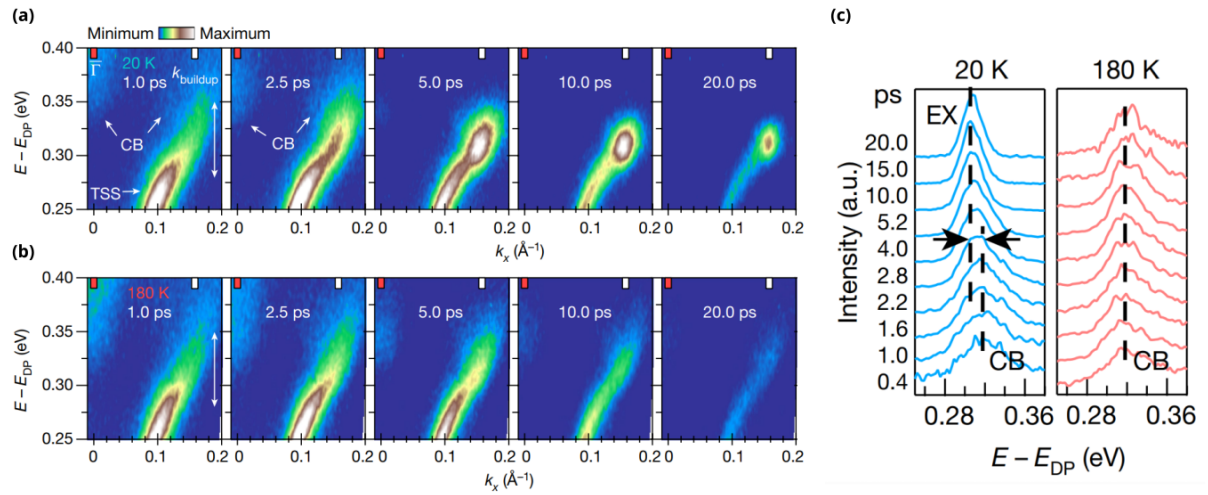


FIGURE 4.13 : Comparison of TR-ARPES map at 20K and 180K. (a,b) Time evolution of the band structure near the bulk–TSS junction at delays $t = 1.0,\ 2.5,\ 5.0,\ 10.0,\ 20.0,$ and 40.0 ps (left to right) at 20 K (a) and 180 k (b) respectively ; red and white bars at the top mark the $\bar{\Gamma}$ momentum and the intensity–build-up location k_{buildup}, respectively. (c) EDCs at ten representative delay times at 20K and 180K, obtained by integration over the momentum range around $k_{buildup}$ (the white bars on the top of (a) and (b). From bottom to top, each EDC corresponds to each labelled delay time. The dashed lines indicate the estimated peak positions. The difference of the two peaks in a corresponds to the exciton binding energy. Adapted from Ref.[52], with permission from the publisher.

renormalization of the bulk dispersion has a substantial impact on the ultrafast electron dynamics. Indeed, as the sample temperature increases, the interplay between thermal expansion and electron-phonon coupling results in a renormalization of the conduction band (CB) [54], opening a new pathway for efficient intervalley scattering towards the center of the Brillouin zone (Γ). Our experimental evidence is reminiscent of what is found in semiconducting transition metal dichalcogenides, where the charge dynamics are dominated by intra- and inter-valley scattering processes, and the relative energy position of the different valleys influences population lifetime [55–57]. Although a temperature-induced reduction of the energy gap at Γ has already been reported [53, 58], our results underscore the crucial, and fairly unexplored, combined role of temperature and the bulk band structure in feeding carriers to the technologically relevant TSS. Furthermore, as the temperature increases, the reduction of the bulk gap, *i.e.* at the Γ point, comes hand-in-hand with an enhancement of the inter-valley electron–phonon coupling. Since thermoelectric figure of merit strongly depends on Intervalley scattering [59, 60] therefore our reported temperature dependence of the bulk gap (and its impact on charge accumulation) may be key to the understanding of the remarkable thermoelectric performance of Bi_2Te_3 [54, 61–64] and potentially allows band engineering for improved thermoelectric performance.

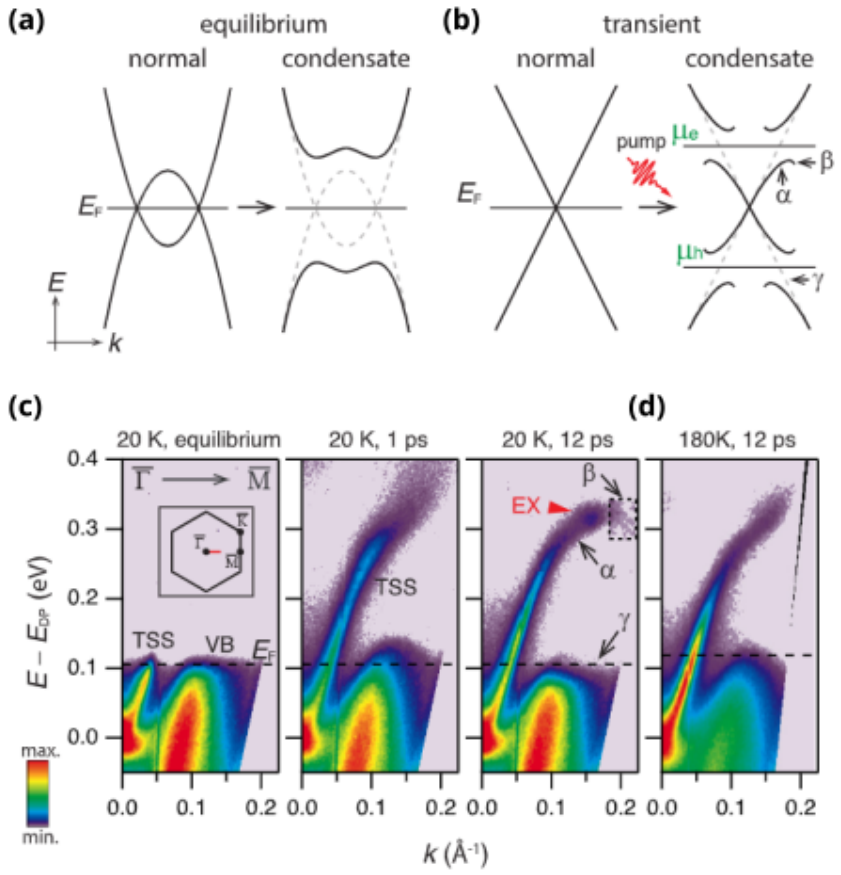


FIGURE 4.14 : Possible excitonic condensation in the topological insulator Bi_2Te_3. (a,b) Schematics illustrating excitonic BCS-like condensation in the equilibrium ground state (a) and in a transient nonequilibrium state (b). In the transient regime, excitonic gaps open at quasi-equilibrium chemical potentials, μ_e for electrons and μ_h for holes. (c) TR-ARPES maps of p-doped Bi_2Te_3 at 20 K, measured at equilibrium, 1 ps, and 12 ps pump–probe delays using ∼6eV probe 1.5 eV pump. At 12 ps, the label EX marks the excitonic electron within the topological surface state (TSS). The feature labeled α corresponds to a renormalization of the topological surface state (TSS), β denotes a back-bending of the TSS near the chemical potential, and γ indicates a downward shift of the valence-band spectral weight accompanied by its renormalization. Adapted from Ref.[53] under CC-BY 4.0 license.

4.2 Results

4.2.1 Time-resolved ARPES mapping of the unoccupied states of p-doped Bi_2Te_3

Figure 4.15 displays TR-ARPES maps acquired at 30 K using 6 eV probe and 300 meV pump pulses at ALLS Laboratory along the Γ-M direction, for different pump-probe delays (additional data at different temperatures are provided in Fig. 4.18). In agreement with Ref. [39], the 300 meV pump excitation enables direct promotion of electrons from the valence band (VB) into the CB of Bi_2Te_3. In particular, we report a direct optical transition into the surface resonance state (SRS) [65–67], slightly off the Γ point.

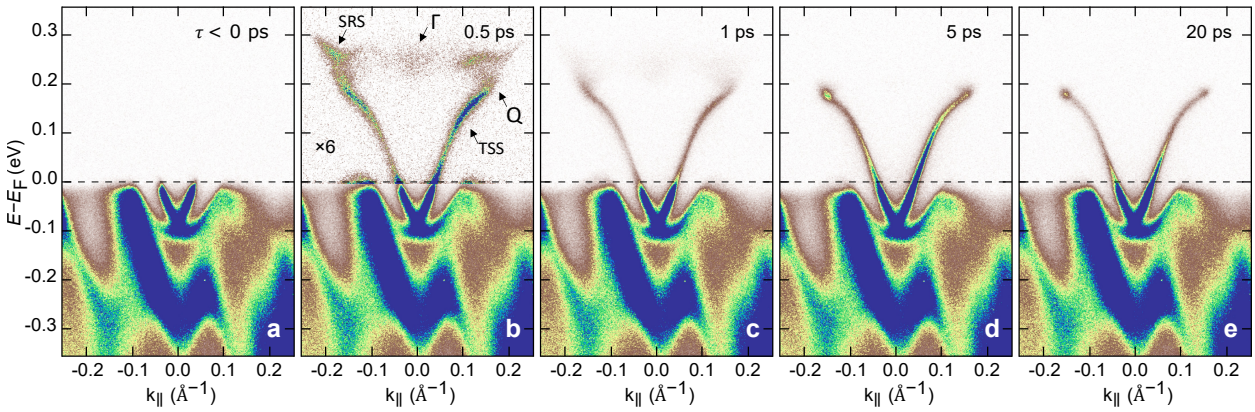


FIGURE 4.15 : Long-lasting intensity buildup in the unoccupied states of p-doped Bi_2Te_3. Spectra acquired (6 eV probe / 300 meV pump) at a temperature of 30 K, along the Γ–M direction, for different pump-probe delays : (a) $\tau < 0$ ps, (b) 0.5 ps, (c) 1 ps, (d) 5 ps and (e) 20 ps. See Supplementary Materials for details of the experimental geometry.

By simple visual inspection of the ARPES map at 0.5 ps pump-probe delay (Fig. 4.15b), it is clear that the pump pulse populates a continuum of states connecting the CB absolute minimum at ± 0.15 Å^{-1}(Q-valleys) and the CB local minimum at the Γ point (Γ-valley). While the CB signal at Γ decays within a few ps, an intensity buildup forms and persists for tens of ps at the bottom of the Q-valleys, where the TSS merges with the CB. This intensity buildup has been previously reported and attributed to the first evidence of a spatially indirect topological exciton as discussed in the introduction section which forms by binding surface electrons (sitting on the TSS) with bulk holes (at the VB maximum) [52].

We verified that this intensity buildup is also observed with 6.2 eV-probe / 1.55 eV-pump photon energies (Fig. 4.16), also with 6 eV-probe and 600 meV-pump (Fig. 4.17). The position in energy of the long-lasting intensity buildup, with respect to the Dirac point, observed in the present work is different from the one reported in Ref.[52]. As a consequence, also the two branches of the Dirac cone are characterized by a different dispersion. To better elucidate the origin of this energy shift, We compare the results of two independent TR-ARPES experiments performed on p-doped Bi_2Te_3 samples from the same batch, but using different detectors (namely, SPECS ASTRAIOS 190 and Scienta DA30L), probe and pump photon energies, and base temperatures. Complementary experiments have been performed at the Quantum Matter Institute at the UBC-Moore Centre for Ultrafast Quantum Matter, using a Scienta DA30L electron analyzer to measure electrons emitted by 6.2 eV photons upon excitation with 1.55 eV-pump (T=10 K). As shown in Fig. 4.16a, the intensity buildup appears consistently at 272 ± 5 meV, as highlighted by the EDCs in Fig. 4.16b. We note that this value corresponds to an energy shift of more than ~ 30 meV with respect to the value reported in Ref. [52], where the same spectroscopic feature is more than 0.30 eV (at 20 ps) above the Dirac point. The consistency between the TR-ARPES experiments in Fig. 4.16 cross-validates the energy-to-pixel calibration of the two different detectors and strongly suggests that the discrepancy with the data in Ref.[52] originates from a calibration error. Furthermore, Fig. 4.17 shows ARPES maps at early (1.5 ps) and late (55 ps) pump–probe delays for a 600 meV excitation. EDC-

derived dispersions of CB (red lines) reveal that the long-lived intensity buildup coincides with the energy–momentum position of the conduction band at early times.

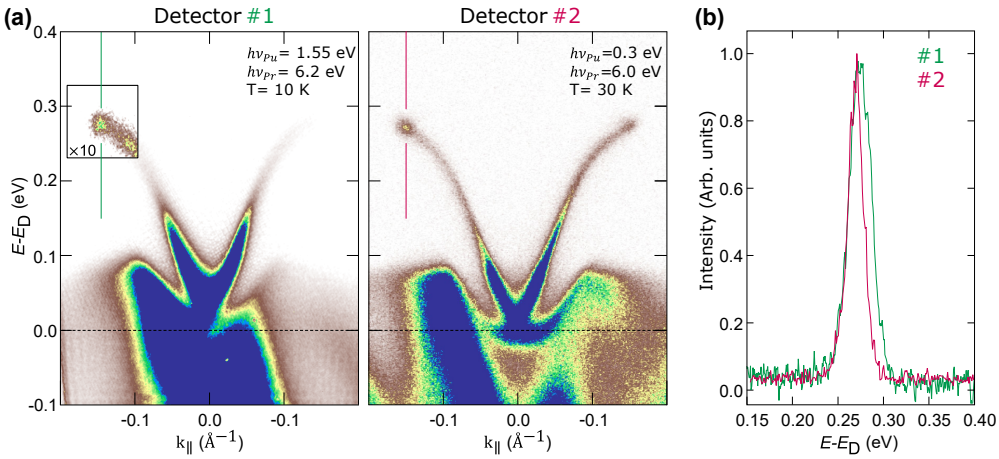


FIGURE 4.16 : Energy position of the intensity buildup. (a) TR-ARPES spectra at 20$\pm$2 ps acquired on Bi_2Te_3 samples using different experimental apparatus. Despite the difference in both pump-probe energies and electron detectors (Scienta DA30L on the left, and SPECS ASTRAIOS 190 on the right), the energy position of the intensity build up is comparable (within 10 meV), as indicated by the EDCs plotted on panel (b).

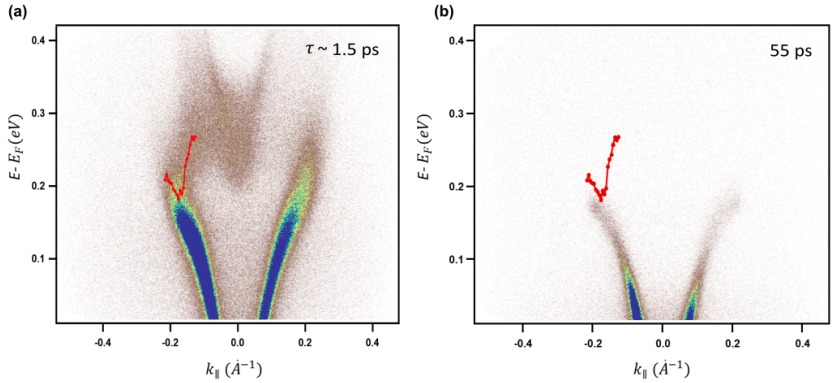


FIGURE 4.17 : Time- and angle-resolved photoemission spectrum of p-doped Bi_2Te_3 along the $\Gamma - M$ direction measured at ALLS laboratory for pump-probe delays of 1.5 ps (a) and 55 ps (b). The red dotted line is the extracted dispersion (by using EDC analysis) of the broad CB dispersion at 1.5 ps.

We have also verified that the intensity buildup fades with increasing temperature, as presented in the next section (Fig. 4.18), as would also be expected in an exciton formation scenario [52]. However, as detailed below, we show that the observed temperature dependence is better consistent with the interpretation of these spectral features as bulk band states, and it can be directly linked to the efficiency of the intervalley scattering between bulk state valleys. We also note that when the TSS is in close proximity to the bulk states, it could possibly inherit their orbital character [52]. In fact, (i) the intensity buildup displays a trigonal pattern reminiscent of the bulk states (k_x-k_y isoenergy contour maps in Fig. 4.25), and (ii) the linear dichroism maps (inspired by Ref. [68–70], see Fig. 4.25) hint at different orbital characters between the intensity buildup and the surrounding TSS. Based on the discussion above, and although our conclusions do not depend on the existence of

the spatially indirect exciton, we adopt the simplest possible model. We then refer to the intensity buildup as a direct signature of the carrier accumulation at the bottom of the Q-valley, and we establish its population density as a measure of the strength of the $\Gamma \leftrightarrow$ Q intervalley electron-phonon scattering channel.

4.2.2 Temperature dependence of bulk band dispersion and ultrafast electron dynamics

We now move on exploring the role of the temperature as tuning knob for the intervalley scattering in the CB. To do so, first, we present Fig. 4.18 which shows TR-ARPES results at all the temperatures investigated in this work (30 K, 70 K, 120 K, and 180 K, top to bottom) at four pump-probe delays (0.5 ps, 1 ps, 5 ps and 20 ps). The sample displayed minimal n-doping ($\sim$10 meV) as the temperature increased (as well already discussed elsewhere [37]). To facilitate the discussion of our experimental results, the energy axis of the TR-ARPES data is referenced with respect to the Dirac point position, E_D, as in [52, 53].

Figure 4.19a presents EDCs at different pump–probe delays for the lowest (30 K) and highest (180 K) temperatures, extracted from the temperature-dependent dataset shown in Fig. 4.18. At low temperature, the EDC initially exhibits two distinct peaks corresponding to the bulk conduction band CB and the TSS. With increasing pump–probe delay, the CB peak gradually shifts toward the TSS peak, as indicated by the dashed line in Fig. 4.19a serving as a guide to the eye, and after approximately 5 ps the two peaks converge at the same energy. A similar behavior is observed at high temperature, with the primary difference being thermal broadening. Importantly, no shift of the EDC peak position is observed, in contrast to previous interpretations that associated such a shift with exciton formation [52]. The corresponding TSS dispersions, extracted using momentum distribution curve (MDC) analysis in the vicinity of the intensity buildup, are shown in Fig. 4.19b for two representative delays (1 ps and 10 ps) at both 30 K and 180 K. The extracted dispersions are essentially identical across temperatures. A minor deviation observed between two different time delays at low temperature very close to the intensity buildup likely reflects limitations of the MDC analysis when two spectral components coexist and partially overlap. If a bound excitonic state were formed, a clear temperature-dependent modification of the dispersion would be expected. The absence of such a systematic change therefore supports the conclusion that the observed intensity buildup originates from charge accumulation at the bulk CB minimum rather than from exciton formation

From the temperature dependent dataset we further extract Fig. 4.20a which displays ARPES maps integrated over the first 5 ps pump–probe delay at different temperatures.By focusing on the Γ point, we report an upward (downward) shift in the energy of the VB (CB) maximum (minimum), thus highlighting a temperature-induced band structure renormalization. This shift is confirmed by inspecting the energy distribution curves (EDCs) at Γ at different temperatures (Fig. 4.20b), and

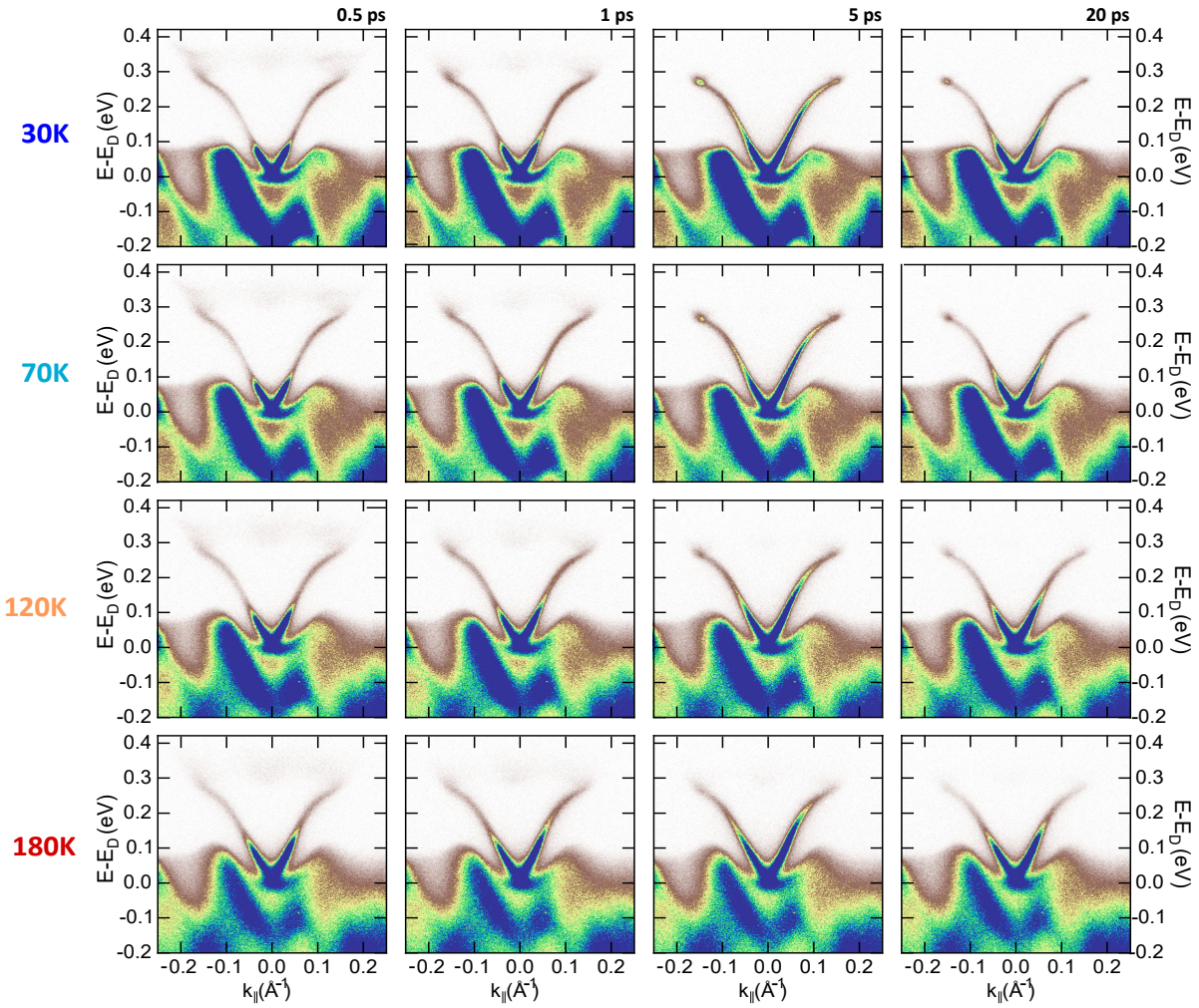


FIGURE 4.18 : Temperature dependent TR-ARPES. TR-ARPES spectra from 30 K to 180 K (from top to bottom) along the ΓM direction, for different pump probe delays (from 0.5 ps, on the left, to 20 ps, on the right).

the temperature evolution of the bulk gap at Γ (Fig. 4.20d). As the temperature increases from 30 K to 180 K, the band gap at Γ reduces by ∼62 meV, in good agreement with the *ab-initio* theoretical estimate of Ref. [54] for bulk Bi_2Te_3, where both thermal expansion and electron-phonon coupling contributions have been accounted for (see red dashed line in Fig. 4.20d). In contrast, the peak position of the EDCs at the Q-valley, where the TSS is affected by trigonal-warping and merges into the CB [2], remains essentially unchanged across all temperatures (∼3 meV shift), as shown in Fig. 4.20b and Fig. 4.21a.

It is now instructive to track how the electronic population evolves at Γ and Q as a function of temperature. To do so, in Fig. 4.20c we show the transient evolution of the momentum distribution curves for four temperatures, in an energy range that includes the entire CB population (vertical line on the left of panel a). At low temperature, the Γ-valley spectral weight vanishes within a few ps and the Q-valley dominates the dynamics. As the temperature increases, a long-lasting slowly-decaying signal appears at the Γ-valley and the spectral weight at the Q-valleys is reduced, in good agreement with what is observed in the EDCs of Fig. 4.20b (see also Fig. 4.21d).

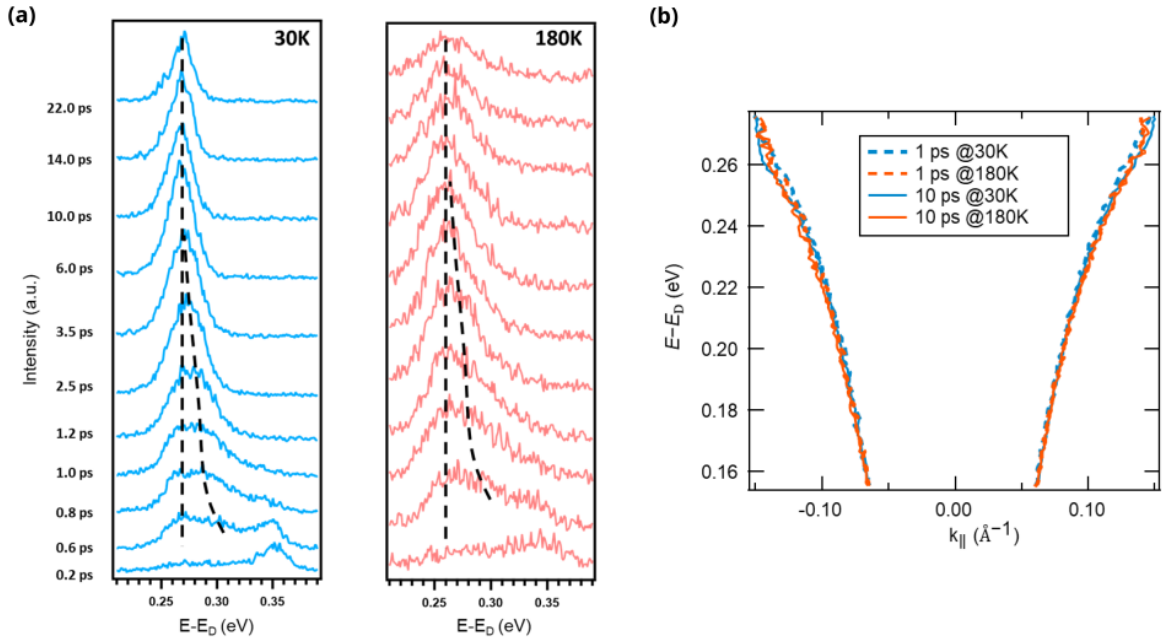


FIGURE 4.19 : (a) EDCs plotted at the intensity buildup momentum location at various pump probe delay from top to bottom corresponds to each labelled delay time both at 30K and 180K. The dashed lines shows the estimated peak positions. (b) Band dispersion extracted from 30K and 180K TR-ARPES at two different pump probe delay at 1ps and at 10ps

Figure 4.20c points towards a temperature-dependent coupling between the Γ- and Q-valleys, which is favored by changes in the CB dispersion. To be more quantitative, and identify a figure of merit that captures the role of the bulk band renormalization in defining electron dynamics, we compare normalized EDCs at the Q-valley (20 ps) and at the Γ-valley (0-5 ps delay range). In particular, we assess the spectral overlap between the Γ- and Q-valleys EDCs, illustrated by the shadow area in Fig. 4.21a, by evaluating the product of the two normalized EDCs (EDC$_{\Gamma \cap Q}$, colored circles in Fig. 4.21b). The increase in the spectral overlap corresponds to an enhancement of the scattering phase space available for an electron to escape a given valley by intervalley scattering. This is also supported by the fact that ratio of spectral intensities at Γ and Q (I^{Γ}/I^{Q}, colored squares in Fig. 4.21b) follows the same trend in temperature as the spectral overlap EDC$_{\Gamma \cap Q}$, thus indicating a transfer of spectral weight from the Q- to the Γ-valley mediated by intervalley electron-phonon scattering.

4.2.3 Temperature-induced changes of the scattering phase space

To better interpret our experimental evidence and the interplay between the Γ- and the Q-valleys, we implemented a toy-model for electron-phonon scattering using a kinetic Monte Carlo (KMC) approach, similar to Ref. [34], but with momentum resolution [71]. We run KMC calculations

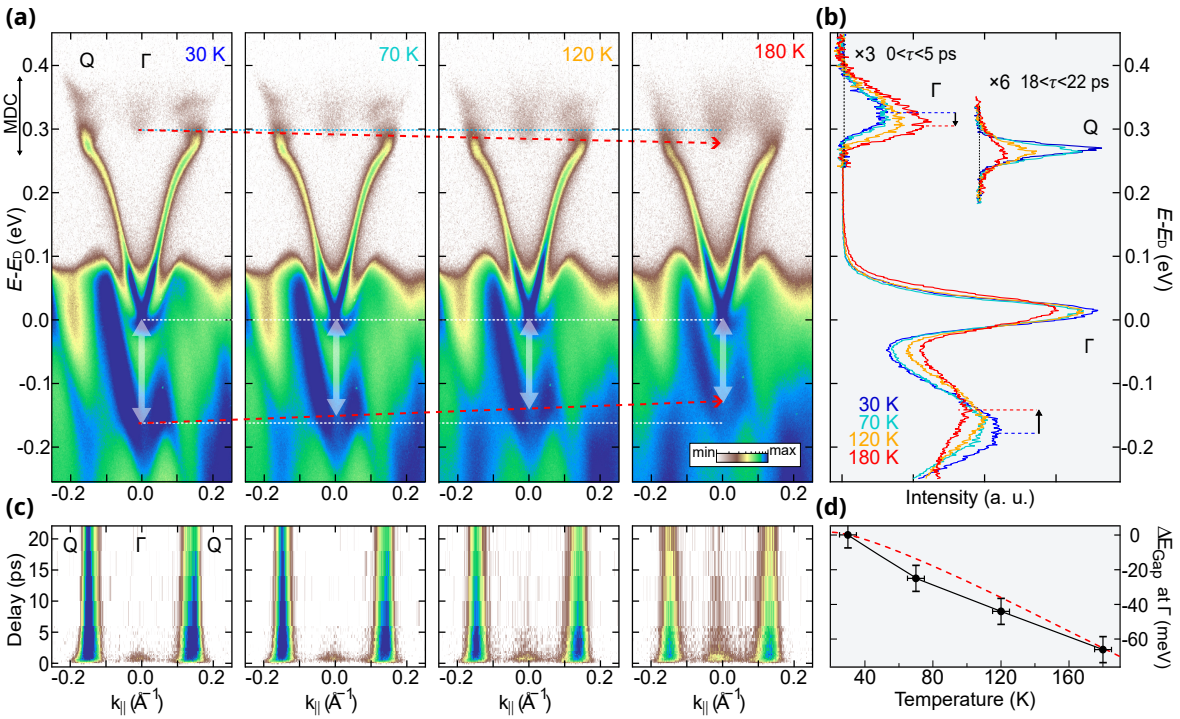


FIGURE 4.20 : Temperature-induced bulk band renormalization. (a) Temperature-dependent TR-ARPES results on p-doped Bi_2Te_3, along the Γ–M direction, and integrated over the first 5 ps. (b) Energy distribution curves at the Γ point ($k_{\parallel} \sim 0 \pm 50$ mÅ^{-1}, up to 5 ps), and at the Q-valley ($k_{\parallel} \sim -150 \pm 25$ mÅ^{-1}, at 20 ps). (c) Momentum distribution curves (MDCs) as a function of pump-probe delay at the corresponding temperatures. The integration window for MDCs is indicated by the double-headed black arrows in panel A. (d) Relative change of the direct bulk band gap at Γ as a function of the temperature. The red dashed line displays ab-initio predictions, digitized from Ref. [54].

for two different electronic band structures, namely at 30 K and 180 K (red and blue curves in Fig. 4.21c), that only differ by a small shift of $\sim$16 meV of the CB minimum at Γ, based on the experimental observation (see Fig. 4.20a). We model the CB using a discrete distribution of equally spaced electronic states, and we tune the mesh density of the KMC model such that the spectral overlap between the KMC occupancies, $\Gamma \cap Q$, approximately follows the temperature dependence of the spectral overlap extracted by TR-ARPES data (circles in Fig. 4.21b). In the KMC calculations, we impose a Gaussian distribution of N electrons centered at 0.4 eV above the Dirac point (to match the experimental condition at $\tau \sim$0.5 ps, see Figs. 4.15-4.20), and then evaluate the electron occupancy as a function of time, $f_i(t)$, by solving the rate equation :

$$\frac{\partial f_i}{\partial t} = \sum_j [W_{j,i} f_j (1 - f_i) - W_{i,j} f_i (1 - f_j)], \tag{4.1}$$

where $W_{i,j}$ is the probability for each electron (k_i, E_i) to have a transition into an unoccupied state (k_j, E_j) by absorption or emission of a phonon, provided by the Fermi's golden rule (see Methods). Black circles in Fig. 4.21c display the electronic distributions obtained via KMC for 30 K and 180 K when a quasi-equilibrium condition is reached (see also Fig. 4.22 for different snapshots

of the KMC toy-model). Fig. 4.21d offers also direct comparison between experimental and KMC time traces at Γ- and Q-valleys (integration boxes shown in Fig. 4.21c).

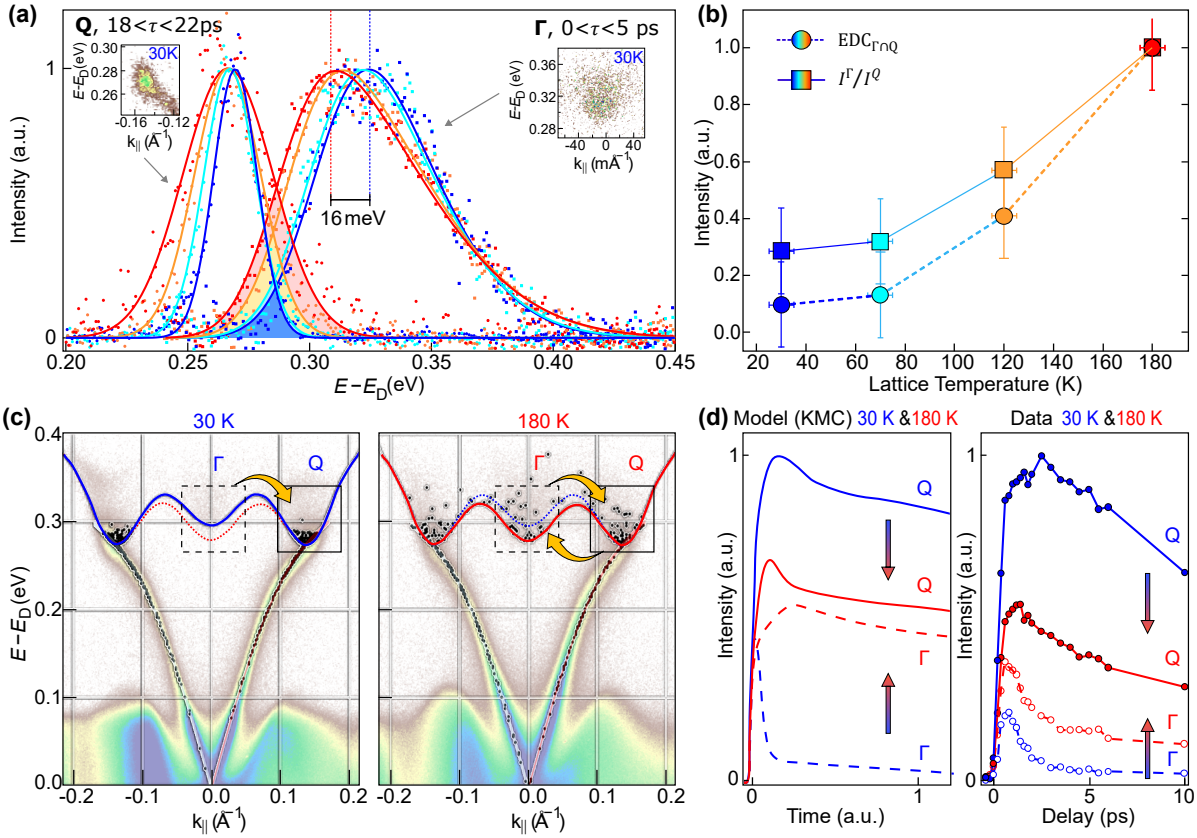


FIGURE 4.21 : Intervalley scattering behinds the emergence of the intensity buildup. (a) Normalized Energy Distribution curves at different temperatures with superimposed an asymmetric gaussian fit for the Γ (0$< \tau <$ 5ps) and Q valleys (18 ps$< \tau <$22 ps). The spectral overlap is indicated as shadow areas with different colors for each temperature. (b) The spectral overlap between the Γ- and Q-valley, $\mathrm{EDC}_{\Gamma\cap Q} = I^{Q}_{norm} \times I^{\Gamma}_{norm}$ (colored circles), is compared with the ratio of the photoemission intensities for the two valleys (colored squares). (c) Electron occupancy obtained by the electron-phonon scattering toy-model at 30 K and 180 K, for the last delay, superimposed on top of the experimental band structure from Fig. 4.20. (d) Comparison between simulated and experimental electron dynamics at Γ (dashed lines) and Q (solid lines) valleys. The band structure renormalization increases the efficiency of intervalley scattering from Q to Γ.

Overall, this toy-model successfully captures (i) the formation of the characteristic long-standing intensity buildup at the Q-valley at low-temperature (Fig. 4.21c), and (ii) the transfer of spectral weight from the Q- to Γ-valley at high temperature (see Fig. 4.21d), due to the increase of the electron-phonon scattering phase space caused by the thermal renormalization of the electronic band structure.

4.2.4 KMC calculations

In KMC calculations, the bulk CB was reproduced by a uniform grid of states that qualitatively captures the momentum-integrated density of states of a 3D system. Considering the absorption or emission of a phonon, the transition matrix of the system, $W_{i,j}$, was obtained using the Fermi's golden rule :

$$W_{i,j} = \frac{2\pi}{\hbar} g_0^2 \{[n(\omega_{i,j}) + 1]\delta(E_j - E_i + \hbar\omega_{i,j}) + n(\omega_{i,j})\delta(E_j - E_i - \hbar\omega_{i,j})]\}, \tag{4.2}$$

where $n(\omega) = (e^{\frac{\hbar\omega}{k_B T}} - 1)^{-1}$ is the Bose-Einstein distribution, $\omega_{i,j}(q) \propto 1 + \alpha \cdot \cos(\pi q)$ is the phonon dispersion evaluated at the scattering vector $q = k_i - k_j$, and g_0 is the electron-phonon matrix element (assumed constant for simplicity). Starting from a Gaussian distribution of electrons centred at 0.4 eV, we evaluate the electron occupancy as a function of time, $f_i(t)$, by solving the differential Eq. 4.1. Each step in the KMC simulation is weighted on the total transition rate $\Delta t = \frac{-\ln r}{\sum_{i,j} W_{i,j}}$, where $r \in (0, 1]$ is a randomly sampled value.

Given the experimental evidence for intervalley scattering, we use an optical phonon dispersion centred at ~ 4 meV with a bandwidth of ± 3 meV [72]. We also assume a constant electron-phonon matrix element for transitions within the CB and the TSS (same spin-polarized branch), and we set $g_0^{CB \to TSS} = g_0/2$ to account for the spin polarization of the TSS. However, note that the particular choice of the phonon dispersion, *i.e.* optical or acoustic modes, and the strength of the electron-phonon matrix element, do not affect the qualitative results of the simulation as long as the (i) phonon emission dominates over phonon absorption, and (ii) phonon population differs from zero in the region of interest ($0 < q < 0.25\,\text{Å}^{-1}$) [34]. Within our simple KMC calculations, electron relaxation dynamics are purely driven by an increase in the electron-phonon scattering phase space. Additionally, since our pump excitation is in a perturbative regime, we neglect any ultrafast renormalization of the electron-phonon matrix element [73].

4.2.5 Electron-phonon toy-model

Fig. 4.22 displays different snapshots of the electron occupancy calculated using the KMC toy-model discussed in the main text (each black circle represents an electron in the energy-momentum space), and using two slightly different band structures of 30 K and 180 K (top and bottom row, respectively). The electron-phonon matrix element for intervalley transitions within the CB is assumed constant, g_0. Regarding electron scattering from the CB to the TSS, we set the electron-phonon matrix element to $g_0/2$ and, owing to its protection against back-scattering events, the scattering between different branches of the TSS is neglected for simplicity. As the arbitrary time of the simulation evolves, the continuous emission of phonons favors the decay of electrons in lower energy states, down to the minima of the CB where the TSS crosses the CB.

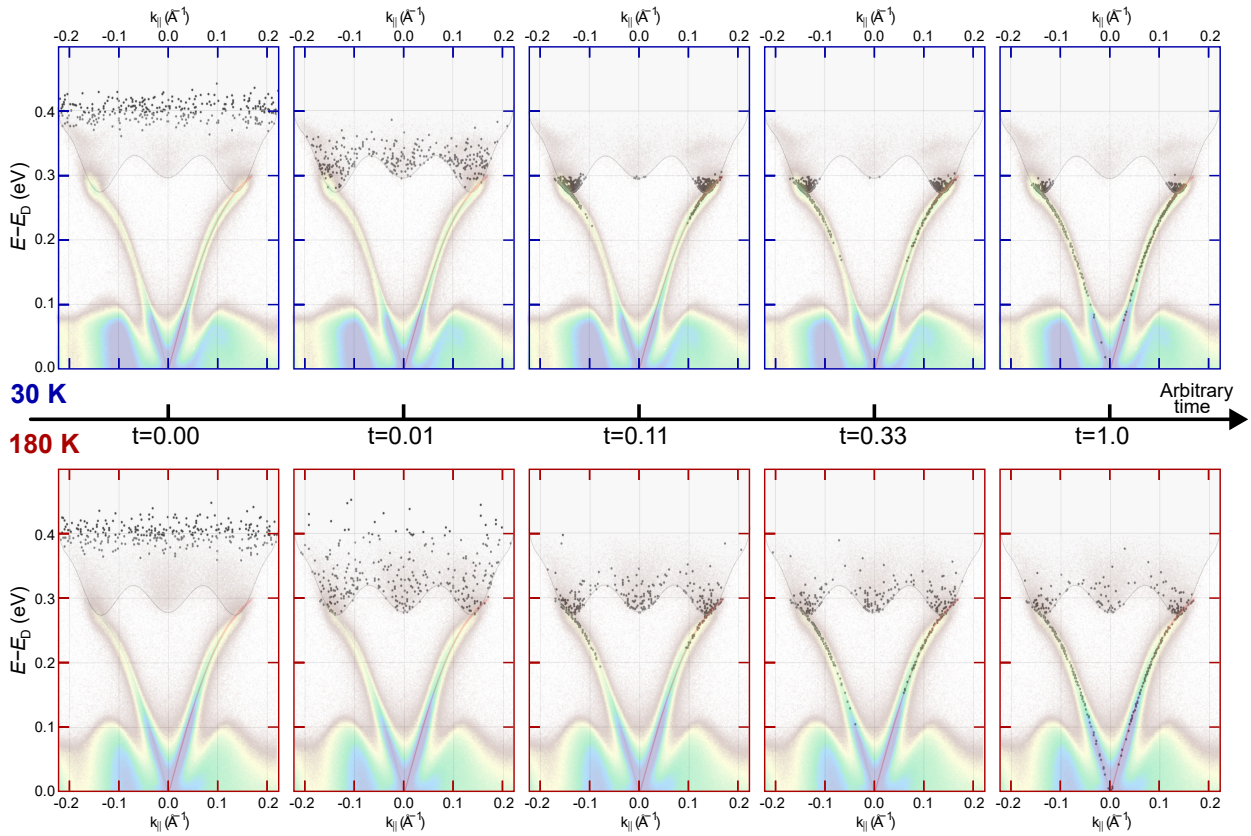


FIGURE 4.22 : Electron-phonon toy-model. Time-resolved electron occupancies calculated by the KMC toy-model at 30 K and 180 K, shown in the top and bottom row, respectively. The time axis is in arbitrary units.

Here, we report a strong bottleneck effect. Indeed, (i) the reduced density of states of TSS compared to that of the CB, and (ii) the lack of TSS at the Γ valley, favour the formation of the characteristic intensity buildup (at high momenta) at low temperatures. However, at high temperature, the higher phonon population due to Bose-Einstein distribution, in combination with the down-shift of the CB minimum at Γ, lead to an enhancement of electron scattering towards the Γ-valley, thus reducing the occupation of the Q-valleys.

4.2.6 Ultrafast charge dynamics in the scattering phase space

To better interpret the observed ultrafast dynamics, Fig. 4.23 shows the same experimental and simulated traces of Fig. 4.21d, but normalized in intensity. At 30 K, due to the minimal thermal phonon population, the Γ valley exhibits a sharp rise followed by a fast decay, while the Q-valley population reaches its maximum only when the Γ valley is empty, thus with a certain delay. This delayed dynamic is well reproduced by the simulations and originates from inefficient $\Gamma \rightarrow$Q intervalley scattering at low temperature, which then develops into slow dynamics at Q. At 180 K, increased phonon absorption combined with band structure renormalization enhances Γ-valley population

by enabling the Q→Γ backscattering channel. Despite its simplicity, the KMC model captures the main experimental trends, supporting its validity at elevated temperatures.

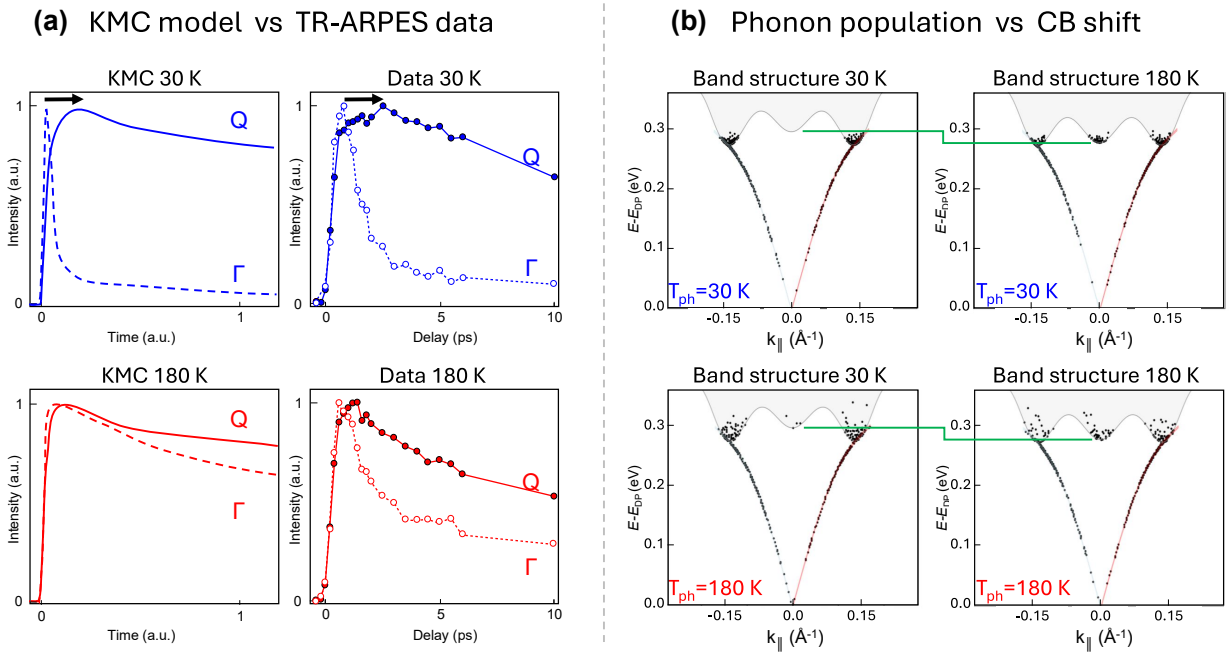


FIGURE 4.23 : Ultrafast charge dynamics in the scattering phase space. Contributions of the phonon population and band renormalization to the ultrafast dynamics. (a) Comparison between KMC simulations and experimental traces at 30 K (blue) and 180 K (red), normalized in intensity to highlight the ultrafast dynamics at Γ (dashed) and Q (solid). (b) Comparison between the calculated occupations for two phonon populations (T_{ph} = 30 K, blue; T_{ph} = 180 K, red) for the two experimentally-retrieved band structures (30 K and 180 K).

To decouple phonon population effects from band gap renormalization at high temperature, the right panel of Fig. 4.23 examines the impact of two thermal phonon distributions (T_{ph} = 30 K and T_{ph} = 180 K) on the carriers dynamics for the conduction band structures extracted experimentally at 30 K and 180 K. For the 30 K band structure, the Γ valley remains unoccupied even for a phonon population of T_{ph} = 180 K. In contrast, for the 180 K band structure (-16 meV shift at Γ), carriers populate the Γ valley already at T_{ph} = 30 K. These results demonstrate that the minor renormalization of the conduction band, which reflects changes in the electron–phonon scattering phase space, controls both the temperature evolution and the ultrafast dynamics of the intensity build-up. This is the reason why the Γ/Q intensity ratio follows the spectral overlap derived from the measured dispersions (Fig. 4.21a,b). We emphasize that, in the simulations, the temperatures and time scales are effective parameters rather than physical quantities. Electron–phonon coupling, electron density, and grid density are phenomenologically tuned; accordingly, the intensity scale and the time axis are in arbitrary units.

4.2.7 Fluence dependence of the energy gap at Γ

In order to demonstrate the crucial role of lattice temperature in determining the bulk gap at $\mathbf{\Gamma}$, Fig. 4.24 compares TR-ARPES spectra acquired at three pump fluences (20, 40, and 80 μJ/cm^2). For each fluence, we use the spectrum at negative delay (left panels) to evaluate the electronic temperature via Fermi–Dirac distribution fit (insets). We report only a minimal average heating effect. Right panels of the ARPES maps display the time-integrated data as in Fig. 2 of the main text (logarithmic color scale), from which we extract the energy-distribution curves at Γ (right panel). The CB and VB band-edge positions at Γ remain unchanged within the explored fluence range, despite the different photoexcited carrier densities (see inset of the right panel). These results indicate that photoexcited carriers alone do not induce the band structure renormalization; rather, the gap at Γ is controlled by lattice temperature, pointing to the key role of thermal expansion and electron–phonon coupling, in agreement with Ref. [54].

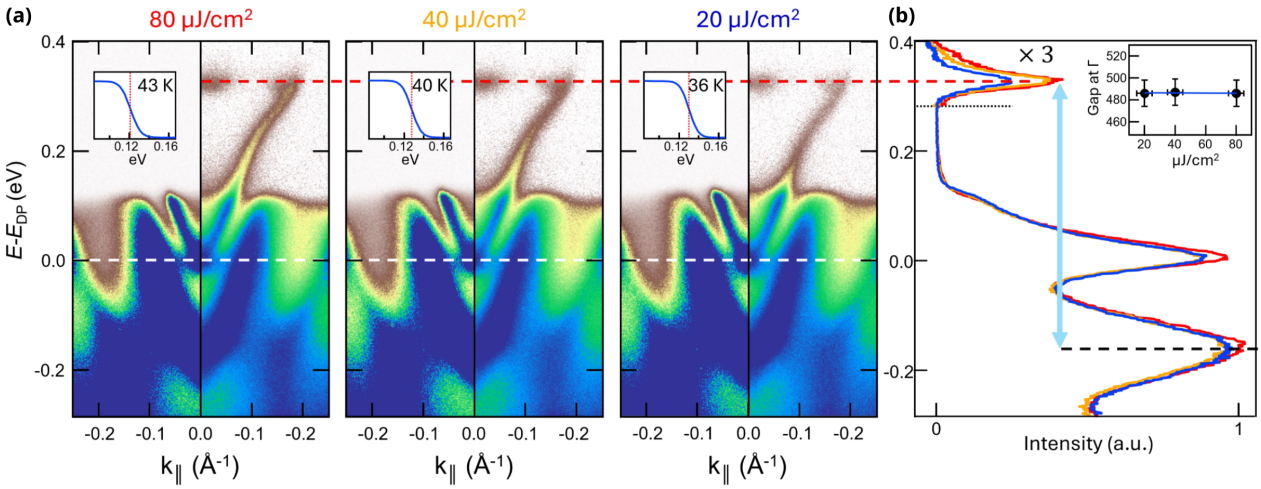


FIGURE 4.24 : Fluence dependence of the energy gap at Γ. (a) TR-ARPES intensity maps at negative delay (left) and time-integrated (right; as in Fig. 2) for different pump fluences. The inset show Fermi–Dirac fits used to extract the electronic temperature. (b) EDCs show that the Γ-point gap remains constant across all fluences (see inset).

4.2.8 Symmetry of the intensity buildup

Owing to the use of a hemispherical analyzer with deflector technology in concert with sample biasing, we acquired high-resolution 4D (k_x, k_y, E, τ), TR-ARPES data of p-doped Bi_2Te_3[74, 75]. Fig. 4.25, top, displays several iso-energy contour maps, at different central energies (± 20 meV integration range) as a function of the pump-probe delay.

Photoexcited electrons populate the conduction band (CB) up to 300 meV above the Fermi level (E_F), and decay and accumulates in states at $\sim$200 meV above E_F within 1-2 ps. These states correspond to the position in the momentum-energy space where the hexagonal warped topological

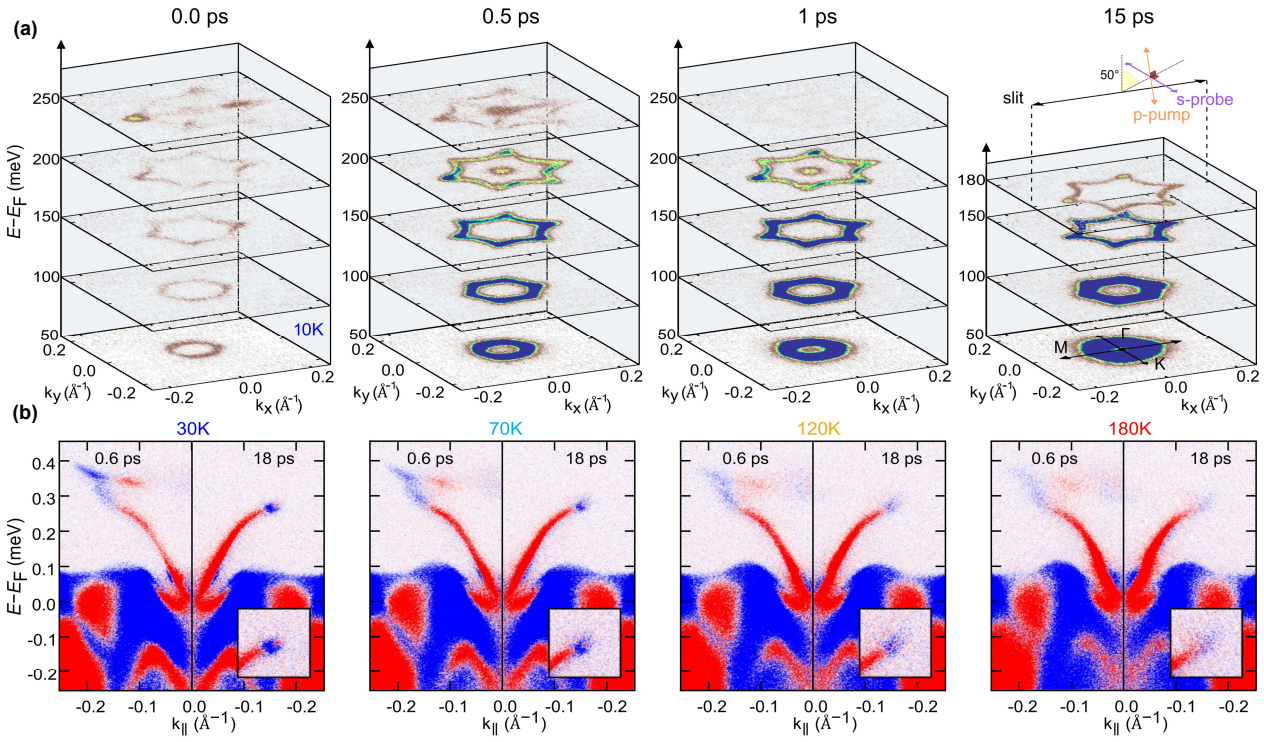


FIGURE 4.25 : Symmetry of the intensity buildup. (a) 3D TR-ARPES maps in the (k_x, k_y, E) space for different pump-probe delays, from 0 to 15 ps. The experimental geometry is schematized in the inset above the 15 ps data. (b) Linear dichroism analysis of TR-ARPES data ($I_{LD} \propto I_{k,E} - I_{-k,E}$) for 0.6 ps and 18 ps at different temperatures.

surface state crosses the CB minima and the intensity buildup appears. We note a trigonal intensity pattern for the intensity buildup energy window at 0.5 ps and 1 ps pump-probe delays, reminiscent of the characteristic bulk trigonal symmetry. At 15 ps delay, the same trigonal pattern is still present up to 180 meV above E_F (± 10 meV integration range for this central energy), indicating that the long-lasting intensity buildup holds the bulk symmetry.

Further evidence in support of the bulk nature of the intensity buildup is presented in Fig. 4.25, bottom. A linear dichroism analysis was performed on TR-ARPES data, with the intention of distinguishing between different orbital characters associated of the bulk and surface states. This is possible due to the precise experimental geometry used in our TR-ARPES experiments, *i.e.* s-polarized probe with mirror plane along the Γ-M direction (time-reversal invariant) [68–70]. Linear dichroism maps were generated by computing $I_{LD} \propto I_{k,E} - I_{-k,E}$. Fig. 4.25, bottom, displays the linear dichroism maps from 30 K to 180 K, at 0.6 ps (left) and 18 ps (right) pump-probe delays. The distinct red (positive) and blue (negative) contrast is a signature of different orbital contributions [68–70]. At 0.6 ps, the TSS exhibits a pronounced positive dichroic signal, while the CB displays a negative dichroic signal. By 18 ps, the positive dichroic contribution from the TSS intrudes into the negative dichroic region (as highlighted in the insets). This observation suggests that the TSS intersect the bulk CB at the intensity buildup location, where there is coexistence of both surface and bulk states.

4.2.9 Shift of bulk valence band and evidence of surface state exposed underneath the VBM

In order to isolate pump-induced modifications, one can examine the differential TR-ARPES map, defined as the photoemission intensity at positive pump–probe delays subtracted by the photoemission intensity before time zero. Figure 4.26a presents the differential TR-ARPES maps at four representative delays (0.6, 1, 6, and 20 ps), where red indicates an increase in photoemission intensity and blue indicates a decrease. Initially (Here 0.5 ps and 1 ps), an increase in photoemission intensity is observed close to the Fermi level at the valence-band maximum (VBM) around $K_{||} \sim \pm 1$ Å^{-1}, as marked by the black arrow in Fig. 4.26a. However at later time delays, this region exhibits a decrease in photoemission intensity. This momentum–energy region has previously been considered as a source of holes for the proposed topological exciton [52], as well as for possible excitonic condensation associated with a Mexican-hat–like Bogoliubov dispersion [53]. In Fig. 4.26b, we plot the temporal evolution of the photoemission intensity extracted from this region together with that intensity buildup position (the integration window is indicated by the box in the 20 ps map of Fig. 4.26a). The dynamics of these two regions are clearly different, in contrast to the behavior reported in Ref. [52]. Moreover, the time trace further reveals initial increase in photoemission intensity in that VBM region. To understand the origin of this increase, we examine the calculated band structure of Bi_2Te_3, shown in Fig. 4.2b. The calculation reveals the presence of a surface state located just below the VBM. This state is also visible in our TR-ARPES measurements (Fig. 4.15), where it merges with the bulk valence-band dispersion on both sides of the Dirac cone. A downward shift of the bulk bands and/or an initial pump induced population of this surface state could therefore provide a natural explanation for the observed increase in photoemission intensity.

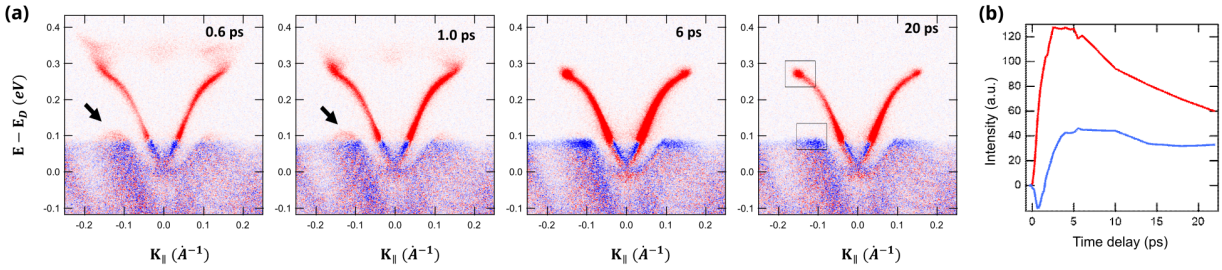


FIGURE 4.26 : (a) Differential TR-ARPES map at 30K at four different pump probe delay. (b) Dynamics of the intensity buildup region and the VB as shown by the box in 20 ps data here

To further examine this scenario, we plot differential TR-ARPES maps along both the $\Gamma - M$ and $\Gamma - K$ directions, as shown in Fig. 4.26 (Note that these measurements were performed at a temperature of 10 K, and the data shown correspond to a pump–probe delay of 15 ps) In these maps, a decrease in photoemission intensity (blue) is observed near the Fermi level that is not localized to a specific valence-band maximum region previously identified as the hole source for

excitonic states in Ref. [52], but instead extends all across the Fermi-level region. Furthermore, inspection of Fig. 4.26 reveals that both the M-shaped valence-band dispersion at higher binding energies and the valence-band dispersion near the Fermi level exhibit simultaneous decreases (blue) and increases in photoemission intensity following the same underlying dispersion. This behavior is consistent with a rigid downward shift of the band structure : if the bulk bands shift uniformly to lower energies, the resulting differential photoemission intensity naturally produces overlapping positive and negative features along the same dispersions. Such a pattern supports a band-shift–driven interpretation rather than the formation of a localized excitonic hole pocket.

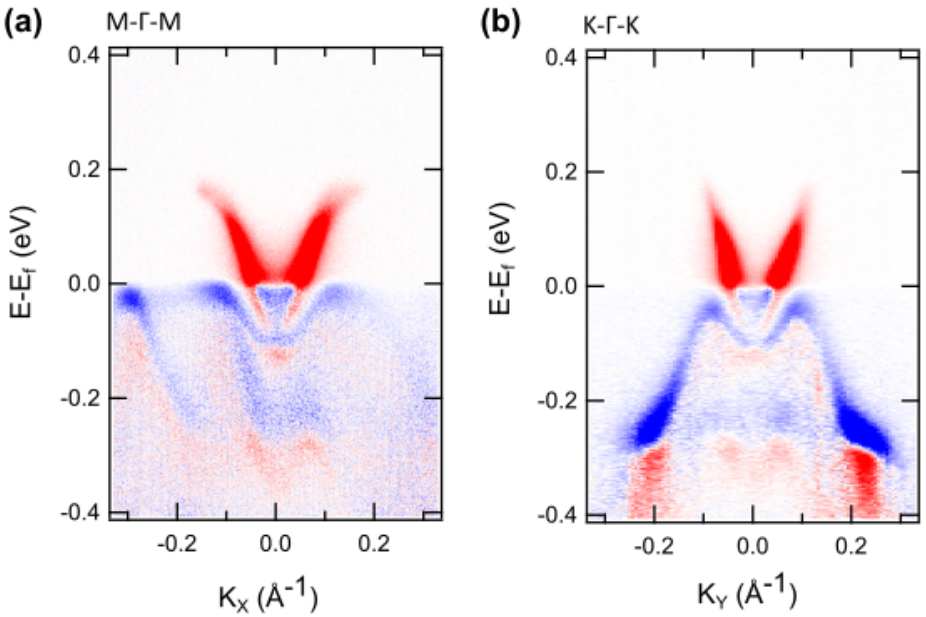


FIGURE 4.27 : Differential TR-ARPES map along (a) $M-\Gamma-M$ and (b) $K-\Gamma-K$ at 15ps time delay. Red color represents increase in photoemission intensity while blue is decrease in photoemission intensity.

To further assess whether an actual band shift is present, we compare TR-ARPES maps at two pump–probe delays : a negative delay before the arrival of the pump pulse and a positive delay at 9 ps, as shown in Fig. 4.28. This comparison reveals a clear shift of the band structure at fermi level. To determine whether this shift is global across all bands—which would typically indicate a surface photovoltage effect—we examine the position of the Dirac point. In such a scenario, a rigid shift of the entire band structure, including the Dirac point, would be expected. However, no measurable shift of the Dirac point is observed. This indicates that the shift is confined to the bulk bands and is therefore driven by a different mechanism rather than a conventional surface photovoltage effect.

Therefore, from the discussion above, we conclude that a pump induced shift of the bulk valence band is present. This observation is consistent with Ref. [53], yet it contradicts with the interpretation put forward in the earlier work Ref. [52], where such a shift was not considered and the observed features at the VBM ($\sim K_{||} \sim \pm 1$ Å^{-1}) close to the fermi level were instead attributed to hole formation. Our high-quality TR-ARPES data further reveal the presence of an

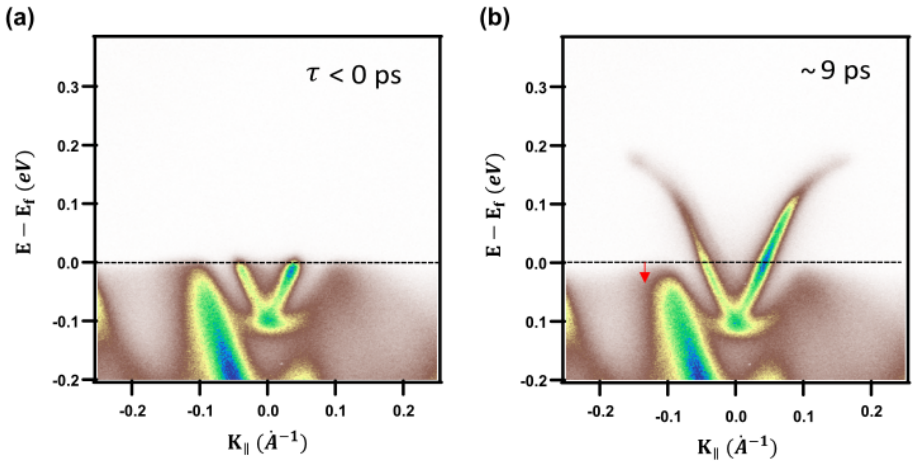


FIGURE 4.28 : TR-ARPES map at negative delay (a) and at 9 ps delay (b). The dashed line act as a guide to show the valence band top is shifting at positive delay.

underlying surface state at this energy–momentum position, which has not been experimentally identified previously. Moreover, the bulk valence-band renormalization reported in Ref. [53] did not account for this underlying surface state, which could naturally explain the observed phenomenology. In addition, the valence-band renormalization shown in Fig. 4.14b of Ref. [53], together with the corresponding simulations presented in the same work, suggests a gap-like feature in the valence band. However, these simulations are based on earlier theoretical studies [76, 77] that predict gap formation in the Dirac surface states, without explicitly considering the valence band.This discrepancy therefore undermines the applicability of the simulation framework used in Ref. [53] to describe the reported valence-band features, and consequently casts doubt on the proposed excitonic condensation scenario.

4.3 Conclusion

This TR-ARPES work demonstrates that temperature-induced renormalization of the conduction band in Bi_2Te_3 plays a critical role in dictating ultrafast electron dynamics. Indeed, as temperature rises, the downward shift of the conduction band minimum at Γ enhances the spectral overlap between the Q- and Γ-valleys. This modification opens a novel scattering channel that facilitates intervalley electron-phonon scattering, as evidenced by the marked transfer of spectral weight from Q to Γ valleys. The experimental trends are supported by kinetic Monte Carlo simulations, which well reproduce the evolution of the photoemission intensity. Importantly, our results indicate that the long-lived intensity buildup does not require the formation of a spatially indirect excitonic state. Instead, it can be consistently explained by temperature-dependent variations in intervalley scattering efficiency within the bulk conduction band, leading to charge accumulation at the conduction-band minimum. While an excitonic contribution cannot be entirely excluded, if present, it likely coexists with scattering-driven dynamics rather than dominating the response. A systematic

photon-energy-dependent study would be required to disentangle these contributions and establish a comprehensive understanding of the underlying mechanism. In addition, our measurements reveal a pump-induced shift of the bulk valence band at the Fermi level in the momentum region previously identified as the hole source in exciton-based interpretations. We further report the observation of a surface state buried beneath the bulk valence band at the same energy–momentum region. Ultimately, our work provides a comprehensive understanding of the intricate mechanisms governing the out-of-equilibrium response of topological insulators, revealing how temperature-induced changes in the bulk band structure can dramatically alter their surface and bulk carrier dynamics. This approach unravels the interplay between carrier density, phonon population, and band structure renormalization, and it can also be applied to other bulk semiconducting compounds with a multi-valley landscape, including two-dimensional layered semiconductors and other three-dimensional topological insulators, which exhibit unique thermoelectric properties. These studies may provide valuable insights that could inform the rational design of advanced thermoelectric and quantum devices, in which precise control of out-of-equilibrium electron dynamics across a broad temperature range is critical.

Bibliographie

[1] A Jabed, F Goto, B Frimpong, D Armanno, A Longa, M Michiardi, A Damascelli, P Hofmann, G Jargot, H Ibrahim, F Légaré, N Gauthier, S Beaulieu, and F Boschini. Control of intervalley scattering in bi2te3 via temperature-dependent band renormalization. *npj Quantum Materials*, January 2026. ISSN 2397-4648. doi : 10.1038/s41535-025-00842-8. URL http://dx.doi.org/10.1038/s41535-025-00842-8.

[2] L Fu, C L Kane, and E J Mele. Topological insulators in three dimensions. *Physical Review Letters*, 98(10) :106803, March 2007. ISSN 1079-7114. doi : 10.1103/physrevlett.98.106803. URL http://dx.doi.org/10.1103/PhysRevLett.98.106803.

[3] J E Moore. The birth of topological insulators. *Nature*, 464(7286) :194–198, March 2010. ISSN 1476-4687. doi : 10.1038/nature08916. URL http://dx.doi.org/10.1038/nature08916.

[4] Y L Chen, J G Analytis, J-H Chu, Z K Liu, S-K Mo, X L Qi, H J Zhang, D H Lu, X Dai, Z Fang, S C Zhang, I R Fisher, Z Hussain, and Z-X Shen. Experimental realization of a three-dimensional topological insulator, Bi_2Te_3. *Science*, 325(5937) :178–181, July 2009. ISSN 1095-9203. doi : 10.1126/science.1173034. URL http://dx.doi.org/10.1126/science.1173034.

[5] M Z Hasan and C L Kane. Colloquium : Topological insulators. *Reviews of Modern Physics*, 82 (4) :3045–3067, November 2010. ISSN 1539-0756. doi : 10.1103/revmodphys.82.3045. URL http://dx.doi.org/10.1103/RevModPhys.82.3045.

[6] G J Ferreira and D Loss. Magnetically defined qubits on 3d topological insulators. *Physical Review Letters*, 111(10) :106802, September 2013. ISSN 1079-7114. doi : 10.1103/physrevlett.111.106802. URL http://dx.doi.org/10.1103/PhysRevLett.111.106802.

[7] K-H Jin, W Jiang, G Sethi, and F Liu. Topological quantum devices : a review. *Nanoscale*, 15 (31) :12787–12817, 2023. ISSN 2040-3372. doi : 10.1039/d3nr01288c. URL http://dx.doi.org/10.1039/D3NR01288C.

[8] X Tao, P Jiang, H Hao, X Zheng, L Zhang, and Z Zeng. Pure spin current generation via photogalvanic effect with spatial inversion symmetry. *Physical Review B*, 102(8) :081402, 2020.

[9] F D M Haldane. Nobel lecture : Topological quantum matter. *Reviews of Modern Physics*, 89(4) :040502, October 2017. ISSN 1539-0756. doi : 10.1103/revmodphys.89.040502. URL http://dx.doi.org/10.1103/RevModPhys.89.040502.

[10] M Michiardi, F Boschini, H-H Kung, M X Na, S K Y Dufresne, A Currie, G Levy, S Zhdanovich, A K Mills, D J Jones, et al. Optical manipulation of rashba-split 2-dimensional electron gas. *nature Communications*, 13(1) :3096, 2022.

[11] X-L Qi and S-C Zhang. Topological insulators and superconductors. *Reviews of Modern Physics*, 83(4) :1057–1110, October 2011. ISSN 1539-0756. doi : 10.1103/revmodphys.83.1057. URL http://dx.doi.org/10.1103/RevModPhys.83.1057.

[12] H F Legg, D Loss, and J Klinovaja. Majorana bound states in topological insulators without a vortex. *Physical Review B*, 104(16) :165405, October 2021. ISSN 2469-9969. doi : 10.1103/physrevb.104.165405. URL http://dx.doi.org/10.1103/PhysRevB.104.165405.

[13] H P Paudel and M N Leuenberger. Three-dimensional topological insulator quantum dot for optically controlled quantum memory and quantum computing. *Physical Review B*, 88 (8) :085316, August 2013. ISSN 1550-235X. doi : 10.1103/physrevb.88.085316. URL http://dx.doi.org/10.1103/PhysRevB.88.085316.

[14] L Fu and C L Kane. Topological insulators with inversion symmetry. *Phys. Rev. B Condens. Matter Mater. Phys.*, 76(4), July 2007.

[15] D Hsieh, D Qian, L Wray, Y Xia, Y S Hor, R J Cava, and M Z Hasan. A topological dirac insulator in a quantum spin hall phase. *Nature*, 452(7190) :970–974, April 2008.

[16] D Hsieh, Y Xia, L Wray, D Qian, A Pal, J H Dil, J Osterwalder, F Meier, G Bihlmayer, C L Kane, Y S Hor, R J Cava, and M Z Hasan. Observation of Unconventional Quantum Spin Textures in Topological Insulators. *Science*, 323(5916) :919–922, 2 2009. ISSN 0036-8075. doi : 10.1126/science.1167733. URL https://www.science.org/doi/10.1126/science.1167733.

[17] Y Xia, D Qian, D Hsieh, L Wray, A Pal, H Lin, A Bansil, D Grauer, Y S Hor, R J Cava, and M Z Hasan. Observation of a large-gap topological-insulator class with a single dirac cone on the surface. *Nat. Phys.*, 5(6) :398–402, June 2009.

[18] H Zhang, C-X Liu, X-L Qi, X Dai, Z Fang, and S-C Zhang. Topological insulators in Bi2Se3, Bi2Te3 and Sb2Te3 with a single dirac cone on the surface. *Nat. Phys.*, 5(6) :438–442, June 2009.

[19] S Basak, H Lin, L A Wray, S-Y Xu, L Fu, M Z Hasan, and A Bansil. Spin texture on the warped dirac-cone surface states in topological insulators. *Phys. Rev. B Condens. Matter Mater. Phys.*, 84(12), September 2011.

[20] D Hsieh, Y Xia, D Qian, L Wray, J H Dil, F Meier, J Osterwalder, L Patthey, J G Checkelsky, N P Ong, A V Fedorov, H Lin, A Bansil, D Grauer, Y S Hor, R J Cava, and M Z Hasan. A tunable topological insulator in the spin helical dirac transport regime. *Nature*, 460(7259) : 1101–1105, August 2009.

[21] S Souma, K Kosaka, T Sato, M Komatsu, A Takayama, T Takahashi, M Kriener, K Segawa, and Y Ando. Direct measurement of the out-of-plane spin texture in the dirac-cone surface state of a topological insulator. *Phys. Rev. Lett.*, 106(21) :216803, May 2011.

[22] Z-H Pan, E Vescovo, A V Fedorov, D Gardner, Y S Lee, S Chu, G D Gu, and T Valla. Electronic structure of the topological insulator Bi2Se3 using angle-resolved photoemission spectroscopy : evidence for a nearly full surface spin polarization. *Phys. Rev. Lett.*, 106(25) :257004, June 2011.

[23] C Jozwiak, C-H Park, K Gotlieb, C Hwang, D-H Lee, S G Louie, J D Denlinger, C R Rotundu, R J Birgeneau, Z Hussain, and A Lanzara. Photoelectron spin-flipping and texture manipulation in a topological insulator. *Nat. Phys.*, 9(5) :293–298, May 2013.

[24] O V Yazyev, J E Moore, and S G Louie. Spin polarization and transport of surface states in the topological insulators Bi2Se3 and Bi2Te3 from first principles. *Phys. Rev. Lett.*, 112(7) : 076802, February 2014.

[25] C-H Park and S G Louie. Spin polarization of photoelectrons from topological insulators. *Phys. Rev. Lett.*, 109(9) :097601, August 2012.

[26] J Sánchez-Barriga, A Varykhalov, J Braun, S-Y Xu, N Alidoust, O Kornilov, J Minár, K Hummer, G Springholz, G Bauer, R Schumann, L V Yashina, H Ebert, M Z Hasan, and O Rader. Photoemission ofBi2Se3with circularly polarized light : Probe of spin polarization or means for spin manipulation? *Phys. Rev. X.*, 4(1), March 2014.

[27] Z Xie, S He, C Chen, Y Feng, H Yi, A Liang, L Zhao, D Mou, J He, Y Peng, X Liu, Y Liu, G Liu, X Dong, L Yu, J Zhang, S Zhang, Z Wang, F Zhang, F Yang, Q Peng, X Wang, C Chen, Z Xu, and X J Zhou. Orbital-selective spin texture and its manipulation in a topological insulator. *Nat. Commun.*, 5(1) :3382, February 2014.

[28] Z-H Zhu, C N Veenstra, S Zhdanovich, M P Schneider, T Okuda, K Miyamoto, S-Y Zhu, H Namatame, M Taniguchi, M W Haverkort, I S Elfimov, and A Damascelli. Photoelectron spin-polarization control in the topological insulator Bi_2Se_3. *Phys. Rev. Lett.*, 112(7) :076802, February 2014.

[29] Y H Wang, D Hsieh, D Pilon, L Fu, D R Gardner, Y S Lee, and N Gedik. Observation of a warped helical spin texture in Bi2Se3 from circular dichroism angle-resolved photoemission spectroscopy. *Phys. Rev. Lett.*, 107(20) :207602, November 2011.

[30] J A Sobota, S Yang, J G Analytis, Y L Chen, I R Fisher, P S Kirchmann, and Z-X Shen. Ultrafast optical excitation of a persistent surface-state population in the topological insulator Bi_2Se_3. *Physical Review Letters*, 108 :117403, 3 2012. ISSN 0031-9007. doi : $10.1103/\mathrm{PhysRevLett.108.117403}$.

[31] A Crepaldi, B Ressel, F Cilento, M Zacchigna, C Grazioli, H Berger, P Bugnon, K Kern, M Grioni, and F Parmigiani. Ultrafast photodoping and effective Fermi-Dirac distribution of the dirac particles in Bi2Se3. *Phys. Rev. B Condens. Matter Mater. Phys.*, 86(20), November 2012.

[32] M Hajlaoui, E Papalazarou, J Mauchain, G Lantz, N Moisan, D Boschetto, Z Jiang, I Miotkowski, Y P Chen, A Taleb-Ibrahimi, L Perfetti, and M Marsi. Ultrafast surface carrier dynamics in the topological insulator Bi_2Te_3. *Nano Letters*, 12 :3532–3536, 7 2012. ISSN 1530-6984. doi : 10.1021/nl301035x.

[33] Y H Wang, D Hsieh, E J Sie, H Steinberg, D R Gardner, Y S Lee, P Jarillo-Herrero, and N Gedik. Measurement of intrinsic dirac fermion cooling on the surface of the topological insulator Bi2Se3 using time-resolved and angle-resolved photoemission spectroscopy. *Phys. Rev. Lett.*, 109(12) :127401, September 2012.

[34] J A Sobota, S-L Yang, D Leuenberger, A F Kemper, J G Analytis, I R Fisher, P S Kirchmann, T P Devereaux, and Z-X Shen. Ultrafast electron dynamics in the topological insulator Bi_2Se_3 studied by time-resolved photoemission spectroscopy. *Journal of Electron Spectroscopy and Related Phenomena*, 195 :249–257, August 2014. ISSN 0368-2048. doi : 10.1016/j.elspec.2014.01.005. URL http://dx.doi.org/10.1016/j.elspec.2014.01.005.

[35] J A Sobota, S-L Yang, D Leuenberger, A F Kemper, J G Analytis, I R Fisher, P S Kirchmann, T P Devereaux, and Z-X Shen. Distinguishing bulk and surface electron-phonon coupling in the topological insulator Bi_2Se_3 using time-resolved photoemission spectroscopy. *Physical Review Letters*, 113 :157401, 10 2014. ISSN 0031-9007. doi : 10.1103/PhysRevLett.113.157401.

[36] J Sánchez-Barriga, M Battiato, M Krivenkov, E Golias, A Varykhalov, A Romualdi, L V Yashina, J Minár, O Kornilov, H Ebert, K Held, and J Braun. Subpicosecond spin dynamics of excited states in the topological insulator Bi_2Te_3. *Physical Review B*, 95 :125405, 3 2017. ISSN 2469-9950. doi : 10.1103/PhysRevB.95.125405.

[37] E Papalazarou, L Khalil, M Caputo, L Perfetti, N Nilforoushan, H Deng, Z Chen, S Zhao, A Taleb-Ibrahimi, M Konczykowski, A Hruban, A Wołoś, A Materna, L Krusin-Elbaum, and M Marsi. Unraveling the dirac fermion dynamics of the bulk-insulating topological system Bi_2Te_2Se. *Physical Review Materials*, 2(10) :104202, October 2018. ISSN 2475-9953. doi : 10.1103/physrevmaterials.2.104202. URL http://dx.doi.org/10.1103/PhysRevMaterials.2.104202.

[38] H Soifer, A Gauthier, A F Kemper, C R Rotundu, S-L Yang, H Xiong, D Lu, M Hashimoto, P S Kirchmann, J A Sobota, and Z-X Shen. Band-resolved imaging of photocurrent in a topological insulator. *Physical Review Letters*, 122(16) :167401, April 2019. ISSN 1079-7114. doi : 10.1103/physrevlett.122.167401. URL http://dx.doi.org/10.1103/PhysRevLett.122.167401.

[39] W Chen, F Wang, T Lin, H Zhong, S Zhou, C Bao, H Zhang, and S Zhou. Distinct light-matter coupling mechanisms in Bi_2Te_3 : Crossover from above-gap photoexcitation to light-field dressing. *Physical Review B*, 110(20) :L201116, 2024.

[40] C Cacho, A Crepaldi, M Battiato, J Braun, F Cilento, M Zacchigna, M C Richter, O Heckmann, E Springate, Y Liu, S S Dhesi, H Berger, P Bugnon, K Held, M Grioni, H Ebert, K Hricovini, J Minár, and F Parmigiani. Momentum-resolved spin dynamics of bulk and surface excited states in the topological insulator Bi(2)Se(3). *Phys. Rev. Lett.*, 114(9) :097401, March 2015.

[41] J Sánchez-Barriga, E Golias, A Varykhalov, J Braun, L V Yashina, R Schumann, J Minár, H Ebert, O Kornilov, and O Rader. Ultrafast spin-polarization control of dirac fermions in topological insulators. *Physical Review B*, 93(15) :155426, April 2016. ISSN 2469-9969. doi : 10.1103/physrevb.93.155426. URL http://dx.doi.org/10.1103/PhysRevB.93.155426.

[42] C Jozwiak, J A Sobota, K Gotlieb, A F Kemper, C R Rotundu, R J Birgeneau, Z Hussain, D-H Lee, Z-X Shen, and A Lanzara. Spin-polarized surface resonances accompanying topological surface state formation. *Nat. Commun.*, 7(1) :13143, October 2016.

[43] Y Fukushima, K Kawaguchi, K Kuroda, M Ochi, H Tanaka, A Harasawa, T Iimori, Z Zhao, S Tani, K Yaji, S Shin, F Komori, Y Kobayashi, and T Kondo. Spin-polarized saddle points in the topological surface states of the elemental bismuth revealed by a pump-probe spin-resolved ARPES. 2023.

[44] S Ciocys, T Morimoto, R Mori, K Gotlieb, Z Hussain, J G Analytis, J E Moore, and A Lanzara. Manipulating long-lived topological surface photovoltage in bulk-insulating topological insulators Bi2Se3 and Bi2Te3. *Npj Quantum Mater.*, 5(1), March 2020.

[45] M Hajlaoui, E Papalazarou, J Mauchain, L Perfetti, A Taleb-Ibrahimi, F Navarin, M Monteverde, P Auban-Senzier, C R Pasquier, N Moisan, D Boschetto, M Neupane, M Z Hasan, T Durakiewicz, Z Jiang, Y Xu, I Miotkowski, Y P Chen, S Jia, H W Ji, R J Cava, and M Marsi. Tuning a schottky barrier in a photoexcited topological insulator with transient dirac cone electron-hole asymmetry. *Nature Communications*, 5 :3003, 1 2014. ISSN 2041-1723. doi : 10.1038/ncomms4003.

[46] M Neupane, S-Y Xu, Y Ishida, S Jia, B M Fregoso, C Liu, I Belopolski, G Bian, N Alidoust, T Durakiewicz, V Galitski, S Shin, R J Cava, and M Z Hasan. Gigantic surface lifetime of an intrinsic topological insulator. *Physical Review Letters*, 115 :116801, 9 2015. ISSN 0031-9007. doi : 10.1103/PhysRevLett.115.116801.

[47] K Sumida, Y Ishida, S Zhu, M Ye, A Pertsova, C Triola, K A Kokh, O E Tereshchenko, A V Balatsky, S Shin, and A Kimura. Prolonged duration of nonequilibrated dirac fermions in neutral topological insulators. *Sci. Rep.*, 7(1), October 2017.

[48] T Yoshikawa, Y Ishida, K Sumida, J Chen, K A Kokh, O E Tereshchenko, S Shin, and A Kimura. Enhanced photovoltage on the surface of topological insulator via optical aging. *Appl. Phys. Lett.*, 112(19) :192104, May 2018.

[49] T Yoshikawa, K Sumida, Y Ishida, J Chen, M Nurmamat, K Akiba, A Miyake, M Tokunaga, K A Kokh, O E Tereshchenko, S Shin, and A Kimura. Bidirectional surface photovoltage on a topological insulator. *Phys. Rev. B.*, 100(16), October 2019.

[50] Y H Wang, H Steinberg, P Jarillo-Herrero, and N Gedik. Observation of Floquet-Bloch states on the surface of a topological insulator. *Science*, 342(6157) :453–457, October 2013.

[51] F Mahmood, C-K Chan, Z Alpichshev, D Gardner, Y Lee, P A Lee, and N Gedik. Selective scattering between Floquet–Bloch and volkov states in a topological insulator. *Nat. Phys.*, 12 (4) :306–310, April 2016.

[52] R Mori, S Ciocys, K Takasan, P Ai, K Currier, T Morimoto, J E Moore, and A Lanzara. Spin-polarized spatially indirect excitons in a topological insulator. *Nature*, 614 :249–255, 2 2023. ISSN 0028-0836. doi : $10.1038/s41586\text{-}022\text{-}05567\text{-}3$.

[53] R Mori, K Takasan, P Ai, S Ciocys, K Kawaguchi, T Kondo, T Morimoto, and A Lanzara. Possible evidence of excitonic condensation in a topological insulator. *Proceedings of the National Academy of Sciences*, 122(18) :e2422667122, 2025.

[54] B Monserrat and D Vanderbilt. Temperature effects in the band structure of topological insulators. *Physical Review Letters*, 117 :226801, 11 2016. ISSN 10797114. doi : $10.1103/\mathrm{PhysRevLett.117.226801}$.

[55] S S Ataei and A Sadeghi. Competitive screening and band gap renormalization in n-type monolayer transition metal dichalcogenides. *Physical Review B*, 104(15) :155301, 2021.

[56] S Ulstrup, A G Cabo, J A Miwa, J M Riley, S S Grønborg, J C Johannsen, C Cacho, O Alexander, R T Chapman, E Springate, et al. Ultrafast band structure control of a two-dimensional heterostructure. *ACS nano*, 10(6) :6315–6322, 2016.

[57] D H Lee, S-J Choi, H Kim, Y-S Kim, and S Jung. Direct probing of phonon mode specific electron–phonon scatterings in two-dimensional semiconductor transition metal dichalcogenides. *Nature Communications*, 12(1) :4520, 2021.

[58] A Kumar, S Kumar, Y Miyai, and K Shimada. Temperature-dependent band modification and energy dependence of the electron-phonon interaction in the topological surface state on bi 2 te 3. *Physical Review B*, 106(12) :L121104, 2022.

[59] E Witkoske, X Wang, M Lundstrom, V Askarpour, and J Maassen. Thermoelectric band engineering : The role of carrier scattering. *J. Appl. Phys.*, 122(17) :175102, November 2017.

[60] V Askarpour and J Maassen. First-principles analysis of intravalley and intervalley electron-phonon scattering in thermoelectric materials. *Phys. Rev. B.*, 107(4), January 2023.

[61] Z M Gibbs, H-S Kim, H Wang, and G J Snyder. Band gap estimation from temperature dependent seebeck measurement—deviations from the 2e| s| maxtmax relation. *Applied Physics Letters*, 106(2), 2015.

[62] F Rittweger, N F Hinsche, P Zahn, and I Mertig. Signature of the topological surface state in the thermoelectric properties of Bi_2Te_3. *Physical Review B*, 89 :035439, 1 2014. ISSN 1098-0121. doi : 10.1103/PhysRevB.89.035439.

[63] J Liang, L Cheng, J Zhang, H Liu, and Z Zhang. Maximizing the thermoelectric performance of topological insulator Bi_2Te_3 films in the few-quintuple layer regime. *Nanoscale*, 8 :8855–8862, 2016. ISSN 2040-3364. doi : 10.1039/C6NR00724D.

[64] T Cao, X-L Shi, M Li, B Hu, W Chen, W-D Liu, W Lyu, J MacLeod, and Z-G Chen. Advances in bismuth-telluride-based thermoelectric devices : Progress and challenges. *eScience*, 3 : 100122, 6 2023. ISSN 26671417. doi : 10.1016/j.esci.2023.100122.

[65] H Hedayat, D Bugini, H Yi, C Chen, X Zhou, G Cerullo, C Dallera, and E Carpene. Ultrafast evolution of bulk, surface and surface resonance states in photoexcited Bi_2Te_3. *Scientific Reports*, 11 :4924, 3 2021. ISSN 2045-2322. doi : 10.1038/s41598-021-83848-z.

[66] C Cacho, A Crepaldi, M Battiato, J Braun, F Cilento, M Zacchigna, M C Richter, O Heckmann, E Springate, Y Liu, et al. Momentum-resolved spin dynamics of bulk and surface excited states in the topological insulator bi 2 se 3. *Physical review letters*, 114(9) :097401, 2015.

[67] C Jozwiak, J A Sobota, K Gotlieb, A F Kemper, C R Rotundu, R J Birgeneau, Z Hussain, D-H Lee, Z-X Shen, and A Lanzara. Spin-polarized surface resonances accompanying topological surface state formation. *Nature Communications*, 7(1) :13143, 2016.

[68] S Beaulieu, M Schüler, J Schusser, S Dong, T Pincelli, J Maklar, A Neef, F Reinert, M Wolf, L Rettig, J Minár, and R Ernstorfer. Unveiling the orbital texture of 1t-tite2 using intrinsic linear dichroism in multidimensional photoemission spectroscopy. *npj Quantum Materials*, 6 (1) :93, November 2021. ISSN 2397-4648. doi : 10.1038/s41535-021-00398-3. URL http://dx.doi.org/10.1038/s41535-021-00398-3.

[69] Y Cao, J A Waugh, X-W Zhang, J-W Luo, Q Wang, T J Reber, S K Mo, Z Xu, A Yang, J Schneeloch, G D Gu, M Brahlek, N Bansal, S Oh, A Zunger, and D S Dessau. Mapping the orbital wavefunction of the surface states in three-dimensional topological insulators. *Nature Physics*, 9(8) :499–504, July 2013. ISSN 1745-2481. doi : 10.1038/nphys2685. URL http://dx.doi.org/10.1038/nphys2685.

[70] C-H Min, H Bentmann, J N Neu, P Eck, S Moser, T Figgemeier, M Ünzelmann, K Kissner, P Lutz, R J Koch, C Jozwiak, A Bostwick, E Rotenberg, R Thomale, G Sangiovanni, T Siegrist, D Di Sante, and F Reinert. Orbital fingerprint of topological fermi arcs in the weyl semimetal tap. *Physical Review Letters*, 122(11) :116402, March 2019. ISSN 1079-7114. doi : 10.1103/physrevlett.122.116402. URL http://dx.doi.org/10.1103/PhysRevLett.122.116402.

[71] M X Na, F Boschini, A K Mills, M Michiardi, R P Day, B Zwartsenberg, G Levy, S Zhdanovich, A F Kemper, D J Jones, et al. Establishing nonthermal regimes in pump-probe electron relaxation dynamics. *Physical Review B*, 102(18) :184307, 2020.

[72] S Li and C Persson. Thermal properties and phonon dispersion of bi2te3 and csbi4te6 from first-principles calculations. *Journal of Applied Mathematics and Physics*, 3(12) :1563–1570, 2015.

[73] Y Zheng, H Zhao, W Li, Z Chen, W Zhu, X Liu, Q Tang, H Wang, C Wang, and Z Li. Enhanced electron–phonon coupling by delocalizing phonon states in monolayer mos_2. *Nano Lett.*, 22 (15) :6102–6109, 2022. doi : $10.1021/acs.nanolett.2c01105$.

[74] A Longa, J-M Parent, B K Frimpong, D Armanno, N Gauthier, F Légaré, F Boschini, and G Jargot. Time-resolved arpes with probe energy of 6.0 ev and tunable mir pump at 250 khz. *Optics Express*, 32 :29549, 8 2024. ISSN 1094-4087. doi : $10.1364/OE.525265$. URL `https://opg.optica.org/abstract.cfm?URI=oe-32-17-29549`.

[75] N Gauthier, J A Sobota, H Pfau, A Gauthier, H Soifer, M D Bachmann, I R Fisher, Z X Shen, and P S Kirchmann. Expanding the momentum field of view in angle-resolved photoemission systems with hemispherical analyzers. *Review of Scientific Instruments*, 92 :123907, 2021. ISSN 10897623. doi : $10.1063/5.0053479$.

[76] C Triola, A Pertsova, R S Markiewicz, and A V Balatsky. Excitonic gap formation in pumped dirac materials. *Phys. Rev. B.*, 95(20), May 2017.

[77] A Pertsova and A V Balatsky. Excitonic instability in optically pumped three-dimensional dirac materials. *Phys. Rev. B.*, 97(7), February 2018.

5 ULTRAFAST LIGHT-INDUCED DYNAMICS MEDIATED BY IN-GAP STATES IN LAYERED SnS_2

Summary : Using time-, angle-, and polarization-resolved extreme-ultraviolet photoemission spectroscopy, we present a comprehensive study of the electronic structure and the role of in-gap states on the ultrafast light-induced dynamics of the layered van der Waals semiconductor SnS_2. We perform polarization-resolved extreme-ultraviolet photoemission measurements and reveal the in-plane and out-of-plane orbital character underlying the electronic band structure of SnS_2. We uncover the presence of two broad in-gap state manifolds within the bandgap of semiconducting SnS_2. The presence of these in-gap states induces a pronounced downward band bending and is responsible for a light-induced dynamical surface photovoltage upon optical photoexcitation. Furthermore, we show that in-gap states allow for optical injection of long-lived carriers into the conduction band via below-bandgap infrared excitation. Our findings provide fundamental insights into the pivotal role of in-gap states in governing the optical response and light-induced dynamics of SnS_2.

Statement of Contribution : In this project, the experimental campaign at the CELIA Laboratory was conducted collaboratively (Samuel Beaulieu, Sotirios Fragkos, Quentin Courtade, and me). I participated in the initial basic analysis, while the advanced analysis procedures were performed by Quentin Courtade, Sotirios Fragkos and Samuel Beaulieu. My main scientific contribution is in the participation in the physical interpretation of the experimental observations. In addition, I prepared a first draft of the manuscript, which was extensively revised by Samuel Beaulieu and Sotirios Fragkos. Fabio Boschini and Francesco Goto also participated in the discussion of the results and in editing the manuscript.

5.1 Introduction

Tin disulfide (SnS_2) [1, 2], a layered semiconducting material often associated with transition metal dichalcogenides (TMDCs) [3–6], has recently gained attention for its distinctive electronic and structural properties, crystallizing in a CdI_2-type 1T structure (space group $P\bar{3}m1$). Although SnS_2 is not strictly a conventional TMDC, as tin (Sn) belongs to group 14 (post-transition metals) rather than the d-block transition metals (groups 4–10) that define traditional TMDCs like MoS_2, it is frequently grouped within the broader TMDC family due to its analogous layered van der Waals (vdW) crystal structure, which enables facile 2D exfoliation, as well as its similar optical and electronic properties. Unlike classic TMDCs, SnS_2 hosts an indirect bandgap in the visible range that remains nearly unchanged across thicknesses [1], making it structurally robust and optoelectronically stable. These features have positioned SnS_2 as a promising platform for applications in photovoltaics [7–9], photodetectors [10–14], solar cells [15], electrodes for Li-ion battery [16–20], thermoelectrics [21], gas sensors [22], photocatalysis [23–28], and nonlinear optical materials [29–32]. The functionality of SnS_2 devices depends not only on their pristine bulk properties but also on native imperfections. Indeed, intrinsic defects, such as sulfur vacancies and tin interstitials, introduce donor-like in-gap states that strongly influence its electronic and optical properties [2, 31, 33, 34]. Such defect-induced in-gap states are particularly significant in SnS_2 due to its ionic bonding nature and low defect formation energies, and they are considered responsible for its intrinsic n-type character. Experimental evidence from photoluminescence quenching, Burstein–Moss shifts [2], and surface photovoltage spectroscopy [31] supports the presence of defect-induced in-gap states in SnS_2. Moreover, the presence of defects is also associated with local variations of the charge distribution at interfaces, leading to a spatial modulation of the electronic structure through surface band bending [35–39]. Typically, upon illumination, photogenerated carriers redistribute in the band bending region, partially screening the field and producing a surface photovoltage (SPV) effect [38, 40–43].

However, the influence of in-gap states on the ultrafast light-induced dynamics of SnS_2 single crystals remains unexplored. Time- and angle-resolved photoemission spectroscopy (TR-ARPES) [44] is a particularly well-suited experimental technique to explore these ultrafast light-induced phenomena. Indeed, it has emerged as a powerful technique for probing out-of-equilibrium electronic structures of photoexcited solids in a time-, energy- and momentum-resolved fashion. It enables excited-state band mapping and associated ultrafast carrier dynamics, providing insight into how electronic structures and populations evolve following photoexcitation. Beyond tracking band dispersions, ARPES also benefits from the sensitivity of photoemission matrix elements to photon energy and polarization state of the ionizing radiation. Indeed, by controlling the probe polarization, one can exploit these matrix-element effects to access information about the underlying electronic wavefunctions. This approach has been widely used to reveal the orbital character of the band structure [45–50] through dichroic ARPES experiments.

In this work, we report time- and polarization-resolved ARPES measurements (using a momentum microscope detection scheme) in photoexcited SnS_2. We report valence band dispersions along with the linear dichroism in photoelectron angular distributions (LDAD) obtained via polarization-resolved measurements on SnS_2, which allows us to reveal the different in-plane and out-of-plane orbital character of the bands. Moreover, we directly observe two broad in-gap state manifolds within the bandgap, which stem from the predicted intrinsic donor-like defects [2, 31, 33, 34]. These donor-like defects are shown to drive downward band bending. Upon photoexcitation, our measurements reveal a pronounced light-induced transient SPV. This transient SPV results in a rigid energy upshift of the photoemission spectra due to the reduction of the downward band bending present at equilibrium. We also demonstrate that these in-gap states enable optical injection of carriers into the conduction band via below-bandgap infrared photoexcitation. Photoexcitation from in-gap states to the conduction band leads to subsequent ultrafast carrier dynamics, characterized by fast photohole redistribution below the Fermi level and long-lived electron population at the conduction band minimum, due to the indirect nature of the bandgap. These results elucidate the essential influence of in-gap states on the optical properties and photoinduced dynamics of SnS_2.

5.2 Background Concepts

To facilitate a clearer interpretation of the results, the following core concepts central to the project are described below.

5.2.1 Transition metal dichalcogenides

Despite not being a conventional transition metal dichalcogenide (TMDC) [3–6], SnS_2 shares close structural and electronic similarities with this material class. It is therefore instructive to briefly outline the key properties of TMDCs, which provide a broader framework for understanding its behavior. TMDCs have emerged as a central class of two-dimensional (2D) materials due to their rich electronic properties, strong Coulomb interactions [51, 52] and pronounced spin–orbit coupling [53–55]. Structurally, TMDCs consist of covalently bonded X–M–X monolayers (M = transition metal, X = chalcogen), vertically stacked via weak van der Waals interactions, allowing mechanical exfoliation down to the monolayer limit [56]. These features have enabled exploration of diverse emergent phenomena, including charge density waves [57–59], superconductivity [60, 61], topological phases [62, 63], and strong excitonic effects [64–66]. In parallel, TMDCs are driving advances in novel device applications spanning optoelectronics [67–69], valleytronics [70–73], spintronics [74], energy harvesting [75, 76], and quantum computing [77].

TMDCs are present in different structural phases that arise due to different configurations of the transition metal atom components. TMDCs exhibit several structural polymorphs that have

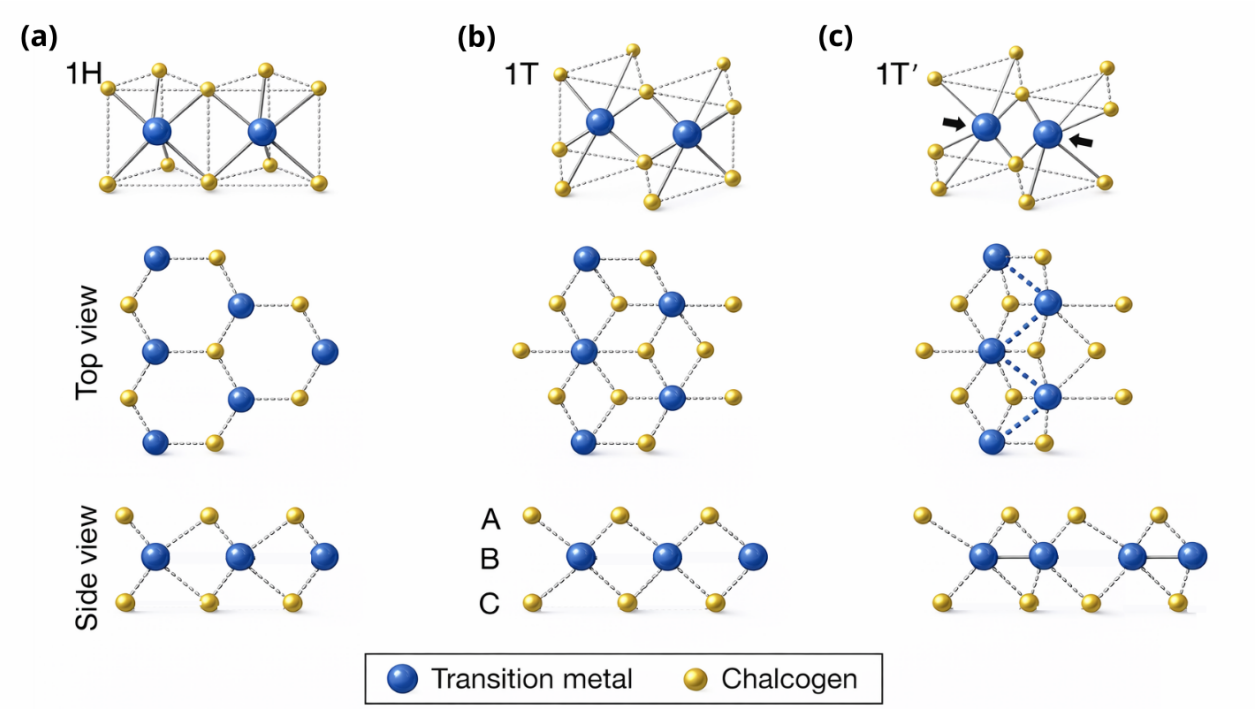


FIGURE 5.1 : Structural polymorphs of 2D TMDCs. Atomic structures of representative 2D TMDCs in the (a) trigonal–prismatic (1H), (b) octahedral (1T), and (c) distorted (1T′) phases. The corresponding stacking configurations of the atomic layers are also indicated.

attracted intense interest over the past decade, both as fundamental studies and for their broad application potential. Each unit layer consists of a transition–metal layer sandwiched between two chalcogen layers. In the monolayer (2D) limit, the most common phases are : the semiconducting trigonal–prismatic 1H phase, the metallic octahedral 1T phase, and the distorted quasi–metallic 1T′ phase. Structurally, the 1H phase refers to an ABA stacking (Fig. 5.1a), in which the top and bottom chalcogen planes are laterally aligned so that the chalcogen atoms sit directly above one another along the out-of-plane direction and the transition metal atom is at the centre. In contrast, the 1T phase adopts ABC stacking (Fig. 5.1b). In freestanding form, it is unstable and relaxes into the distorted 1T′ structure, where the transition-metal atoms shift. This distortion doubles the lattice periodicity to a 2×1 superstructure and, in top view, yields parallel one-dimensional zigzag chains of transition-metal atoms (Fig. 5.1c).

5.2.2 Tin disulfide (SnS_2) atomic and electronic structure

SnS_2 layers crystallize in a hexagonal atomic arrangement of a CdI_2-type structure (space group $P\bar{3}m1$), with Sn in octahedral coordination. A schematic of the real and reciprocal lattices is shown in Fig. 5.2a, along with the first Brillouin zone (Fig. 5.2b) and its two-dimensional in-plane projection with labeled high-symmetry points (Fig. 5.2c). This is the most stable polytype of SnS_2 is termed 2H (using the Ramsdell nomenclature), a label that is often confused with the 2H phase

in TMDCs, where the metal exhibits trigonal–prismatic coordination. Using the notation common to TMDCs, the $P\bar{3}m1$ SnS_2 structure is denoted 1T.

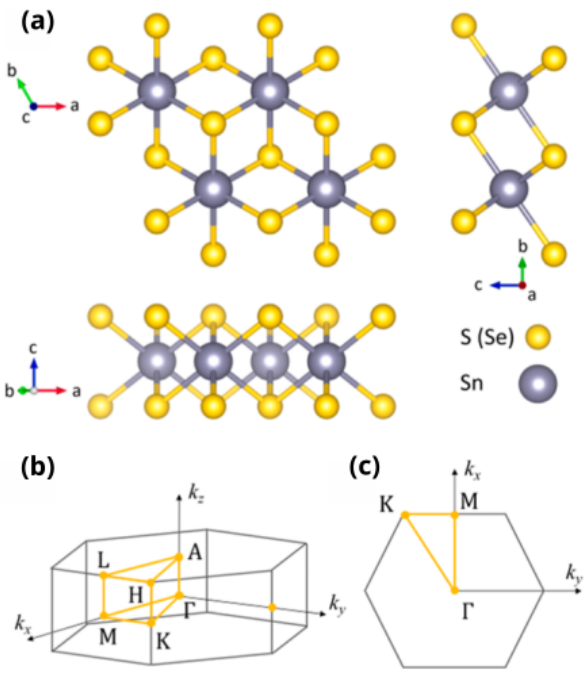


FIGURE 5.2 : Crystal structure and reciprocal-space geometry of SnS_2. (a) Schematic representation of the atomic structure of SnS_2, showing the top view of the layer plane and side views along the principal crystallographic axes. (b) Illustration of the first Brillouin zone (BZ) of the reciprocal lattice, and (c) two-dimensional projection onto the central plane of the three-dimensional unit cell. Adapted from [2] under CC-BY 4.0 license.

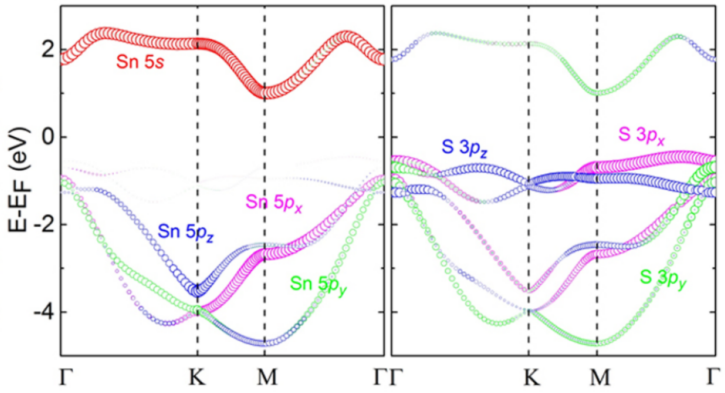


FIGURE 5.3 : Orbital-resolved band structure of SnS_2. Calculated orbital-projected band structure of multilayer SnS_2 where the contributions from Sn and S orbitals are indicated by color : Sn s (red), S p_x (pink), p_y (green), and p_z (blue). The size of each symbol reflects the corresponding orbital weight. Adapted from [78], with permission from the publisher.

The orbital-resolved band structure obtained from DFT calculations for SnS_2 is presented in Fig. 5.3[78]. The electronic states are primarily derived from the s orbital of Sn and p orbitals of S atoms. A detailed examination reveals that the valence-band maximum (VBM) lies slightly away from the Γ point, where the first and second valence bands are doubly degenerate. These states

originate mainly from the p_x and p_y orbitals of the top and bottom S atoms, which are symmetric with respect to the inversion center. At lower energy levels, an additional pair of doubly degenerate bands appears, arising from p_x and p_y orbitals of both Sn and S atoms. The conduction-band minimum (CBM), in contrast, is located at the M point and is dominated by the s orbital contributions of Sn atoms.

5.2.3 Gap states

In an ideal crystalline semiconductor, the periodic arrangement of atoms gives rise to well-defined electronic bands separated by forbidden energy gaps. Within the allowed bands, the probability of finding an electron in any unit cell remains identical due to perfect three-dimensional translational symmetry. However, this symmetry is disrupted at the crystal surface, where termination of the lattice along the direction normal to the surface breaks periodicity. As a result, the surface unit cells become inequivalent to those in the bulk, and electronic states localized near the surface—commonly known as surface states—can emerge. The formation of such surface-localized states can be further enhanced by additional structural or chemical perturbations. Typical examples include the presence of dangling bonds, surface reconstruction or relaxation (where atomic positions and bonding configurations adjust to minimize surface energy), atomic steps and kinks, or adsorbed impurity atoms. Similar localized electronic states can also occur at semiconductor interfaces due to analogous symmetry-breaking and bonding effects.

Although TMDCs are 2D layered materials stacked via van der Waals–bond forces are largely free from dangling bonds. However, structural imperfections/defects are natural while growing the sample. These defects, intrinsic or extrinsic, create gap states within the bandgap, which profoundly influence the optical, electrical, and chemical properties of the material. Common defect types in TMDCs include : (i) vacancies—missing chalcogen (S, Se, Te) or metal atoms, with chalcogen vacancies being the most prevalent; (ii) antisite defects—where a chalcogen atom occupies a metal site or vice versa; (iii) adatoms and substitutional impurities—foreign atoms that adsorb on or replace lattice atoms, altering carrier density and introducing new electronic levels; (iv) grain boundaries—disordered interfaces between crystal domains composed of non-hexagonal ring structures; and (v) edge defects—present along armchair or zigzag terminations of TMDC flakes, each exhibiting distinct electronic characteristics etc. Defects thus play a dual role in determining material functionality. On one hand, they can act as charge traps, scattering centers, or nonradiative recombination sites, degrading carrier mobility and optoelectronic performance. On the other hand, they may introduce desirable functionalities—such as sub-gap emission centers, catalytic sites, or dopant-like behavior—that can be harnessed for tailored electronic and photonic applications.

5.2.4 Band bending

The concept of band bending was introduced by Schottky and Mott to explain the rectifying behavior observed in metal–semiconductor contacts[38]. Band bending is a common phenomenon in semiconductors, particularly at semiconductor–metal interfaces and in heterostructure materials. It can arise in various situations; however, for this project, our primary focus is on surface-state-induced band bending.

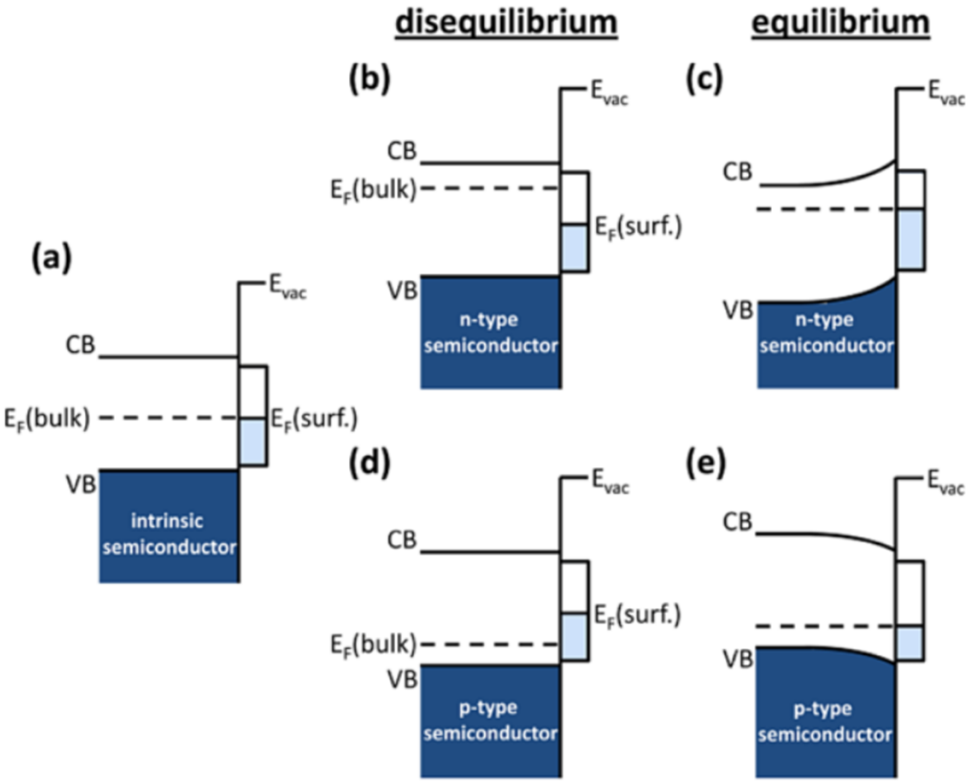


FIGURE 5.4 : Surface band bending in semiconductors. Schematic illustration of the electronic energy levels near the surface of a clean semiconductor : (a) intrinsic (undoped) semiconductor; (b) nonequilibrium/disequilibrium and (c) equilibrium conditions for an n-type semiconductor; (d) nonequilibrium and (e) equilibrium conditions for a p-type semiconductor. Adapted from Ref.[38], with permission from the publisher.

Figure 5.4 illustrates the concept of band bending in typical scenarios. In Fig. 5.4a, we show the case of an intrinsic (undoped) semiconductor, where the bulk Fermi level E_F (bulk) is located at the midgap, and the surface state Fermi level E_F (surface) is assumed to also be at midgap. Since E_F (bulk) $= E_F$ (surface), no charge transfer occurs between the bulk and surface states. For an n-type semiconductor, E_F (bulk) lies closer to the conduction band and is therefore above E_F (surface), as shown in Fig. 5.4b under disequilibrium conditions. To reach equilibrium, electrons transfer from the bulk to the surface states, causing E_F (bulk) to decrease and E_F (surface) to increase, resulting in upward band bending (Fig. 5.4c). The charge accumulated in the surface states is supplied by the bulk region near the surface, which is referred to as the space charge

region. Since this region is depleted of electrons in an n-type semiconductor, it is also called the depletion layer. This creates an internal electric field pointing from the bulk to the surface within the space charge region. In a p-type semiconductor, E_F (bulk) is closer to the valence band and thus below E_F (surface) under disequilibrium (Fig. 5.4d). To reach equilibrium, electrons transfer from the surface to the bulk, leading to accumulation in the space charge region. The resulting built-in electric field points from the surface to the bulk, causing downward band bending.

5.2.5 Surface Photovoltage

Surface Photovoltage (SPV) is an illumination-induced change in the surface potential of a semiconductor. This effect arises from charge transfer or redistribution within the space-charge region under incident illumination. It is important to note that the formation of an SPV requires that carrier generation is followed by a net spatial redistribution of charge. The SPV strongly depends on whether the excitation energy is super-bandgap or sub-bandgap.

In the case of an n-type semiconductor with upward band bending, electrons are driven away from the bulk and accumulate near the surface. This transfer leaves behind positively charged ionized donor atoms, forming a positively charged depletion region and a built-in electric field pointing from the bulk toward the surface. This electric field, in turn, pushes electrons back toward the bulk, creating an energy barrier that causes the bands to bend upward. Conversely, in a p-type semiconductor, electrons accumulate in the bulk, generating an electric field from the surface to the bulk, which causes the bands to bend downward.

Upon illumination with photon energies exceeding the bandgap (super-bandgap), photogenerated electron and hole carriers redistribute within the band-bending region, typically partially screening the internal electric field. This reduces the band bending and results in the surface photovoltage (SPV) effect [38, 40, 43]. Figure 5.5 illustrates the SPV effect in conventional p-type and n-type semiconductors under super-bandgap illumination.

However, under sub-bandgap excitation, the probability of direct valence to conduction bulk band transitions is negligible. Instead, transitions occur between surface defect states and the bulk bands. We consider that these defect/surface states are associated with a trap state E_T. Fig. 5.6 illustrates the possible transitions between trap states and bulk states in conventional p-type and n-type semiconductors, along with the corresponding SPV effects. In Fig. 5.6a and 5.6c, photon excitation with energy greater than the difference between the conduction band E_C and the trap state E_T can promote electrons from E_T to E_C. This transition reduces the band bending in both p-type (Fig. 5.6a) and n-type (Fig. 5.6c) semiconductors, leading to a flattening of the bands and a corresponding increase or decrease of the SPV signal, respectively. Conversely, transitions from the valence band to the trap states increase band bending. This results in a decrease of the SPV signal in p-type semiconductors (Fig. 5.6b) and an increase in n-type semiconductors (Fig. 5.6d).

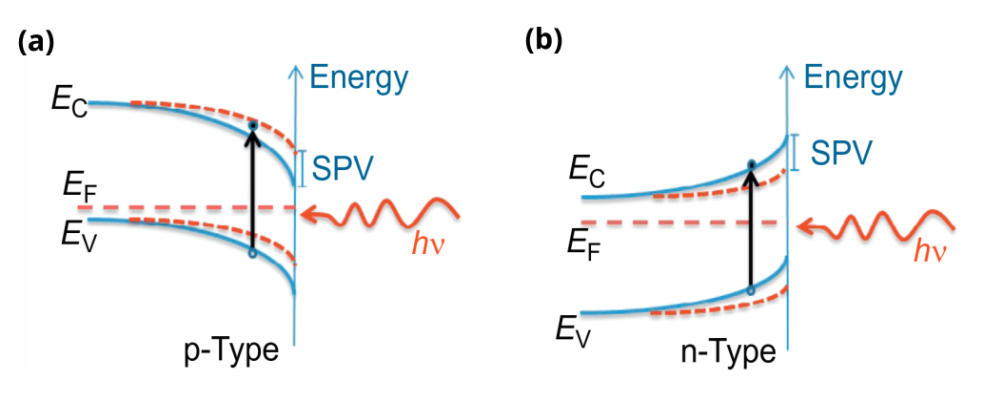


FIGURE 5.5 : Surface photovoltage response under super-bandgap excitation. Schematic illustration of the surface photovoltage (SPV) effect in (a) p-type and (b) n-type semiconductors following super-bandgap photoexcitation. Adapted from [79]

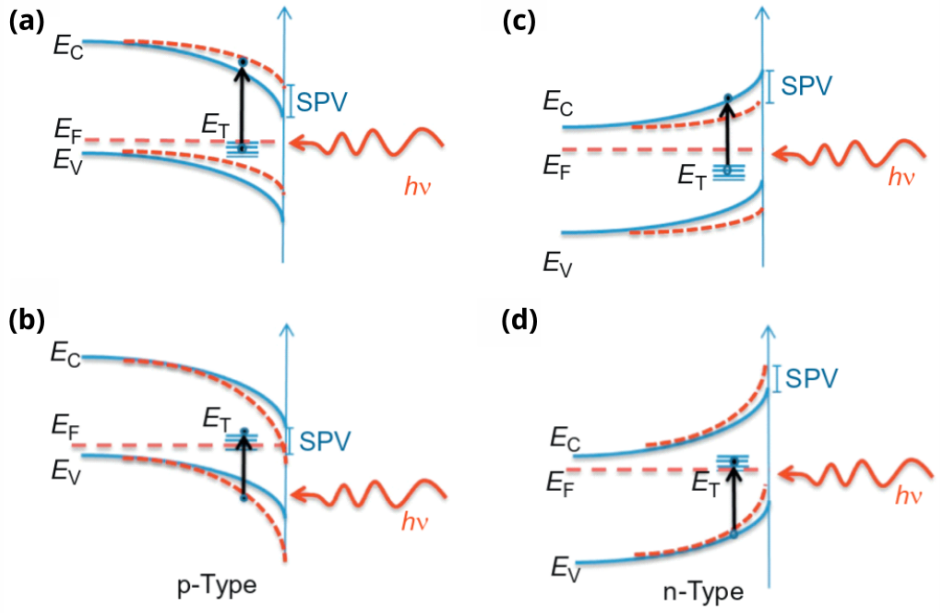


FIGURE 5.6 : Surface photovoltage under sub-bandgap excitation mediated in the presence of surface defect states. (a,b) Schematic illustration of the surface photovoltage (SPV) effect in a p-type semiconductor and (c,d) an n-type semiconductor in the presence of surface defect (trap) states under below-bandgap excitation. Panels (a) and (c) depict photoinduced electron transfer from the trap states into the conduction band, resulting in a redistribution of surface charge and a modification of band bending. Panels (b) and (d) illustrate where optical excitation promotes electrons from the valence band into trap states, leading to an opposite SPV response. Adapted from Ref.[79], with permission from the publisher.

5.3 Results and discussion

5.3.1 Experimental Methodology

Figure 5.7a shows a schematic of the experimental setup and associated photoemission geometry. Time- and polarization-resolved ARPES measurements were performed at the Centre Lasers Intenses et Applications (CELIA) laboratory. We use a commercial high-repetition-rate (166 kHz) ytterbium (Yb) fiber laser from Amplitude (Tangerine SP) operating at 1030 nm with a pulse duration of 135 fs (FWHM) and average power of 50 W. For the probe, we generate the 9th harmonic of the frequency-doubled (second harmonic) fundamental pulses, leading to 21.6 eV extreme ultraviolet (XUV) pulses. For the pump, we use a small portion of the infrared (IR) fundamental (1.2 eV). Both the pump and probe are fully polarization-tunable. The samples are mounted on a motorized six-axis hexapod inside an ultra-high vacuum (UHV) chamber with a base pressure of 2×10^{-10} mbar, at room temperature. Photoemitted electrons are collected using a custom time-of-flight momentum microscope (GST mbH) [80] that allows simultaneous detection of electrons across the full surface Brillouin zone over an extended binding energy range [81]. Post-processing of the acquired data was carried out using an open-source workflow [82, 83], which enables efficient conversion of raw single-event data into binned, calibrated data hypervolumes of the desired dimensions. More details about our instrument are provided in chapter 3.

Figure 5.7b presents constant energy contours (CECs) at various binding energies for photoexcited SnS_2 : CEC taken near E_{VBM} shows the momentum distribution of the valence band maximum (VBM) located in the vicinity of Γ high-symmetry point, CEC taken at an energy within the bandgap ($E - E_{\mathrm{VBM}}$ = 0.66 eV) indicates the presence of in-gap states, whereas the CEC at $E - E_{\mathrm{VBM}} = 2.6$ eV is associated with excited states located around the conduction band minima at the M points.

5.3.2 Band Structure Mapping and XUV Photoemission Linear Dichroism

We start by presenting static band structure mapping, along with the associated XUV photoemission linear dichroism, to reveal the band dispersion and the in-plane and out-of-plane orbital character underlying the electronic structure of SnS_2. We conducted polarization-resolved measurements by recording the energy- and momentum-dependent photoemission intensity while continuously rotating the angle of the XUV linear polarization axis, as described in Ref. [84]. Figure 5.8 presents the photoemission intensity along M–Γ–M and K–Γ–K high-symmetry directions. Consistent with previous reports [1, 85], the spectra reveal a broad manifold of S 3p valence-band states within the top 2 eV below VBM (located at Γ), with relatively stronger dispersion along M–Γ–M than along K–Γ–K. More specifically, Figs. 5.8a,b present energy-momentum cuts along

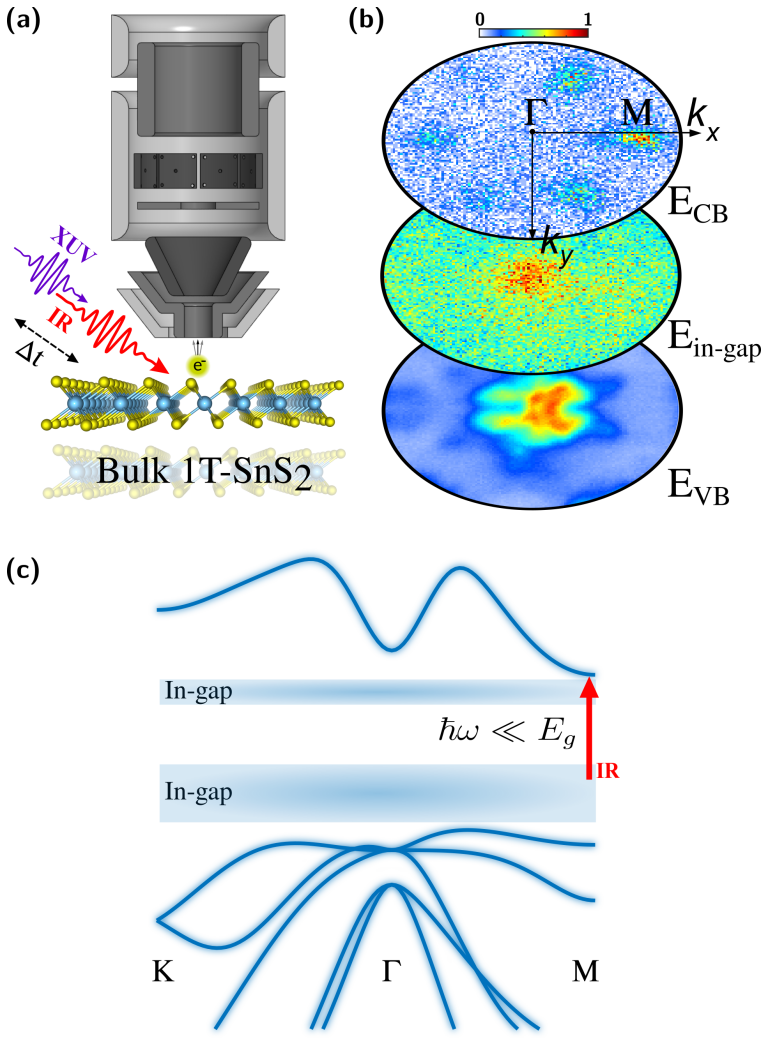


FIGURE 5.7 : Schematic of the experiment. (a) An infrared (p-polarized, 1.2 eV) pump and a polarization-tunable XUV (s- or p-polarized, 21.6 eV) probe pulses are focused onto an SnS_2 sample in the interaction chamber of a time-of-flight momentum microscope, which allows measuring the time-, energy- and momentum-resolved photoemission intensity. (b) Constant energy contours (CECs) for different binding energies in photoexcited SnS_2. The light scattering plane is aligned with the crystal mirror plane, *i.e.* along the Γ-M direction. (c) Schematic representation of the electronic band structure and the photoexcitation process mediated by in-gap states in SnS_2.

M-Γ-M measured using p- and s-polarized XUV, respectively, while Figs. 5.8d,e display the corresponding cuts along K-Γ-K high-symmetry direction.

Previous orbital-resolved band structure calculations indicate that near the Fermi level, the dominant contribution to electronic states originates from the S atoms [78]. Along M-Γ-M, the uppermost valence band (VB) is predominantly composed of in-plane orbitals (p_x and p_y), whereas the second uppermost VB mainly consists of out-of-plane p_z orbitals. In contrast, along K-Γ-K, the uppermost VB exhibits an in-plane orbital character at Γ but transitions to an out-of-plane configuration (p_z) as it approaches the K point. The LDAD differential maps (p-s) reveal a strong dichroic response, with red and blue regions indicating enhanced photoemission for p- and s-polarized light, respectively (Fig. 5.8c and f). Along M-Γ-M (Fig. 5.8c), the dominant positive dichroic features at

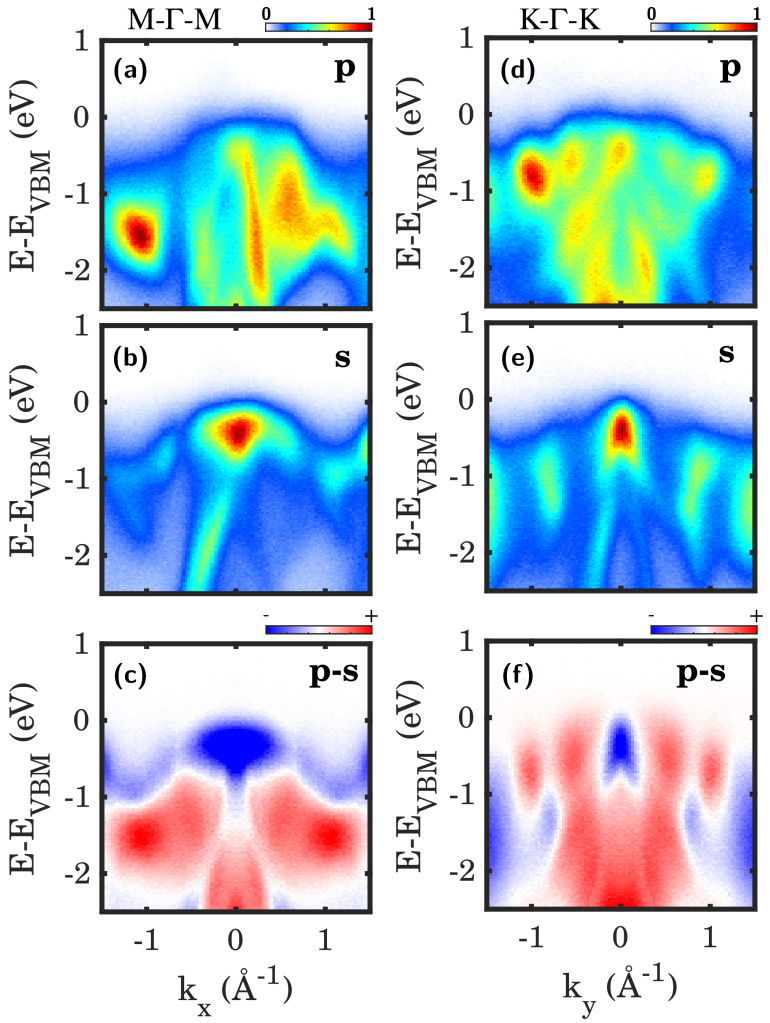


FIGURE 5.8 : Band mapping and XUV photoemission linear dichroism of SnS_2. Static band structure mapping of SnS_2 along M-Γ-M and K-Γ-K directions using p- and s-polarized XUV probe pulses. (a) and (b) Energy-momentum cuts along M-Γ-M measured with p- and s-polarized light, respectively. (c) XUV LDAD obtained by subtracting the corresponding photoemission intensities. (d) and (e) Energy-momentum cuts along K-Γ-K measured with p- and s-polarized light, respectively. (f) XUV LDAD extracted analogously for K-Γ-K.

higher binding energies (lower VB) suggest significant contributions from p_z orbitals, which are preferentially photoemitted by p-polarized light. Conversely, the uppermost VB, which is shown to have in-plane (p_x, p_y) character, exhibits a clear negative differential (blue) response, indicating its stronger photoemission intensity when using s-polarized XUV light. A similar trend is observed along K-Γ-K (Fig. 5.8f), where the in-plane orbital character near Γ manifests as a negative differential (blue) response, while the transition to out-of-plane (p_z) character near K leads to a strong positive differential response (red). The XUV LDAD, shown in Figs. 5.8c,f, thus exhibits good agreement with the DFT-predicted in-plane and out-of-plane orbital texture from Ref. [78].

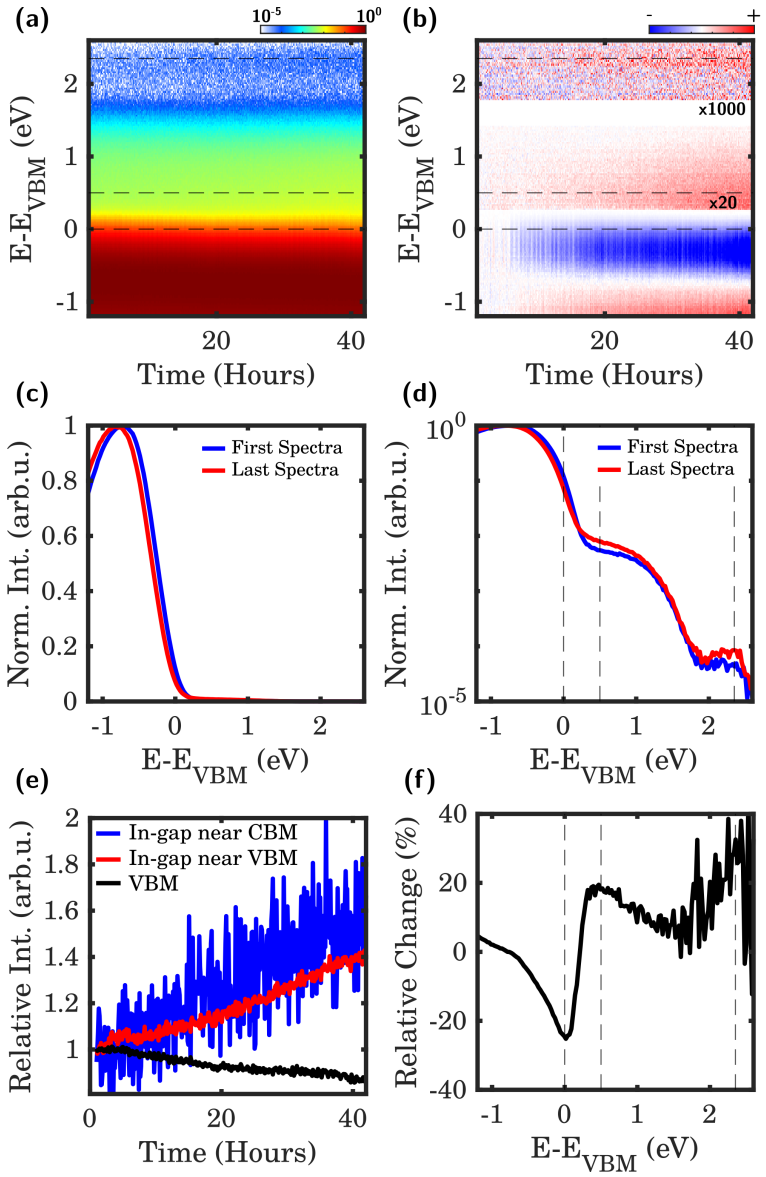


FIGURE 5.9 : Long-term evolution of photoemission spectra following SnS_2 surface cleavage. (a) Momentum-integrated photoemission intensity at the pump-probe overlap as a function of acquisition time following surface cleavage, over 42 hours. (b) Associated differential photoemission intensity obtained by subtracting the initial 4 hours of data, highlighting the increasing spectral weight of in-gap states near the conduction band minima (CBM) and valence band maximum (VBM), as well as the energy downshift of the VB. (c) Comparison of the energy distribution curves (EDCs) from the first and last spectra, revealing a downward energy shift of the VB. (d) Logarithmic-scale EDCs (same as (c)) further emphasize the downward energy shift of the VB, as well as the increase of in-gap state photoemission intensities. (e) Photoemission intensity evolution of around the VBM (black), in-gap states near the VBM (red), and in-gap states close to the CBM (blue). (f) Normalized difference of photoemission intensity between the first and last scans, showing depletion at the VBM and a significant increase in in-gap states.

5.3.3 In-Gap States and Band Bending

Next, we explore the presence of in-gap states in SnS_2 and highlight their direct impact on surface band bending. To do so, we measured the evolution of photoemission spectra over more than

40 hours following sample cleavage. Fig. 5.9a shows momentum-integrated photoemission intensities as a function of time after cleaving the sample, revealing the presence and evolution of two broad in-gap state manifolds within the bandgap of SnS_2 : (i) a broad photoemission feature that extends from the valence band maximum (VBM) to $\mathrm{E} - \mathrm{E_{VBM}} = 1.5$ eV (ii) another sharper photoemission feature is visible approximately 2.4 eV above the VBM, located just below the conduction band minimum (CBM). It should be noted that these two in-gap state manifolds are already present immediately after cleaving the sample. The presence of such in-gap spectral weights is in agreement with previous findings in SnS_2 [2, 31]. In Fig. 5.9b, to emphasize variation of photoemission intensity following sample cleavage, we plot the differential momentum-integrated photoemission intensity by subtracting, from each recorded spectrum, the mean signal obtained during the initial four hours of measurement. Photoemission intensity associated with both in-gap states exhibits an increasing differential intensity (red), indicating a growing spectral weight over time. On the same time scale, the valence band exhibits a shift towards higher binding energy (energy downshift), leading to a strong build-up of negative differential intensity near VBM. Fig. 5.9e quantifies the photoemission intensity variations from the VB, in-gap states slightly above the VBM, and in-gap states slightly below CBM as a function of time. Complementary ways to look at the data are presented in Fig. 5.9c,d and f. Indeed, Fig. 5.9c, which compares the energy distribution curves (EDCs) acquired during the first and last hour of the scan, shows a clear downward shift (towards higher binding energies) of the VB. Additionally, in Fig. 5.9d, we plot the same EDCs on a logarithmic scale, further confirming the increasing photoemission intensity of the in-gap states. In Fig. 5.9f, we quantitatively capture the relative modification of the spectral weight between the first and last hour of the long-term scan by taking the normalized difference between the first and last EDCs. As already observed in Fig. 5.9 a-e, Fig. 5.9f confirms the spectral downshift of the VBM concomitant with the build-up of in-gap spectral weight. It should be noted that while our technique allows for capturing the unambiguous increase of in-gap spectral weights, it is difficult to provide an estimate of the absolute defect state densities.

The observations reported above point to a downward band bending, similar to what has been reported in some topological insulators and semiconductors [86–95]. Our measurements also reveal that the VB downward band bending is enhanced with the increasing spectral weight of in-gap states. Previous studies on SnS_2 have shown that these in-gap states originate primarily from sulfur vacancies, with a smaller contribution from Sn interstitials. Both types of defects introduce donor-like states [2, 31, 34].

One illustrative example showing similar physics is the case of alkali-metal-doped black phosphorus. Since alkali atoms act as electron donors, an n-type surface region forms, resulting in downward band bending from bulk to surface (upward band bending would occur for acceptor surface doping) [94, 95]. Similarly, in the topological insulator Bi_2Se_3, positively charged Se vacancies act as donors, inducing n-type doping and downward surface band bending [89, 96]. By analogy, donor-like sulfur vacancies in SnS_2 likely play a similar role, donating electrons and generating downward band bending. Theoretical calculations on Bi_2Se_3 further indicate that surface

Se vacancies can rearrange charge in a manner comparable to K adsorption [91], suggesting that donor-like defects in SnS_2 function analogously to alkali atoms in black phosphorus. Consistently, recent studies on n-type $SnSe_2$, which has a closely related electronic structure to SnS_2, support this scenario [97]. Transport measurements and Raman spectroscopy on $SnSe_2$ reveal a temperature- and thickness-dependent insulator-to-metal transition, attributed to intrinsic n-type doping from selenium vacancies. These donor-like surface states induce downward band bending near the surface, in agreement with our observations in SnS_2.

5.3.4 Pump-Induced Dynamical Surface Photovoltage

Having established surface-defect-driven downward band bending, we next investigate how photoexcitation influences this band bending through the pump-induced dynamical surface photovoltage (SPV) effect in SnS_2. To do so, we performed measurements over a large pump-probe delay range, i.e., from -50 ps to 50 ps, for pump fluence ranging between 0.5 and 3.9 mJ/cm^2 (Fig. 5.10). By integrating the photoemission intensity over all momenta at very early negative (between -50 ps and -30 ps, blue dots in Fig. 5.10a) and very late positive (between 30 ps and 50 ps, red dots in Fig. 5.10a) pump-probe delays, we observe a distinct light-induced upward energy shift of the VB due to SPV. To quantify this VB energy shift induced by the SPV, we performed a double-Gaussian fitting of the VB (Fig. 5.10a), as a function of pump-probe delay, for each pump fluence. In Fig. 5.10b, we show the time-resolved dynamics of the SPV-induced VB energy shift as a function of pump fluence. First, we observe that the time-domain behavior of the SPV shift is characterized by a pronounced linear energy upshift starting at very early negative time delays, followed by a sudden change in slope at time zero. These observations are very similar to SPV dynamics observed in bulk-insulating topological insulators [41], where the negative delay dynamics have been attributed to electromagnetic interactions between SPV-induced fields at the surface with the photoelectrons, occurring in vacuum. The timescale of these negative delays energy shift is known to be dictated by the photoelectrons' kinetic energy as they travel away from the sample in vacuum, along with the geometry of the pump spot [41, 98]. Furthermore, the SPV-induced shift exhibits an approximately linear dependence on pump fluence, attaining 70 meV at 3.9 mJ/cm^2. This stands in contrast to the logarithmic behavior observed in, e.g., topological insulators [41], which was reported under significantly lower fluences. However, it was recently shown that this logarithmic scaling of the SPV shift with fluence is not universal. Indeed, Roth and coworkers recently demonstrated a dynamical nonlinear inversion of the surface photovoltage in p-doped Si(001) [43], highlighting that the fluence-dependent behavior of surface photovoltage, more specifically in the high fluence regime, is a complex phenomena that does not follows simple scaling laws.

Based on the experimental observations reported up to this point, the following conclusions can be drawn : (i) surface donor defects are leading to the emergence of in-gap states and are driving a downward band bending, and (ii) upon IR photoexcitation, a dynamical SPV leads to an energy upshift of the photoemission spectra, i.e. counterbalancing the surface band bending present at

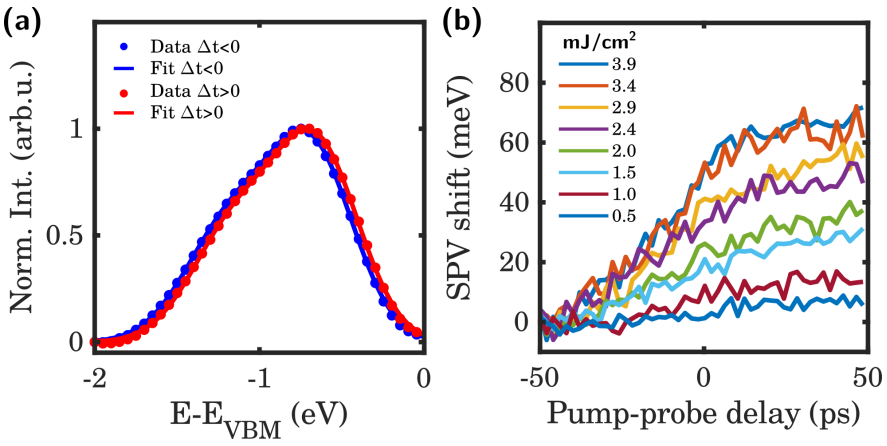


FIGURE 5.10 : Time-resolved and fluence-dependent surface photovoltage in SnS_2. (a) Momentum-integrated photoemission intensity of the valence band integrated before the pump excitation (between -50 ps and -30 ps, blue dots) and after the pump excitation (between 30 ps and 50 ps, red dots) with the corresponding double Gaussian fitting (red and blue lines), showing a clear upward energy shift due to the SPV effect. (b) Extracted SPV energy shift from the Gaussian fittings as a function of the pump-probe delay for different pump fluences.

equilibrium. In this case, it is not trivial to explain how exactly photoexcitation redistributes charge in the band bending region. Indeed, since the in-gap defect states are localized at the surface and the band bending is downward, the relevant physics most likely occurs near the surface. Electrons originating from these in-gap states and being photoinjected into the downward-bent conduction band probably remain confined close to the surface. Based on our observations, this photoexcitation process appears to lead to a compensation of the electric field responsible for the downward band bending at equilibrium.

While the microscopic mechanism associated with carrier redistribution following photoexcitation is surely different, our observations, i.e., downward band bending and light-induced upward SPV, are similar to prior reports on alkali-doped black phosphorus [94, 95]. Indeed, these studies demonstrated that the strong surface electric dipole and associated downward band bending induced by alkali-dopant can be compensated under illumination through the emergence of light-induced SPV. Under the preexisting electric field, photogenerated electrons and holes are redistributed within the space-charge region, generating a compensating potential that reduces (or even neutralizes) the intrinsic band bending. However, it is important to note that surface defect-mediated band banding and light-induced surface photovoltage are strongly material and dopant-type-dependent. Indeed, in a very recent study, Abdul-Aziz and coworkers have shown that in $PdSe_2$, surface Se vacancies are negatively charged, leading to upward band bending and subsequent upward light-induced surface photovoltage [99], which is exactly opposite to what we measured in SnS_2.

5.3.5 Surface Photovoltage Correction Method

After establishing and quantifying the pump-induced SPV dynamics, we describe a methodology to correct for the SPV-induced rigid energy shift in the data, with the goal of disentangling it from the light-driven ultrafast carrier dynamics. Figure 5.11a shows the momentum-integrated photoemission intensity as a function of pump–probe delay (between -1 ps to 10 ps), with the corresponding normalized differential map (Fig. 5.11c), obtained by normalizing the photoemission intensity at each energy, and then subtracting the signal at negative delays.

The resulting time-resolved differential map (Fig. 5.11c) is dominated by the pump-induced SPV rigid energy upshift, which appears as long-lived alternating positive and negative features, but it also contains more subtle signatures of ultrafast light-induced carrier dynamics. To correct for the SPV-induced rigid energy upshift, we fit the time-dependent energy position of the valence band (VB) and applied an opposite, time-dependent rigid energy downshift to the entire spectrum. Interestingly, our time-dependent Gaussian fitting of the VB also reveals an additional broadening of the VB, which evolves on a timescale comparable to the SPV shift. Nevertheless, this procedure allows the removal of the dominant effect of the SPV from the data, namely the time-dependent rigid energy upshift of the photoemission spectra. The corrected time-dependent spectra and the corresponding differential maps are shown in Figs. 5.11b and d.

The detailed procedure for correcting the SPV-induced rigid energy upshift is described as follows. For each pump-probe delay at a given pump fluence, the intensity of the valence band is computed by integration over all momenta. A background is subtracted from the resulting signal : we use an iterative Shirley background, a method commonly used in photoelectron spectroscopy[100]. Then this intensity of the valence band I as a function of the binding energy E is fitted with a double Gaussian model :

$$I(E) = a \exp\left(-\frac{E-b}{c^2}\right) + \alpha a \exp\left(-\frac{(E-(b+\beta))^2}{(\gamma c)^2}\right). \tag{5.1}$$

The coefficients of the second Gaussian are related to the coefficients of the first Gaussian; we therefore have three free parameters : the amplitude a, the shift b and the width c. The coefficients α, β and γ were determined using a fit of the first pump-probe delay using Eq. 5.1 with 6 free parameters. These values were consistent with the fittings of all the other delays. The SPV shift is defined as the coefficient b. An example of such a fitting is presented in Fig. 5.12 (obtained with a pump fluence of 4.1 mJ/cm^2, 1030 nm, 141 fs, at a pump-probe delay of -1 ps).

This analysis is then reproduced at every pump-probe delay in order to obtain the temporal evolution of the SPV shift. This evolution is presented in Fig. 5.13 with a pump fluence of 4.1 mJ/cm^2. This fitting procedure has also been applied to different pump fluences in order to obtain the evolution of the SPV shift as a function of the pump fluence and of the pump-probe delay (see Fig.4(b) in the main text).

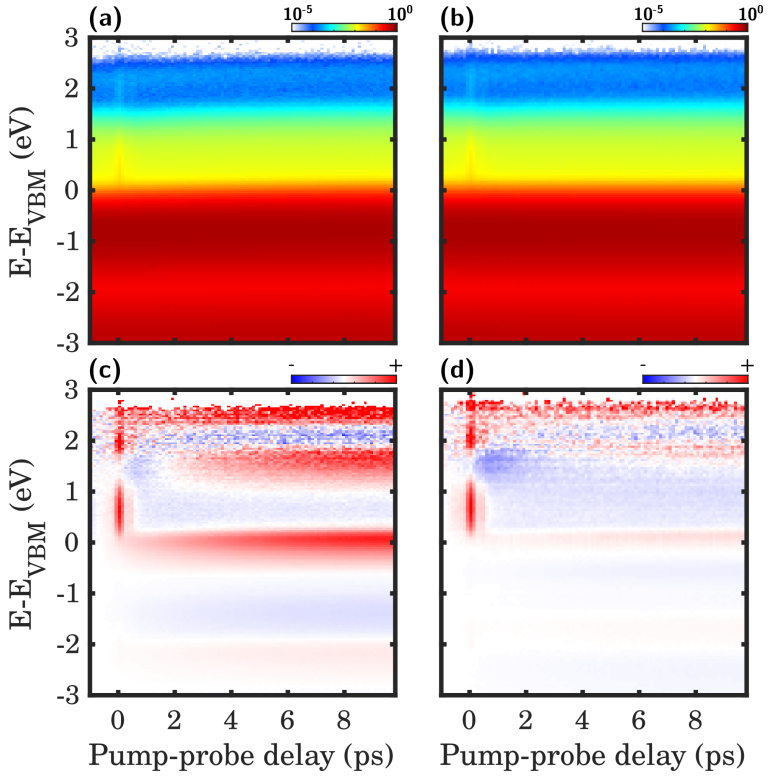


FIGURE 5.11 : Effect of SPV rigid energy shift correction on time-resolved photoemission spectra. (a) and (b) Momentum-integrated photoemission intensity as a function of pump-probe delay, before and after applying the rigid energy shift correction, respectively. (c) and (d) Differential (pre-time-zero signal subtracted) momentum-integrated photoemission intensity as a function of pump-probe delay, before and after applying the rigid energy shift correction, respectively.

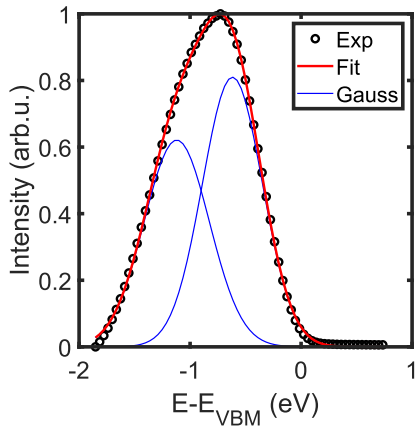


FIGURE 5.12 : Fitting of the valence band intensity. Example of a double Gaussian fitting of the valence band following Eq. 5.1 to extract the SPV rigid shift. The black points are experimental data, the red curve is the double Gaussian fitting and the two blue curves are the two single Gaussians used in the fitting.

The SPV shift is then applied to the raw data at each pump-probe delay in order to correct these shifts in the Figs. 5.11b,d. To do so, at each pump-probe delay of a given scan, we rigidly shifted the energy axis of the value of the SPV shift. Because of the small shift values, we first interpolated the original data in order to enhance the number of pixels that it contains ($\times 100$). We also applied

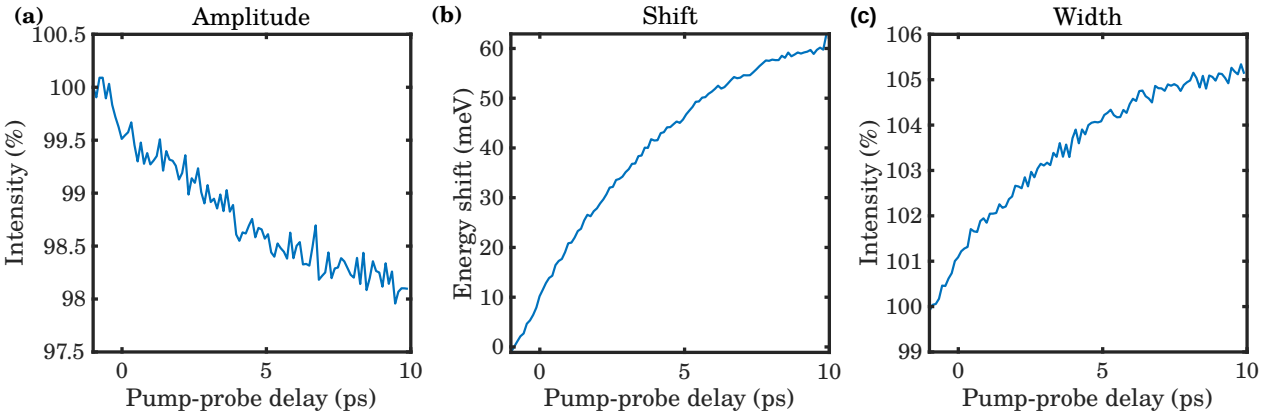


FIGURE 5.13 : Surface photovoltage shift. (a) is the amplitude coefficient, (b) is the the shift coefficient and (c) is the width coefficient. The SPV shift is defined as the b coefficient. The evolution of the width shows that the SPV also induces a band broadening.

a multiplying factor (1.125) for a better SPV correction. It is worth noting that we only corrected the SPV shifts and not the amplitude and the width leading to a broadening of the bands.

5.3.6 Conduction Band Mapping and Ultrafast Carrier Dynamics

After correcting for the SPV-induced rigid energy upshift in the data, we can now focus on the investigation of the light-induced ultrafast carrier dynamics. Since our pump photon energy is well below the bandgap, photoexcitation of carriers to the conduction band can only be mediated via in-gap states. This is the reason why most of the interesting dynamics in the SPV-corrected differential maps lie above $E - E_{\mathrm{VBM}}$ = 1 eV. In Fig. 5.14a and b, we thus show the time-resolved momentum-integrated photoemission intensity and associated differential maps (SPV rigid shift corrected) in a restricted energy range (between 1 eV and 2.9 eV above VBM). In the differential maps (Fig. 5.14b), four dominant features can be distinguished : (i) strong and extremely short-lived positive (red) differential signals around time-zero, at energy near 1 eV and above 2 eV, which originate from laser-assisted photoemission (LAPE) from the VB and in-gap states, respectively. This is a non-resonant two-photon process that reflects the optical cross-correlation between IR pump and XUV probe pulses, and allows for a precise *in-situ* determination of the time zero and the time-resolution of the experiments, (ii) a pronounced short-lived depletion of in-gap states around 1.5 eV (between the two red dashed lines), (iii) negative differential signal accumulation close to the in-gap states below the CBM (between the two orange dashed lines), and (iv) concomitant appearance of positive differential signal (red) above 2.5 eV (between the two black dashed lines), which is associated with the excited states population in the CB. Indeed, by looking at the CECs for energy above 2.5 eV (Fig. 5.14d), we can see the accumulation of excited carriers in the CBM at the M-points. Our results thus demonstrate that photoexcitation with a 1.2 eV sub-bandgap pump populates the CB by promoting electrons from the in-gap states. Moreover, these results confirm the indirect nature of the bandgap in this semiconductor, where VBM is located in the vicinity of Γ,

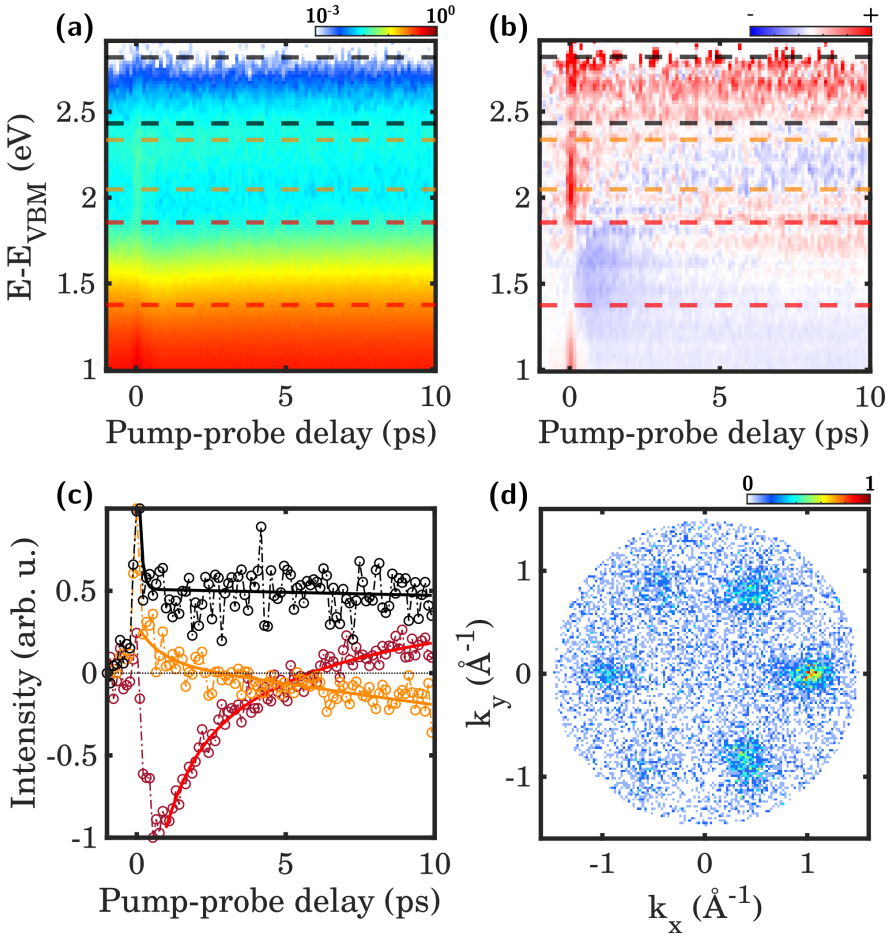


FIGURE 5.14 : In-gap states and conduction band dynamics. (a) Momentum integrated photoemission intensity as a function of pump-probe delay, after applying the SPV rigid energy shift correction. The dashed lines indicate regions of interest (ROIs) associated with the conduction band (black) and in-gap states slightly below the CBM (orange) and above the VBM (red), respectively. (b) Associated time-resolved differential spectrum, i.e., pre-time-zero signal substracted. (c) Temporal evolution of the excited (black) and in-gap (orange and red) states. Dotted lines are experimental data, and solid lines are double exponential fittings. (d) Constant energy contour at the energy of the conduction band, i.e., integrated between 2.4 eV and 2.8 eV, showing the momentum-space localization of the excited carrier at the M pockets.

while CBMs are located at the Brillouin zone edge, i.e., at M high-symmetry points. Additionally, it is interesting to mention that DFT calculations for SnS_2 indicate that the matrix element for VB–CB interband optical transitions nearly vanish at M high-symmetry points, implying intrinsically weak resonant transitions from VB to CBM [2]. The in-gap states thus facilitate optical transition to the CB and enhance infrared and visible light absorption, consistent with prior reports linking them to the photocatalytic activity of SnS_2 [24].

Next, to gain further insight into the ultrafast carrier dynamics, we integrate the photoemission intensity over three regions of interest marked by dashed lines in Fig. 5.14a,b : (i) black, corresponding to electron dynamics in the CB, (ii) orange, tracking the dynamics near the in-gap states slightly below the CBM, and (iii) red, associated with ultrafast dynamics within the in-gap states above the valence-band maximum (VBM). Time-resolved photoemission intensities from these three regions of interest are shown in Fig. 5.14c. The electron dynamics within the conduction

band feature a very sharp and short-lived increase during the cross-correlation between pump and probe, which originates from LAPE, as discussed in the previous section. More interestingly, it reveals long-lived conduction band (CB) population dynamics that do not decay within the time scale of our pump–probe scan (black curve), suggesting a lifetime way longer than tens of picoseconds. The dynamics within the energy window where the optical transition takes place (red curve) show drastically different behavior. Indeed, it is characterized by a strong depletion (negative differential signal) following photoexcitation, followed by a recovery that can be fitted by a double-exponential function with a fast ($\tau_f = 947 \pm 204$ fs) and a slower component ($\tau_s = 5.2 \pm 0.3$ ps). In contrast, the in-gap states located just below the conduction-band minimum (orange curve) display a different trend : a rapid and short-lived increase of photoemission intensity during the optical cross-correlation due to LAPE, followed by an increasing depletion at extended pump–probe delay, that can also be fitted using a double-exponential function with a fast ($\tau_f = 743 \pm 173$ fs) and a slower component ($\tau_s = 51 \pm 2$ ps). While pinning down the complete mechanism of ultrafast carrier redistributions from these data is challenging, a plausible scenario can be deduced : (i) first, optical excitation creates photoholes in the lower in-gap states and long-lived excited electrons in the CB, and (ii) scattering of the photohole from the lower to high in-gap states, leading to photohole accumulation within in-gap states near the CBM.

5.3.7 Conclusions

In this work, we performed time-, angle-, and polarization-resolved photoemission spectroscopy to investigate the electronic structure and ultrafast light-induced dynamics in the layered van der Waals semiconducting SnS_2. The linear dichroic XUV ARPES measurements provided experimental characterization of the in-plane and out-of-plane nature of orbital texture underlying the electronic band structure of SnS_2. Moreover, we provide direct evidence of defect-induced in-gap states leading to a downward band bending. This band bending can be partially and transiently counterbalanced by light-induced surface photovoltage. We demonstrate that in-gap states enable optical injection of long-lived carriers into the conduction band via below-bandgap infrared photoexcitation. These findings underscore the central role of donor-like defects in shaping both the static electronic structure and nonequilibrium light-induced dynamics of layered SnS_2.

Bibliographie

[1] Y Huang, E Sutter, J Sadowski, M Cotlet, O Monti, D Racke, M Neupane, D Wickramaratne, R Lake, B Parkinson, and P Sutter. Tin disulfide—an emerging layered metal dichalcogenide semiconductor : Materials properties and device characteristics. *ACS Nano*, 8(10) :10743–10755, September 2014. ISSN 1936-086X. doi : 10.1021/nn504481r. URL http://dx.doi.org/10.1021/nn504481r.

[2] A K Tołłoczko, M Peter, M Rybak, S Gorantla, A Bachmatiuk, and R Kudrawiec. Influence of native defects on the optical properties of SnX_2 (x = S and se) van der waals crystals. *J. Phys. Chem. C Nanomater. Interfaces*, 128(39) :16640–16651, October 2024.

[3] Q H Wang, K Kalantar-Zadeh, A Kis, J N Coleman, and M S Strano. Electronics and optoelectronics of two-dimensional transition metal dichalcogenides. *Nat. Nanotechnol.*, 7(11) : 699–712, November 2012.

[4] W Choi, N Choudhary, G Han, J Park, D Akinwande, and Y H Lee. Recent development of two-dimensional transition metal dichalcogenides and their applications. *Mater. Today (Kidlington)*, 20(3) :116–130, April 2017.

[5] S Manzeli, D Ovchinnikov, D Pasquier, O Yazyev, and A Kis. 2D transition metal dichalcogenides. *Nature Reviews Materials*, 2(8), June 2017. ISSN 2058-8437. doi : 10.1038/natrevmats.2017.33. URL http://dx.doi.org/10.1038/natrevmats.2017.33.

[6] M Hossen, S Shendokar, and S Aravamudhan. Defects and defect engineering of two-dimensional transition metal dichalcogenide (2D TMDC) materials. *Nanomaterials*, 14(5) : 410, February 2024. ISSN 2079-4991. doi : 10.3390/nano14050410. URL http://dx.doi.org/10.3390/nano14050410.

[7] J Al Mahmud, M Rahman, A Kuddus, M Ali, A Islam, M Haque, S Ahmed, M Mushtaq, and A Ismail. Design and analysis of a $SnS_2/WS_2/V_2O_5$ double-heterojunction toward high-performance photovoltaics. *Energy Advances*, 2(11) :1843–1858, 2023. ISSN 2753-1457. doi : 10.1039/d3ya00231d. URL http://dx.doi.org/10.1039/D3YA00231D.

[8] R Sivasamy, S Kaliyamoorthy, A S, G Kalyan, and E Mosquera-Vargas. A vertically staged 2D van der Waals SnS_2/SiS_2 heterostructures for photovoltaic and photocatalytic application. *Materials Science in Semiconductor Processing*, 185 :108845, January 2025. ISSN 1369-8001. doi : 10.1016/j.mssp.2024.108845. URL http://dx.doi.org/10.1016/j.mssp.2024.108845.

[9] S Gedi, S Alhammadi, J Noh, V Minnam Reddy, H Park, A Rabie, J Shim, D Kang, and W Kim. SnS_2 nanoparticles and thin film for application as an adsorbent and photovoltaic buffer. *Nanomaterials*, 12(2) :282, January 2022. ISSN 2079-4991. doi : 10.3390/nano12020282. URL http://dx.doi.org/10.3390/nano12020282.

[10] G Su, V Hadjiev, P Loya, J Zhang, S Lei, S Maharjan, P Dong, P M Ajayan, J Lou, and H Peng. Chemical vapor deposition of thin crystals of layered semiconductor SnS_2 for fast photodetection application. *Nano Letters*, 15(1) :506–513, December 2014. ISSN 1530-6992. doi : 10.1021/nl503857r. URL http://dx.doi.org/10.1021/nl503857r.

[11] L Gao, C Chen, K Zeng, C Ge, D Yang, H Song, and J Tang. Broadband, sensitive and spectrally distinctive SnS_2 nanosheet/pbs colloidal quantum dot hybrid photodetector. *Light : Science &; Applications*, 5(7) :e16126–e16126, March 2016. ISSN 2047-7538. doi : 10.1038/lsa.2016.126. URL http://dx.doi.org/10.1038/lsa.2016.126.

[12] J Yu, A Suleiman, Z Zheng, X Zhou, and T Zhai. Giant-enhanced SnS_2 photodetectors with broadband response through oxygen plasma treatment. *Advanced Functional Materials*, 30 (24), April 2020. ISSN 1616-3028. doi : 10.1002/adfm.202001650. URL http://dx.doi.org/10.1002/adfm.202001650.

[13] M Kumar, B Huang, A Saravanan, H Sun, and S Chen. Self-powered broadband photodetectors based on Si/SnS_2 and Si/$SnSe_2$ p–n heterostructures. *Advanced Electronic Materials*, 10(11), April 2024. ISSN 2199-160X. doi : 10.1002/aelm.202400164. URL http://dx.doi.org/10.1002/aelm.202400164.

[14] M Xu, X Zhu, G Fan, X Jia, Y Zhang, M Wang, H Zheng, P Zhou, and C Fan. Nickel doping in tin disulfide enables visible photodetectors with extended detection range and high responsivity. *ACS Applied Materials&; Interfaces*, 17(11) :17045–17054, March 2025. ISSN 1944-8252. doi : 10.1021/acsami.4c22051. URL http://dx.doi.org/10.1021/acsami.4c22051.

[15] X Cui, W Xu, Z Xie, and Y Wang. High-performance dye-sensitized solar cells based on ag-doped SnS_2 counter electrodes. *J. Mater. Chem. A*, 4(5) :1908–1914, 2016. ISSN 2050-7496. doi : 10.1039/c5ta10234k. URL http://dx.doi.org/10.1039/C5TA10234K.

[16] T Yang, J Zhu, Y Zhang, Y Zhang, and R Lin. Si/SnS_2 nanocomposite for lithium ion battery anodes. *ACS Applied Nano Materials*, 6(24) :22767–22773, December 2023. ISSN 2574-0970. doi : 10.1021/acsanm.3c03823. URL http://dx.doi.org/10.1021/acsanm.3c03823.

[17] B Venugopal, R Mudike, R Ravi, P Sahoo, A Tripathi, and I Shown. Harnessing enhanced stability and high-rate capability in lithium-ion batteries using synergistic SnS_2/MoS_2 2d nanostructures with optimized conversion/alloying reactions. *Journal of Alloys and Compounds*, 984 :173886, May 2024. ISSN 0925-8388. doi : 10.1016/j.jallcom.2024.173886. URL http://dx.doi.org/10.1016/j.jallcom.2024.173886.

[18] J Jang, M Lee, S Park, J Oh, J Park, and S Paek. Long-term cycling stability of a SnS_2-based covalent organic nanosheet anode for lithium-ion batteries. *Journal of Materials Chemistry A*, 11(25) :13320–13330, 2023. ISSN 2050-7496. doi : 10.1039/d3ta01537h. URL http://dx.doi.org/10.1039/D3TA01537H.

[19] X Shi, J Li, X Zhang, M Li, Q Jing, G Fang, and M Long. Utilizing the built-in electric field of SnS_2/C_3N heterostructure to promote high-performance lithium-ion batteries. *The Journal of Physical Chemistry C*, 128(15) :6189–6197, April 2024. ISSN 1932-7455. doi : 10.1021/acs.jpcc.3c07488. URL http://dx.doi.org/10.1021/acs.jpcc.3c07488.

[20] X Xu, D Feng, L You, Y Xie, F Wu, Y Zhu, Y Mei, and D Xie. Carbon-encrusted SnS_2 decorated on mxene nanosheets for advanced li-ion battery anodes. *Energy Material Advances*, 5, January 2024. ISSN 2692-7640. doi : 10.34133/energymatadv.0146. URL http://dx.doi.org/10.34133/energymatadv.0146.

[21] S Zhan, L Zheng, Y Xiao, and L Zhao. Phonon and carrier transport properties in low-cost and environmentally friendly SnS_2 : A promising thermoelectric material. *Chemistry of Materials*, 32(24) :10348–10356, December 2020. ISSN 1520-5002. doi : 10.1021/acs.chemmater.0c04184. URL http://dx.doi.org/10.1021/acs.chemmater.0c04184.

[22] W Yan, D Chen, H Fuh, Y Li, D Zhang, H Liu, G Wu, L Zhang, X Ren, J Cho, M Choi, B Chun, C Coileáin, H Xu, Z Wang, Z Jiang, C Chang, and H Wu. Photo-enhanced gas sensing of SnS_2 with nanoscale defects. *RSC Advances*, 9(2) :626–635, 2019. ISSN 2046-2069. doi : 10.1039/c8ra08857h. URL http://dx.doi.org/10.1039/C8RA08857H.

[23] I Shown, S Samireddi, Y Chang, R Putikam, P Chang, A Sabbah, F Fu, W Chen, C Wu, T Yu, P Chung, M Lin, L Chen, and K Chen. Carbon-doped SnS_2 nanostructure as a high-efficiency solar fuel catalyst under visible light. *Nature Communications*, 9(1), January 2018. ISSN 2041-1723. doi : 10.1038/s41467-017-02547-4. URL http://dx.doi.org/10.1038/s41467-017-02547-4.

[24] L Li, Z Chai, W Jin, H Sun, J He, G Wu, and W Xia. Sulfur vacancy in SnS_2 nanoflake adjusted by precursor and improved photocatalytic performance. *Journal of Alloys and Compounds*, 932 :167658, January 2023. ISSN 0925-8388. doi : 10.1016/j.jallcom.2022.167658. URL http://dx.doi.org/10.1016/j.jallcom.2022.167658.

[25] A Jena, K Pichaimuthu, G Leniec, S Kaczmarek, H Chang, C Su, S Hu, and R Liu. Defect mediated improvements in the photoelectrochemical activity of MoS_2/SnS_2 ultrathin sheets on si photocathode for hydrogen evolution. *ACS Applied Materials&; Interfaces*, 14(35) : 39896–39906, August 2022. ISSN 1944-8252. doi : 10.1021/acsami.2c06797. URL http://dx.doi.org/10.1021/acsami.2c06797.

[26] S Guo, B Yang, Z Hu, M Zhen, B Gu, and B Shen. Uncovering mechanism of photocatalytic performance enhancement induced by multivariate defects on SnS_2. *Nano Research*, 16 (2) :2102–2110, October 2022. ISSN 1998-0000. doi : 10.1007/s12274-022-4926-x. URL http://dx.doi.org/10.1007/s12274-022-4926-x.

[27] S Mondal, S Das, and U Gautam. Defect-rich, negatively-charged SnS_2 nanosheets for efficient photocatalytic Cr(VI) reduction and organic dye adsorption in water. *Journal of*

Colloid and Interface Science, 603 :110–119, December 2021. ISSN 0021-9797. doi : 10.1016/j.jcis.2021.06.092. URL http://dx.doi.org/10.1016/j.jcis.2021.06.092.

[28] Y Zhao, D Sun, K Hu, W Zhao, and F Huang. Surface defect engineering of SnS_2 nanocrystals for enhanced photocatalytic reduction of Cr (VI) under visible light. *Inorganic Chemistry Communications*, 114 :107849, April 2020. ISSN 1387-7003. doi : 10.1016/j.inoche.2020.107849. URL http://dx.doi.org/10.1016/j.inoche.2020.107849.

[29] H Yang and X Liu. Nonlinear optical response and applications of tin disulfide in the near- and mid-infrared. *Applied Physics Letters*, 110(17), April 2017. ISSN 1077-3118. doi : 10.1063/1.4982624. URL http://dx.doi.org/10.1063/1.4982624.

[30] T Feng, D Zhang, X Li, Q Abdul, Z Shi, J Lu, P Guo, Y Zhang, J Liu, and Q Wang. SnS_2 nanosheets for er-doped fiber lasers. *ACS Applied Nano Materials*, 3(1) :674–681, December 2019. ISSN 2574-0970. doi : 10.1021/acsanm.9b02194. URL http://dx.doi.org/10.1021/acsanm.9b02194.

[31] M Diao, H Li, Y Sun, Y Liang, Z Yu, D W Boukhvalov, Z Huang, and C Zhang. Enhancing reverse saturable absorption in SnS_2 nanosheets by plasma treatment. *ACS Appl. Mater. Interfaces*, 13(3) :4211–4219, January 2021.

[32] Z Lei, Y Huang, W Du, Z Fan, J Chang, H Wang, Y Jin, and X Xu. Nonlinear optical response on the surface of semiconductor SnS_2 probed by terahertz emission spectroscopy. *The Journal of Physical Chemistry C*, 124(39) :21559–21567, September 2020. ISSN 1932-7455. doi : 10.1021/acs.jpcc.0c06370. URL http://dx.doi.org/10.1021/acs.jpcc.0c06370.

[33] Y Kumagai, L Burton, A Walsh, and F Oba. Electronic structure and defect physics of tin sulfides : SnS, Sn_2S_3, and SnS_2. *Phys. Rev. Appl.*, 6 :014009, Jul 2016. doi : 10.1103/PhysRevApplied.6.014009. URL https://link.aps.org/doi/10.1103/PhysRevApplied.6.014009.

[34] H Lu, Y Guo, and J Robertson. Band edge states, intrinsic defects, and dopants in monolayer HfS_2 and SnS_2. *Appl. Phys. Lett.*, 112(6) :062105, February 2018.

[35] L F J Piper, T D Veal, M J Lowe, and C F McConville. Electron depletion at InAs free surfaces : Doping-induced acceptorlike gap states. *Phys. Rev. B Condens. Matter Mater. Phys.*, 73(19), May 2006.

[36] L F J Piper, L Colakerol, P D C King, A Schleife, J Zúñiga-Pérez, P Glans, T Learmonth, A Federov, T D Veal, F Fuchs, V Muñoz-Sanjosé, F Bechstedt, C F McConville, and K E Smith. Observation of quantized subband states and evidence for surface electron accumulation in CdO from angle-resolved photoemission spectroscopy. *Phys. Rev. B Condens. Matter Mater. Phys.*, 78(16), October 2008.

[37] L Colakerol, T D Veal, H K Jeong, L Plucinski, A DeMasi, T Learmonth, P A Glans, S Wang, Y Zhang, L F J Piper, P H Jefferson, A Fedorov, T C Chen, T D Moustakas, C F McConville, and K E Smith. Quantized electron accumulation states in indium nitride studied by angle-resolved photoemission spectroscopy. *Phys. Rev. Lett.*, 97(23) :237601, December 2006.

[38] Z Zhang and J Yates. Band bending in semiconductors : Chemical and physical consequences at surfaces and interfaces. *Chemical Reviews*, 112(10) :5520–5551, July 2012. ISSN 1520-6890. doi : 10.1021/cr3000626. URL http://dx.doi.org/10.1021/cr3000626.

[39] M Speckbacher, J Treu, T Whittles, W Linhart, X Xu, K Saller, V Dhanak, G Abstreiter, J Finley, T Veal, and G Koblmüller. Direct measurements of fermi level pinning at the surface of intrinsically n-type ingaas nanowires. *Nano Letters*, 16(8) :5135–5142, July 2016. ISSN 1530-6992. doi : 10.1021/acs.nanolett.6b02061. URL http://dx.doi.org/10.1021/acs.nanolett.6b02061.

[40] L Kronik. Surface photovoltage phenomena : theory, experiment, and applications. *Surface Science Reports*, 37(1–5) :1–206, December 1999. ISSN 0167-5729. doi : 10.1016/s0167-5729(99)00002-3. URL http://dx.doi.org/10.1016/S0167-5729(99)00002-3.

[41] S Ciocys, T Morimoto, R Mori, K Gotlieb, Z Hussain, J G Analytis, J E Moore, and A Lanzara. Manipulating long-lived topological surface photovoltage in bulk-insulating topological insulators Bi_2Se_3 and Bi_2Te_3. *Npj Quantum Mater.*, 5(1), March 2020.

[42] M Michiardi, F Boschini, H-H Kung, M X Na, S K Y Dufresne, A Currie, G Levy, S Zhdanovich, A K Mills, D J Jones, J L Mi, B B Iversen, Ph Hofmann, and A Damascelli. Optical manipulation of rashba-split 2-dimensional electron gas. *Nat. Commun.*, 13(1) :3096, June 2022.

[43] F Roth, J Mahl, M Borgwardt, L Wenthaus, F Brausse, V Garbe, O Gessner, and W Eberhardt. Dynamical nonlinear inversion of the surface photovoltage at si(100). *Physical Review Letters*, 132(14), April 2024. ISSN 1079-7114. doi : 10.1103/physrevlett.132.146201. URL http://dx.doi.org/10.1103/PhysRevLett.132.146201.

[44] F Boschini, M Zonno, and A Damascelli. Time-resolved arpes studies of quantum materials. *Reviews of Modern Physics*, 96(1), February 2024. ISSN 1539-0756. doi : 10.1103/revmodphys.96.015003. URL http://dx.doi.org/10.1103/RevModPhys.96.015003.

[45] X Wang, P Richard, Y Huang, H Miao, L Cevey, N Xu, Y Sun, T Qian, Y Xu, M Shi, J Hu, X Dai, and H Ding. Orbital characters determined from fermi surface intensity patterns using angle-resolved photoemission spectroscopy. *Phys. Rev. B*, 85 :214518, Jun 2012. doi : 10.1103/PhysRevB.85.214518. URL https://link.aps.org/doi/10.1103/PhysRevB.85.214518.

[46] A Sterzi, G Manzoni, A Crepaldi, F Cilento, M Zacchigna, M Leclerc, Ph Bugnon, A Magrez, H Berger, L Petaccia, and F Parmigiani. Probing band parity inversion in the topological insulator $GeBi_2Te_4$ by linear dichroism in ARPES. *J. Electron Spectros. Relat. Phenomena*, 225 :23–27, May 2018.

[47] H Bentmann, H. Maaß, J. Braun, C. Seibel, K. A. Kokh, O. E. Tereshchenko, S. Schreyeck, K. Brunner, L. W. Molenkamp, K. Miyamoto, M. Arita, K. Shimada, T. Okuda, J. Kirschner, C. Tusche, H. Ebert, J. Minár, and F. Reinert. Profiling spin and orbital texture of a topological insulator in full momentum space. *Phys. Rev. B*, 103 :L161107, Apr 2021. doi : $10.1103/\mathrm{PhysRevB.103.L161107}$. URL `https://link.aps.org/doi/10.1103/PhysRevB.103.L161107`.

[48] S Beaulieu, J Schusser, S Dong, M Schüler, T Pincelli, M Dendzik, J Maklar, A Neef, H Ebert, K Hricovini, M Wolf, J Braun, L Rettig, J Minár, and R Ernstorfer. Revealing hidden orbital pseudospin texture with time-reversal dichroism in photoelectron angular distributions. *Phys. Rev. Lett.*, 125 :216404, Nov 2020. doi : $10.1103/\mathrm{PhysRevLett.125.216404}$. URL `https://link.aps.org/doi/10.1103/PhysRevLett.125.216404`.

[49] S Beaulieu, M Schüler, J Schusser, S Dong, T Pincelli, J Maklar, A Neef, F Reinert, M Wolf, L Rettig, J Minár, and R Ernstorfer. Unveiling the orbital texture of 1T-$TiTe_2$ using intrinsic linear dichroism in multidimensional photoemission spectroscopy. *Npj Quantum Mater.*, 6(1), November 2021.

[50] S Fragkos, E Symeonidou, E Lasserre, B Fabre, D Descamps, S Petit, P Tsipas, Y Mairesse, A Dimoulas, and S Beaulieu. Excited state band mapping and ultrafast nonequilibrium dynamics in topological dirac semimetal 1T-$ZrTe_2$. *Nano Lett.*, 24(42) :13397–13404, October 2024.

[51] K F Mak, K He, C Lee, G H Lee, J Hone, T F Heinz, and J Shan. Tightly bound trions in monolayer MoS_2. *Nat. Mater.*, 12(3) :207–211, March 2013.

[52] A Chernikov, T C Berkelbach, H M Hill, A Rigosi, Y Li, O B Aslan, D R Reichman, M S Hybertsen, and T F Heinz. Exciton binding energy and nonhydrogenic rydberg series in monolayer WS_2. *Phys. Rev. Lett.*, 113(7) :076802, August 2014.

[53] Z Y Zhu, Y C Cheng, and U Schwingenschlögl. Giant spin-orbit-induced spin splitting in two-dimensional transition-metal dichalcogenide semiconductors. *Phys. Rev. B Condens. Matter Mater. Phys.*, 84(15), October 2011.

[54] D Xiao, G-B Liu, W Feng, X Xu, and W Yao. Coupled spin and valley physics in monolayers of MoS_2 and other group-VI dichalcogenides. *Phys. Rev. Lett.*, 108(19) :196802, May 2012.

[55] N Alidoust, G Bian, S-Y Xu, R Sankar, M Neupane, C Liu, I Belopolski, D-X Qu, J D Denlinger, F-C Chou, and M Z Hasan. Observation of monolayer valence band spin-orbit effect and induced quantum well states in mox_2. *Nat. Commun.*, 5(1) :4673, August 2014.

[56] J A Wilson and A D Yoffe. The transition metal dichalcogenides discussion and interpretation of the observed optical, electrical and structural properties. *Adv. Phys.*, 18(73) :193–335, May 1969.

[57] J A Wilson, F J Di Salvo, and S Mahajan. Charge-density waves in metallic, layered, transition-metal dichalcogenides. *Phys. Rev. Lett.*, 32(16) :882–885, April 1974.

[58] J A Wilson, F J Di Salvo, and S Mahajan. Charge-density waves and superlattices in the metallic layered transition metal dichalcogenides. *Adv. Phys.*, 24(2) :117–201, March 1975.

[59] X Xi, L Zhao, Z Wang, H Berger, L Forró, J Shan, and K F Mak. Strongly enhanced charge-density-wave order in monolayer $NbSe_2$. *Nat. Nanotechnol.*, 10(9) :765–769, September 2015.

[60] J T Ye, Y J Zhang, R Akashi, M S Bahramy, R Arita, and Y Iwasa. Superconducting dome in a gate-tuned band insulator. *Science*, 338(6111) :1193–1196, November 2012.

[61] X Xi, Z Wang, W Zhao, J-H Park, K T Law, H Berger, L Forró, J Shan, and K F Mak. Ising pairing in superconducting $nbse_2$ atomic layers. *Nat. Phys.*, 12(2) :139–143, February 2016.

[62] M A Cazalilla, H Ochoa, and F Guinea. Quantum spin hall effect in two-dimensional crystals of transition-metal dichalcogenides. *Phys. Rev. Lett.*, 113(7) :077201, August 2014.

[63] X Qian, J Liu, L Fu, and J Li. Solid state theory. quantum spin hall effect in two-dimensional transition metal dichalcogenides. *Science*, 346(6215) :1344–1347, December 2014.

[64] A Splendiani, L Sun, Y Zhang, T Li, J Kim, C-Y Chim, G Galli, and F Wang. Emerging photoluminescence in monolayer MoS_2. *Nano Lett.*, 10(4) :1271–1275, April 2010.

[65] T Korn, S Heydrich, M Hirmer, J Schmutzler, and C Schüller. Low-temperature photocarrier dynamics in monolayer MoS_2. *Applied Physics Letters*, 99(10) :102109, September 2011. ISSN 1077-3118. doi : $10.1063/1.3636402$. URL `http://dx.doi.org/10.1063/1.3636402`.

[66] G Wang, A Chernikov, M Glazov, T Heinz, X Marie, T Amand, and B Urbaszek. Colloquium : Excitons in atomically thin transition metal dichalcogenides. *Reviews of Modern Physics*, 90 (2), April 2018. ISSN 1539-0756. doi : $10.1103/\mathrm{revmodphys.90.021001}$. URL `http://dx.doi.org/10.1103/RevModPhys.90.021001`.

[67] O Lopez-Sanchez, D Lembke, M Kayci, A Radenovic, and A Kis. Ultrasensitive photodetectors based on monolayer MoS_2. *Nat. Nanotechnol.*, 8(7) :497–501, July 2013.

[68] C Gong, Y Zhang, W Chen, J Chu, T Lei, J Pu, L Dai, C Wu, Y Cheng, T Zhai, L Li, and J Xiong. Electronic and optoelectronic applications based on 2D novel anisotropic transition metal dichalcogenides. *Advanced Science*, 4(12), October 2017. ISSN 2198-3844. doi : $10.1002/\mathrm{advs.201700231}$. URL `http://dx.doi.org/10.1002/advs.201700231`.

[69] M X Low, T Ahmed, S K Saini, M Panahandeh-Fard, J O Mendes, A S R Chesman, C Xu, J Van Embden, L Wang, M Kumar, S Sriram, M Bhaskaran, and S Walia. $FePS_3$-MoS_2 p-n junctions for broadband optoelectronics. *Npj 2D Mater. Appl.*, 9(1) :1–10, March 2025.

[70] T Cao, G Wang, W Han, H Ye, Chuanrui Zhu, Junren Shi, Qian Niu, Pingheng Tan, Enge Wang, Baoli Liu, and Ji Feng. Valley-selective circular dichroism of monolayer molybdenum disulphide. *Nat. Commun.*, 3(1) :887, June 2012.

[71] K F Mak, K He, J Shan, and T F Heinz. Control of valley polarization in monolayer MoS_2 by optical helicity. *Nat. Nanotechnol.*, 7(8) :494–498, August 2012.

[72] S A Vitale, D Nezich, J O Varghese, P Kim, N Gedik, P Jarillo-Herrero, D Xiao, and M Rothschild. Valleytronics : Opportunities, challenges, and paths forward. *Small*, 14(38) : e1801483, September 2018.

[73] S Yang, H Long, W Chen, B Sa, Z Guo, J Zheng, J Pei, H Zhan, and Y Lu. Valleytronics meets straintronics : Valley fine structure engineering of 2D transition metal dichalcogenides. *Advanced Optical Materials*, 12(14), March 2024. ISSN 2195-1071. doi : $10.1002/\mathrm{adom.}$ 202302900. URL `http://dx.doi.org/10.1002/adom.202302900`.

[74] Z Zhao, Y Lin, and A Avsar. Novel spintronic effects in two-dimensional van der waals heterostructures. *npj 2D Materials and Applications*, 9(1), April 2025. ISSN 2397-7132. doi : $10.1038/\mathrm{s41699\text{-}025\text{-}00546\text{-}4}$. URL `http://dx.doi.org/10.1038/s41699-025-00546-4`.

[75] K Nassiri Nazif, A Daus, J Hong, N Lee, S Vaziri, A Kumar, F Nitta, M E Chen, S Kananian, R Islam, K-H Kim, J-H Park, A S Y Poon, M L Brongersma, E Pop, and K C Saraswat. High-specific-power flexible transition metal dichalcogenide solar cells. *Nat. Commun.*, 12(1) : 7034, December 2021.

[76] F Fan and W Wu. Emerging devices based on two-dimensional monolayer materials for energy harvesting. *Research*, 2019, January 2019. ISSN 2639-5274. doi : $10.34133/2019/$ 7367828. URL `http://dx.doi.org/10.34133/2019/7367828`.

[77] J Tsai, J Pan, H Lin, A Bansil, and Q Yan. Antisite defect qubits in monolayer transition metal dichalcogenides. *Nature Communications*, 13(1), January 2022. ISSN 2041-1723. doi : $10.1038/\mathrm{s41467\text{-}022\text{-}28133\text{-}x}$. URL `http://dx.doi.org/10.1038/s41467-022-28133-x`.

[78] J Yu, E van Veen, M I Katsnelson, and S Yuan. Effective lattice hamiltonian for monolayer tin disulfide : Tailoring electronic structure with electric and magnetic fields. *Phys. Rev. B.*, 97 (24), June 2018.

[79] D Cavalcoli, B Fraboni, and A Cavallini. Surface and defect states in semiconductors investigated by surface photovoltage. In *Semiconductors and Semimetals*, Semiconductors and semimetals, pages 251–278. Elsevier, 2015.

[80] O Tkach, S Fragkos, Q Nguyen, S Chernov, M Scholz, N Wind, S Babenkov, O Fedchenko, Y Lytvynenko, D Zimmer, A Hloskovskii, D Kutnyakhov, F Pressacco, J Dilling, L Bruckmeier, M Heber, F Scholz, J Sobota, J Koralek, N Sirica, M Kallmayer, M Hoesch, C Schlueter, L Odnodvorets, Y Mairesse, K Rossnagel, H Elmers, S Beaulieu, and G Schoenhense. Multimode front lens for momentum microscopy : Part ii experiments, 2024.

[81] K Medjanik, O Fedchenko, S Chernov, D Kutnyakhov, M Ellguth, A Oelsner, B. Schönhense, T. R. F. Peixoto, P. Lutz, C.-H. Min, F. Reinert, S. Däster, Y. Acremann, J. Viefhaus, W. Wurth, H. J. Elmers, and G. Schönhense. Direct 3D mapping of the fermi surface and fermi velocity. *Nature Materials*, 16(6) :615–621, 2017. ISSN 1476-4660. doi : $10.1038/\mathrm{nmat4875}$. URL `https://doi.org/10.1038/nmat4875`.

[82] R Xian, Y Acremann, S Agustsson, M Dendzik, Kevin Bühlmann, Davide Curcio, Dmytro Kutnyakhov, Federico Pressacco, Michael Heber, Shuo Dong, Tommaso Pincelli, Jure Demsar, Wilfried Wurth, Philip Hofmann, Martin Wolf, Markus Scheidgen, Laurenz Rettig, and Ralph Ernstorfer. An open-source, end-to-end workflow for multidimensional photoemission spectroscopy. *Scientific Data*, 7(1) :442, Dec 2020. ISSN 2052-4463. doi : $10.1038/\mathrm{s41597\text{-}020\text{-}00769\text{-}8}$. URL `https://doi.org/10.1038/s41597-020-00769-8`.

[83] R P Xian, LRettig, and R Ernstorfer. Symmetry-guided nonrigid registration : The case for distortion correction in multidimensional photoemission spectroscopy. *Ultramicroscopy*, 202 : 133 – 139, 2019. ISSN 0304-3991. doi : $\mathrm{https://doi.org/10.1016/j.ultramic.2019.04.004}$. URL `http://www.sciencedirect.com/science/article/pii/S0304399118303474`.

[84] S Fragkos, Q Courtade, O Tkach, J Gaudin, D Descamps, G Barrette, S Petit, G Schönhense, Y Mairesse, and S Beaulieu. Time- and polarization-resolved extreme ultraviolet momentum microscopy. 2025.

[85] D A Racke, M R Neupane, and O L A Monti. Valence and conduction band structure of the quasi-two-dimensional semiconductor SnS_2. *Phys. Rev. B.*, 93(8), February 2016.

[86] D Hsieh, Y Xia, D Qian, L Wray, J H Dil, F Meier, J Osterwalder, L Patthey, J G Checkelsky, N P Ong, A V Fedorov, H Lin, A Bansil, D Grauer, Y S Hor, R J Cava, and M Z Hasan. A tunable topological insulator in the spin helical dirac transport regime. *Nature*, 460(7259) : 1101–1105, August 2009.

[87] D Hsieh, Y Xia, D Qian, L Wray, F Meier, J H Dil, J Osterwalder, L Patthey, A V Fedorov, H Lin, A Bansil, D Grauer, Y S Hor, R J Cava, and M Z Hasan. Observation of time-reversal-protected single-dirac-cone topological-insulator states in Bi_2Te_3 and Sb_2Te_3. *Phys. Rev. Lett.*, 103(14) :146401, October 2009.

[88] M Bianchi, D Guan, S Bao, J Mi, B B Iversen, Philip D C King, and P Hofmann. Coexistence of the topological state and a two-dimensional electron gas on the surface of Bi_2Se_3. *Nat. Commun.*, 1(1) :128, November 2010.

[89] H M Benia, C Lin, K Kern, and C R Ast. Reactive chemical doping of the Bi_2Se_3 topological insulator. *Phys. Rev. Lett.*, 107(17), October 2011.

[90] P Rakyta, B Ujfalussy, and L Szunyogh. Band bending at the surface of Bi_2Se_3 studied from first principles. *New J. Phys.*, 17(12) :123011, December 2015.

[91] T Förster, P Krüger, and M Rohlfing. Ab initio studies of adatom- and vacancy-induced band bending in Bi_2Se_3. *Phys. Rev. B Condens. Matter Mater. Phys.*, 91(3), January 2015.

[92] H Lohani, P Mishra, A Banerjee, K Majhi, R Ganesan, U Manju, D Topwal, P S Anil Kumar, and B R Sekhar. Band structure of topological insulator $BiSbTe_{1.25}Se_{1.75}$. *Sci. Rep.*, 7(1) : 4567, July 2017.

[93] Z W Deng, R W M Kwok, W M Lau, and L L Cao. Time-resolved measurement of surface band bending of cleaved GaAs(110) and InP(110) by high resolution XPS. *Appl. Surf. Sci.*, 158(1-2) :58–63, May 2000.

[94] G Kremer, M Rumo, C Yue, A Pulkkinen, C W Nicholson, T Jaouen, F O von Rohr, P Werner, and C Monney. Ultrafast dynamics of the surface photovoltage in potassium-doped black phosphorus. *Phys. Rev. B.*, 104(3), July 2021.

[95] H Hedayat, A Ceraso, G Soavi, S Akhavan, A Cadore, C Dallera, G Cerullo, A C Ferrari, and E Carpene. Non-equilibrium band broadening, gap renormalization and band inversion in black phosphorus. *2D Mater.*, 8(2) :025020, April 2021.

[96] Y S Hor, A Richardella, P Roushan, Y Xia, J G Checkelsky, A Yazdani, M Z Hasan, N P Ong, and R J Cava. p-type Bi_2Se_3 for topological insulator and low-temperature thermoelectric applications. *Phys. Rev. B Condens. Matter Mater. Phys.*, 79(19), May 2009.

[97] A Lakhara, L Thole, R J Haug, and P A Bhobe. Anomalous electrical transport in $SnSe_2$ nanosheets : Role of thickness and surface defect states. 2025.

[98] S-L Yang, J A Sobota, P S Kirchmann, and Z-X Shen. Electron propagation from a photo-excited surface : implications for time-resolved photoemission. *Appl. Phys. A Mater. Sci. Process.*, 116(1) :85–90, July 2014.

[99] O Abdul-Aziz, M Tuniz, W Bronsch, F Parmigiani, F Cilento, D Wolverson, C Sayers, G Cerullo, C Dallera, E Carpene, P Loosdrecht, and H Hedayat. Photoinduced electronic band dynamics and defect-mediated surface potential evolution in $PdSe_2$, 2025. URL `https://arxiv.org/abs/2510.26011`.

[100] M Engelhard, D Baer, A Herrera-Gomez, and P Sherwood. Introductory guide to backgrounds in xps spectra and their impact on determining peak intensities. *Journal of Vacuum Science&; Technology A : Vacuum, Surfaces, and Films*, 38(6), September 2020. ISSN 1520-8559. doi : $10.1116/6.0000359$. URL `http://dx.doi.org/10.1116/6.0000359`.

6 ELECTRON-PHONON-DOMINATED CHARGE-DENSITY-WAVE FLUCTUATIONS IN $\mathrm{TiSe_2}$ ACCESSED BY ULTRAFAST NONEQUILIBRIUM DYNAMICS

Summary : The complex phase diagram of 1T-$TiSe_2$ consists of a charge density wave (CDW) below 200 K, and CDW fluctuations of still unknown origin at higher temperatures. Here, we use time-resolved extreme ultraviolet momentum microscopy and density functional perturbation theory to uncover the formation mechanism of CDW fluctuations and their spectral features at 295 K. Surprisingly, our results show that the coherent amplitude mode modulating ultrafast CDW recovery persists above T_{CDW}, and reveal that CDW fluctuations are dominated by the electron-phonon interaction rather than excitonic correlations as commonly believed. Our findings on these microscopic CDW fluctuations clarify the complex interplay between electronic and lattice degrees of freedom at elevated temperatures and, therefore, could be useful in understanding the nature of the CDW phase transition in 1T-$TiSe_2$ and similar quantum materials.

Statement of Contribution : The work presented in this chapter corresponds directly to the results published in Ref. [1]. My primary contribution to this study was my involvement in the experimental campaign carried out at the CELIA Laboratory. Specifically, I supported the preparation and execution of the measurements, assisted in the operation and optimization of the experimental setup, and contributed to the acquisition of the data that form the basis of the results reported in both the publication and this chapter.

6.1 Introduction

Understanding the interplay between electronic and lattice degrees of freedom is essential for comprehending phase transitions, superconductivity, transport properties, and the underlying mechanism of complex quantum phases. Disentangling the origin of the charge density wave (CDW) phase in 1T-$TiSe_2$, with $T_{\mathrm{CDW}} = 200\,\mathrm{K}$ and a $2 \times 2 \times 2$ lattice reconstruction [2, 3], provides the right platform to do so. Despite extensive experimental and theoretical investigations, the driving mechanism of the CDW phase remains a debated question [4]. One perspective attributes the origin to electron-hole coupling [5], as in the excitonic insulator scenario [2, 6–11], while alternative argues that the dominant mechanism is electron-phonon coupling, represented by the band-type Jahn-Teller effect [12–16]. Recently, a series of ultrafast time-resolved studies made an effort to disentangle the two contributions [17–24], and reach a consensus that electron-hole and electron-lattice interactions are intertwined in driving the CDW transition [25]. The ultrafast femtosecond dynamics (i.e., melting and recovery) of the order parameter (e.g., the CDW gap) [26, 27] was used as an argument for the former, while the laser-induced coherent phonon motion of the CDW amplitude mode [17, 18, 20, 28] for the latter interaction.

Several studies have reported that the CDW phase persists above T_{CDW} due to the fluctuation of the order parameter related to enigmatic CDW fluctuations [6, 7, 9, 18, 29–32], where the presence of finite correlation lengths leads to phase-incoherent CDW domains across the sample. Despite recent reports discussing the CDW fluctuations in 1T-$TiSe_2$ at such elevated temperatures [23, 33–35] with some reporting CDW fluctuation signatures in static angle-resolved photoemission spectroscopy (ARPES) [36], none of these directly mapped the nonequilibrium light-induced dynamics of these fluctuations in energy and momentum space. Applying the latter technique to explore this exotic phase could provide fertile ground to scrutinize the interplay and robustness of electron-hole and electron-phonon interactions at elevated temperatures. Indeed, a study using time-resolved ARPES (TR-ARPES) demonstrated sub-100 fs melting of the fluctuating phase, which was used as evidence for the exciton-driven CDW fluctuations [18]. Contrary to these claims, a recent time-dependent density functional theory study showed that exciton order is melted above T_{CDW} [37]. Moreover, the coherent oscillation of the CDW amplitude mode was observed under ambient conditions using time-resolved optical spectroscopy [33], suggesting a lattice involvement in the dynamics of CDW fluctuations. As evidenced by these opposing claims, the CDW fluctuating phase in 1T-$TiSe_2$ is still an elusive puzzle, while it would be highly valuable to understand its origin considering its recently discovered connection to unconvetional superconductivity [36, 38, 39], as well as its resemblance to the fluctuations preceding ordered phases (e.g., pseudogap) in other transition metal dichalcogenides (TMDCs) [40] and strongly correlated materials, such as cuprates [41] and kagome metals [42, 43]. Unraveling nonequilibrium properties of CDW fluctuations in $TiSe_2$ would also be highly useful for comprehending recently discovered light-induced hidden phases in $TiSe_2$ [44, 45].

In this work, we resolve the debate on the origin of CDW fluctuations in 1T-$TiSe_2$ by using time-resolved extreme ultraviolet (XUV) momentum microscopy, which allows ultrafast light-induced dynamics directly in energy-momentum space. The band structure mapping reveals that the back-folded Se 4p band associated with the CDW phase remains detectable even at room temperature (RT), in agreement with previous reports [6, 7, 36]. We also measured the partial melting of these CDW fluctuations on an ultrafast timescale, followed by a rapid recovery (~ 700 fs). This ultrafast melting signal of CDW fluctuations is offset from the maximum of the hot electron temperature by around $100 - 200$ fs, and overlaps with the population dynamics of excited Ti 3d states. Together, this demonstrate that CDW fluctuations are able to withstand a strong laser excitation and are not directly linked to the hot electron temperature, suggesting an involvement of the phonon mechanism. Interestingly, we also observe that the recovery of the CDW fluctuations is modulated by coherent CDW amplitude phonon modes. We challenge the belief that the fluctuating phase is ruled solely by the excitonic correlations [18] by reporting the periodic modulations of the backfolded band spectral weight at RT together with density-functional-theory (DFT) based calculations, indicating not only the preserved electron-phonon coupling mechanism at elevated temperatures but also confirming this to be the main contributor in the hybrid mechanism. More specifically, our calculations incorporating the dynamical electron-phonon scattering confirm that the strongly-coupled CDW-related soft phonon is relevant for the observed equilibrium and transient spectral features of CDW fluctuations. Namely, strong interaction between the soft (yet stable) phonon and Se 4p states leads to the fluctuating replica, while light-induced excitations harden the phonon and screen this interaction, consequently quenching the electron-phonon-driven CDW fluctuations. More generally, our study poses a series of strong arguments favoring the electron-phonon mechanism of CDW fluctuation formation at elevated temperature, which also puts a strong emphasis on the electron-phonon scenario in the debate on the origin of the regular CDW phase. Besides the fundamental importance, the correct interpretation of this mechanism could unleash the full potential of unconventional CDW-related features, such as CDW chirality [46], tunable nonlinear optical response [34], optical gyrotropy [47], and superconductivity [48]

6.2 Background Concept

6.2.1 $TiSe_2$

1T–$TiSe_2$ is a layered transition–metal dichalcogenide (TMDC) crystallizing in the 1T polytype with a CdI_2–type structure (space group $P\bar{3}m1$). Each titanium atom is octahedrally coordinated by six selenium atoms, forming a sandwich–like Se–Ti–Se trilayer. Adjacent layers are held together by weak van der Waals forces, which enables easy exfoliation and clean surface preparation. Figure 6.1a illustrates the real-space unit cell of the normal phase 1T–$TiSe_2$, while Fig. 6.1b shows the corresponding First Brillouin zone with its high-symmetry points. The band structure of the normal phase measured with ARPES (photon energy 119 eV) at room temperature is presented in

Fig. 6.1e. The valence band maximum near the $\bar{\Gamma}$ originates primarily from Se 4p orbitals and the conduction-band minimum at the Brillouin-zone edge $\bar{M}$ arises from Ti 3d orbitals, both lie close to the Fermi level. The momentum space geometry presented in Fig. 6.1b thus highlights the circular pocket of Se 4p valence band maximum at $\bar{\Gamma}$ and the elliptical pocket of Ti 3d states at the BZ edge at $\bar{M}$ whose interaction will determine the wave vector of the CDW.

Upon cooling, 1T–$TiSe_2$ undergoes a structural transition from the normal phase with a $1a \times 1b \times 1c$ unit cell to a $2a \times 2b \times 2c$ charge–density–wave (CDW) superlattice, effectively doubling the unit-cell dimensions in all three crystallographic directions, as shown in Fig. 6.1c. This transition lowers the crystal symmetry from $P\bar{3}m1$ to $P\bar{3}c1$. In momentum space (Fig. 6.1d), the new periodicity folds the original Brillouin-zone points onto each other, making $\bar{\Gamma}$ and $\bar{M}$ symmetry-equivalent in the CDW phase. This folding enables direct interaction between the Ti 3d and Se 4p states. A prominent signature of the this band folding appears in the ARPES map as backfolded Se 4p valence bands at the $\bar{M}$ points, accompanied by the opening of an energy gap at $\bar{\Gamma}$, as shown in Fig. 6.1f. Figure 6.1e,f together shows the evolution of the electronic structure across the phase transition, contrasting the normal metallic phase with the charge density wave phase, where the hybridization between Ti $3d$ and Se $4p$ states opens an energy gap at the Fermi level.

6.2.2 Charge Density Wave

A charge–density–wave (CDW) phase is a macroscopic quantum state characterized by a periodic modulation of the electronic charge density within a material, typically accompanied by a corresponding periodic lattice distortion. In 1T–$TiSe_2$, the CDW ($T_{\mathrm{CDW}} \approx 200$ K) has been extensively studied; however, its microscopic origin remains under debate, with two leading mechanisms proposed : the excitonic insulator model and the band-type Jahn–Teller (JT) effect. The excitonic insulator scenario is based on the proximity of the Ti 3d conduction band and Se 4p valence band, which are nearly overlapping or just separated by a very small energy gap. As temperatures decrease, the screening of Coulomb interactions weakens, allowing electrons from the conduction band and holes from the valence band to strongly attract and form bound pairs — excitons. If these excitons have a binding energy larger than the bandgap, the system becomes unstable due to the formation of excitons. This instability can cause a transition to a coherent ground state of exciton condensation. This condensation leads to a periodic modulation in the charge density and effectively drives a CDW; the lattice distortion then follows as a secondary response to this electronic order. On the other hand, the Jahn-Teller model emphasizes that primary instability lies in the lattice. In this model, the near-degenerate Ti 3d and Se 4p bands cause the lattice instability; therefore, the lattice undergoes a periodic distortion that reconstructs the bands and yields the CDW. Here, the lattice distortion is the primary driver : atomic displacements directly reduce electronic energy by removing band degeneracy, while the charge modulation follows as a consequence.

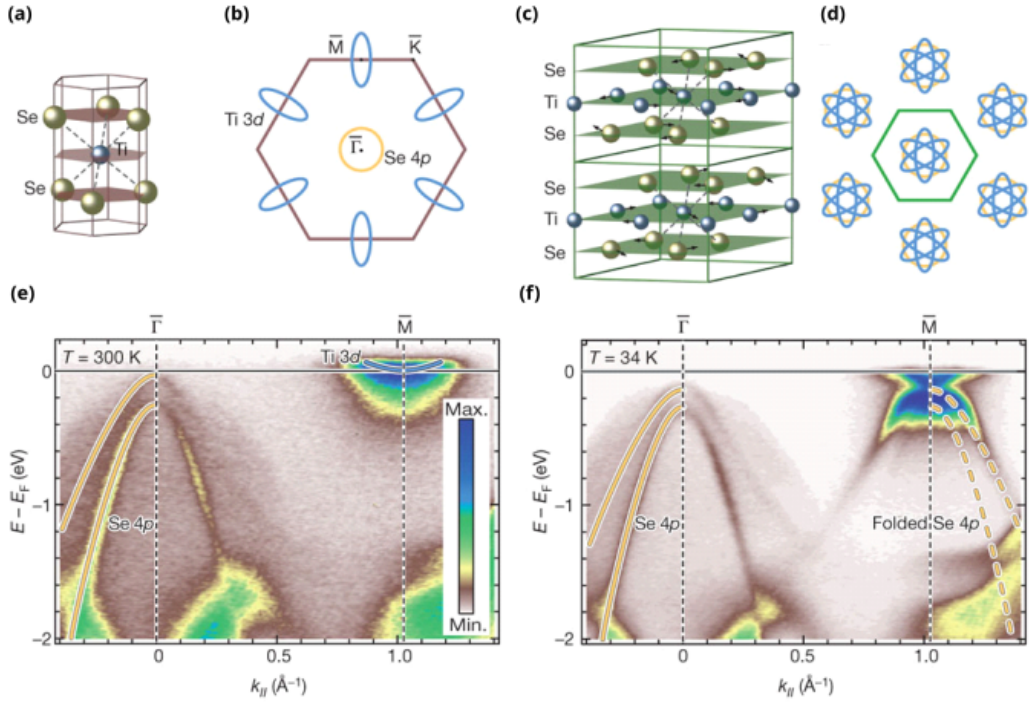


FIGURE 6.1 : Structural and electronic reconstruction across the CDW transition in 1T–$TiSe_2$. (a) Real-space unit cell of the normal phase 1T–$TiSe_2$ at room temperature. (b) First Brillouin zone of the normal phase, the high-symmetry points $\overline{\Gamma}$,$\overline{M}$, $\overline{K}$. The blue ellipses represent the Fermi surface topology of the Ti 3d band, while the yellow circle correspond to the Se 4p bands. (c) Real-space unit cell of the 1T–$TiSe_2$ charge-density-wave (CDW) phase, whose unit cell is doubled along all three crystallographic directions compared with the normal phase. Atomic displacements from the normal-phase structure are shown by arrows, while dashed lines outline the extension of the unit cell in the normal phase. (d) First Brillouin zone of 1T–$TiSe_2$, outlined in green. The folding of Se 4p and Ti 3d states associated with the CDW phase is indicated. (e) ARPES map of 1T–$TiSe_2$ at room temperature. (f) ARPES map of charge density phase of 1T–$TiSe_2$ at 34K. Adapted from [26], with permission from the publisher.

So unlike the purely electronic process of excitonic condensation, this mechanism fundamentally involves strong electron-lattice (phonon) coupling.

6.3 Results

6.3.1 Equilibrium and Nonequilibrium Electronic Band Structure Mapping

The experiments were performed at the Centre Lasers Intenses et Applications (CELIA) in Bordeaux, France. The time-resolved momentum microscopy setup featuring a polarization-tunable infrared (1.2 eV, sub-150μm) pump and XUV probe (21.6 eV, sub-50μm) pulses [Fig. 6.2a] allows for mapping of the occupied and unoccupied states (up to 1.2 eV above the Fermi level) over the full photoemission horizon [Fig. 6.2b]. The details about the experimental setup can be found in Chapter 2 and in Ref. [49–51].

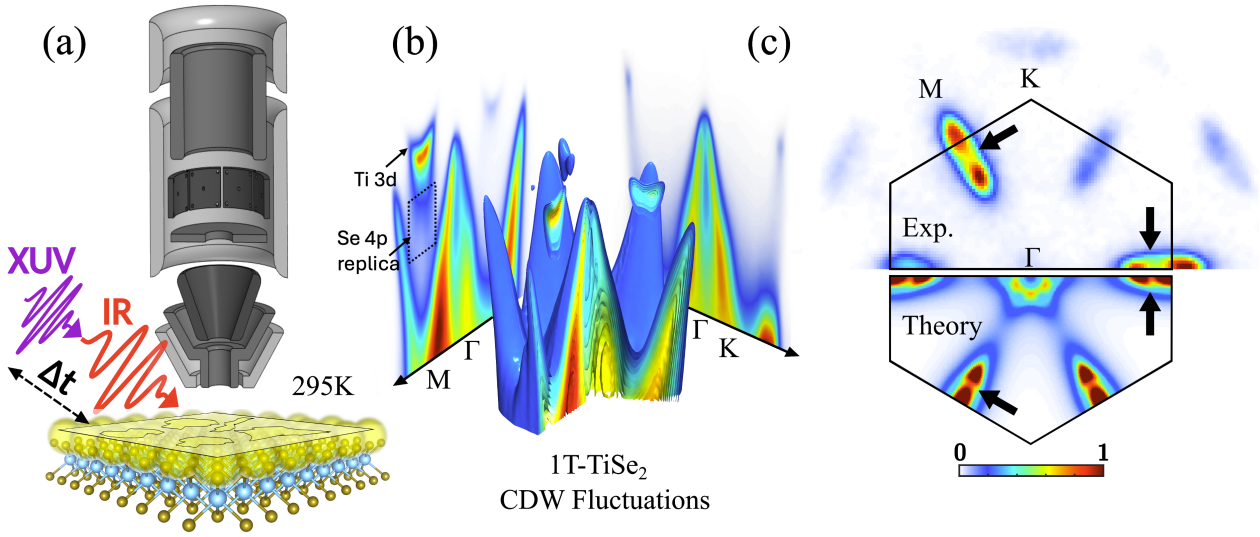


FIGURE 6.2 : Experimental and theoretical methodologies for investigating CDW fluctuations in 1T-$TiSe_2$. (a) Polarization-tunable infrared pump (1030 nm, 135 fs, 0.95 mJ/cm^2) and XUV probe pulses (21.6 eV) are focused at an incidence angle of 65° on a 1T-$TiSe_2$ sample at room temperature (295 K) in the interaction chamber of a time-of-flight momentum microscope, capable of collecting photoelectrons from the entire 2π solid angle in an energy range of several eV. (b) Three-dimensional photoemission intensity $I(E_\mathrm{B}, k_x, k_y)$ and associated energy-momentum cut along M-Γ-M' and K-Γ-K', acquired using s-polarized IR pump pulse (1.2 eV, 135 fs, $\sim$0.95 mJ/cm^2) and while continuously rotating the linear polarization axis angle of the XUV probe beam (21.6 eV) at the pump-probe temporal overlap. The photoemission intensity is integrated for all XUV polarization axis angles. (c) Comparison between experimental and theoretical constant energy contours (CECs), near the Fermi level. The measured loss of spectral weight within M pockets (black arrows) is well captured by theoretical calculations, which include dynamical electron-phonon interaction for temperatures above the CDW transition temperature T_CDW.

To perform photoexcited band mapping, we sit at the pump-probe temporal overlap (s-polarized pump pulse) and measure the photoemission intensity while continuously modulating the XUV linear polarization axis angle (going from s- to p-polarization through all intermediate linear polarization axis angles). The three-dimensional photoemission intensity $I(E_B, k_x, k_y)$ shown in Fig. 6.2b is obtained by summing over all XUV polarization states, allowing for minimized spectral weight suppression caused by photoemission matrix-element effects [49, 52–54]. The low-energy electronic band structure of 1T-$TiSe_2$ is characterized by a Se 4p valence band located at the Γ(A) point and Ti 3d conduction band pocket at the M(L) point. As shown in Fig. 6.2b, one clear indication of the CDW phase in static ARPES is the backfolded Se 4p band at the M point [6, 7]. Figure 6.2c) shows a comparison between experimental and theoretical constant energy contours (CEC), near the Fermi level. The measured loss of spectral weight within M pockets (black arrows) at RT is another fingerprint of the CDW fluctuations, and it is well captured by theoretical calculations, which include dynamical electron-phonon interaction for temperatures above T_CDW. Detailed analysis of the theoretical calculations will be given later. These scattering hot spots are reminiscent of the pseudogap openings and loss of spectral weight at $T > T_\mathrm{CDW}$ and certain momenta relevant for the CDW in other TMDCs, such as 2H-$TaSe_2$ [40] and 2H-$NbSe_2$ [55].

To gain further insight into the signatures of RT-CDW fluctuations, we perform an in-depth analysis of the spectral features around the M(L) pocket for unexcited [Figs. 6.3 (a)-(b)] and photoexcited

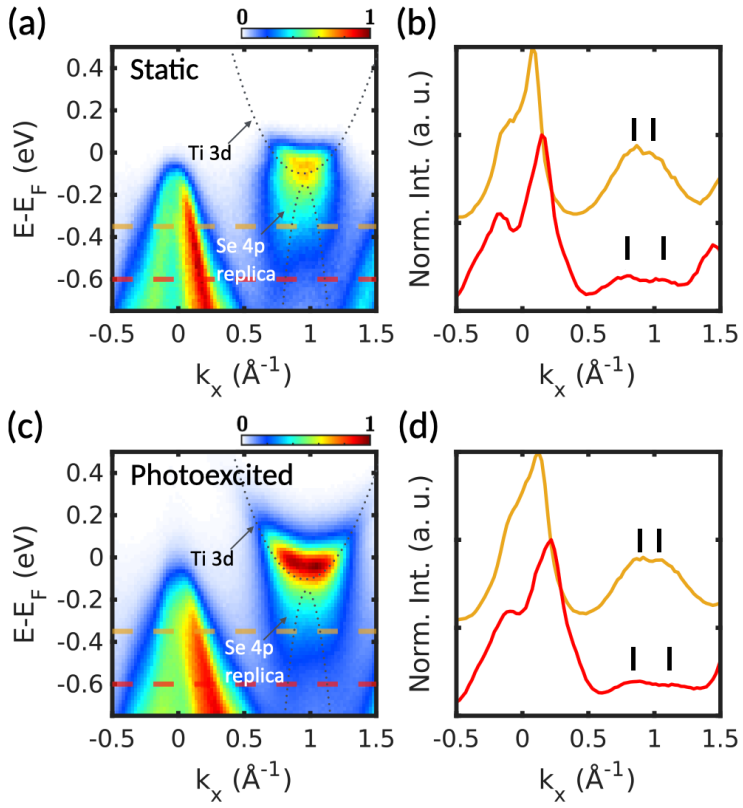


FIGURE 6.3 : Equilibrium and excited state band structure in 1T-$TiSe_2$ at Room Temperature. The first row (a,b) presents the static band structure before IR pump excitation. In contrast, the second row (c,d) describes the excited band structure at the pump-probe pulse time overlap at time zero. (a, c) Energy-momentum cut along the M-Γ-M' direction before and at the excitation by the pump pulse. The intensity is integrated for continuously varied linear polarization between horizontal and vertical. Dashed markers indicate where the momentum distribution curves (MDCs) in (b, d) were extracted. The lines in (b, d) indicate the position of Se 4p replica, and (a,c) are overlaid with a sketch of the normal phase band structure.

1T-$TiSe_2$ (at pump-probe temporal overlap) [Figs. 6.3 (c)-(d)]. The photoemission intensity along the Γ(A) - M(L) cut [Fig. 6.3a] reveal spectral features associated with RT-CDW fluctuations. First, we note the presence of the well-established backfolded Se 4p valence band, typically used as the ARPES evidence of the emergence of CDW order, exhibited by a faint yet discernible down-dispersive band feature at the M(L) point below the Ti 3d band in Fig. 6.3a. This feature is more apparent in the momentum distribution curves (MDC) around $k_x \approx 1.0$ Å^{-1}, as indicated by the black bars in Fig. 6.3b. The distance between the two peaks increases with higher binding energies, demonstrating the hole-like Se 4p band character. The backfolded Se 4p feature is also observed at pump-probe overlap in both the photoemission intensity image and MDC cut [Figs. 6.3c and (d)], indicating that CDW fluctuations are not completely melted and persist upon photoexcitation at this relatively high fluence (0.95 mJ/cm^2). Additionally, a first-principles theoretical study of the electronic response demonstrated that the excitonic mode is quenched upon heating above T_{CDW} [37], while ultrafast pump-probe optical spectroscopy and TR-ARPES studies of 1T-$TiSe_2$ in the CDW regime ($T < T_{\mathrm{CDW}}$) argued that the excitonic correlations should be destroyed above the critical fluence of 0.04 mJ/cm^2 [17, 23, 56]. This robustness of the fluctuating replica band at RT and high fluence conditions suggests that the CDW fluctuations are not solely of excitonic origin.

6.3.2 Ultrafast Melting and Recovery of RT-CDW Fluctuations

Now that we have established the equilibrium spectral signatures associated with RT-CDW fluctuations, we turn our attention to their ultrafast melting and recovery upon photoexcitation to gain detailed insight into the microscopic origin underlying the formation of this exotic phase [57]. The TR-ARPES enables systematic temporal separation of fundamental electronic and structural processes, allowing the identification of the dominant interactions [27].

In this spirit, we record the three-dimensional photoemission intensity as a function of pump-probe delay (between -0.5 ps to 3 ps), yielding a four-dimensional dataset $I(E_{\mathrm{B}}, k_x, k_y, \Delta t)$. From this multidimensional dataset, one can hunt for subtle signatures of RT-CDW fluctuations melting and recovery along energy, momentum, and time axes. We start by looking at the differential (pre-time-zero signal subtracted) CEC near the Fermi level (E_B = -0.07 eV), at a time delay of $\Delta t = 0$ [Figs. 6.4 (a) and (b)]. These CECs reveal the population of the conduction Ti 3d band (hollow elliptical positive differential signal) and suppression of the CDW backfolded band spectral weight (central negative differential signal) upon photoexcitation, around M(L) pockets. At this binding energy, after 400 fs, the negative differential signal associated with the melting of CDW order vanishes, as the filling of the bottom of the conduction band becomes dominant. This behavior is also evidenced in the differential energy-momentum region around the L(M) point, extracted for the same pump-probe delays.

To get more insight into the concomitant dynamics of hot electrons and CDW melting/recovery, we analyze the time-resolved photoemission intensities [Fig. 6.4c] in selected regions-of-interest (ROIs), shown as colored boxes in Fig. 6.4b. The purple dots represent the IR/XUV cross-correlation extracted from the time-dependent laser-assisted photoemission signal (ROI not shown), with an FWHM duration of 171 fs (Gaussian fit, yellow line). The dark red curve represents hot electron populations in Ti 3d conduction band, showing a fast light-induced rise followed by a single exponential decay behavior. The timescale of this relaxation process is strongly dependent on the excess energy of these hot electrons, as shown in the Fig 6.5. As discussed in the context of the analysis of the CECs, the black ROI is spectrally congested, with some overlapping contribution of both the bottom of the Ti 3d conduction band and the top of the Se 4p CDW backfolded band. The dynamics in this ROI feature a fast decay (experimental-resolution-limited) associated with the melting of CDW fluctuations, followed by a refilling and subsequent decay associated with the intraband hot electron dynamics.

To track the CDW fluctuation melting and recovery dynamics in a background-free manner, i.e., in an energy-momentum area where there is no overlap with the spectral feature from the normal phase, we look at the time-resolved photoemission intensity in the blue ROI, which emerges solely due to CDW-fluctuation-driven backfolded bands. The dynamics in this ROI is characterized by an ultrafast melting on a timescale limited by our temporal resolution ($\sim$170 fs), followed by a recovery on a sub-picosecond timescale, i.e., $\tau \sim 700$ fs. On top of the sub-picosecond recovery dynamics,

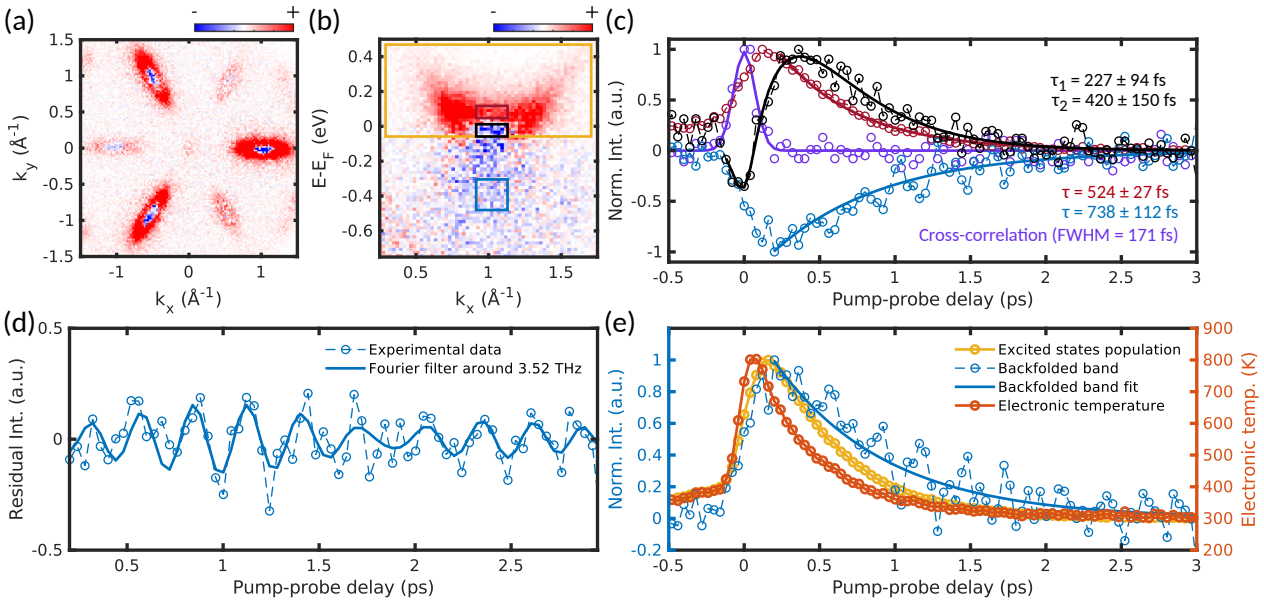


FIGURE 6.4 : Ultrafast melting and recovery of RT-CDW fluctuations in 1T-$TiSe_2$. (a)-(b) Differential constant energy contour (integrated over -23 meV$< \mathrm{E}-\mathrm{E_F} <$12 meV) and energy-momentum cut near the M pocket, obtained by subtracting photoemission intensity before (integration between -880 fs and -720 fs) and during pump-probe temporal overlap (integration between -80 fs and 80 fs). (c) Time-dependent photoemission intensity for different regions of interest (ROIs) along with corresponding fits. Purple dots represent the IR/XUV cross-correlation extracted from the time-dependent laser-assisted photoemission signal (ROI not shown), with an FWHM duration of 171 fs (Gaussian fit, purple line). Red, black, and blue dots denote time-resolved photoemission intensity from the respective ROIs shown in (b), while the associated lines indicate fits. (d) Blue dots and dashed line represent the residual intensity obtained by subtracting the double exponential fit from the photoemission intensity in the blue ROI in (b) (CDW backfolded band), while the thick blue line represents the Fourier filtered data (bandpass filter around 3.52 THz) indicating coherent oscillation of the CDW amplitude mode. (e) The electronic temperature as a function of pump-probe delay (orange) extracted by Fermi-Dirac distribution fitting, alongside with the backfolded band intensity (blue) and the excited state population dynamics (yellow).

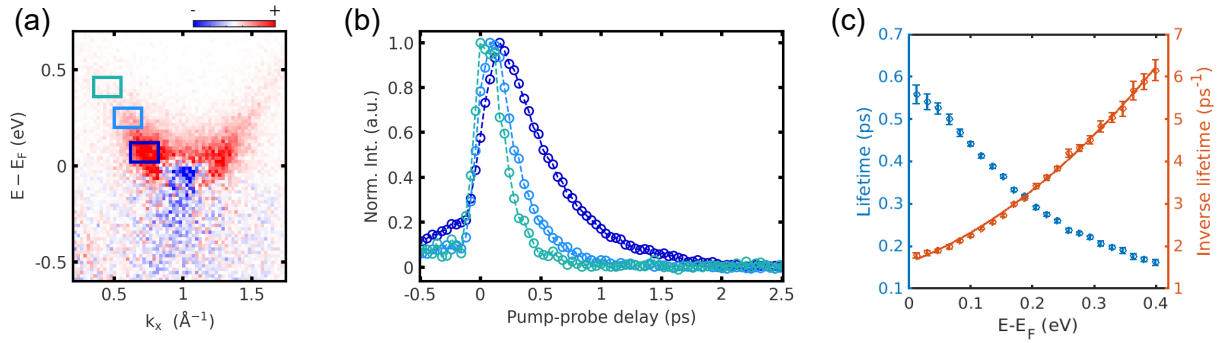


FIGURE 6.5 : (a) Differential energy-momentum cut near M with several regions of interest (ROI) boxes. The red and blue intensities denote the contrast between the pre-pump (integrated from -880 fs to -720 fs) and pump-probe overlap (integrated from -80 fs to 80 fs). (b) Intensity dynamics within each ROI, illustrating the faster decay of photoexcited electrons at higher energies. (c) Momentum-integrated electron population lifetime and corresponding inverse lifetime as a function of $E - E_F$.

some (low contrast) periodic modulations of the photoemission intensity can be observed with a long lifetime. To isolate the contribution from these periodic oscillations, we subtracted the single exponential fitted function from the experimental signal, yielding the residual intensity shown in Fig. 6.4d. By performing Fourier analysis, we found that the CDW fluctuations recovery dynamics is periodically modulated by a mode around 3.5 THz. This mode was previously observed in time-resolved photoemission measurements in 1T-$TiSe_2$ below T_{CDW} [17, 18, 20, 28] and has been identified as the A_{1g} CDW amplitude phonon mode corresponding to displacements along the CDW periodic lattice distortions. This represents the first time-resolved photoemission observation of coherent amplitude phonon mode surviving in the CDW-fluctuations regime at a temperature strongly exceeding the transition temperature and characterized by an unusually long lifetime.

Another interesting feature in the time-resolved photoemission signal is evident in panel 6.4e, where we compare the dynamics of the backfolded Se 4p band with the time evolution of the electronic temperature (extracted from the Fermi-Dirac distribution fitting) and of the total excited state population taken from the yellow ROI in Fig. 6.4b, representing the excitation and thermalization of Ti 3d states in a wider energy and momentum region. Note that the increase in electronic temperature and excited-state population observed at negative time delays is attributed to a weak prepulse extending up to a few hundred femtoseconds in the temporal profile of the infrared pump pulses. More importantly, the minimum of the backfolded band intensity is offset from the maximum of the electronic temperature, while it approximately follows the early dynamics of the excited state population of Ti 3d bands. This comparison suggests a mechanism beyond the excitonic insulator scenario, considering that the excitonic order is expected to be melted when the electron temperature reaches its maximum. Namely, exciton, if it exists, would be formed from the holes in Se 4p and electrons in Ti 3d bands, and, therefore, its quenching should be correlated with the total photo-excited carrier density, which can be described with the effective temperature. Furthermore, it is expected that the suppression of the excitonic mode is very fast and that it should correspond to the fastest signal, however, the RT-CDW signal suppression is offset from $\Delta t = 0$ by approximately 140 fs.

The concomitant observation of partial melting under relatively high-fluence condition (0.95 mJ/cm^2), the finite delay between the peak of transient electronic temperature and quenching of the backfolded Se 4p band, as well as coherent CDW amplitude phonon mode modulating the recovery dynamics, supports the idea of the dominant phonon contribution in the assumed hybrid exciton and electron-phonon mechanisms at such elevated temperatures. The idea of dominant phonon contribution is further supported by a recent study [58] which shows that while the band gap is sensitive to substrate screening, the temperature-dependent evolution of its electronic structure remains unaffected, indicating that excitons are not a primary mechanism that drives the CDW transition in $TiSe_2$.

6.4 Discussion

To further elaborate on the physical mechanism of CDW-fluctuation melting, two possible suppression pathways can be considered : (i) incoherent suppression, in which coherence is abruptly destroyed by hot electrons on a fast timescale (10–100 fs), and (ii) coherent suppression, mediated by the excitation of the amplitude mode. As previously noted, the comparison of timescales for the maximum suppression of the backfolded band in Fig. 6.4e reveals a near coincidence with the peak in the excited-state population above the Fermi level. Both are delayed relative to the peak in electronic temperature by approximately 140 fs, which closely corresponds to half the period of the amplitude mode oscillation. While it is likely that both coherent and incoherent mechanisms contribute to the suppression, this characteristic time delay—matching half an amplitude mode cycle—indicates a dominant role for coherent suppression.

Further insight can be gained by comparing the time-resolved dynamics of the backfolded band with the timescale of signal suppression at the M point in RT ultrafast electron diffraction [22]. It was shown that the diffuse signal at M point is quenched within the first 130 fs (limited by the instrument response function), and subsequently recovered within the time scale of 700 fs, which remarkably follows the melting time scales of backfolded Se 4p band observed here. The latter quench of the M point diffuse intensity was attributed to hardening of the M acoustic phonon mode by the photo-excited carriers, following the same time dynamics. This directly relates the quenching of the CDW fluctuating band with the hardening of the CDW-related M acoustic phonon.

Another recent ultrafast low-energy electron diffuse scattering study investigated the melting process of charge order in $TiSe_2$ and estimated roughly 30 :70 ratio of excitonic versus electron-phonon contributions to the total lattice distortion in the low-temperature CDW phase [59]. These findings highlight that both excitonic effects and electron-phonon coupling play significant roles in stabilizing the CDW order. While short-range CDW fluctuations are a dynamical phenomenon—fluctuating over both time and space—the mechanisms that govern their stabilization and ultrafast dynamics are similar to those in conventional low-temperature CDW phases. These short-range CDW fluctuations and their coexistence with some normal (non-CDW) domains can explain the low contrast of the coherent oscillations associated with the CDW amplitude phonon mode. Indeed, in low-temperature standard CDW phases, high-contrast modulations were measured by TR-ARPES [18, 20, 28].

Theoretical Analysis of Dynamical Electron-Phonon Interactions.

To further disentangle the influence of the electron-phonon coupling on the bare electronic structure above the transition temperature, we turn our attention to the theoretical framework that includes electron self-energy corrections necessary for the inclusion of electron-phonon interaction. Notably, no term responsible for the electron-hole coupling was used here. Yet, the spectral function strikingly matches the experimentally measured features that we attribute to the CDW-fluctuating phase. In Fig. 6.6, we show the impact of dynamical electron-phonon scattering on the

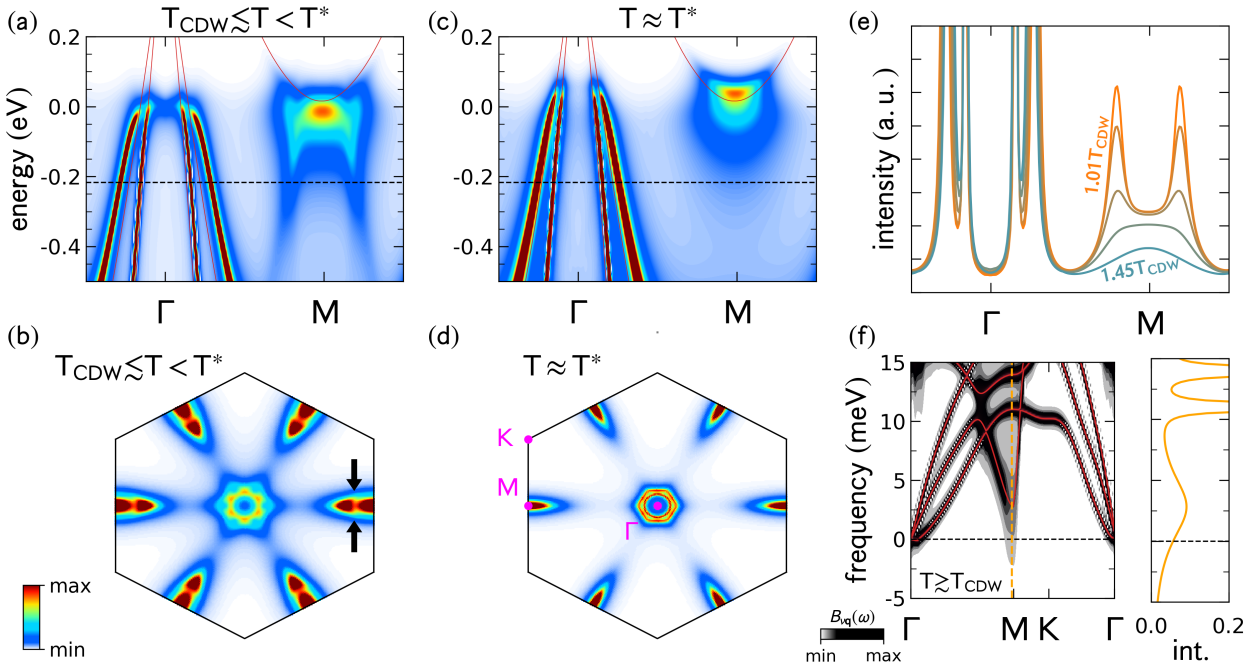


FIGURE 6.6 : Signatures of CDW fluctuations from dynamical electron-phonon scattering. (a) Electron spectral function of 1T-$TiSe_2$ along Γ-M high symmetry direction with dynamical electron-phonon interaction included for temperature just above the CDW transition temperature $T_{\rm CDW}$ (i.e., $T = 1150$ K). The theoretical value for the transition temperature as obtained with harmonic DFPT is $T_{\rm CDW} = 1105$ K. (b) The corresponding constant energy contour, where black arrows show the loss of spectral weight within the M pocket. (c)-(d) Same as (a)-(b) but close to the temperature T^*, i.e. when CDW fluctuations are diminished. Our theoretical calculations give $T^* \approx 1600$ K. Red lines represent the bare bands without dynamical electron-phonon coupling included. (e) MDC cuts for several temperatures above the $T_{\rm CDW}$ for energy well below the Ti-3d conduction band [see dashed line in panels (a) and (b)]. (f) Phonon spectral function $B_{\nu\mathbf{q}}(\omega)$ along the Γ-M-K-Γ high-symmetry path, with dynamical electron-phonon coupling included. The temperature is 50 K above $T_{\rm CDW}$ (i.e., $T = 1150$ K). The red curve shows the phonon dispersions without including spectral broadening due to electron-phonon scattering. The right panel shows the intensity profile of the phonon spectral function at the M point (orange dashed line in the left panel).

electron and phonon properties of 1T-$TiSe_2$ when the system is just above the structural instability $T > T_{\rm CDW}$. Temperatures used in the theoretical simulations are scaled with respect to the $T_{\rm CDW}$ value from density functional perturbation theory (DFPT), which is 1105 K. The DFPT $T_{\rm CDW}$ is the electronic temperature at which the acoustic mode at the M point becomes soft in the harmonic Born-Oppenheimer approximation. Panels (a)-(d) show the electron spectral functions along the Γ-M high symmetry direction and CECs (at Fermi energy) in the first Brillouin zone. The results for a temperature above but close to the CDW instability $T_{\rm CDW}$ are depicted in Fig. 6.6 (a) and (b), while the other two panels are for $T = T^* \gg T_{\rm CDW}$, when the CDW fluctuating replica are gone and system enters into the normal phase. The electron-phonon interaction is included into the spectral function by using the dynamical Fan-Migdal electron self-energy $\Sigma_{n\mathbf{k}}(\omega)$ [60, 61] based on inputs derived within the density functional perturbation theory [62, 63]. Even though we use the original unit cell with no CDW periodic lattice distortions, we observe strong renormalizations of electron bands for $T \geq T_{\rm CDW}$ very similar to the characteristic modifications observed in the CDW state, i.e., (i) finite spectral weight below the Ti 3d conduction band at the M point, coming from replicas

of Se 4p states at the Γ point, (ii) the flower-shaped contour at the Γ point close to the Fermi level coming from the replicas of the three non-equivalent Ti 3d M pockets, and (iii) the loss of spectral weight at the particular momentum of the M pocket close to the Fermi level [see Fig. 6.2 (c)]. These signatures come from the electron-phonon fluctuations and very much resemble the CDW fluctuations observed in our ARPES data at RT. With the rise of the temperature, these electron-phonon fluctuations are reduced [see Fig. 6.6e and Fig. 6.7], and the electronic band structure becomes closer to the bare DFT result [red curves in Fig. 6.6c].

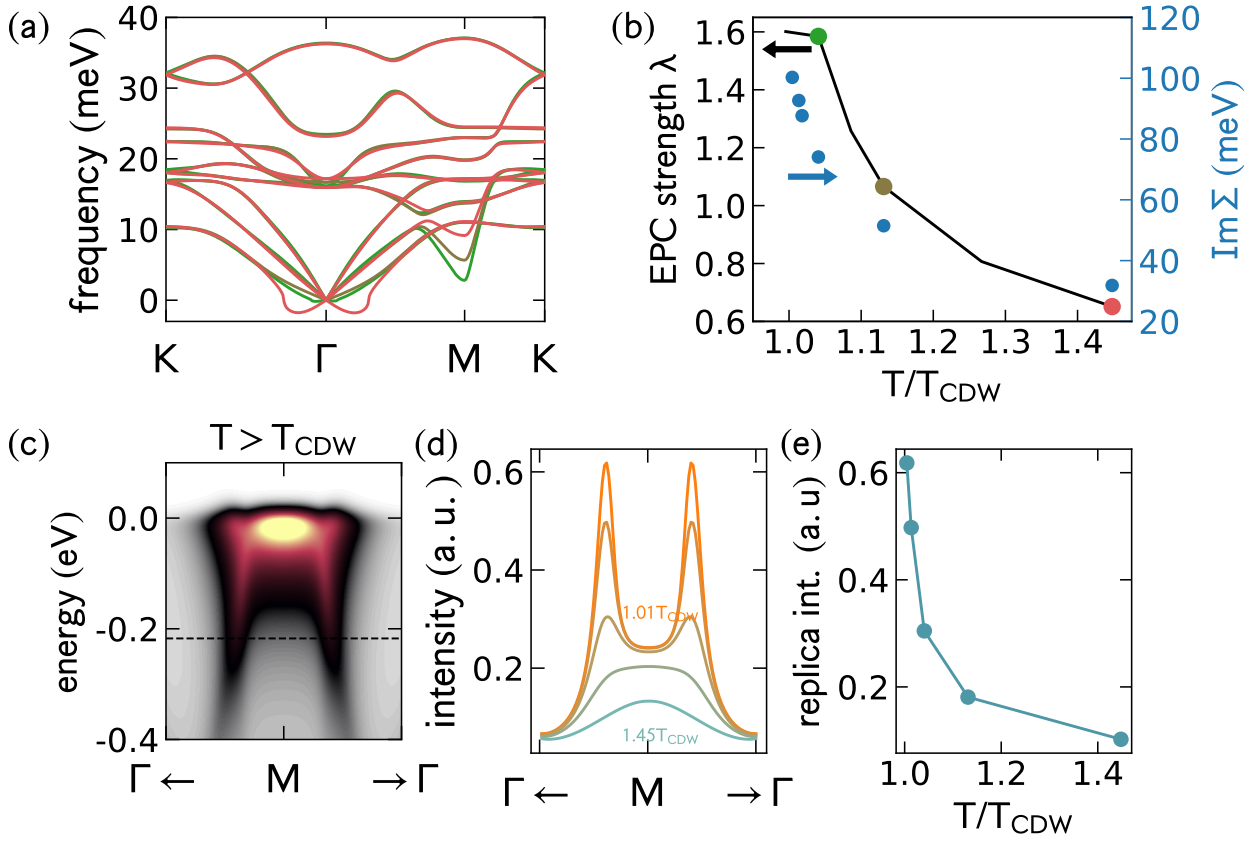


FIGURE 6.7 : (a) Phonon band structure of non-distorted $TiSe_2$ along the high-symmetry points and for several temperatures above the T_{CDW}, i.e., for 1150 K, 1300 K, and 1600 K. Note that this is done within the harmonic approximation for which $T_{\mathrm{CDW}} \approx 1100$ K. Also, note the hardening of the CDW-related acoustic phonon at the M point. (b) The calculated total electron-phonon coupling (EPC) strength λ for each temperature above T_{CDW}. The right axis shows the values for the imaginary part of the electron self-energy due to EPC (i.e., electron scattering rate), averaged over the states around the Fermi level. (c) Fluctuating replica at the M point for temperatures above T_{CDW} as obtained from the dynamical EPC scatterings. (d) The corresponding intensity of the fluctuating CDW replica coming from dynamical EPC as a function of temperature and along the M point. (e) The intensity of the replica is decreasing as a function of temperature. Note the connection between the hardening of the M acoustic phonon, the weaking of the EPC strength, and quenching of the CDW fluctuating replica as a function of increasing temperature.

Note that the bimodal intensity profile in our simulations disappears continuously, while it is completely vanished above T^*=1600 K, which is 500 K above the theoretical T_{CDW}. We observe that these features are related to the soft acoustic phonon mode at the M point [see Fig.6.6f] and are strongest when the energy of this mode is close to zero, while the electron-phonon coupling

is the strongest (see Fig. 6.7). When the temperature is elevated, the M-point acoustic phonon hardens, which quenches the electron-phonon scatterings between Se 4p and Ti 3d states. This further supports the correlation discussed above between the melting and recovery dynamics of the CDW fluctuating Se 4p band and hardening of the M phonon mode [22]. Similar microscopic explanation, which includes an active soft bosonic mode, was used many years ago to explain the fluctuating (or so-called pseudogap) region above the CDW phase [64] in the quasi-1D Peierls systems [65, 66], as well as in the high-T_c cuprates [67], and more recently in metallic 2H-$NbSe_2$ and 2H-$TaSe_2$ [68]. Further, spectral weight redistribution around the Fermi level due to electron-phonon-related fluctuations for $T \geq T_{\mathrm{CDW}}$ was once discussed for 1T-$TiSe_2$ [**?**], but it was never thoroughly appreciated and later connected to the replicas and other photoemission signatures in 1T-$TiSe_2$. Our microscopic interpretation is also in line with the observation that the CDW fluctuations reach a maximum at T_{CDW}, as observed with X-ray thermal diffuse scattering [31]. The temperature dependence of the phonon scattering lifetime characterized by hardening of the soft phonon mode with increasing temperature and a concomitant reduction of the electron scattering rates (i.e., $\mathrm{Im}\,\Sigma$), consistent with transport measurements [69], is shown in Fig. 6.7 and Fig. 6.8. It shows the proportionality between the larger CDW gap and the longer lifetime of the amplitude mode. This is most likely caused by less quasiparticle damping and suggests that even in the short-range ordered CDW regions, there is a finite CDW gap that suppresses the damping of the coherent (and re-hardened) amplitude mode oscillation. Notably, the figures also show that artificial introduction of small periodic lattice distortions leads to an increase in the amplitude mode lifetime and better lifetime agreement with the experiment. However, the dynamical electron-phonon scattering alone redistributes the density of states enough to account for a pseudogap formation, as shown in Fig. 6.8. We therefore conclude that while static CDW gaps vanish above the transition temperature, the dynamic pseudogap persists. This affects both the electronic scattering and phonon suppression rates.

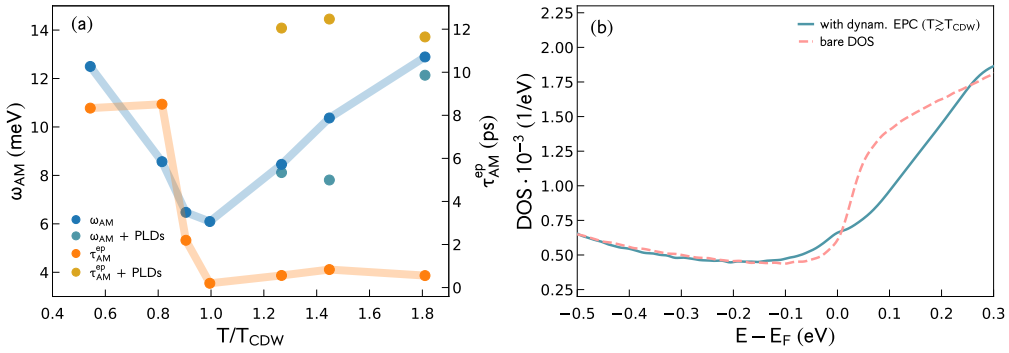


FIGURE 6.8 : (a) Frequency (blue) and lifetime (orange) of the CDW amplitude mode calculated from DFPT. We also show the corresponding results where small periodic lattice distortions are introduced also for $T > T_{\mathrm{CDW}}$ to mimic the CDW fluctuations. (b) Density of states for the bare $TiSe_2$ electronic structure, as well as when the dynamical electron-phonon scatterings are included for $T > T_{\mathrm{CDW}}$. The opening of the pseudogap is evident for the latter.

Figure 6.6f additionally shows the phonon spectral function of 1T-$TiSe_2$ in the fluctuation regime with included phonon-electron coupling, where part of the M phonon spectral weight extends up to negative frequencies. This indicates that in the fluctuation region where $T_{\mathrm{CDW}} < T < T^*$, the atomic motions fluctuate between normal and CDW states. Note that equilibrium electron diffraction measurements [23] as well as X-ray diffuse scattering [29, 35] observed both L and M diffusive peaks at RT, suggesting the presence of the fluctuating periodic lattice distortions above T_{CDW}. In Fig. 6.9 we demonstrate how the dynamical electron-phonon scattering introduces very similar modification to the electronic structure as the symmetry-breaking periodic lattice distortions in the CDW state.

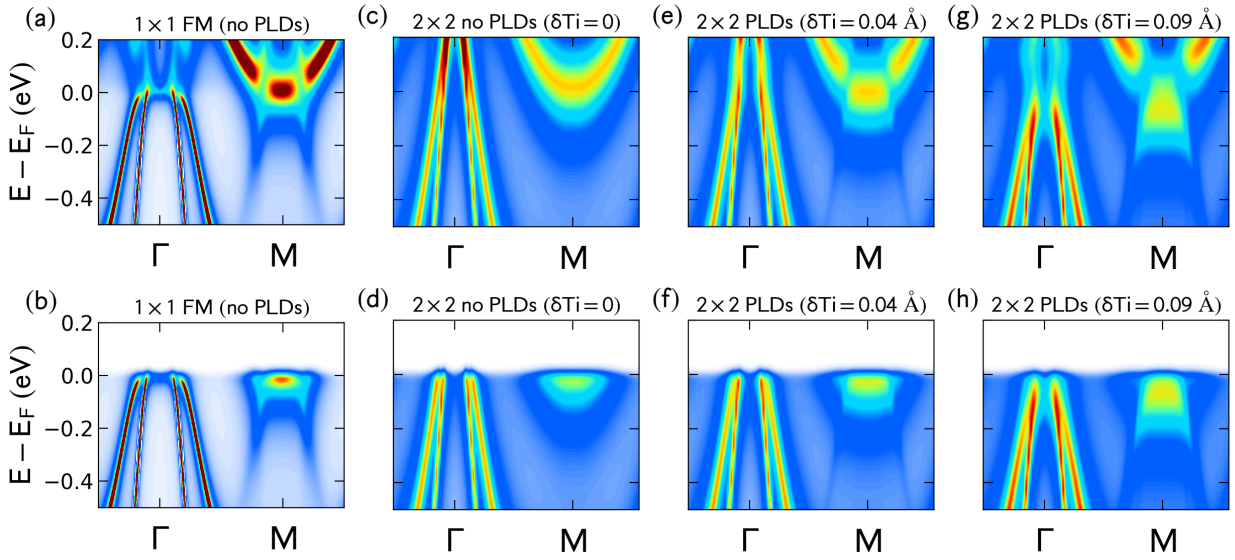


FIGURE 6.9 : (a)-(b) Electron spectral function of 1T-$TiSe_2$ with dynamical electron-phonon interaction included via Fan-Migdal self-energy (FM) for temperature just above the CDW transition temperature $T \geq T_{\mathrm{CDW}}$. These calculations are done for 1×1 unit cell with no periodic lattice distortions (PLDs). (c)-(h) The band structures of the 2×2 CDW phase with various values of PLDs mapped to the 1×1 unit cell. In these calculations we do not include the FM self-energy. The lower panels are equivalent to the plots in the upper panels, but weighted with the Fermi-Dirac distribution function. The comparison between the results of 1×1 band structure with FM self-energy and 2×2 result with PLDs shows that the dynamical electron-phonon scattering introduces very similar modifications to the band structure as the symmetry-breaking CDW PLDs.

The system could, therefore, support the excitation of the CDW amplitude mode at $T > T_{\mathrm{CDW}}$, as it is observed experimentally following optical photoexcitation [Fig. 6.4f]. These theoretical results demonstrate that the features (i)-(iii) as well as the CDW amplitude mode observed in the CDW fluctuation regime could be explained by the dynamical electron-phonon effects also supported by our scanning tunneling microscopy measurements - see Fig. 6.10, which opposes the common belief that the fluctuation regime is dominated by the electron-hole correlations [10, 70]. The latter mechanism could still be present in the formation process of the CDW fluctuations in 1T-$TiSe_2$, but more likely as a higher-order correcting effect. This is further corroborated by the fact that the equivalent electron-related collective soft mode (e.g., plasmon or exciton), which could

produce the above features in scattering with Ti 3d or Se 4p states, is not observed in the normal phase above T_{CDW}, neither in experiments [11, 71] nor theoretical studies [37].

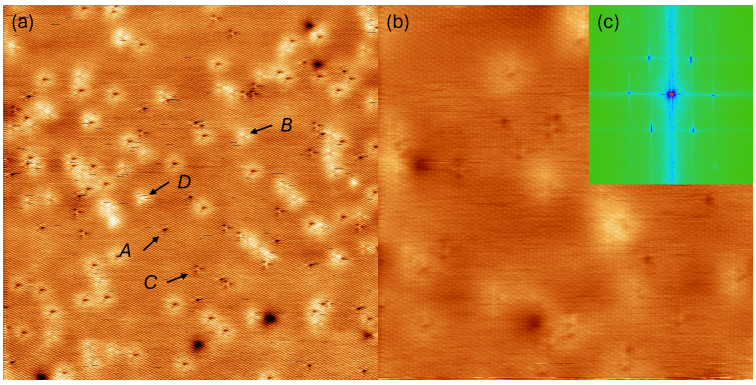


FIGURE 6.10 : To characterize the CDW fluctuations dynamics in real space and find the fingerprints of finite fluctuating periodic lattice distortions (PLD), we measured the 1T-$TiSe_2$ at RT with scanning tunneling microscopy (STM) and observed no visible signatures of the 2×2 CDW patches beyond the signal corresponding to the 1×1 unit cell charge modulation. This implies that the fluctuations likely occur at timescales below the scanning rate of the STM, further supporting our result that the localization of each CDW modulationin $TiSe_2$ at a given position is inherently dynamical, while the system as a whole is constantly in a fluctuation phase. Despite that, L and M diffusive peaks at RT were spotted in equilibrium electron diffraction measurements [23], as well as in X-ray diffuse scattering [29, 35], suggesting the presence of the fluctuating PLD at RT, and possibly the appearance of the corresponding pseudogap [30]. (a) Atomically resolved empty-states STM image showing native defects (60×60 nm^2, $I_t = 1.2$ nA, $V_{\mathrm{bias}} = 0.01$ V). Different defects are labeled *A*, *B*, *C*, *D* following (PRL [72]). (b) Atomically resolved filled-states STM image (32×32 nm^2, $I_t = 0.1$ nA, $V_{\mathrm{bias}} = -0.1$ V). (c) FFT-amplitude plot from (b) showing no 2×2 CDW charge modulation associated spots.

6.5 Conclusions

Our study provides direct evidence of charge density wave (CDW) fluctuations in 1T-$TiSe_2$ at room temperature using time-resolved extreme ultraviolet (XUV) momentum microscopy. We observe the persistence of the backfolded Se 4p band well above T_{CDW}, demonstrating that CDW fluctuations remain detectable even at elevated temperatures. The ultrafast melting and recovery of these fluctuations, featuring the presence of coherent CDW amplitude phonon modes, highlight the importance of electron-phonon interactions in stabilizing the CDW phase at elevated temperatures.

Our experimental results, combined with density functional theory (DFT) calculations incorporating electron self-energy corrections, show that the electron-phonon interaction remains the dominant contributor to the CDW mechanism at room temperature. The observation of coherent amplitude phonon oscillations further supports this assertion, challenging the notion that the CDW fluctuating phase is purely driven by excitonic correlations. Instead, our findings suggest that while electron-hole coupling could also play a role, electron-phonon interactions are essential for the persistence of CDW fluctuations above T_{CDW} with strong implications for the low-temperature CDW phase formation.

These results not only refine the understanding of CDW physics in 1T-$TiSe_2$ but also have broader consequences for the study of fluctuating phases in other transition metal dichalcogenides and strongly correlated materials. Given the emerging connection between CDW fluctuations and unconventional superconductivity, our findings may provide valuable insights into the interplay between these two phenomena. Future studies leveraging advanced ultrafast techniques could further elucidate the microscopic mechanisms governing the fluctuating CDW phase, potentially unveiling new pathways for manipulating correlated electron systems in quantum materials.

Bibliographie

[1] S Fragkos, H Orio, N G Erhardt, A Jabed, S Sasi, Q Courtade, M P T Masilamani, M Ünzelmann, F Diekmann, B Hildebrand, D Descamps, S Petit, F Boschini, J Minár, Y Mairesse, F Reinert, K Rossnagel, D Novko, S Beaulieu, and J Schusser. Electron-phonon-dominated charge-density-wave fluctuations in $TiSe_2$ accessed by ultrafast nonequilibrium dynamics. 2025. doi : arXiv:2507.12430v2. URL https://doi.org/10.48550/arXiv.2507.12430.

[2] F Di Salvo, D Moncton, and J Waszczak. Electronic properties and superlattice formation in the semimetal $TiSe_2$. *Phys. Rev. B*, 14 :4321–4328, Nov 1976. doi : 10.1103/PhysRevB.14.4321. URL https://link.aps.org/doi/10.1103/PhysRevB.14.4321.

[3] K Woo, F Brown, W McMillan, R Miller, M Schaffman, and M Sears. Superlattice formation in titanium diselenide. *Phys. Rev. B*, 14 :3242–3247, Oct 1976. doi : 10.1103/PhysRevB.14.3242. URL https://link.aps.org/doi/10.1103/PhysRevB.14.3242.

[4] K Rossnagel. On the origin of charge-density waves in select layered transition-metal dichalcogenides. *Journal of Physics : Condensed Matter*, 23(21) :213001, may 2011. doi : 10.1088/0953-8984/23/21/213001. URL https://dx.doi.org/10.1088/0953-8984/23/21/213001.

[5] D Jérome, T M Rice, and W Kohn. Excitonic insulator. *Phys. Rev.*, 158 :462, Jun 1967. doi : 10.1103/PhysRev.158.462. URL https://link.aps.org/doi/10.1103/PhysRev.158.462.

[6] T Kidd, T Miller, M Chou, and T Chiang. Electron-hole coupling and the charge density wave transition in $TiSe_2$. *Phys. Rev. Lett.*, 88 :226402, May 2002. doi : 10.1103/PhysRevLett.88.226402. URL https://link.aps.org/doi/10.1103/PhysRevLett.88.226402.

[7] H Cercellier, C Monney, F Clerc, C Battaglia, L Despont, M Garnier, H Beck, P Aebi, L Patthey, H Berger, and L Forr'o. Evidence for an excitonic insulator phase in 1T-$TiSe_2$. *Phys. Rev. Lett.*, 99 :146403, Oct 2007. doi : 10.1103/PhysRevLett.99.146403. URL https://link.aps.org/doi/10.1103/PhysRevLett.99.146403.

[8] C Monney, H Cercellier, F Clerc, C Battaglia, E Schwier, C Didiot, M Garnier, H Beck, P Aebi, H Berger, L Forr'o, and L Patthey. Spontaneous exciton condensation in 1T-$TiSe_2$: Bcs-like approach. *Phys. Rev. B*, 79 :045116, Jan 2009. doi : 10.1103/PhysRevB.79.045116. URL https://link.aps.org/doi/10.1103/PhysRevB.79.045116.

[9] C Monney, E Schwier, M Garnier, N Mariotti, C Didiot, H Beck, P Aebi, H Cercellier, J Marcus, C Battaglia, H Berger, and A Titov. Temperature-dependent photoemission on 1T-$TiSe_2$: Interpretation within the exciton condensate phase model. *Phys. Rev. B*, 81 :155104, Apr 2010. doi : 10.1103/PhysRevB.81.155104. URL https://link.aps.org/doi/10.1103/PhysRevB.81.155104.

[10] C Monney, G Monney, P Aebi, and H Beck. Electron-hole fluctuation phase in 1T-$TiSe_2$. *Phys. Rev. B*, 85 :235150, Jun 2012. doi : 10.1103/PhysRevB.85.235150. URL https://link.aps.org/doi/10.1103/PhysRevB.85.235150.

[11] A Kogar, M S Rak, S Vig, A A Husain, F Flicker, Y I Joe, L Venema, G . MacDougall, T C Chiang, E Fradkin, J v Wezel, and P Abbamonte. Signatures of exciton condensation in a transition metal dichalcogenide. *Science*, 358(6368) :1314, 2017. doi : 10.1126/science.aam6432. URL https://www.science.org/doi/abs/10.1126/science.aam6432.

[12] H P Hughes. Structural distortion in $TiSe_2$ and related materials-a possible jahn-teller effect? *Journal of Physics C : Solid State Physics*, 10(11) :L319, jun 1977. doi : 10.1088/0022-3719/10/11/009. URL https://dx.doi.org/10.1088/0022-3719/10/11/009.

[13] Y Yoshida and K Motizuki. Electron lattice interaction and lattice instability of 1T-$TiSe_2$. *Journal of the Physical Society of Japan*, 49(3) :898, 1980. doi : 10.1143/JPSJ.49.898. URL https://doi.org/10.1143/JPSJ.49.898.

[14] M Whangbo and E Canadell. Analogies between the concepts of molecular chemistry and solid-state physics concerning structural instabilities. electronic origin of the structural modulations in layered transition metal dichalcogenides. *Journal of the American Chemical Society*, 114(24) :9587–9600, 1992. doi : 10.1021/ja00050a044.

[15] K Rossnagel, L Kipp, and M Skibowski. Charge-density-wave phase transition in 1T-$TiSe_2$ excitonic insulator versus band-type jahn-teller mechanism. *Phys. Rev. B*, 65 :235101, May 2002. doi : 10.1103/PhysRevB.65.235101. URL https://link.aps.org/doi/10.1103/PhysRevB.65.235101.

[16] F Weber, S Rosenkranz, J Castellan, R Osborn, G Karapetrov, R Hott, R Heid, K Bohnen, and A Alatas. Electron-phonon coupling and the soft phonon mode in $TiSe_2$. *Phys. Rev. Lett.*, 107 :266401, Dec 2011. doi : 10.1103/PhysRevLett.107.266401. URL https://link.aps.org/doi/10.1103/PhysRevLett.107.266401.

[17] M Porer, U Leierseder, J-M M'enard, H Dachraoui, L Mouchliadis, I E Perakis, U Heinzmann, J Demsar, K Rossnagel, and R Huber. Non-thermal separation of electronic and structural orders in a persisting charge density wave. *Nature Materials*, 13(9) :857–861, jul 2014. doi : 10.1038/nmat4042. URL https://doi.org/10.1038%2Fnmat4042.

[18] C Monney, M Puppin, C Nicholson, M Hoesch, R Chapman, E Springate, H Berger, A Magrez, C Cacho, R Ernstorfer, and M Wolf. Revealing the role of electrons and phonons in the ultrafast recovery of charge density wave correlations in 1T-$TiSe_2$. *Phys. Rev. B*, 94 :165165, Oct 2016. doi : 10.1103/PhysRevB.94.165165. URL https://link.aps.org/doi/10.1103/PhysRevB.94.165165.

[19] T Karam, J Hu, and G Blake. Strongly coupled electron–phonon dynamics in few-layer $TiSe_2$ exfoliates. *ACS Photonics*, 5(4) :1228, 2018. doi : 10.1021/acsphotonics.7b00878. URL https://doi.org/10.1021/acsphotonics.7b00878.

[20] H Hedayat, C Sayers, D Bugini, C Dallera, D Wolverson, T Batten, S Karbassi, S Friedemann, G Cerullo, J van Wezel, S Clark, E Carpene, and E Da Como. Excitonic and lattice contributions to the charge density wave in 1T-$TiSe_2$ revealed by a phonon bottleneck. *Phys. Rev. Research*, 1 :023029, Sep 2019. doi : 10.1103/PhysRevResearch.1.023029. URL https://link.aps.org/doi/10.1103/PhysRevResearch.1.023029.

[21] C Lian, S J Zhang, S Q Hu, M X Guan, and S Meng. Ultrafast charge ordering by self-amplified exciton–phonon dynamics in $TiSe_2$. *Nature Communications*, 11(1) :43, 12 2020. ISSN 20411723. doi : 10.1038/s41467-019-13672-7.

[22] M R Otto, J Pöhls, L P R de Cotret, M J Stern, M Sutton, and B J Siwick. Mechanisms of electron-phonon coupling unraveled in momentum and time : The case of soft phonons in $TiSe_2$. *Science Advances*, 7(20) :eabf2810, 2021. doi : 10.1126/sciadv.abf2810.

[23] Y Cheng, A Zong, J Li, W Xia, S Duan, W Zhao, Y Li, F Qi, J Wu, L Zhao, et al. Light-induced dimension crossover dictated by excitonic correlations. *Nature communications*, 13(1) :963, 2022. doi : https://doi.org/10.1038/s41467-022-28309-5.

[24] T Heinrich, H Chang, S Zayko, K Rossnagel, M Sivis, and C Ropers. Electronic and structural fingerprints of charge-density-wave excitations in extreme ultraviolet transient absorption spectroscopy. *Phys. Rev. X*, 13 :021033, Jun 2023. doi : 10.1103/PhysRevX.13.021033. URL https://link.aps.org/doi/10.1103/PhysRevX.13.021033.

[25] J van Wezel, P Nahai-Williamson, and S Saxena. Exciton-phonon-driven charge density wave in $TiSe_2$. *Phys. Rev. B*, 81 :165109, Apr 2010. doi : 10.1103/PhysRevB.81.165109. URL https://link.aps.org/doi/10.1103/PhysRevB.81.165109.

[26] T Rohwer, S Hellmann, M Wiesenmayer, C Sohrt, A Stange, B Slomski, A Carr, L Miaja-Avila, M Kallaene, S Mathias, L Kipp, K Rossnagel, and M Bauer. Collapse of long-range charge order tracked by time-resolved photoemission at high momenta. *Nature*, 471(7339) :490, MAR 24 2011. ISSN 0028-0836. doi : 10.1038/nature09829.

[27] S Hellmann, T Rohwer, M Kall{"a}ne, K Hanff, C Sohrt, A Stange, A Carr, MM Murnane, HC Kapteyn, L Kipp, et al. Time-domain classification of charge-density-wave insulators. *Nature communications*, 3(1) :1069, 2012. doi : https://doi.org/10.1038/ncomms2078.

[28] S Duan, Y Cheng, W Xia, Y Yang, C Xu, F Qi, C Huang, T Tang, Y Guo, We Luo, D Qian, D Xiang, J Zhang, and W Zhang. Optical manipulation of electronic dimensionality in a quantum material. *Nature*, 595(7866) :239, jul 2021. doi : 10.1038/s41586-021-03643-8. URL https://doi.org/10.1038%2Fs41586-021-03643-8.

[29] K Woo, F Brown, W McMillan, R Miller, M Schaffman, and M Sears. Superlattice formation in titanium diselenide. *Phys. Rev. B*, 14 :3242–3247, Oct 1976. doi : 10.1103/PhysRevB.14.3242. URL https://link.aps.org/doi/10.1103/PhysRevB.14.3242.

[30] Y Miyahara, H Bando, and H Ozaki. Tunnelling spectroscopic study of the cdw energy gap in $TiSe_2$. *Journal of Physics : Condensed Matter*, 7(13) :2553, 1995. doi : 10.1088/0953-8984/7/13/006. URL https://dx.doi.org/10.1088/0953-8984/7/13/006.

[31] M Holt, P Zschack, H Hong, M Chou, and T Chiang. X-ray studies of phonon softening in $TiSe_2$. *Phys. Rev. Lett.*, 86 :3799–3802, Apr 2001. doi : 10.1103/PhysRevLett.86.3799. URL https://link.aps.org/doi/10.1103/PhysRevLett.86.3799.

[32] P Chen, Y Chan, X Fang, S Mo, Z Hussain, A Fedorov, M Chou, and T Chiang. Hidden order and dimensional crossover of the charge density waves in $TiSe_2$. *Scientific reports*, 6 (1) :37910, 2016. doi : https://doi.org/10.1038/srep37910. URL https://doi.org/10.1038/srep37910.

[33] Y Mizukoshi, T Fukuda, Y Komori, R Ishikawa, K Ueno, and M Hase. Ultrafast melting of charge-density wave fluctuations at room temperature in 1T-$TiSe_2$ monitored under non-equilibrium conditions. *Applied Physics Letters*, 122(24) :243101, 06 2023. ISSN 0003-6951. doi : 10.1063/5.0153161. URL https://doi.org/10.1063/5.0153161.

[34] R Zhang, W Ruan, J Yu, L Gao, H Berger, L Forró, K Watanabe, T Taniguchi, A Ranjbar, R Belosludov, T Kühne, M Bahramy, and X Xi. Second-harmonic generation in atomically thin 1T-$TiSe_2$ and its possible origin from charge density wave transitions. *Phys. Rev. B*, 105 : 085409, Feb 2022. doi : 10.1103/PhysRevB.105.085409. URL https://link.aps.org/doi/10.1103/PhysRevB.105.085409.

[35] X Guo, A Kogar, J Henke, F Flicker, F de Juan, S L Sun, I Khayr, Y Peng, S Lee, M J Krogstad, S Rosenkranz, R Osborn, J P C Ruff, D B Lioi, G Karapetrov, D J Campbell, J Paglione, J van W, T C Chiang, and P Abbamonte. In-plane anisotropy of charge density wave fluctuations in 1T-$TiSe_2$. *arXiv*, page 2501.09968, 2025. URL https://arxiv.org/abs/2501.09968.

[36] T Jaouen, B Hildebrand, M Mottas, M Di Giovannantonio, P Ruffieux, M Rumo, C Nicholson, E Razzoli, C Barreteau, A Ubaldini, E Giannini, F Vanini, H Beck, C Monney, and P Aebi. Phase separation in the vicinity of fermi surface hot spots. *Phys. Rev. B*, 100 :075152, Aug 2019. doi : 10.1103/PhysRevB.100.075152. URL https://link.aps.org/doi/10.1103/PhysRevB.100.075152.

[37] C Lian, Z Ali, and B Wong. Charge density wave hampers exciton condensation in $TiSe_2$. *Phys. Rev. B*, 100 :205423, Nov 2019. doi : 10.1103/PhysRevB.100.205423. URL https://link.aps.org/doi/10.1103/PhysRevB.100.205423.

[38] Y Joe, X Chen, P Ghaemi, K Finkelstein, G. A. de la Peña, Y. Gan, J. C. T. Lee, S. Yuan, J. Geck, G. J. MacDougall, T. C. Chiang, S. L. Cooper, E. Fradkin, and P. Abbamonte. Emergence of charge density wave domain walls above the superconducting dome in 1T-$TiSe_2$. *Nature Physics*, 10(6) :421, Jun 2014. doi : 10.1038/nphys2935. URL https://doi.org/10.1038/nphys2935.

[39] R D H Hinlopen, O N Moulding, W R Broad, J Buhot, F Bangma, A McCollam, J Ayres, C J Sayers, E Da Como, F Flicker, J van Wezel, and S Friedemann. Lifshitz transition enabling superconducting dome around a charge-order critical point. *Science Advances*, 10 (27) :eadl3921, 2024. doi : 10.1126/sciadv.adl3921. URL https://www.science.org/doi/abs/10.1126/sciadv.adl3921.

[40] S Borisenko, A Kordyuk, A Yaresko, V Zabolotnyy, D Inosov, R Schuster, B Büchner, R Weber, R Follath, L Patthey, and H Berger. Pseudogap and charge density waves in two dimensions. *Phys. Rev. Lett.*, 100 :196402, May 2008. doi : 10.1103/PhysRevLett.100.196402. URL https://link.aps.org/doi/10.1103/PhysRevLett.100.196402.

[41] R Arpaia, S Caprara, R Fumagalli, G De Vecchi, Y Y Peng, E Andersson, D Betto, G M De Luca, N B Brookes, F Lombardi, M Salluzzo, L Braicovich, C Di Castro, M Grilli, and G Ghiringhelli. Dynamical charge density fluctuations pervading the phase diagram of a Cu-based high-T_c superconductor. *Science*, 365(6456) :906, 2019. doi : 10.1126/science.aav1315. URL https://www.science.org/doi/abs/10.1126/science.aav1315.

[42] Y Zhong, T Suzuki, H Liu, K Liu, Z Nie, Y Shi, S Meng, B Lv, H Ding, T Kanai, J Itatani, S Shin, and K Okazaki. Unveiling van hove singularity modulation and fluctuated charge order in kagome superconductor CsV_3Sb_5 via time-resolved arpes. *Phys. Rev. Res.*, 6 :043328, Dec 2024. doi : 10.1103/PhysRevResearch.6.043328. URL https://link.aps.org/doi/10.1103/PhysRevResearch.6.043328.

[43] H Liu, S Duan, X Liu, Z Liu, S Wang, L Gu, J Huang, W Yang, J Liu, D Qian, Y Guo, and W Zhang. Fluctuated lattice-driven charge density wave far above the condensation temperature in kagome superconductor KV_3Sb_5. *Science Bulletin*, 70(8) :1211–1214, 2025. ISSN 2095-9273. doi : https://doi.org/10.1016/j.scib.2025.02.018. URL https://www.sciencedirect.com/science/article/pii/S209592732500180X.

[44] S Duan, W Xia, C Huang, S Wang, L Gu, H Liu, D Xiang, D Qian, Y Guo, and W Zhang. Ultrafast switching from the charge density wave phase to a metastable metallic state in $TiSe_2$. *Phys. Rev. Lett.*, 130 :226501, May 2023. doi : 10.1103/PhysRevLett.130.226501. URL https://link.aps.org/doi/10.1103/PhysRevLett.130.226501.

[45] M Huber, Y Lin, G Marini, L Moreschini, C Jozwiak, A Bostwick, M Calandra, and A Lanzara. Ultrafast creation of a light-induced semimetallic state in strongly excited 1T-$TiSe_2$. *Science Advances*, 10(19) :eadl4481, 2024. doi : 10.1126/sciadv.adl4481. URL https://www.science.org/doi/abs/10.1126/sciadv.adl4481.

[46] J Ishioka, Y Liu, K Shimatake, T Kurosawa, K Ichimura, Y Toda, M Oda, and S Tanda. Chiral charge-density waves. *Phys. Rev. Lett.*, 105 :176401, Oct 2010. doi : 10.1103/PhysRevLett.105.176401. URL https://link.aps.org/doi/10.1103/PhysRevLett.105.176401.

[47] S Xu, Q Ma, Y Gao, A Kogar, A Zong, A Mier Valdivia, T Dinh, S Huang, B Singh, C Hsu, T Chang, J Ruff, K Watanabe, T Taniguchi, H Lin, G Karapetrov, D Xiao, P Jarillo-Herrero, and N Gedik. Spontaneous gyrotropic electronic order in a transition-metal dichalcogenide. *Nature*, 578(7796) :545–549, February 2020. ISSN 1476-4687. doi : 10.1038/s41586-020-2011-8. URL http://dx.doi.org/10.1038/s41586-020-2011-8.

[48] E Morosan, H W Zandbergen, B S Dennis, J W G Bos, Y Onose, T Klimczuk, A P Ramirez, N P Ong, and R J Cava. Superconductivity in Cu_xTiSe_2. *Nature Physics*, 2(8) :544, jul 2006. doi : 10.1038/nphys360. URL https://doi.org/10.1038/nphys360.

[49] S Fragkos, Q Courtade, O Tkach, J Gaudin, D Descamps, G Barrette, S Petit, G Schönhense, Y Mairesse, and S Beaulieu. Time- and polarization-resolved extreme ultraviolet momentum microscopy. *Rev. Sci. Instrum.*, 96(11), November 2025.

[50] O Tkach and G Schönhense. Multimode objective lens for momentum microscopy and xpeem : Theory. *Ultramicroscopy*, 276 :114167, 2025. ISSN 0304-3991. doi : https://doi.org/10.1016/j.ultramic.2025.114167. URL https://www.sciencedirect.com/science/article/pii/S030439912500066X.

[51] O Tkach, S Fragkos, Q Nguyen, S Chernov, M Scholz, N Wind, S Babenkov, O Fedchenko, Y Lytvynenko, D Zimmer, A Hloskovskii, D Kutnyakhov, F Pressacco, J Dilling, L Bruckmeier, M Heber, F Scholz, J Sobota, J Koralek, N Sirica, M Kallmayer, M Hoesch, C Schlueter, L V Odnodvorets, Y Mairesse, K Rossnagel, H J Elmers, S Beaulieu, and G Schoenhense. Multi-mode front lens for momentum microscopy : Part II experiments, 2024. URL https://arxiv.org/abs/2401.10084.

[52] S Moser. An experimentalist's guide to the matrix element in angle resolved photoemission. *Journal of Electron Spectroscopy and Related Phenomena*, 214 :29–52, 2017. ISSN 0368-2048. doi : https://doi.org/10.1016/j.elspec.2016.11.007. URL https://www.sciencedirect.com/science/article/pii/S0368204816301724.

[53] J Schusser, H Orio, M Ünzelmann, J Heßdörfer, M P T Masilamani, F Diekmann, K Rossnagel, and F Reinert. Towards robust dichroism in angle-resolved photoemission. *Communications Physics*, 7 :270, 2024. ISSN 2399-3650. doi : 10.1038/s42005-024-01762-y. URL https://doi.org/10.1038/s42005-024-01762-y.

[54] J Schusser, H Bentmann, M Ünzelmann, T Figgemeier, C Min, S Moser, J Neu, T Siegrist, and F Reinert. Assessing nontrivial topology in weyl semimetals by dichroic photoemission. *Phys. Rev. Lett.*, 129 :246404, Dec 2022. doi : 10.1103/PhysRevLett.129.246404. URL https://link.aps.org/doi/10.1103/PhysRevLett.129.246404.

[55] S Borisenko, A Kordyuk, V Zabolotnyy, D Inosov, D Evtushinsky, B Büchner, A Yaresko, A Varykhalov, R Follath, W Eberhardt, L Patthey, and H Berger. Two energy gaps and fermi-surface "arcs" in $NbSe_2$. *Phys. Rev. Lett.*, 102 :166402, Apr 2009. doi : 10.1103/PhysRevLett.102.166402. URL https://link.aps.org/doi/10.1103/PhysRevLett.102.166402.

[56] M Huber, Y Lin, N Dale, R Sailus, S Tongay, R Kaindl, and A Lanzara. Revealing the order parameter dynamics of 1T-$TiSe_2$ following optical excitation. *Scientific Reports*, 12(1) :15860, September 2022. ISSN 2045-2322. doi : 10.1038/s41598-022-19319-w. URL http://dx.doi.org/10.1038/s41598-022-19319-w.

[57] F Boschini, M Zonno, and A Damascelli. Time-resolved arpes studies of quantum materials. *Rev. Mod. Phys.*, 96 :015003, Feb 2024. doi : 10.1103/RevModPhys.96.015003. URL https://link.aps.org/doi/10.1103/RevModPhys.96.015003.

[58] S Buchberger, Y in 't Veld, A Rajan, P Murgatroyd, B Edwards, B Saika, N Kushwaha, M Vischer, J Berges, D Carbone, J Osiecki, C Polley, T Wehling, and P King. Persistence of charge ordering instability to coulomb engineering in the excitonic insulator candidate $TiSe_2$, 2025. URL https://arxiv.org/abs/2506.01470.

[59] F Kurtz, T Dauwe, S Yalunin, G Storeck, J Horstmann, H Böckmann, and C Ropers. Nonthermal phonon dynamics and a quenched exciton condensate probed by surface-sensitive electron diffraction. *Nature Materials*, 23(7) :890, April 2024. ISSN 1476-4660. doi : 10.1038/s41563-024-01880-6. URL http://dx.doi.org/10.1038/s41563-024-01880-6.

[60] F Giustino. Electron-phonon interactions from first principles. *Rev. Mod. Phys.*, 89 :015003, Feb 2017. doi : 10.1103/RevModPhys.89.015003. URL https://link.aps.org/doi/10.1103/RevModPhys.89.015003.

[61] H Lee, S Poncé, K Bushick, S Hajinazar, J Lafuente-Bartolome, J Leveillee, C Lian, J Lihm, F Macheda, H Mori, H Paudyal, W Sio, S Tiwari, M Zacharias, X Zhang, N Bonini, E Kioupakis, E Margine, and F Giustino. Electron–phonon physics from first principles using the epw code. *npj Computational Materials*, 9(1) :156, 2023. ISSN 2057-3960. doi : 10.1038/s41524-023-01107-3. URL http://dx.doi.org/10.1038/s41524-023-01107-3.

[62] S Baroni, S de Gironcoli, A Dal Corso, and P Giannozzi. Phonons and related crystal properties from density-functional perturbation theory. *Rev. Mod. Phys.*, 73 :515–562, Jul 2001. doi : 10.1103/RevModPhys.73.515. URL https://link.aps.org/doi/10.1103/RevModPhys.73.515.

[63] P Giannozzi, O Andreussi, T Brumme, O Bunau, M Buongiorno Nardelli, M Calandra, R Car, C Cavazzoni, D Ceresoli, M Cococcioni, N Colonna, I Carnimeo, A Dal Corso, S de Gironcoli, P Delugas, R DiStasio, A Ferretti, A Floris, G Fratesi, G Fugallo, R Gebauer, U Gerstmann, F Giustino, T Gorni, J Jia, M Kawamura, H Ko, A Kokalj, E Küçükbenli, M Lazzeri, M Marsili, N Marzari, F Mauri, N Nguyen, H Nguyen, A Otero-de-la Roza, L Paulatto, S Poncé, D Rocca,

R Sabatini, B Santra, M Schlipf, A Seitsonen, A Smogunov, I Timrov, T Thonhauser, P Umari, N Vast, X Wu, and S Baroni. Advanced capabilities for materials modelling with quantum espresso. *Journal of Physics : Condensed Matter*, 29(46) :465901, oct 2017. doi : 10.1088/1361-648X/aa8f79. URL https://dx.doi.org/10.1088/1361-648X/aa8f79.

[64] M V Sadovskii. Pseudogap in high-temperature superconductors. *Physics-Uspekhi*, 44(5) : 515, may 2001. doi : 10.1070/PU2001v044n05ABEH000902. URL https://iopscience.iop.org/article/10.1070/PU2001v044n05ABEH000902.

[65] P Lee, T Rice, and P Anderson. Fluctuation effects at a peierls transition. *Phys. Rev. Lett.*, 31 :462–465, Aug 1973. doi : 10.1103/PhysRevLett.31.462. URL https://link.aps.org/doi/10.1103/PhysRevLett.31.462.

[66] R McKenzie. Microscopic theory of the pseudogap and peierls transition in quasi-one-dimensional materials. *Phys. Rev. B*, 52 :16428–16442, Dec 1995. doi : 10.1103/PhysRevB.52.16428. URL https://link.aps.org/doi/10.1103/PhysRevB.52.16428.

[67] D Pines. Understanding high temperature superconductors : Progress and prospects. *Physica C : Superconductivity*, 282 :273–278, 1997. ISSN 0921-4534. doi : https://doi.org/10.1016/S0921-4534(97)00253-0. URL https://www.sciencedirect.com/science/article/pii/S0921453497002530.

[68] E Kuchinskii, I Nekrasov, and M Sadovskii. Electronic structure of two-dimensional hexagonal diselenides : Charge density waves and pseudogap behavior. *Journal of Experimental and Theoretical Physics*, 114(4) :671, April 2012. ISSN 1090-6509. doi : 10.1134/s1063776112020252. URL http://dx.doi.org/10.1134/s1063776112020252.

[69] K Velebit, P. Popčević, I. Batistić, M. Eichler, H. Berger, L. Forró, M. Dressel, N. Barišić, and E. Tutiš. Scattering-dominated high-temperature phase of 1T-$TiSe_2$: An optical conductivity study. *Phys. Rev. B*, 94 :075105, Aug 2016. doi : 10.1103/PhysRevB.94.075105. URL https://link.aps.org/doi/10.1103/PhysRevB.94.075105.

[70] G Monney, C Monney, B Hildebrand, P Aebi, and H Beck. Impact of electron-hole correlations on the $TiSe_2$ electronic structure. *Phys. Rev. Lett.*, 114 :086402, Feb 2015. doi : 10.1103/PhysRevLett.114.086402. URL https://link.aps.org/doi/10.1103/PhysRevLett.114.086402.

[71] Z Lin, C Wang, A Balassis, J Echeverry, A Vasenko, V Silkin, E Chulkov, Y Shi, J Zhang, J Guo, and X Zhu. Dramatic plasmon response to the charge-density-wave gap development in $TiSe_2$. *Phys. Rev. Lett.*, 129 :187601, Oct 2022. doi : 10.1103/PhysRevLett.129.187601. URL https://link.aps.org/doi/10.1103/PhysRevLett.129.187601.

[72] B Hildebrand, C Didiot, A Novello, G Monney, A Scarfato, A Ubaldini, H Berger, D Bowler, C Renner, and P Aebi. Doping nature of native defects in $TiSe_2$. *Phys. Rev. Lett.*, 112 :

197001, May 2014. doi : 10.1103/PhysRevLett.112.197001. URL https://link.aps.org/doi/10.1103/PhysRevLett.112.197001.

7 CONCLUSION AND FUTURE PERSPECTIVES

The general goal of this thesis was to probe and control quantum materials' properties by using time- and angle-resolved photoemission spectroscopy (TR-ARPES). We investigated three different quantum materials : a three-dimensional topological insulator (Bi_2Te_3), a layered van der Waals semiconductor (SnS_2), and a charge-density-wave (CDW) compound (1T–$TiSe_2$). Taken together, these case studies reveal how electron–phonon coupling, band renormalization, electron-electron interactions, defect states, and collective ordering dictate the ultrafast dynamics of quantum materials.

A crucial foundation of this work is the dual TR-ARPES endstation at the ALLS and CELIA laboratories, where all the experiments presented in this thesis were performed. Chapter 3 presented the ALLS endstation, based on a Yb ultrafast laser, a 6 eV probe, a tunable mid-infrared pump, and a hemispherical analyzer optimized for ultrahigh energy and momentum resolution near the Γ point. In parallel, the CELIA endstation was introduced, combining a 21.6 eV polarization-tunable XUV probe, an infrared pump, and a time-of-flight momentum microscope that enables full Brillouin-zone coverage and detailed polarization-resolved measurements. These two platforms are complementary by design : ALLS provides exceptional resolution for probing dynamics near Γ, while CELIA offers wide momentum reach for studying physics within the entire Brillouin zone. Throughout this thesis, we leveraged both setups to access the out-of-equilibrium electronic structure and to directly visualize how excited carriers, collective modes, and defect states evolve in energy, momentum, and time.

In Chapter 4, we studied p-doped Bi_2Te_3 and demonstrated that intervalley scattering between the Γ and Q valleys can be controlled through temperature-induced band renormalization. Using high-resolution TR-ARPES at ALLS, we mapped the unoccupied conduction-band landscape and followed the population dynamics in the valleys as a function of temperature. Increasing the sample temperature produces a downward shift of the conduction band minimum at Γ, driven by thermal expansion and electron–phonon coupling. This reduces the bulk bandgap at Γ and enhances the spectral overlap between Γ and Q, thereby opening a new intervalley electron–phonon scattering channel from Q to Γ. The TR-ARPES data reveal a pronounced transfer of spectral weight from Q to Γ at elevated temperatures, accompanied by a long-lived population buildup at Γ. Kinetic Monte Carlo simulations, supported by a simplified electron–phonon model, reproduce these effects and confirm that the observed long-lived population does not require invoking a spatially indirect exciton. Instead, the dynamics arise naturally from temperature-dependent changes to the scattering phase space and intervalley electron–phonon coupling. Overall, this study shows that modest changes to the bulk band structure can dramatically reshape ultrafast electron dynamics in topological insulators and identifies intervalley scattering as a key factor in understanding carrier

transport and thermoelectric performance in Bi_2Te_3. These insights may help guide the engineering of materials with enhanced thermoelectric performance

Chapter 5 examined the layered semiconductor SnS_2, where we used time-, angle-, and polarization-resolved XUV ARPES with a momentum microscope detection scheme to investigate the interplay between intrinsic defects, band bending, and ultrafast carrier dynamics. Linear dichroic XUV ARPES enabled a detailed mapping of the valence-band dispersions and the separation of in-plane and out-of-plane orbital characters. Importantly, we provided direct evidence of defect-induced in-gap states, attributed primarily to donor-like sulfur vacancies. These states generate a downward band bending at the surface and create an electron accumulation layer. Long-term evolution of the surface electronic structure after cleavage showed an increase in in-gap spectral weight and a continuous downward shift of the valence band, revealing the sensitivity of band bending to the evolving defect landscape. Using TR-ARPES with a below-bandgap infrared pump, we demonstrated that these in-gap states enable optical injection of carriers into the conduction band via sub-bandgap excitation. This process generates long-lived electrons at the conduction band minimum, photoholes in the deep in-gap states. Simultaneously, we observed a pronounced transient surface photovoltage (SPV), manifested as a rigid upward shift of the spectral features, corresponding to a partial flattening of the downward band bending. These results establish that effects govern both the static band bending and the nonequilibrium light-induced response in SnS_2, making it a model system where defect physics, band bending, and ultrafast dynamics are intrinsically linked. Furthermore, this study suggests that although surface photovoltage is generally well understood, certain aspects remain unclear and warrant further investigation in the future. The SnS_2 results highlight the central role of intrinsic donor-like defects in shaping both equilibrium band bending and nonequilibrium dynamics.

In Chapter 6, we turned to the charge-density-wave material 1T–$TiSe_2$ to study the nature of CDW fluctuations above the transition temperature. Using time-resolved XUV momentum microscopy, we directly mapped the nonequilibrium evolution of the CDW signatures at room temperature. Our equilibrium measurements confirmed the presence of the backfolded Se 4p band associated with the $2\times2\times2$ CDW superlattice far above T_{CDW}, demonstrating persistent CDW fluctuations. Upon ultrafast excitation, these fluctuations partially melt—seen as a reduction of the backfolded spectral weight—followed by rapid recovery on a timescale of ~ 700 fs. The melting dynamics lag behind the peak of the electronic temperature by 100–200 fs and correlate with the transient population of excited Ti 3d states, indicating that the fluctuating CDW is not simply tied to instantaneous electronic heating. Remarkably, the recovery of the fluctuations exhibits coherent oscillations corresponding to the CDW amplitude-mode phonon. This behaviour directly links the fluctuating CDW to a specific soft phonon mode, highlighting the importance of electron–phonon coupling. Density functional theory calculations incorporating dynamical electron–phonon self-energy corrections support this picture : the soft phonon strongly renormalizes the Se 4p states and naturally produces fluctuating replica features similar to those observed experimentally. Light-induced excitations suppress this interaction by hardening the phonon and screening the coupling, thereby quenching the

fluctuations. These results provide strong evidence that electron–phonon interactions are the dominant driver of CDW fluctuations in 1T–$TiSe_2$ at room temperature, with electron–hole correlations playing a secondary or cooperative role. This refined understanding has broader implications for fluctuating orders in quantum materials, especially given the proposed connection between CDW fluctuations and unconventional superconductivity. The dynamics of CDW fluctuations in 1T–$TiSe_2$ observed here demonstrate how optical excitation can transiently melt and reestablish fluctuating order with clear signatures of coherent amplitude modes. This opens exciting opportunities : tracking and controlling CDW amplitude and phase modes with tailored pump pulses, exploring the interplay between CDW fluctuations and superconductivity in $TiSe_2$-derived compounds, studying nonequilibrium CDW behaviour across a broader class of materials (e.g., VSe_2, $NbSe_2$, TaS_2), investigating how tuning electron–phonon coupling (via pressure, doping, or ultrafast excitation) modifies the stability of fluctuating CDW states.

Across all three materials, the key physics arises from the interplay between the electronic structure and additional degrees of freedom. In Bi_2Te_3, temperature-dependent band renormalization reshapes the scattering phase space and controls intervalley electron–phonon scattering. In SnS_2, donor-like defects generate in-gap states and band bending, which govern SPV, sub-bandgap excitation pathways, and long-lived carrier populations. In 1T–$TiSe_2$, a soft lattice phonon coupled to Se 4p states stabilizes CDW fluctuations above T_{CDW} and dictates their ultrafast melting and recovery. A unifying theme emerging from this thesis is that nonequilibrium behaviour in quantum materials cannot be understood by considering band structures in isolation. Instead, it is the dynamic balance between electron–phonon coupling, defect landscapes, collective ordering, and external driving fields that determines the ultrafast response. TR-ARPES—especially when combined with advanced detection capabilities and theoretical modelling—provides a uniquely powerful way to probe this balance by resolving the momentum-resolved spectral function and carrier populations in real time.

In summary, our results contribute to a deeper understanding of how quasiparticles, defects, and collective modes interact out of equilibrium, and lay the groundwork for future efforts aimed at controlling and engineering nonequilibrium electronic states for emerging quantum and optoelectronic technologies. As quantum materials continue to evolve as a major frontier of condensed matter physics, the ability to probe and manipulate their electronic structure on ultrafast timescales will only grow in importance. Future directions include : systematic polarization-resolved mapping of orbital textures in excited states, ultrafast circular dichroism measurements to probe Berry curvature and chirality dynamics, valley-selective excitation and detection schemes in transition-metal dichalcogenides, and symmetry-selective tracking of electronic populations across phase transitions. Such measurements will deepen our understanding of how orbital, spin, and valley degrees of freedom evolve out of equilibrium.

To fully unravel the coupling between electrons, phonons, and spins, TR-ARPES increasingly needs to be combined with complementary techniques. For example, ultrafast electron diffraction

can track lattice dynamics and phonon softening; time-resolved Raman and THz spectroscopy can follow collective modes; and time-resolved X-ray absorption or resonant scattering can probe element-specific dynamics. Multimodal approaches, i.e., incorporating time, spin, polarization, and tunable photon energy, offer a comprehensive view of how charge, lattice, and orbital degrees of freedom evolve on ultrafast timescales. There is also growing interest in operando ARPES measurements, such as applying current or strain, and in efforts to apply localized magnetic fields to samples.

As light sources become brighter, detectors faster, and theoretical tools more sophisticated, the field is poised to uncover new non-equilibrium phases, manipulate collective excitations, and deepen our understanding of electron, phonon, and spin dynamics far from equilibrium. The increasing complexity and richness of TR-ARPES data naturally motivate the use of machine learning for tasks such as faster and automated feature extraction, denoising and super-resolution reconstruction, and discovering hidden correlations or emergent structures in nonequilibrium datasets. Such tools will enable researchers to interpret complex multidimensional datasets and identify subtle dynamical signatures that might otherwise be overlooked.

8 APPENDIX

8.1 Appendix I : Light-induced Asymmetric Pseudogap below T_c in cuprates [1]

To this day, high-temperature cuprate superconductors remain an unparalleled platform for studying the competition and coexistence of emergent, static and dynamic quantum phases of matter exhibiting high transition temperature non-*s*-wave superconductivity, non-Fermi-liquid transport, and a still enigmatic pseudogap regime. However, our understanding of how superconductivity emerges alongside and competes with the pseudogap regime remains elusive.

In this work, a high-resolution, time- and angle-resolved photoemission study of the near-antinodal region of optimally doped $Bi_2Sr_2CaCu_2O_{8+\delta}$ is presented. Using mid-infrared light, we disrupt superconductivity and, for sufficiently high excitation fluence, reveal a particle–hole asymmetric, pseudogap-like density of states (DOS). We measure the electronic temperature in the nonequilibrium state and show that the pseudogap-like DOS persists for electronic temperatures well below the equilibrium superconducting critical temperature.

Supported by phenomenological theory, we demonstrate that this transient, light-induced spectral asymmetry directly reflects the interplay between superconductivity and the pseudogap. Moreover, when superconductivity is restored, a particle–hole symmetric DOS is reinstated. Our results reveal an intrinsic pseudogap DOS that is fundamentally distinct from the superconducting DOS, strongly suggesting that the two phenomena are at least partially independent and competitive in nature. In the superconducting state, the pseudogap contribution to the DOS is weak, whereas suppressing superconductivity allows pseudogap physics to emerge and modify the DOS, providing a new framework for understanding the complex interplay between intertwined phases in correlated electron systems.

Bibliographie

[1] D Armanno, O Gingras, F Goto, J-M Parent, A Longa, A Jabed, B Frimpong, R D Zhong, J Schneeloch, G D Gu, G Jargot, H Ibrahim, F Legare, B J Siwick, N Gauthier, A Georges, A J Millis, and F Boschini. Light-induced asymmetric pseudogap below T_c in cuprates. *arXiv*, nov 2025. doi : arXiv:2511.20768. URL https://doi.org/10.48550/arXiv.2511.20768.

8.2 Appendix II : Enhancing Momentum Coverage in Angle-Resolved Photoemission Spectroscopy with Hemispherical Analyzer

The momentum range accessible in an ARPES experiment depends strongly on the photon energy of the probe, and low photon energies—such as the 6 eV sources commonly used in time-resolved ARPES—are insufficient to photoemit electrons across the full Brillouin zone of most quantum materials. Moreover, although photoelectrons are emitted into a full 2π solid angle, conventional hemispherical analyzers detect only a narrow angular slice, typically $\pm 15^{\circ}$ along a single direction.

Earlier work has shown that a complete angular slice can be recorded in a fixed geometry by accelerating photoelectrons toward the analyzer with a bias voltage. However, that approach is limited to configurations where the sample surface is perfectly normal to the analyzer axis, and the full 2π solid angle can only be accessed through azimuthal sample rotation.

In this project, we extend this concept by exploiting the electrostatic deflector technology available in modern ARPES analyzers. We demonstrate that all 2π photoemitted electrons can be detected in a single, fixed configuration without requiring any mechanical rotation of the sample. This method was validated on materials such as gold and cuprate superconductors, confirming its robustness across different electronic structures and work functions. This capability is particularly beneficial for TR-ARPES, since it provides ultrafast electron dynamics over a large momentum range under identical measurement conditions.

8.3 Appendix III : Testing a Parabolic Mirror Mount for HHG probe Beam at the ALLS Laboratory

In this side project, I evaluated the feasibility of using an off-axis parabolic (OAP) mirror mounted on an XY translation stage to control the focal position of the XUV probe beam for the TR-ARPES endstation at the ALLS Laboratory. The broader motivation behind this test was to determine whether such a mount could reliably steer and focus the high-harmonic–generated (HHG) probe beam onto the sample location inside the ARPES chamber, without compromising the beam quality required for momentum-resolved photoemission measurements.

For the characterization, a He–Ne laser was used as a surrogate for the HHG beam, reproducing the optical geometry of the ARPES beamline. The mirror assembly was aligned externally, and a camera was placed at the nominal sample position to record the beam footprint, including its centroid position, size, and spatial profile. By systematically scanning the XY stage, we assessed the degree of control achievable over the focal spot.

The tests demonstrated that, in principle, the XY translation of the OAP mount allows one to adjust the focal position. However, in practice, achieving precise and repeatable alignment while preserving a clean Gaussian beam profile proved extremely challenging. Small mechanical shifts in the mount introduced significant distortions, and the iterative adjustments required to recover an undistorted beam spot were prohibitively time-consuming. These observations indicate that, although the approach is conceptually viable, it is not sufficiently efficient for routine use in an HHG-based ARPES beamline, where long-term stability and rapid alignment are essential.

8.4 Appendix IV : Developing a Reflectivity Measurement Setup for SnSe at the CELIA Laboratory

During our TR-ARPES investigation of the layered semiconductor SnSe, it proved highly valuable to complement the photoemission data with independent optical measurements to better interpret the polarization-resolved pump-induced dynamics. In particular, a quantitative understanding of how the reflectivity of SnSe varies with pump polarization and angle of incidence is essential for assessing the absorbed fluence and the anisotropic coupling of the infrared field to the crystal's two in-plane eigenaxes (Γ–X and Γ–Y).

To address this need, we developed a dedicated reflectivity measurement setup capable of probing the polarization dependence of the 1030 nm pump beam using a motorized half-wave plate (HWP). The setup allows precise control of both the incidence angle of the incoming beam and the azimuthal orientation of the SnSe crystal, enabling measurements along both Γ–X and Γ–Y high-symmetry directions. Two incidence geometries were explored : a near-normal configuration ($\sim 5°$) and an oblique configuration at $65°$, matching the pump incidence angle used in the TR-ARPES beamline.

In parallel with the experimental platform, we implemented a Fresnel-equation–based model to calculate the expected reflectivity as a function of polarization for an anisotropic dielectric tensor. This model successfully reproduces the qualitative evolution and symmetry of the measured reflectivity curves, capturing the strong anisotropy between the two eigenaxes. However, despite this qualitative agreement, the experimental setup does not provide sufficiently precise control over the angle of incidence or the laser spot position on the sample to extract reliable quantitative values of the dielectric constants. As a result, while the measurements offer valuable qualitative insight into the polarization-dependent optical response of SnSe, they cannot yet be used for a full dielectric-function reconstruction.

8.5 Appendix V : Scientific Contributions

1. **Speaker :**
   School on UV and X-ray Spectroscopy of Correlated Electron Systems,
   Les Houches School of Physics, Les Houches, France, September 15-26, 2025.
2. **Speaker :**
   Groupement de Recherche Ultrafast Phenomenat : GDR UP Conference,
   Paris, France, March 13-14, 2025.
3. **Poster :**
   LIGHT S&T Annual Student Conference, University of Bordeaux,
   Bordeaux, France, February 26, 2025.
4. **Speaker :**
   Journée 2024 du Thrust 1 du GPR LIGHT,
   Bordeaux, France, December 4, 2024.
5. **Poster :**
   Electron and Spin Dynamics - 7th Workshop,
   Paris, France, November 29, 2024.
6. **Poster :**
   Montréal Photonics Networking Event,
   Montréal, Québec, Canada, November 22, 2023.
7. **Poster :**
   Advanced Laser Light Source Workshop,
   Saint-Sauveur, Québec, Canada, September 6-8, 2023.

8.6 Appendix VI : List of Publications

- **A Jabed**, F Goto, B Frimpong, D Armanno, A Longa, M Michiardi, A Damascelli, P Hofmann, G Jargot, H Ibrahim, F Légaré, N Gauthier, S Beaulieu, and F Boschini, "Control of intervalley scattering in Bi_2Te_3 via temperature-dependent band renormalization," *npj Quantum Materials*, Jan. 2026. DOI : 10.1038/s41535-025-00842-8.
- S Fragkos, H Orio, N G Erhardt, **A Jabed**, S Sasi, Q Courtade, M P T Masilamani, M Ünzelmann, F Diekmann, B Hildebrand, D Descamps, S Petit, F Boschini, J Minár, Y Mairesse, F Reinert, K Rossnagel, D Novko, S Beaulieu, and J Schusser, "Electron-phonon-dominated charge-density-wave fluctuations in $TiSe_2$ accessed by ultrafast nonequilibrium dynamics," *Communications Physics*, Feb. 2026. DOI : 10.1038/s42005-026-02521-x.
- D Armanno, O Gingras, F Goto, J-M Parent, A Longa, **A Jabed**, B Frimpong, R D Zhong, J Schneeloch, G D Gu, G Jargot, H Ibrahim, F Légaré, B J Siwick, N Gauthier, A Georges, A J Millis, and F Boschini, "Light-induced asymmetric pseudogap below T_c in cuprates," arXiv preprint (Nov. 2025). DOI : 10.48550/arXiv.2511.20768; submitted to *Nature Physics*.
- N Gauthier, B Frimpong, D Armanno, **A Jabed**, F Goto, V Hasse, C Felser, G Gu, H Ibrahim, F Légaré, and F Boschini, "Detecting the full photoemission cone from laser-based ARPES experiments by leveraging deflector technology," arXiv preprint (Jan. 2026). DOI : 10.48550/arXiv.2601.17099; submitted to *Review Scientific Instruments*.
- **A Jabed**, Q Courtade, F Goto, D Descamps, S Petit, F Boschini, S Fragkos, and S Beaulieu, "Ultrafast light-induced dynamics mediated by in-gap states in layered SnS_2," *In preparation*.